Design, Synthesis, and Study of Novel Platforms for Iron-N_2 Chemistry and Photoinduced, Copper-mediated C-N Bond Formation

Thesis by

Sidney E. Creutz

In Partial Fulfillment of the Requirements for the degree of

Doctor of Philosophy

CALIFORNIA INSTITUTE OF TECHNOLOGY

Pasadena, California

2016

(Defended February 8th, 2016)

ACKNOWLEDGEMENTS

The last approximately 5.5 years of graduate school have been, though never easy and often frustrating, almost universally enjoyable. It cannot be overstated how extremely privileged I feel to have been able to spend this time learning and exploring inorganic chemistry. For that, I must first and foremost thank Jonas for allowing me to work in his lab and creating an excellent research environment. Jonas has given me a huge amount of freedom to pursue problems that interested me, while still providing guidance and advice as needed. The other members of the Peters lab have also shaped my experience during grad school, and every graduate student, postdoc, and undergrad with whom I've overlapped has contributed positively to my growth as a scientist in more ways than I can list here. I must particularly thank Caroline Saouma for helping me get started when I first arrived (and allowing me to inherit what is inarguably the best hood in the lab), and Jon Rittle, who joined the lab at the same time as me and whose example has continuously pushed me to be a better chemist. I am also grateful to Prof. Greg Fu for his invaluable mentorship during my work on copper chemistry, and to the other members of my committee, Prof. Theo Agapie and Prof. Mitchio Okumura, for their time and advice.

I would also like to acknowledge the training and mentorship I received during my undergraduate years working in the labs of Prof. Mo Movassaghi, Prof. Moungi Bawendi, and Prof. Kit Cummins, and the graduate students who mentored me, including Omar Ahmad, Lisa Marshall, and Nick Piro, along with many others who provided informal guidance. The skills (and confidence) I acquired in all of those labs proved essential during my graduate work.

Finally, I'd like to sincerely thank my family for their support, and my friends outside of lab who've contributed to making the last five and a half years awesome. I've had the opportunity to explore many of the off-trail bits of California and the southwest in general, and I'm extremely grateful to those who've accompanied me on those explorations. I'd particularly like to thank the Southern California Grotto and all the people I've met through that organization; they have helped me feel at home in California. The list of people who I've been privileged to go on adventures with during my time here is far too long to enumerate; in any case, it's very unlikely any of them will ever read this—with the possible exception of Chris Roske and Kevin Hwang, who I believe share the dubious distinction of being the only other inorganic chemists to go caving and canyoneering with me (so far).

ABSTRACT

Several new ligand platforms designed to support iron dinitrogen chemistry have been developed. First, we report Fe complexes of a tris(phosphino)alkyl (CP^{iPr}_3) ligand featuring an axial carbon donor intended to conceptually model the interstitial carbide atom of the nitrogenase iron-molybdenum cofactor (FeMoco). It is established that in this scaffold, the iron center binds dinitrogen trans to the C_{alkyl} anchor in three structurally characterized oxidation states. Fe-C_{alkyl} lengthening is observed upon reduction, reflective of significant ionic character in the Fe-C_{alkyl} interaction. The anionic $(CP^{iPr}_3)FeN_2^-$ species can be functionalized by a silyl electrophile to generate (CP^{iPr}_3)Fe-N_2SiR_3. This species also functions as a modest catalyst for the reduction of N_2 to NH_3. Next, we introduce a new binucleating ligand scaffold that supports an Fe(μ-SAr)Fe diiron subunit that coordinates dinitrogen (N_2-Fe(μ-SAr)Fe-N_2) across at least three oxidation states ($Fe^{II}Fe^{II}$, $Fe^{II}Fe^{I}$, and $Fe^{I}Fe^{I}$). Despite the sulfur-rich coordination environment of iron in FeMoco, synthetic examples of transition metal model complexes that bind N_2 and also feature sulfur donor ligands remain scarce; these complexes thus represent an unusual series of low-valent diiron complexes featuring thiolate and dinitrogen ligands. The (N_2-Fe(μ-SAr)Fe-N_2) system undergoes reduction of the bound N_2 to produce NH_3 (~50% yield) and can efficiently catalyze the disproportionation of N_2H_4 to NH_3 and N_2. The present scaffold also supports dinitrogen binding concomitant with hydride as a co-ligand. Next, inspired by the importance of secondary-sphere interactions in many metalloenzymes, we present complexes of iron in two new ligand scaffolds ($[SiP^{NMe}_3]$ and $[SiP^{iPr}_2P^{NMe}]$) that incorporate hydrogen-bond acceptors (tertiary amines) which engage in interactions with nitrogenous substrates bound to the iron center (NH_3 and N_2H_4). Cation binding is also facilitated in anionic Fe(0)-N_2 complexes. While Fe-N_2 complexes of a related ligand ($[SiP^{iPr}_3]$) lacking hydrogen-bond acceptors produce a substantial amount of ammonia when treated with acid and reductant, the presence of the pendant amines instead facilitates the formation of metal hydride species.

Additionally, we present the development and mechanistic study of copper-mediated and copper-catalyzed photoinduced C-N bond forming reactions. Irradiation of a copper-amido complex, ((*m*-tol)$_3$P)$_2$Cu(carbazolide), in the presence of aryl halides furnishes N-phenylcarbazole under mild conditions. The mechanism likely proceeds *via* single-electron transfer from an excited state of the copper complex to the aryl halide, generating an aryl radical. An array of experimental data are consistent with a radical intermediate, including a cyclization/stereochemical investigation and a reactivity study, providing the first substantial experimental support for the viability of a radical pathway for Ullmann C-N bond formation. The copper complex can also be used as a precatalyst for

Ullmann C-N couplings. We also disclose further study of catalytic C_{alkyl}-N couplings using a CuI precatalyst, and discuss the likely role of $[Cu(carbazolide)_2]^-$ and $[Cu(carbazolide)_3]^-$ species as intermediates in these reactions.

Finally, we report a series of four-coordinate, pseudotetrahedral P_3Fe^{II}-X complexes supported by tris(phosphine)borate ($[PhBP_3^R]^-$) and phosphiniminato X-type ligands (-N=PR'$_3$) that in combination tune the spin-crossover behavior of the system. Low-coordinate transition metal complexes such as these that undergo reversible spin-crossover remain rare, and the spin equilibria of these systems have been studied in detail by a suite of spectroscopic techniques.

PUBLISHED CONTENT AND CONTRIBUTIONS

This dissertation contains material adapted with permission from the following published manuscripts:

1. Creutz, S. E.; Peters, J. C. *J. Am. Chem. Soc.* **2014**, *136*, 1105. [doi: 10.1021/ja4114962]
2. Creutz, S. E.; Peters, J. C. *J. Am. Chem. Soc.* **2015**, *137*, 7310. [doi: 10.1021/jacs.5b04738]
3. Creutz, S. E.; Lotito, K. J.; Fu, G. C.; Peters, J. C. *Science*, **2012**, *338*, 647. [doi: 10.1126/science.1226458]
4. Bissember, A. C.; Lundgren, R. J.; Creutz, S. E.; Peters, J. C.; Fu, G. C. *Angew. Chem. Int. Ed.* **2013**, *52*, 5129. [doi: 10.1002/anie.201301202]

TABLE OF CONTENTS

Acknowledgements……...iii
Abstract ……iv
Published Content and Contributions…….....vi
Table of Contents…….... vii
Detailed Table of Contents.....viii
List of Illustrations and/or Tables……..x
List of Abbreviations…….……..…...xix
Chapter 1.: Introduction..... 1
Chapter 2: Catalytic reduction of N_2 to NH_3 by an Fe-N_2 complex featuring a C-atom anchor..... 26
Chapter 3: Diiron bridged-thiolate complexes that bind N_2 at the $Fe^{II}Fe^{II}$, $Fe^{II}Fe^{I}$, and $Fe^{I}Fe^{I}$ redox states..... 67
Chapter 4: Incorporating secondary-sphere interactions into Fe complexes relevant to N_2 fixation..... 98
Chapter 5: Development of photoinduced, copper-mediated and copper-catalyzed C-N coupling reactions 140
Chapter 6: Spin-state tuning at pseudotetrahedral d^6 ions—reversible spin-crossover in $[BP_3]Fe^{II}$-X complexes 176
Appendix A: Supplementary data for Chapter 4 221
Appendix B: Supplementary data for Chapter 6..... 258

DETAILED TABLE OF CONTENTS

Chapter I: Introduction 1
1.1 Motivation 2
1.2 Earth-abundant transition metals in catalysis 2
1.2.1 Copper coupling catalysis and photochemistry 4
1.3 Controlling metal reactivity through ligand design 5
1.3.1 Bioinspired ligand and complex design 6
1.4 Nitrogen activation by molecular systems 8
1.4.1 The mechanism of N_2 fixation by molecular iron systems 11
1.4.2 Analogy to nitrogenase 17
1.5 Chapter summaries 19
1.6 References 22

Chapter 2: Catalytic reduction of N_2 to NH_3 by an Fe-N_2 complex featuring a C-atom anchor 26
2.1 Introduction 27
2.2 Results and discussion 30
2.2.1 Ligand synthesis 30
2.2.2 Metallation at iron and precursor complexes 33
2.2.3 Synthesis and characterization of $\{(CP^{iPr}_3)FeN_2\}^n$ (n = 0, -1, +1) 37
2.2.4 Reactivity studies 44
2.3 Conclusions 48
2.4 Experimental methods 50
2.5 References 62

Chapter 3: Diiron bridged-thiolate complexes that bind N_2 at the $Fe^{II}Fe^{II}$, $Fe^{II}Fe^{I}$, and $Fe^{I}Fe^{I}$ redox states 67
3.1 Introduction 68
3.2 Results and discussion 69
3.3 Concluding remarks 81
3.4 Experimental methods 82
3.5 References 94

Chapter 4: Incorporating secondary-sphere interactions into Fe complexes relevant to N_2 fixation 98
4.1 Introduction 99
4.2 Results and discussion 103
4.2.1 Ligand design and synthesis 103

4.2.2 Synthesis of precursor iron complexes of L_1 and L_2 105
4.2.3 Synthesis and characterization of Fe-N_xH_y complexes 107
4.2.4 Synthesis and reactivity of reduced Fe-N_2 complexes 112
4.2.5 Complexes of a zwitterionic ligand 116
4.2.6 Synthesis of a boratrane ligand variant 119
4.3 Conclusions 121
4.4 Experimental methods 121
4.5 References 136

Chapter 5: Development of photoinduced, copper-mediated and copper-catalyzed C-N coupling reactions 140
5.1 Introduction 141
5.2 Results and discussion 142
5.2.1 Stoichiometric C_{aryl}-N coupling reactivity 142
5.2.2 Mechanistic probes 148
5.2.3 Catalytic C_{aryl}-N coupling reactivity 152
5.2.4 Photoinduced, copper-catalyzed C_{alkyl}-N coupling and mechanistic studies 154
5.3 Conclusions 159
4.4 Experimental methods 160
4.5 References and notes 172

Chapter 6: Spin-state tuning at pseudotetrahedral d^6 ions—reversible spin-crossover in $[BP_3]Fe^{II}$-X complexes 176
6.1 Introduction 177
6.2 Results 179
6.2.1 Synthesis of $[PhBP^R_3]Fe(N{=}PR'_3)$ complexes 179
6.2.2 Structural characterization 181
6.2.3 UV-visible spectroscopy 183
6.2.4 NMR characterization and solution magnetic susceptibility measurements 188
6.2.5 Solid state (SQUID) magnetometry 192
6.2.6 Solid state infrared spectroscopy 194
6.2.7 Mossbauer spectroscopy 195
6.3 Discussion 197
6.4 Experimental details 206
6.5 References 216

Appendix A: Supplementary data for Chapter 4 221
Appendix B: Supplementary data for Chapter 6 258

LIST OF ILLUSTRATIONS AND TABLES

Chapter 1

Figure 1.1: Examples of ligand design 5
Figure 1.2: Biomimetic and bioinspired synthetic metal complexes 7
Figure 1.3: Biological and synthetic N_2 fixation catalysts 9
Figure 1.4: Generalized limiting pathways for N_2 fixation 11
Figure 1.5: Mechanistic outline of N_2 fixation by (TPB)FeN_2^- 13
Figure 1.6: Branching between different protonation pathways 17
Figure 1.7: Geometric changes upon N_2 binding to FeMoco 18
Scheme 1.1: Some model reactions relevant to N_2 fixation 15

Chapter 2

Figure 2.1: Design of analogues for the carbide ligand of FeMoco 28
Figure 2.2: Trigonal bipyramidal ligand scaffolds 29
Figure 2.3: Structures of some {(CP_3)H}Fe and (CP_3)Fe complexes 33
Figure 2.4: Structures of {(CP_3)H}Co complexes 37
Figure 2.5: Structures of a series of [(CP_3)FeN_2](-1, 0, +1) complexes 38
Figure 2.6: Cyclic voltammogram of (CP_3)FeN_2 40
Figure 2.7: DFT-computed orbital interactions in [(CP_3)FeN_2]$^-$ 44
Figure 2.8: Spectroscopic analysis of catalytic reaction mixtures 47
Scheme 2.1: Synthesis of (CP_3)H 31
Scheme 2.2: Synthesis of iron complexes of (CP_3)H 35
Scheme 2.3: Synthesis of a series of (CP_3)FeN_2 complexes 35
Table 2.1: Characterization data for (CP_3)FeN_2 adducts 42

Chapter 3

Figure 3.1: Fe-S-Fe motif in FeMoco 68

Figure 3.2: Structure of {Cl-Fe(μ-SAr)Fe-Cl}$^{-}$ 70
Figure 3.3: Structure of {N_2-Fe(μ-SAr)Fe-N_2}$^{-}$ 72
Figure 3.4: Structures of {N_2-Fe(μ-SAr)Fe-N_2}^{0} and {N_2-Fe(μ-SAr)Fe-N_2}$^{+}$ 73
Figure 3.5: Cyclic voltammogram of $(N_2)_2Fe_2$ adducts 74
Figure 3.6: Spectroscopic characterization of N_2-Fe(μ-SAr)Fe(H)-N_2 77
Figure 3.7: Structure of a bridging formate complex 78
Figure 3.8: Structure of {N_2-Fe(μ-SAr)Fe(H)-N_2}$^{-}$ 79
Scheme 3.1: Synthesis of protected thiolate ligand 69
Scheme 3.2: Metallation of μ-thiolate ligand 71
Scheme 3.3: Synthesis of $(N_2)_2Fe_2$ adducts 74
Scheme 3.4: Synthesis of hydride complexes 76
Scheme 3.5: NH_3 generation from N_2 or N_2H_4 80
Scheme 3.6: Synthesis of ligand precursor 83
Table 3.1: Comparison of select parameters for Fe-(μ-SAr)-Fe complexes 75
Table 3.2: Ammonia production by hydrazine disproportionation 94

Chapter 4

Figure 4.1: Interaction of His-195 with FeMoco 100
Figure 4.2: Iron systems incorporating hydrogen-bonding ligands 101
Figure 4.3: Structures of [Fe]Cl and [Fe]N_2 complexes 106
Figure 4.4: Structure of NH_3 and N_2H_4 adducts 109
Figure 4.5: Synthesis of a terminal –NH_2 complex 111
Figure 4.6: Synthesis of Fe-N_2 anions and protonation reactivity 113
Figure 4.7: Structure of Fe-N_2 anions 114
Figure 4.8: Kinetic and thermodynamic protonation sites 116
Figure 4.9: Synthesis and characterization of zwitterionic complex 117
Figure 4.10: Structure of ($TP^{NMe}B$)FeBr 120

Scheme 4.1: Synthesis of ligand arm 103
Scheme 4.2: Synthesis of ligands with pendant amines 104
Scheme 4.3: Synthesis of Fe(II) and Fe(I) precursor complexes 105
Scheme 4.4: Synthesis of cationic NH_3 and N_2H_4 adducts 107
Scheme 4.5: Synthesis of boratrane ligand 119
Table 4.1: Comparison data for [Fe]Cl and [Fe]N_2 complexes 106

Chapter 5

Chart 5.1: Isotopomers of deuterated radical clock 166
Figure 5.1: Generalized equation and mechanisms for Ullmann coupling to form an arylamine 142
Figure 5.2: Possible pathway for photoinduced C-N bond formation 143
Figure 5.3: Structure of Cu[P(*m*-tol)$_3$]$_2$(carbazolide) 144
Figure 5.4: Properties of Cu[P(*m*-tol)$_3$]$_2$(carbazolide) 145
Figure 5.5: EPR spectrum of photolytic reaction mixture 149
Figure 5.6: Cyclization of a radical probe 150
Figure 5.7: Stereochemical study of a photoinduced Ullmann reaction .. 150
Figure 5.8: Competition study of a photoinduced Ullmann reaction 151
Figure 5.9: Formation of C_{alkyl}-N bonds 154
Figure 5.10: Possible pathway for photoinduced, Cu-catalyzed N-alkylation of carbazole 155
Figure 5.11: Structure of [Cu(carbazolide)$_2$]$^-$ 155
Figure 5.12: Reactivity of [Cu(carbazolide)$_2$]$^-$ 156
Figure 5.13: EPR detection of photogenerated a Cu^{II} complex 157
Figure 5.14: EPR detection of a Cu^{II} complex generated by chemical oxidation 158
Scheme 5.1: Formation of isotopomers from deteurated radical clock reaction 168

Table 5.1: Photoinduced C-N bond formation using Cu[P(*m*-tol)$_3$]$_2$(carbazolide) and PhX 146
Table 5.2: Photoinduced catalytic C-N bond formation..... 151

Chapter 6

Figure 6.1: Structures of [PhBP$^R_3$]Fe(NPR'$_3$) complexes..... 182
Figure 6.2: Changes in metrical parameters between low- and high-spin complexes 183
Figure 6.3: Temperature-dependent UV-vis spectra 186
Figure 6.4: Modeling of UV-vis spectra..... 187
Figure 6.5: Fitting of spin state populations from UV-vis data 187
Figure 6.6: Temperature-dependent NMR spectra..... 189
Figure 6.7: VT solution magnetic susceptibility data..... 191
Figure 6.8: Solid-state SQUID magnetometry data 192
Figure 6.9: Effect of sample preparation on SQUID magnetometry..... 194
Figure 6.10: Infrared spectroscopy data..... 195
Figure 6.11: Mossbauer spectroscopy data..... 196
Figure 6.12: Qualitative electronic structure 198
Figure 6.13: Valence molecular orbitals calculated by DFT 199
Figure 6.14: Trends in spin-crossover parameters..... 201
Figure 6.15: Assignments of UV-vis transitions 204
Scheme 6.1: Synthesis of [PhBP$^R_3$]Fe(NPR'$_3$) complexes 180
Table 6.1: Metrical parameters for [PhBP$^R_3$]Fe(NPR'$_3$) complexes 182
Table 6.2: UV-vis data 186
Table 6.3: Thermodynamic parameters derived from UV-vis data 188
Table 6.4: Thermodynamic parameters derived from NMR data..... 190
Table 6.5: Mossbauer parameters 197

Appendix A

Figure A.1: ^{1}H NMR of (2-bromophenyl)divinylphosphine oxide 222
Figure A.2: ^{31}P NMR of (2-bromophenyl)divinylphosphine oxide..... 222
Figure A.3: ^{1}H NMR of 4-(2-bromophenyl)-1-methyl-1,4-azaphosphinane-4-oxide 223
Figure A.4: ^{31}P NMR of 4-(2-bromophenyl)-1-methyl-1,4-azaphosphinane-4-oxide..... 223
Figure A.5: ^{13}C NMR of 4-(2-bromophenyl)-1-methyl-1,4-azaphosphinane-4-oxide 224
Figure A.6: ^{1}H NMR of **L$_0$**..... 224
Figure A.7: ^{31}P NMR of **L$_0$** 225
Figure A.8: ^{13}C NMR of **L$_0$**..... 225
Figure A.9: ^{1}H NMR of **L$_1$**..... 226
Figure A.10: ^{31}P NMR of **L$_1$** 226
Figure A.11: ^{13}C NMR of **L$_1$**..... 227
Figure A.12: ^{1}H NMR of **L$_2$**..... 227
Figure A.13: ^{31}P NMR of **L$_2$** 227
Figure A.14: ^{13}C NMR of **L$_2$**..... 228
Figure A.15: ^{1}H NMR of **4.1**..... 228
Figure A.16: UV-vis spectrum of **4.1** 228
Figure A.17: ^{1}H NMR of **4.1'** 229
Figure A.18: UV-vis spectrum of **4.1'** 229
Figure A.19: ^{1}H NMR of **4.2**..... 229
Figure A.20: IR spectrum of **4.2** 230
Figure A.21: UV-vis spectrum of **4.2** 230
Figure A.22: ^{1}H NMR of **4.2'** 230
Figure A.23: IR spectrum of **4.2'** 231
Figure A.24: ^{1}H NMR of **4.3**..... 231
Figure A.25: UV-vis spectrum of **4.3** 231
Figure A.26: ^{1}H NMR of **4.3'** 232

Figure A.27: UV-vis spectrum of **4.3'** 232
Figure A.28: ^{1}H NMR of **4.4** 232
Figure A.29: UV-vis spectrum of **4.4** 233
Figure A.30: ^{1}H NMR of **4.6** 233
Figure A.31: ^{31}P NMR of **4.6** 234
Figure A.32: IR spectrum of **4.6** 234
Figure A.33: UV-vis spectrum of **4.6** 234
Figure A.34: ^{1}H NMR spectrum of **4.6'** 235
Figure A.35: ^{31}P NMR spectrum of **4.6'** 235
Figure A.36: IR spectrum of **4.6'** 235
Figure A.37: UV-vis spectrum of **4.6'** 236
Figure A.38: ^{1}H NMR of **4.5** 236
Figure A.39: UV-vis spectrum of **4.5** 237
Figure A.40: ^{1}H NMR of oxidation of **4.5** 238
Figure A.41: EPR spectrum of oxidation of **4.5** 238
Figure A.42: ^{1}H NMR of[SiP$^{i\mathrm{Pr}}{}_{2}$P$^{\mathrm{NMe2}}$FeCl]OTf 239
Figure A.43: ^{31}P NMR of **4.7** 239
Figure A.44: Cyclic voltammogram of **4.7** 240
Figure A.45: Cyclic voltammogram of **4.6** 240
Figure A.46: Cyclic voltammogram of **4.6'** 241
Figure A.47: ^{1}H NMR of protonation of **4.6'** 242
Figure A.48: ^{31}P NMR of protonation of **4.6'** 243
Figure A.49: ^{31}P NMR of protonation of **4.6** 243
Figure A.50: ^{1}H NMR of protonation of **4.6** 244
Figure A.51: ^{1}H NMR of protonation of **4.6** (hydride region) 244
Figure A.52: IR spectrum of protonation of **4.6** 245
Figure A.53: Structure of the SiP$^{i\mathrm{Pr}}{}_{2}$P$^{\mathrm{NMe}}$Fe(N$_2$)(H) 245
Figure A.54: ^{1}H NMR of protonation of **4.7** 246
Figure A.55: IR of protonation of **4.7** 246

Figure A.56: ^{1}H NMR of protonation of [SiP$^{i\text{Pr}}_{3}$FeN$_2$][Na(THF)$_3$] 247
Figure A.57: IR spectrum of protonation of [SiP$^{i\text{Pr}}_{3}$FeN$_2$][Na(THF)$_3$] ... 248
Figure A.58: ^{1}H NMR of decomposition of **4.4** 248
Figure A.59: Decomposition of **4.4** 249
Figure A.60: Calculated structures of ligand boat and chair conformations 250
Figure A.61: Electrostatic potential maps for **4.7** and **4.6** 251
Figure A.62: Calculated structures of protonation products 252
Table A.1: Crystallographic data for **4.1', 4.2',** and **4.4** 254
Table A.2: Crystallographic data for **4.3'**, **4.7**, and **4.6** 255
Table A.3: Crystallographic data for **4.6'**, **4.5**, and **4.3** 256
Table A.4: Crystallographic data for SiP$^{i\text{Pr}}_{2}$P$^{\text{NMe}}$Fe(N$_2$)(H) 257

Appendix B

Figure B.1: **^{1}**H NMR spectrum of **6.1** 259
Figure B.2: ^{1}H NMR spectrum of **6.2** 259
Figure B.3: **^{1}**H NMR spectrum of **6.3** 260
Figure B.4: ^{1}H NMR spectrum of **6.4** 260
Figure B.5: ^{1}H NMR spectrum of **6.5** 261
Figure B.6: ^{1}H NMR of **6.6** 261
Figure B.7: ^{1}H NMR of **6.7** 262
Figure B.8: ^{1}H NMR of **6.8** 262
Figure B.9: ^{1}H NMR of **6.9** 263
Figure B.10: ^{31}P NMR of **6.3** 263
Figure B.11: ^{31}P NMR of **6.4** 264
Figure B.12: ^{31}P NMR of **6.5** 264
Figure B.13: ^{31}P NMR of **6.6** 264
Figure B.14: Infrared spectrum of **6.1** 265
Figure B.15: Infrared spectrum of **6.2** 265

Figure B.16: Infrared spectrum of **6.4** 266
Figure B.17: Variable-temperature ^{1}H NMR of **6.1** 266
Figure B.18: Variable temperature ^{1}H NMR spectra of **6.2** 267
Figure B.19: Variable-temperature ^{1}H NMR spectra of **6.4** 267
Figure B.20: Variable-temperature ^{1}H NMR spectra of **6.5** 268
Figure B.21: Variable-temperature ^{1}H NMR spectra of **6.9** 268
Figure B.22: Variation of the chemical shifts in the ^{1}H NMR of **6.1** with temperature 270
Figure B.23: Variation of the chemical shifts in the ^{1}H NMR of **6.2** with temperature 270
Figure B.24: Variation of the chemical shifts in the ^{1}H NMR of **6.3** with temperature 271
Figure B.25: Variation of the chemical shifts in the ^{1}H NMR of **6.4** with temperature 271
Figure B.26: Variation of the chemical shifts in the ^{1}H NMR of **6.5** with temperature 272
Figure B.27: Variable temperature Evans method data 273
Figure B.28: Spectral decomposition of the VT UV-vis spectra of **6.1**... 274
Figure B.29: Spectral decomposition of the VT UV-vis spectra of **6.2**... 275
Figure B.30: Spectral decomposition of the VT UV-vis spectra of **6.3**... 275
Figure B.31: Spectral decomposition of the VT UV-vis spectra of **6.4**... 276
Figure B.32: Spectral decomposition of the VT UV-vis spectra of **6.6**... 276
Figure B.33: Spectral decomposition of the VT UV-vis spectra of **6.9**... 277
Figure B.34: Fit parameters for VT UV-vis modeling 278
Figure B.35: More fit parameters for VT UV-vis modeling 278
Figure B.36: More fit parameters for VT UV-vis modeling 279
Figure B.37: More fit parameters for VT UV-vis modeling 279
Figure B.38: Fits to UV-vis spectra for **6.1** 280
Figure B.39: Density correction to fit parameters 281

Figure B.40: Fits to intensity vs. total area 282
Figure B.41: Attempted fits to intensity data..... 282
Figure B.42: Variable temperature Mossbauer spectra of **6.3** 283
Figure B.43: Additional SQUID data: changes upon heating..... 285
Figure B.44: Effect of heating pre-treatment on SQUID data 285
Figure B.45: Crystal structure of complex **6.8** 287
Figure B.46: TDDFT results 288
Figure B.47: Calculated spectrum..... 289
Table B.1: Fits to variable-temperature Evans method data 273
Table B.2: Fits to variable-temperature Mossbauer data 284
Table B.3: Crystallographic details for **6.1**, **6.2**, **6.4**, and **6.5**. 286
Table B.4: Crystallographic details for compounds **6.7**-**6.9** 286

ABBREVIATIONS

A^X	Hyperfine coupling constant due to nucleus X
Anal	Analysis
atm	Atmosphere
Avg	Average
BAr^F_4	$[B(3,5\text{-}C_6H_3(CF_3)_2)_4]^-$
br	broad
Bu	n-Butyl
C	constant
ca	circa
calcd	Calculated
C_{alkyl}	sp^3-hybridized carbon atom
C_{aryl}	sp^2-hybridized carbon atom in an aromatic fragment
CCD	Charge-coupled device
cm	centimeter
cm^{-1}	Wave number
CO	Carbon monoxide
Cp	Cyclopentadienyl
Cp*	Pentamethylcyclopentadienyl
CP_3	$(o\text{-}PR_2C_6H_4)_3C^-$ ligand
CP^{iPr}_3	$(o\text{-}PiPr_2C_6H_4)_3C^-$ ligand
CV	cyclic voltammogram
d	doublet or deuterium
dd	doublet of doublets
d_x	compound with x deuterium atoms
DFT	Density Functional Theory
DME	1,2-dimethoxyethane
e	electron
ENDOR	Electron nuclear double resonance
EPR	Electron paramagnetic resonance
ESI-MS	Electrospray ionization mass spectrometry
eq	Equivalents
equiv	Equivalents
EXAFS	Extended X-ray absorption fine structure
eV	Electron volt
E	Any element
E^0	Reduction or oxidation potential

F	Structure factor
Fc	Ferrocene
FeMoco	Iron-molybdenum cofactor of the nitrogenase enzyme
GC	gas chromatography
G	Gauss
g	Gram
g	Electron g-factor
GC	Gas chromatography
GHz	Gigahertz
H	Enthalpy
HIPT	*h*exa-*iso*propyl-*t*erphenyl
HMQC	heteronuclear multiple quantum coherence
HOMO	Highest-Occupied Molecular Orbital
Hz	Hertz
iPr	isopropyl
IR	Infrared
$^{x}J_{AB}$	NMR coupling constant between atoms A and B along X number of bonds
J	NMR coupling constant or magnetic coupling constant
K	Kelvin or equilibrium constant
L	Generic neutral dative ligand
LUMO	Lowes-Unoccupied Molecular Orbital
kcal	Kilocalorie
m	multiplet
M	Concentration in molarity
max	Maximum
Me	Methyl
mg	Milligram
MHz	Megahertz
mL	Milliliter
mM	Millimolar
mm	Millimeter
mV	Millivolt
mmol	Millimole
MO	Molecular orbital
mol	Mole
MS	Mass spectrum
n	generic number
NBO	Natural Bond Orbital
nm	nanometer
NMR	Nuclear magnetic resonance

N_xH_y	Generic nitrogenous ligand with x N atoms and y H atoms
o	*ortho*
OA	Oxidative addition
OTf	OSO_2CF_3
Ph	Phenyl
pK_a	Acid dissociation constant
q	quartet
R	generic organic group or R-factor
RE	Reductive elimination
RT	Room temperature
S	Entropy
S	Spin quantum number
s	Singlet or second
SET	Single electron transfer
SiP_3	$(o\text{-}PR_2C_6H_4)_3Si^-$
$SiP^{iPr}{}_3$	$(o\text{-}P(iPr)_2C_6H_4)_3Si^-$
t	Triplet or time
TBA	Tetra-*n*-butyl ammonium
tBu	*tert*-Butyl
Tf	SO_2CF_3
THF	Tetrahydrofuran
TMS	Trimethylsilyl
TPB	$o\text{-}iPr_2P(C_6H_4))_3B$ or generically $o\text{-}R_2P(C_6H_4))_3B$
UV	Ultraviolot
V	Volt
vis	Visible
wR	Weighted R-factor
X	Generic anionic atom or molecule
XAS	X-ray absorption spectroscopy
XANES	X-ray Absorption Near Edge Spectroscopy
XRD	X-ray diffraction
$^{\alpha}N$	Proximal nitrogen atom of a bound N_2 ligand
$^{\beta}N$	Terminal nitrogen atom of a bound N_2 ligand
γ	High frequency electromagnetic radiation
ΔEQ	Mössbauer quadrupole splitting
δ	Chemical shift or Mössbauer isomer shift
°	Degree
°C	Degrees Celsius
*	Excited state
ε	Extinction coefficient in units of $M^{-1}cm^{-1}$

η^x	Hapticity of order x
λ	Wavelength
λ_{max}	Wavelength of local maximum intensity
μ	Bridging
μ-X	Bridging X ligand
μB	Bohr magneton
μeff	Effective magnetic moment
μL	Microliter
Σ	Summation
σ	Sigma symmetry orbital or interaction
σ*	Sigma symmetry antibonding interaction
π	Pi symmetry orbital or interaction
π*	Pi symmetry antibonding interaction
Å	Angstrom
12-c-4	12-crown-4
^{1}H	Hydrogen-1
^{2}H	Hydrogen-2
^{11}B	Boron-11
^{13}C	Carbon-13
^{15}N	Nitrogen-15
^{31}P	Phosphorus-31
{^{1}H}	Proton-decoupled
{^{31}P}	Phosphorus-decoupled
2-MeTHF	2-Methyl-tetrahydrofuran
6-31G, etc.	Basis sets for DFT
BP86 etc.	DFT functional

Chapter 1. Introduction

1.1 Motivation

A unifying theme of this thesis concerns the manipulation of structure and environment to elicit new properties and reactivity from earth-abundant, mid-to-late first-row transition metal ions (in particular, Fe and Cu). This introduction will serve to motivate our interest in studying these metals and provide background information on the iron-catalyzed nitrogen fixation reaction.

1.2 Earth-abundant transition metals in catalysis

In most fields of synthetic and industrial catalysis, 2nd- and 3rd-row transition metals, often the relatively rare and expensive "platinum group" metals (Pd, Pt, Rh, Ir, Os, and Ru) dominate the literature and provide the most effective known catalysts for a given transformation.[1-4] This includes small-molecule activation reactions of relevance to large-scale renewable energy problems (e.g. Ru, Rh, and Ir for water oxidation, and Pt for proton reduction)[4-6] as well as reactions useful for the synthesis of commodity chemicals—e.g. hydrogenation, cross-coupling, and metathesis—on both large- and small-scales.[1,2] It has long been recognized that if large-scale, even planet-wide implementation of catalytic systems for small-molecule activation reactions is to be achieved, the catalyst must use earth-abundant metals such as Mn, Co, Fe, Ni, and Cu, and considerable progress has been made on this front in many areas.[4,5,7]

In addition to the economic incentive for studying earth-abundant metals as catalysts, first-row transition metals often provide divergent reactivity compared to 2nd- and 3rd-row analogues, sometimes even facilitating transformations that cannot be efficiently achieved with the platinum-group metals.[1,2,3,8,9] For instance, the divergent reactivity of copper and palladium catalysts in C-N cross-coupling reactions has recently been reviewed in depth,

illustrating the complementarity of the two metals.[8] Although there are several reasons for the differences in reactivity between first-row metals and their heavier congeners, one of the most apparent differences in many cases is their greater propensity to undergo single-electron reactivity, often resulting in mechanisms involving radical intermediates.[2,9] Though this has often been regarded as an impediment to the development of well-behaved catalytic reactions using Fe, Co, Ni, and Cu, chemists have increasingly learned how to control the reactivity of these species using judicious design of ligand environment and reaction conditions, resulting in the development of powerful new reactivity. For instance, radical chemistry and single-electron transformations appear to be common in nickel-catalyzed cross-coupling chemistry, and contribute to the utility of nickel in carrying out challenging organometallic transformations.[9] Additionally, the ability of a metal ion to readily sample several different spin states—as is more typical for first-row metals—has been suggested as a method to help lower the energetic barrier of catalytic reaction steps *via* "spin acceleration."[2]

The application of light is another way to access divergent reactivity in metal systems. The complementarity of thermochemical and photochemical conditions is well-recognized for a variety of both catalyzed and uncatalyzed reactions.[10-12] The application of photolysis to catalytic reactions, often in conjunction with a metal catalyst, has proven extremely fruitful in achieving otherwise inaccessible reactivity.[13] Often, first-row metal catalysts are particularly well-suited for these reactions due to their propensity to undergo the sort of single-electron reactions which are also a hallmark of photoredox chemistry.[14,15] One of the projects discussed in this thesis (Chapter 5) capitalizes on this synergy to develop photolytic, Cu-mediated, and Cu-catalyzed C-N coupling reactions.

1.2.1 Copper coupling catalysis and photochemistry

The history of copper-catalyzed coupling dates back to the beginning of the 20th century, making it the earliest recognized example of a metal-catalyzed cross-coupling, predating the development of similar reactivity using nickel and palladium catalysts.[16] However, the early incarnations of these Ullmann-type couplings, relying on simple copper salts or copper metal, almost universally required harsh reaction conditions (e.g. temperatures >200 ^{o}C) and suffered from poor selectivity and scope; as a result, nickel and palladium coupling chemistry quickly overtook Ullmann coupling in synthetic utility.[17] Copper catalysis enjoyed a renaissance around the early 2000s when several groups found that the addition of certain ligands such as chelating amines and imines facilitated Ullmann coupling under milder conditions (albeit still typically >90 ^{o}C).[18] Since then, there has a been a steady flow of reports improving the selectivity, scope, and conditions of copper-catalyzed coupling reactions, although these reactions still remain difficult to understand and tune rationally, and reaction development still largely rests on trial and error.[17,18]

In addition to their utility as catalysts, copper coordination complexes (especially Cu(I)) have long been noted for their photophysical properties (e.g. long-lived luminescence, and often highly reducing excited states).[19] Even simple copper halide clusters have notable emission properties. In this context, our group has studied a number of bimetallic and monometallic copper complexes coordinated by amide and phosphine donors that exhibited notably long-lived luminescent excited states, including a set of simple and readily accessible three-coordinate copper bis(phosphine) amide complexes.[20-22] The favorable photochemical and chemical properties of copper complexes has led to the development of a number of photolytic, copper-mediated or -catalyzed transformations

such as cycloadditions, other addition reactions, atom transfer radical addition/cyclization,[15] and the cross-coupling reactions which we have developed and are discussed in Chapter 5. This work thus demonstrates the use of photochemical reaction conditions to help guide the reactivity of first-row transition metals towards desirable processes.

1.3 Controlling metal reactivity through ligand design

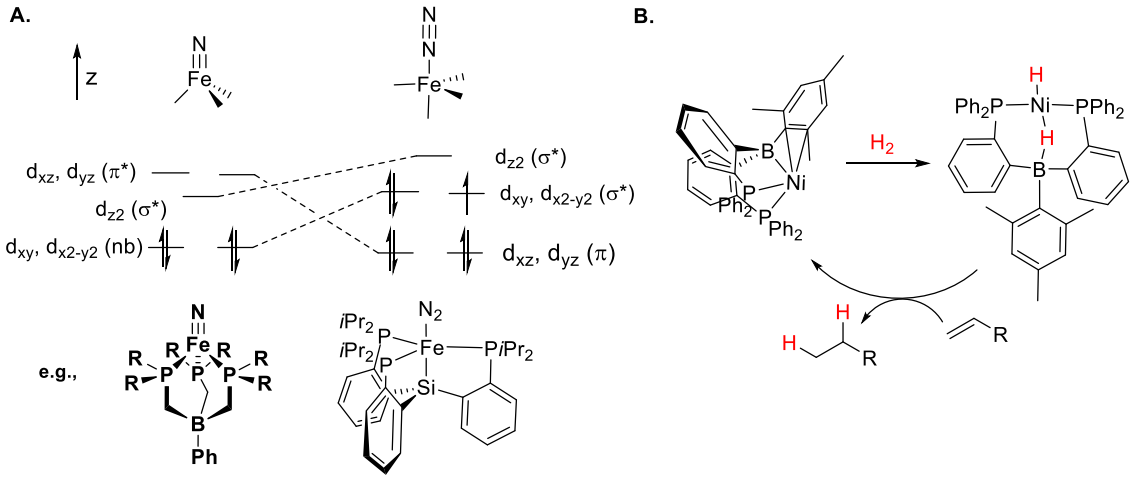

Figure 1.1. (A) Ligands designed to enforce specific geometries (pseudotetrahedral or trigonal bipyramidal) can support the coordination of different types of substrates (π-donating or π-accepting) based on whether the π-symmetry orbitals are occupied. **(B)** Ligands can incorporate non-innocent functionalities such as boranes that can engage in cooperative reactivity with the metal center.

The rational design of ligand scaffolds to stabilize desired complexes or access challenging reactivity, including small-molecule activation, is one of the hallmarks of synthetic inorganic chemistry; chapters 2-4 and 6 of this thesis deal broadly with this topic. This can involve the design of ligands that simply engender the metal with the appropriate

geometry and degree of electron density to bind and/or activate a targeted substrate, or it may involve non-innocent ligands that participate directly in the reaction chemistry in a variety of ways. To draw upon examples from our own work, we have demonstrated that ligands which enforce a trigonal geometry—pseudotetrahedral or trigonal bipyramidal—can facilitate the binding of either π-donating or π-accepting substrates due to the resulting arrangement of valence metal d-orbitals (Figure 1.1A).[23-26] Additionally, we have demonstrated metal-ligand cooperativity through the use of borane-containing ligands that act in concert with the metal to activate a variety of E-H bonds, which can then often be delivered to unsaturated substrates (Figure 1.1B).[27,28]

1.3.1 Bioinspired ligand and complex design

Metalloenzymes display an incredible ability to tune the reactivity of earth-abundant metals by exquisite design of the primary and secondary coordination spheres in order to carry out challenging small-molecule activation reactions; this aptitude has yet to be fully matched by synthetic chemists. For this reason, such metalloenzymes often serve as inspiration for the design of metal complexes that we hope will display similar reactivity—although this goal is often difficult to achieve in practice. Bioinspired inorganic chemistry can be viewed along a spectrum from complexes that seek to model precisely the immediate coordination environment of a metal ion or the precise structure of a cluster, to those that do not specifically model an existing active site but instead seek to draw upon the design principles of those active sites.[29,30]

The former category—structural models of metalloenzymes—includes substantial work on, for instance, Fe-Fe hydrogenases, where close structural models have been achieved;[31-33] photosystem II, where structurally faithful models of the Mn_4CaO_5 cluster have long

been sought and recently achieved;[34-36] iron-sulfur clusters, whose synthetic chemistry has been extensively explored;[37,38] and the FeMo cofactor of nitrogenase, a challenging target whose synthesis has not yet been achieved artificially (Figure 1.2).[38-40] Chapters 2 and 3 of this thesis fall into this category as they primarily involve modeling important structural features of FeMoco.

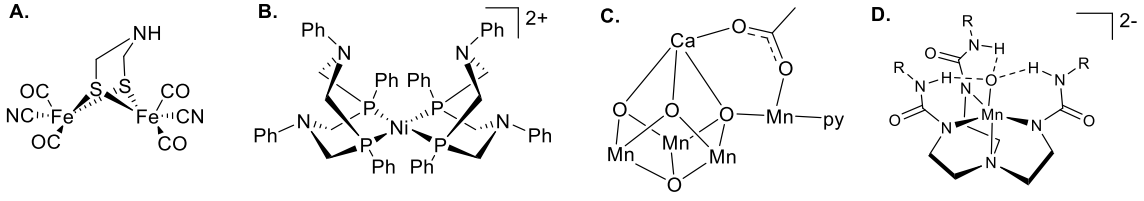

Figure 1.2. Biomimetic and bioinspired synthetic metal complexes. (**A**) Synthetic model of the [FeFe] hydrogenase active site.[33] (**B**) Proton reduction catalyst which uses secondary-sphere interactions (amine groups that can engage in hydrogen bonding) conceptually similar to those present in [FeFe] hydrogenase.[45] (**C**) Synthetic cluster model of the water-oxidizing active site of photosystem II.[36] (**D**) Bioinspired manganese complex that uses a ligand incorporating hydrogen-bonding interactions to stabilize a metal oxo.[41]

The latter category—bioinspired but not biomimetic complexes—includes, among other things, many examples of complexes which incorporate secondary-sphere interactions into the ligand design.[42,43] These interactions—especially hydrogen bonding—are ubiquitous in metalloenzymes and often speculated to be responsible in part for their superior reactivity as compared to small-molecule models that don't incorporate the surrounding protein environment. The incorporation of such interactions into synthetic systems has proven very fruitful, especially in the context of small molecule activation, as can be

illustrated by the work of DuBois *et al* on hydrogen production[44,45] and of Borovik *et al* on the stabilization of metal oxos and activation of dioxygen (Figure 1.2).[42,43,46] Such strategies will likely continue to be applied with success to a variety of challenging problems in small-molecule activation, and chapter 4 of this thesis deals with our attempt to apply these principles to the problem of N_2 fixation.

1.4 Nitrogen activation by molecular systems

Molecular nitrogen (N_2) constitutes a particularly challenging but important substrate for activation by transition metals. While atmospheric N_2 is ultimately the source of essentially all functionalized nitrogen compounds on Earth (including the amino acids which are a ubiquitous component of life), the kinetic inertness of the triply-bonded N_2 molecule makes its conversion into a more chemically useful form extremely difficult.[47-49] Notably, essentially all known systems capable of catalyzing this transformation require the participation of a transition metal;[50] these systems range from the conceptually simple (e.g., the metallic iron catalyst of the Haber-Bosch process which combines H_2 and N_2 at high temperatures and pressures to furnish NH_3) to the extremely complex—such as the Fe_7MoS_9 multimetallic cluster (FeMoco) of the nitrogenase enzyme, which is the centerpiece of a complex biological machinery for nitrogen fixation whose mechanism is still largely shrouded in mystery despite decades of study (Figure 1.3A).[51,52] Given the critical importance of N_2 fixation for the continued sustenance of the human population, there is considerable interest both in understanding the mechanism of the extant catalysts for this reaction, and in designing new catalysts that might facilitate the design of more energy-efficient or scalable systems for ammonia production.

The locus of initial N_2 binding and reduction (Mo, Fe, or perhaps both) on FeMoco has yet to be clearly established and has been a source of considerable debate. While many chemists have focused on molybdenum as the likely active site—bolstered by decades of research on the protonation of Mo-N_2 complexes[53,54]—there is some biochemical and computational evidence suggesting that iron may in fact be the site of N_2 binding. For instance, single-point mutations that block access to the "beltway" irons in the FeMoco cluster shut down N_2 reduction activity, and some computational studies support intial N_2 binding at one of these iron sites.[55,56] Additionally, some variants of the nitrogenase enzyme which include either vanadium or iron in place of the molybdenum center are known, although they are both less efficient and less well-studied than FeMoco itself.[57]

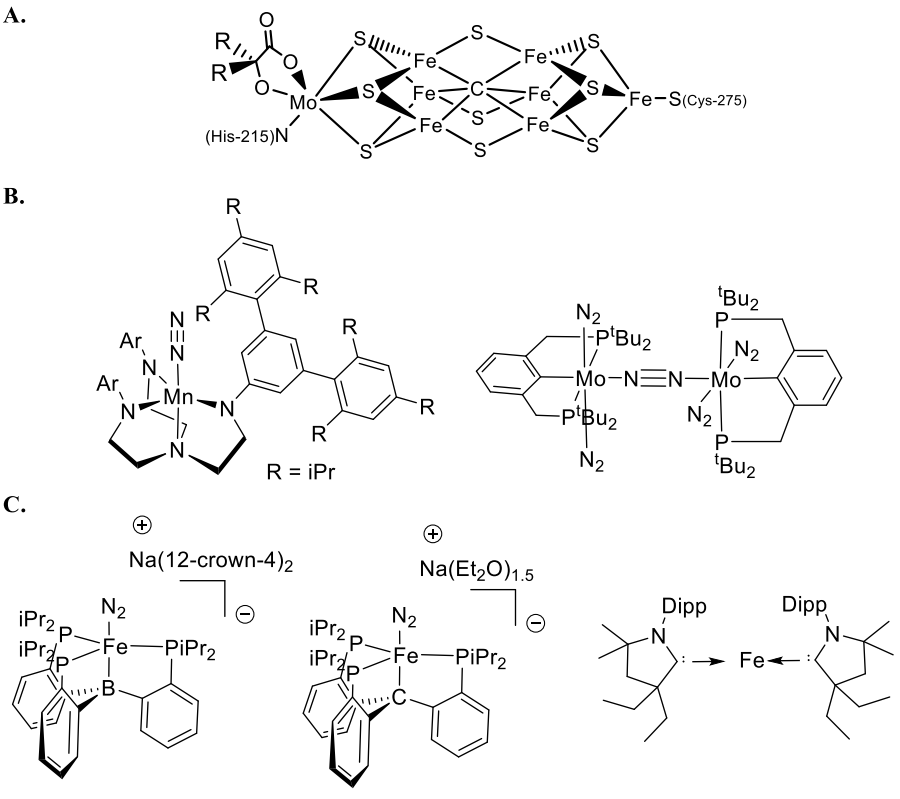

Figure 1.3. (A) Structure of FeMoco. (B) The first molecular molybdenum catalysts reported for N_2 fixation. (C) Molecular iron catalysts for N_2 fixation.

However, it was on molybdenum that the first examples of catalytic N_2 fixation by synthetic small-molecule metal complexes were achieved, providing some circumstantial evidence for the hypothesis that molybdenum was the key active center in FeMoco. The first such system was reported in 2003 by Yandulov and Schrock, who described a (HIPT)Mo catalyst that could furnish up to ~8 equivalents of ammonia when treated with decamethylchromocene and [lutidinium][BAr_4^F] at room temperature in heptane (Figure 1.3B).[58] Mechanistic studies on this system, including the characterization of many of the purported intermediates, suggest that it proceeds *via* a "distal" path (*vide infra*) including the intermediacy of a molybdenum nitride complex.[59] It was not until 2011 that the second catalytically competent system, based on a (PNP)Mo complex, was reported by Nishibayashi *et al* (Figure 1.3B); optimization studies allowed up to 26 equivalents of ammonia to be produced per Mo atom with a substituted variant of this system, using cobaltocene and [LutH][OTf].[60,61]

One reason for long-standing skepticism about a single-site nitrogen-fixation pathway on iron, both in biological and synthetic systems, was an implicit belief that a single iron center in a fixed coordination environment could not support the range of oxidation states needed to facilitate nitrogen fixation. Work in our lab over the past several years has demonstrated that this is not the case—not only is iron capable of supporting the full range of proposed intermediate nitrogenous species (*vide infra*),[24-26] it is indeed capable of facilitating catalytic nitrogen fixation using a well-defined, molecular, and monometallic iron catalyst. This fact was established in 2013 with our report of the first molecular Fe system for catalytic N_2 fixation to ammonia, using a [(TPB)Fe(N_2)]$^-$ precatalyst treated at -78 ^{o}C with KC_8 and $HBAr^F_4{\cdot}2Et_2O$ (Figure 1.3C).[62] Initially, 7 equivalents of ammonia

(3.5 TON) were reported, although further work has demonstrated that much higher turnover numbers are accessible. We have since established that several other iron complexes furnish catalytic yields of ammonia under similar conditions, including a $(CAAC)_2Fe$ biscarbene complex and the trisphosphinoalkyl-supported $[(CP_3)FeN_2]^-$ complex which will be discussed in detail in Chapter 2 of this thesis (Figure 1.3C).[63,64] To date, however, $[(TPB)FeN_2]^-$ stands as the most effective synthetic iron precatalyst for this transformation.

1.4.1 The Mechanism of N_2 Fixation by Molecular Iron Systems

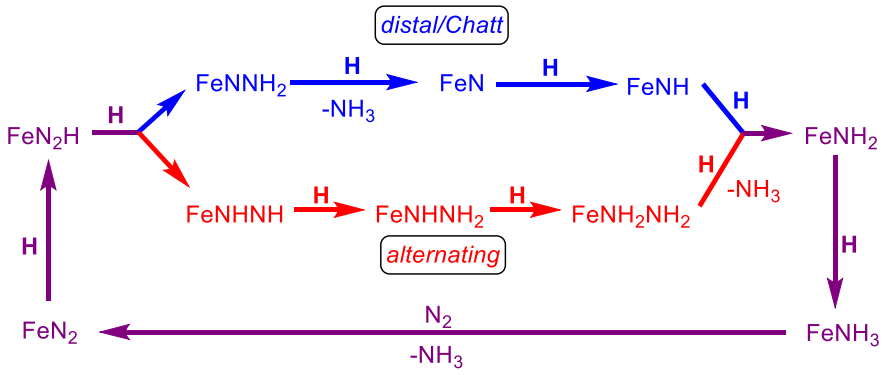

Figure 1.4. Generalized schematic of the *limiting* pathways (distal and alternating) proposed for the conversion of N_2 to $2NH_3$ at a single metal center. Addition of H-atoms is shown to represent the sequential addition of H^+ and e^- in either order. "Crossover" pathways are not shown.

Discussion surrounding the mechanism of nitrogen reduction often focuses on the two limiting pathways—distal (Chatt-type) and alternating—which differ fundamentally in the location of sequential additions of protons to the coordinated N_XH_y substrate (Figure 1.4).

However, when considered in a step-wise fashion, and allowing for "crossover" between the two limiting mechanisms, the number of pathways which must be considered becomes enormous; one can tabulate dozens of plausible intermediates and hundreds of possible paths traversing them. The task of settling on a single, most plausible, and experimentally supported pathway is therefore daunting. Moreover, in addition to the mechanism of N_2 fixation itself, if the rational design of improved catalysts is sought, it is desirable and necessary to attempt to understand the occurrence and mechanism of *undesired* reaction pathways such as iron-catalyzed H_2 evolution and catalyst decomposition.

Of the iron-based catalytic systems thus far established, the most well-studied remains the most efficient, $[TP^{iPr}B]FeN_2^-$, and although we recognize that even superficially similar catalysts may follow different paths, this system serves as an instructive initial platform for mechanistic discussion. The identification (by a combination of low-temperature EPR, Mossbauer, EXAFS, and ENDOR spectroscopy) of a thermally unstable $[TP^{iPr}B]FeNNH_2^+$ (**A**) complex formed under catalytically relevant conditions has provided considerable insight into the early steps of nitrogen fixation on this scaffold.[65] Hydrazido^{2-} complexes of this type are a crucial intermediate in a Chatt-type nitrogen reduction cycle and have been well-characterized on the [HIPT]Mo scaffold, but had not previously been identified on iron.[59] Complex **A** is formed by the treatment of the precatalyst $[TP^{iPr}B]FeN_2^-$ in Et_2O with > 2 equiv. of $HBAr^F{\cdot}2Et_2O$ at temperatures of -78 ^oC or lower, the same conditions that are used in the catalytic reaction, but without the subsequent addition of reductant. Conversion is observed to be immediate upon addition of acid; the use of stoichiometric (1 equiv.) acid results only in oxidation, suggesting that a putative diazenido (FeNNH) intermediate is unstable even at low temperatures. While the observation of a species under

catalytic conditions does not prove its involvement in the catalytic cycle, it is clear that **A** is formed at the beginning of the catalytic reaction (upon addition of acid), and that its formation is sufficiently rapid to be kinetically competent for involvement in the catalytic cycle. Moreover, even in the absence of added reductant, **A** decomposes at temperatures above -78 °C to give some ammonia (as $[TP^{iPr}B]FeNH_3^+$). Taken together these facts provide strong support that **A** is a true intermediate in the catalytic cycle, and suggest that at least the beginning of the cycle follows a distal, Chatt-type path (Figure 1.5).

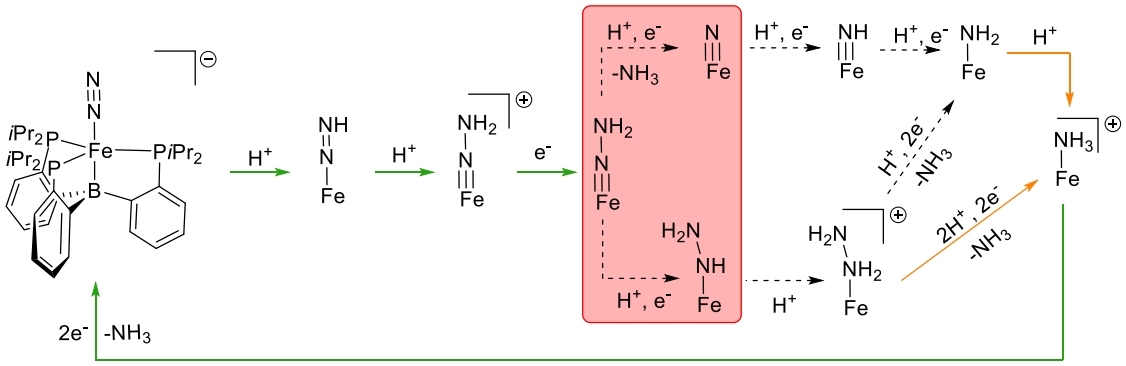

Figure 1.5. Mechanistic outline for the catalytic reduction of N_2 to ammonia by [TPBFe]. Green arrows denote steps for which strong evidence exists supporting their involvement in the catalytic cycle. Orange arrows denote steps which have been observed in stoichiometric reactions but for which involvement in the catalytic cycle has not been clearly established. A shaded red box highlights the "lynchpin" step of the cycle, which controls whether a distal (nitride) path or an alternating (hydrazine) path is followed for the final phase of the reaction.

Given that **A** is not converted further even in the presence of excess acid under the catalytic conditions (-78 °C in Et_2O, lacking only the reductant), it follows that the

immediate next step in the catalytic cycle must be a reduction, presumably to a putative neutral [TP^{iPr}B]FeNNH$_2$ complex; we have not yet been able to characterize such a species. From this point, however, multiple possible routes diverge which may lead to either a distal (nitride) pathway or an alternating (hydrazine) pathway. The next elementary step is likely the delivery of a proton. This could occur either at the β nitrogen, following a distal pathway and presumably leading rapidly to loss of NH_3 to form a FeN^+ nitride intermediate, or at the α nitrogen, following an alternating pathway to form an $FeNHNH_2^+$ hydrazido^{1-} complex. While the hydrazido^{2-} ligand could in principle isomerize to a diazene, such a conversion has never been observed; if it does occur, subsequent protonation would again lead to the hydrazido^{-1} complex. We do not yet have direct evidence for either pathway; instead, model chemistry and stoichiometric reactivity suggest that both routes are plausible.

An $FeNHNH_2^+$ hydrazido^{1-} complex could likely be readily converted by the addition of an additional H-atom equivalent (H^+ and e- in either order) to the well-characterized [TPB]$FeN_2H_4^+$ hydrazine complex.[66] The decomposition of this complex to give ammonia, presumably *via* a disproportionation pathway also producing N_2, has been demonstrated (Scheme 1.1);[66] while the disproportionation reaction itself is not kinetically competent to participate in the catalytic nitrogen fixation reaction, it lends credence to the idea that, especially in the presence of additional proton and electron equivalents, a bound hydrazine could be converted to ammonia. In the presence of added acid and reductant additional pathways for hydrazine decomposition may become available. No hydrazine has ever been observed in the product mixture of a catalytic run, even when small amounts of exogeneous

hydrazine are added at the beginning of the reaction, suggesting that if it is formed, it is rapidly consumed.[62]

Scheme 1.1. Model reactions relevant to the conversion of nitride or hydrazine intermediates to NH_3

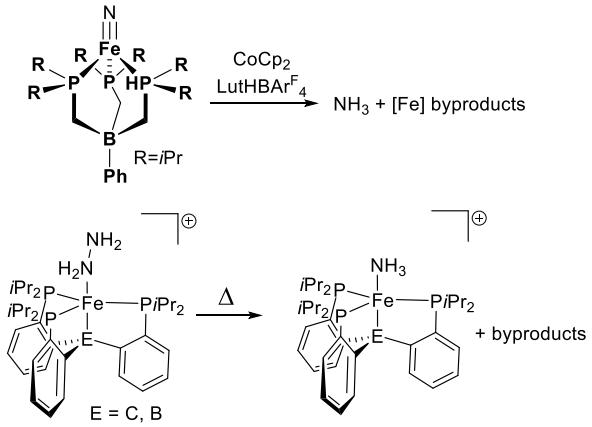

The possible involvement of an iron nitride complex—a key intermediate in a hypothetical Chatt cycle—is an intriguing idea. Iron nitride complexes remain very rare, in contrast to the more common molybdenum nitride complexes. Because a multiply-bonded iron nitride is not expected to be electronically accessible on a five-coordinate trigonal-bipyramidal scaffold, the intermediacy of such a species would require the catalytic system to capitalize upon the geometric flexibility of the TPBFe scaffold to access a pseudotetrahedral species.[24] While efforts to generate a TPBFeN species sufficiently stable for extensive characterization have not yet been successful, a pseudotetrahedral trisphosphine iron nitride complex is known from our previous work ($PhBP_3FeN$),[25] and work on crystallographically characterized imide complexes suggest that the TPBFe scaffold has sufficient flexibility to achieve a similar geometry.[24] Moreover, a nitride need not be stable in order to participate transiently in the catalytic cycle, and the conversion of

a nitride complex to ammonia in the presence of proton and/or electron sources has been demonstrated in several instances (Scheme 1.1).[25,67] However, the necessary geometric flexibility has not been demonstrated for the CP^{iPr}_3Fe system, and as a result a nitride intermediate is perhaps less plausible for this system.

While the comparison of the catalytic activity of a series of related complexes can often provide considerable insight, we must first be able to answer the question of *why* some iron complexes are competent catalysts under our reaction conditions and why some are not, and further, why (TPB)Fe is a superior catalyst to other iron complexes that have been previously studied (e.g. $(SiP_3)Fe$) and/or will be discussed in this thesis (e.g. $(CP_3)Fe$). These are still largely open questions. While there is a correlation between the geometric flexibility of the X-Fe bond (X = B, C, Si) and the catalytic activity of the trigonal bipyramidal systems, it is not clear that a causative relationship exists between the two. Indeed, the stoichiometric reactivity of the five-coordinate scaffolds, and especially $(CP_3)Fe$ and $(SiP_3)Fe$, towards nitrogenous substrates is generally quite similar. Despite its lack of geometric flexibility, substituted imides and diazenidos have been shown to have at least transient stability on $(SiP_3)Fe$. Therefore, with our current understanding of the mechanism, we cannot clearly point to any particular individual step as the source of the differences between these three scaffolds.

In the cases we have studied, the lifetime and turnover number of the catalyst appears to be terminally limited by the conversion of the iron catalyst into inactive species. For $(CP_3)Fe$ and (TPB)Fe, it appears that one major pathway for catalyst deactivation is the formation of metal-hydride species: the hydride complex $(CP_3)Fe(N_2)(H)$ and the hydride-borohydride complex $(TPB)(\mu\text{-}H)Fe(H)(N_2)$ are present in substantial amounts after a

standard catalytic reaction and have been shown to be inactive or less active as precatalysts, suggesting that their formation serves as a shunt pathway that sequesters iron in a catalytically inactive form.[62,64] $CP_3Fe(N_2)(H)$ can form by protonation of $CP_3FeN_2^-$ at the metal center rather than at the β-nitrogen; in stoichiometric reactions on this and related systems it appears that both protonations can occur to some extent under catalytically relevant conditions. The branching between the two possible protonation sites for this initial step may be a significant factor in determining the competence of different systems towards catalytic ammonia production (Figure 1.6), and structural and electronic factors that favor protonation at N_2 rather than at the metal are an important target for catalyst optimization. Furthermore, the ability of a system to escape from catalytically inactive sinks (e.g. *via* hydrogen evolution from metal hydrides) may be a key design factor in both synthetic and biological systems.

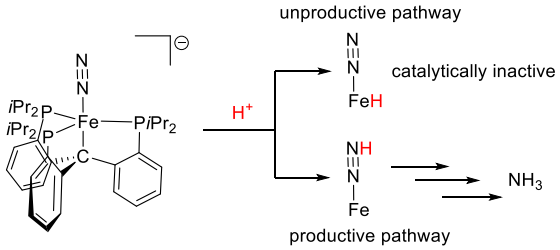

Figure 1.6. Branching between different protonation pathways may, in part, control catalyst efficiency.

1.4.2 Analogy to nitrogenase

The monometallic iron systems discussed here are by no means faithful structural models for the Fe_7MoS_9 cofactor of nitrogenase. While the synthetic chemistry of iron-sulfur clusters is extensive, and close structural models of FeMoco have been

synthesized—albeit lacking the recently identified interstitial carbide—they are not catalytically active nor do they show any discernible interaction with N_2.[38,39] Instead, as the only well-defined, molecular, iron-containing *functional* models of FeMoco, the reactivity of complexes such as $[(TPB)FeN_2]^-$ may provide some insight into the biological mechanism of nitrogen reduction. At a minimum, we have firmly established that a single iron center can possess the requisite coordinative and redox flexibility to mediate the complete conversion of N_2 to NH_3, a fact which was far from clear prior to our work.

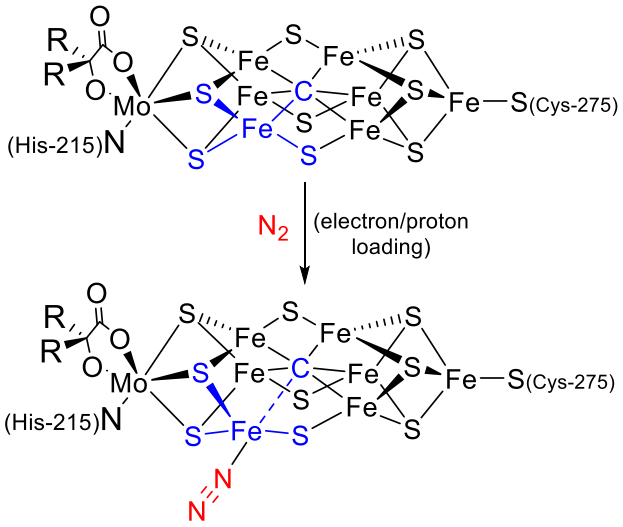

Figure 1.7. Proposed geometric change upon substrate binding in FeMoco. Possible protonation of sulfides not shown.

If the site of substrate coordination and reduction is one of the "belt" irons of FeMoco, as is suggested by a number of theoretical, spectroscopic, and biochemical studies, the catalytically active iron center will reside in a distorted trigonal environment and many of the same electronic structure arguments that have been explored in our synthetic small-molecule systems will be applicable. In particular, a hemi-labile interaction with the

interstitial carbide (C^{4-}) ligand would allow the iron center to shuttle between 5-coordinate trigonal bipyramidal and 4-coordinate pseudotetrahedral geometries in accordance with the electronic requirements of various steps in the catalytic cycle.[64,68] Indeed, spectroscopic studies on at least one substrate (propargyl alcohol) have been suggestive of considerable flexibility in the Fe-C interaction, including an elongation of 0.35 Å upon substrate binding.[69]

In this vein, it is one of the tenets of bioinorganic modeling chemistry that a feedback mechanism could exist between enzymes such as nitrogenase, the various hydrogenases, Photosystem II, etc, and inorganic small molecules which function as structural and/or functional models, wherein the model chemistry can provide insight into the mechanism of the biological system, and in turn a greater understanding of the structural elements of the metalloenzymes can be incorporated into synthetic systems to yield better-performing catalysts. Some of the research presented in this thesis is aimed in that direction, as discussed further below.

1.5 Chapter summaries

The first three chapters detail several projects concerning the synthesis of iron complexes of relevance to dinitrogen fixation by iron in the FeMo cofactor of nitrogenase. In each case, a novel ligand platform is developed which is intended to model some aspect of the primary or secondary coordination sphere of the iron centers in FeMoco, and the structure and reactivity of the resulting complexes are studied. Insights and conclusions are drawn with respect to plausible roles of different features of the FeMoco structure, and possible design principles for improved molecular catalysts for N_2 fixation are elucidated.

Chapter 2 discusses the synthesis and metalation of a tris(phosphino)alkyl ligand scaffold on iron, pursued in part in order to interrogate the possible role of the carbide ligand in FeMoco. This ligand complements the various tetradentate trisphosphine ligands previously investigated by our group, including tris(phosphino)silyl and tris(phosphino)borane ligands. Although the carbon-anchored ligand was of obvious interest given the spectroscopic studies published in 2011 that firmly established that the FeMoco cluster contains a central carbide ligand, synthetic difficulties had for some time stymied explorations of this scaffold. Once synthetic access to this system was achieved, however, we were able to establish that an iron(0)-dinitrogen complex of this ligand serves as an active precatalyst for N_2 fixation for ammonia, only the second synthetic molecular iron complex known to display this reactivity.

Chapter 3 explores a synthetic, structural model for a different aspect of the FeMoco structure—specifically, the presence of bridging, anionic S-donor ligands and Fe-S-Fe type fragments. We used a binucleating ligand scaffold which supports a bridging thiolate between two iron atoms in an attempt to address the deficit of thiolate and/or sulfide-coordinated iron centers that bind dinitrogen. Prior to our work, no such systems were known where N_2 binding was spectroscopically or crystallographically observed. We illustrate that, through judicious ligand design, this structural motif can be achieved synthetically. Moreover, our system shows biomimetic reactivity in its ability to fix (non-catalytically) N_2 and to disproportionate hydrazine more effectively than previously known iron catalysts.

Chapter 4 explores the multifaceted topic of secondary sphere interactions as they relate to nitrogen fixation at a monometallic iron center. Secondary sphere interactions

encompass all those aspects of the ligand environment (including the protein environment in metalloenzymes) around, but not directly bound to, a metal center, including hydrogen bonds, Coulombic interactions, steric shielding, etc. Incorporating such interactions into synthetic small-molecule systems encompasses an additional synthetic and design challenge beyond just controlling the primary coordination sphere. We have designed a ligand scaffold based on pendant tertiary amine groups to help investigate some of these effects on the structure and reactivity of iron complexes with various nitrogenous ligands. Among other things, we found that the presence of these amines as "proton shuttles" has a remarkably *suppressive* effect on N_2 fixation reactivity by promoting the formation of Fe-H rather than N_2-H bonds, a discovery which will help aid the design of future N_2 fixation catalysts.

Chapter 5 travels further right across the periodic table from iron to copper. While we again focus on the development of new reactivity with first-row transition metals, here this reactivity is elicited not by ligand design, but by the application of novel reaction conditions. We discuss the development of a *photo-induced* C-N coupling reaction that uses copper complexes both stoichiometrically and catalytically to form C_{aryl}-N and C_{alkyl}-N under unusually mild conditions. The mechanisms of these reactions are explored using a variety of mechanistic probes and spectroscopic techniques, and we provide very strong evidence for a radical mechanism involving single-electron-transfer steps, differentiating these reactions from previous reports of C-N coupling reactions and providing the first experimental evidence for the viability of such a pathway.

Chapter 6 expands on the general concepts described above—eliciting function through rational system design—by providing a detailed and quantitative case study of tuning the

electronic structure of a series of iron complexes through ligand design. The ligands employed—tridentate tris(phosphine)borate ligands which enforce a pseudotetrahedral geometry, and phosphiniminato ligands which display notable electronic flexibility—act in concert to enable a four-coordinate Fe(II) center to display unusual spin-crossover properties. We demonstrate that the careful analysis of spectroscopic data can elucidate detailed structure-function correlations that may aid in the development of inorganic complexes with useful electronic and magnetic properties.

1.6 References

1. Chirik, P.; Morris, R. *Acc. Chem. Res.* **2015**, *48*, 2495.

2. Holland, P. L. *Acc. Chem. Res.* **2015**, *48*, 1696.

3. Enthaler, S.; Junge, K.; Beller, M. *Angew. Chem. Int. Ed.* **2008**, *47*, 3317.

4. Du, P.; Eisenberg, R. *Energy Environ. Sci.* **2012**, *5*, 6012.

5. Blakemore, J. D; Crabtree, R. H.; Brudvig, G. W. *Chem. Rev.* **2015**, *115*, 12974.

6. Gray, H. B. *Nature Chem.* **2009**, *1*, 7.

7. Thoi, V. S.; Sun, Y.; Long, J. R.; Chang, C. J. *Chem. Soc. Rev.* **2013**, *42*, 2388.

8. Beletskaya, I. P.; Cheprakov, A. V. *Organometallics*, **2012**, *31*, 7753.

9. Ananikov, V. P. *ACS Catalysis* **2015**, *5*, 1964.

10. Woodward, R. B.; Hoffmann, R. *Angew. Chem. Int. Ed.* **1969**, *8*, 781.

11. Palmisano, G.; Augugliaro, V.; Pagliaro, M.; Palmisano, L. *Chem. Commun.* **2007**, 3425.

12. Schultz, D. M.; Yoon, T. P. *Science* **2014**, *343*, 985.

13. Prier, C. K.; Rankic, D. A.; MacMillan, D. W. C. *Chem. Rev.* **2013**, *113*, 5322.

14. Ye, Y.; Sanford, M. S. *J. Am. Chem. Soc.* **2012**, *134*, 9034.

15. Paria, S.; Reiser, O. *ChemCatChem* **2014**, *6*, 2477.

16. (a) Ullmann, F; Bielecki, J.; *Ber. Dtsch. Chem. Ges.* **1901**, *34*, 2174. (b) Goldberg, I. *Ber. Dtsch. Chem. Ges.* **1906**, *39*, 1691. (c) Ullmann, F. *Ber. Dtsch. Chem. Ges.* **1903**, *36*, 2382.

17. Ley, S. V.; Thomas, A. W. *Angew. Chem. Int. Ed.* **2003**, *42*, 5400.

18. Monnier, F.; Taillefer, M. *Angew. Chem. Int. Ed.* **2009**, *48*, 6954.

19. Armaroli, N.; Accorsi, G.; Cardinali, F.; Listorti, A. *Top. Curr. Chem.* **2007**, *280*, 69.

20. Harkins, S. B.; Peters, J. C. *J. Am. Chem. Soc.* **2005**, *127*, 2030.

21. Miller, A. J. M.; Dempsy, J. M.; Peters, J. C. *Inorg. Chem.* **2007**, *46*, 7244.

22. Lotito, K. J.; Peters, J. C. *Chem. Commun.* **2010**, *46*, 3690.

23. Saouma, C. T.; Peters, J. C. *Coord. Chem. Rev.* **2011**, *255*, 920.

24. Moret, M.-E.; Peters, J. C. *Angew. Chem. Int. Ed.* **2011**, *50*, 2063.

25. Betley, T.A.; Peters, J. C. *J. Am. Chem. Soc.* **2004**, *126*, 6252.

26. Lee, Y.; Mankad, N. P.; Peters, J. C. *Nature Chem.* **2010**, *2*, 558.

27. Harman, W.H.; Peters, J. C. *J. Am. Chem. Soc.* **2012**, *134*, 5080.

28. Lin, T.-P.; Peters, J. C. *J. Am. Chem. Soc.* **2014**, *136*, 13672.

29. Holm, R. H.; Solomon, E. I. *Chem. Rev.* **2004**, *104*, 347.

30. Tolman, W. B. *Inorg. Chem.* **2013**, *52*, 7307.

31. Tard, C.; Pickett, C. J. *Chem. Rev.* **2009**, *109*, 2245.

32. Camara, J. M.; Rauchfuss, T. B. *Nature Chem.* **2012**, *4*, 26.

33. Berggren, G.; Adamska, A.; Lambertz, C.; Simmons, T. R.; Esselborn, J.; Atta, M.; Gambarelli, S.; Mouesca, J.-M.; Reijerse, E.; Lubitz, W.; Happe, T.; Artero, V.; Fontecave, M. *Nature* **2013**, *499*, 66.

34. Grundmeier, A.; Dau, H. *Biochim. et Biophys. Acta – Bioenerg.* **2012**, *1817*, 88.

35. Kanady, J. S.; Tsui, E. Y.; Day, M. W.; Agapie, T. *Science*, **2011**, *333*, 733.

36. Zhang, C.; Chen, C.; Dong, H.; Shen, J.-R.; Dau, H.; Zhao, J. *Science* **2015**, *348*, 690.

37. Rao, P. V.; Holm, R. H. *Chem. Rev.* **2004**, *104*, 527.

38. Lee, S. C.; Lo, W.; Holm, R. H. *Chem. Rev.* **2014**, *114*, 3579.

39. Karlin, K. D.; Malinak, S. M.; Coucouvanis, D. *Progress in Inorg. Chem.* **2007**, *49*, 599.

40. Lee, S. C.; Holm, R. H. *Chem. Rev.* **2004**, *104*, 1135.

41. Parsell, T. H.; Behan, R. K.; Green, M. T.; Hendrich, M. P.; Borovik, A. S. *J. Am. Chem. Soc.* **2006**, *128*, 8728.

42. Borovik, A.S. *Acc. Chem. Res.* **2005**, *38*, 54.

43. Cook, S. A.; Hill, E. A.; Borovik, A. S. *Biochemistry* **2015**, *54*, 4167.

44. Wilson, A. D.; Newell, R. H.; McNevin, M. J.; Muckerman, J. T.; DuBois, M. R.; DuBois, D. L. *J. Am. Chem. Soc.* **2006**, *128*, 358.

45. Helm, M. L.; Stewart, M. P.; Bullock, R. M.; DuBois, M. R.; DuBois, D. L. *Science* **2011**, *333*, 863.

46. Shook, R. L.; Borovik, A. S. *Inorg. Chem.* **2010**, *49*, 3646.

47. Jia, H.-P.; Quadrelli, E. A. *Chem. Soc. Rev.* **2014**, *43*, 547.

48. Hazari, N. *Chem. Soc. Rev.* **2010**, *39*, 4044.

49. Fryzuk, M.D.; Johnson, S. A. *Coord. Chem. Rev.* **2000**, *200*, 379.

50. Some nitrogen fixation in nature occurs by processes that don't involve transition metals, such as in lightning strikes: Hill, R. D.; Pinker, R. G.; Wilson, H. D. *J. Atmos. Sci.* **1980**, *37*, 179.

51. Burgess, B. K.; Lowe, D. J. *Chem. Rev.* **1996**, *96*, 2983.

52. Hoffman, B. M.; Lukoyanov, D.; Dean, D. R.; Seefeldt, L. C. *Acc. Chem. Res.* **2013**, *46*, 587.

53. Chatt, J.; Dilworth, J. R.; Richards, R. L. *Chem. Rev.* **1978**, *78*, 589.

54. Chatt, J.; Pearman, A. J.; Richards, R. L. *Nature*, **1975**, *253*, 39.

55. Hoffman, B. M.; Dean, D. R.; Seefeldt, L. C. *Acc. Chem. Res.* **2009**, *42*, 609.

56. Dos Santos, P. C.; Igarashi, R. Y.; Lee, H.-I.; Hoffman, B. M.; Seefeldt, L. C.; Dean, D. R. *Acc. Chem. Res.* **2005**, *38*, 208.

57. Eady, R. B. *Chem. Rev.* **1996**, *96*, 3013.

58. Yandulov, D. V.; Schrock, R. R. *Science* **2003**, *301*, 76.

59. Schrock, R. R. *Angew. Chem. Int. Ed.* **2008**, *47*, 5512.

60. Arashiba, K.; Miyake, Y.; Nishibayashi, Y. *Nat. Chem.* **2011**, *3*, 120.

61. Kuriyama, S.; Arashiba, K.; Nakajima, K.; Tanaka, H.; Kamaru, N.; Yoshizawa, K.; Nishibayashi, Y. *J. Am. Chem. Soc.* **2014**, *136*, 9719.

62. Anderson, J. S.; Rittle, J.; Peters, J. C. *Nature* **2013**, *501*, 84.

63. Ung, G.; Peters, J. C. *Angew. Chem. Int. Ed.* **2015**, *54*, 532.

64. Creutz, S. E.; Peters, J. C. *J. Am. Chem. Soc.* **2014**, *136*, 1105.

65. Anderson, J. S.; Cutsail, G. E.; Rittle, J.; Connor, B. A.; Gunderson, W. A.; Zhang, L.; Hoffman, B. M.; Peters, J. C. *J. Am. Chem. Soc.* **2015**, *137*, 7803.

66. Anderson, J. S.; Moret, M.-E.; Peters, J. C. *J. Am. Chem. Soc.* **2013**, *135*, 534.

67. Smith, J. M.; Subedi, D. *Dalton Trans.* **2012**, *41*, 1423.

68. Rittle, J.; Peters, J. C. *Proc. Natl. Acad. Sci.* **2013**, *110*, 15898.

69. George, S.J. *et al*. *J. Inorg. Biochem.* **2012**, *112*, 85.

Chapter 2. Catalytic reduction of N_2 to NH_3 by an Fe-N_2 complex featuring a C-atom anchor.

Reproduced in part with permission from:

Creutz, S. E.; Peters, J. C. *J. Am. Chem. Soc.* **2014**, *136*, 1105.

2.1 Introduction

The biological reduction of atmospheric N_2 to NH_3 is a fascinating yet poorly understood transformation that is essential to life.[1] The iron-molybdenum cofactor (FeMoco) of MoFe nitrogenase catalyzes N_2 reduction and has been extensively studied.[2] This cofactor has attracted the attention of inorganic and organometallic chemists for decades who have sought inspiration to explore the ability of synthetic iron and molybdenum complexes to bind and reduce dinitrogen.[3,4,5,6] Advances in the past decade have included two molybdenum systems that facilitate catalytic turnover of N_2 to NH_3 in the presence of inorganic acid and reductant sources,[7,8,9] and iron complexes that support a range of N_xH_y ligands relevant to nitrogen fixation,[10,11,12,13] effect reductive N_2 cleavage,[14,15] and facilitate N_2 functionalization.[16,17,18]

The presence of an interstitial light atom in the MoFe nitrogenase cofactor was established in 2002,[19] and structural, spectroscopic, and biochemical data have more recently established its identity as a C-atom.[20] The role of the C-atom is unknown. This state of affairs offers an opportunity for organometallic chemists to undertake model studies that can illuminate plausible roles for this interstitial C-atom, and hence critical aspects of the mechanism of N_2 reduction catalysis. In particular, Fe-alkyl complexes that are more ionic in nature than a prototypical transition metal-alkyl may be relevant to modeling the Fe-$C_{interstitial}$ interaction of the possible N_2 binding site in the cofactor (Figure 2.1).

We have suggested that a possible role played by the interstitial C-atom is to provide a flexible Fe-$C_{interstitial}$ interaction that exposes an Fe-N_2 binding site on a belt iron atom trans to the Fe-C linkage (Figure 2.1).[3,15,21,22,23] Subsequent modulation of the Fe-C interaction and hence the local Fe geometry as a function of the N_2 reduction state might ena-

ble the Fe center to stabilize the various N_xH_y intermediates sampled along a pathway to NH_3.

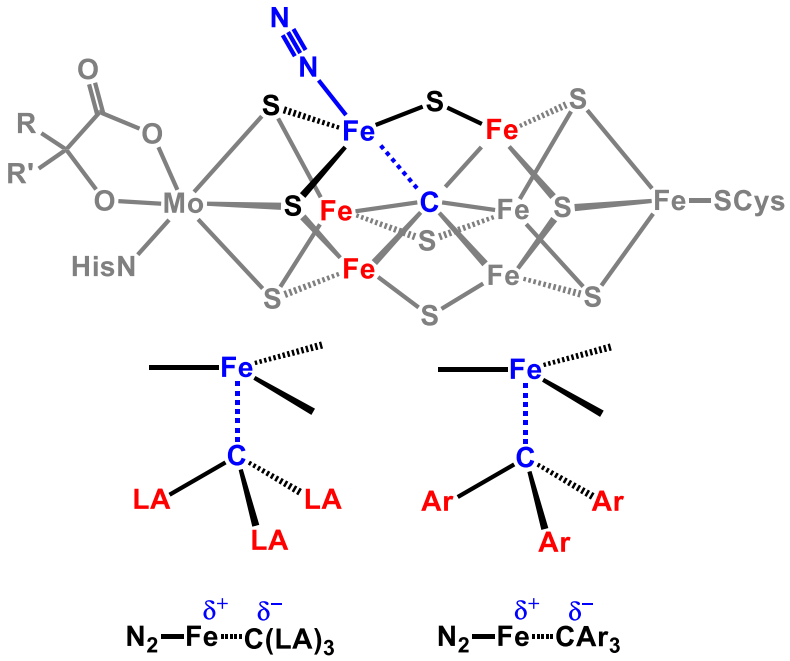

Figure 2.1. (Top) Structure of the FeMo cofactor of nitrogenase, showing a putative site for dinitrogen binding and highlighting the trigonal bipyramidal coordination environment at Fe. Possible sites of H-atoms on cofactor prior to N_2 binding not shown. (Bottom) Possible role of Lewis acidic (LA) or aryl substituents in stabilizing ionic character in the N_2-Fe-C_{alkyl} interaction.

To test the chemical feasibility of this hypothesis for Fe-mediated N_2 reduction, our group has previously employed phosphine-supported Fe complexes in approximately trigonal geometries (pseudotetrahedral, trigonal pyramidal, or trigonal bipyramidal) to bind and functionalize dinitrogen. Tripodal trisphosphine ligands featuring an axial donor (X = N, Si, B) and aryl backbones have been used to canvass the ability of low-valent

iron in such geometries to bind and activate dinitrogen (Figure 2.2).[23,24,25] The (TP$^{i\mathrm{Pr}}$B)Fe-system (TP$^{\mathrm{R}}$B = tris(*o*-phosphinoaryl)borane) has proven rich in this context, and has most recently been shown to be a modestly effective catalyst for the reduction of N_2 to NH_3 in the presence of proton and electron sources at low temperature and 1 atm N_2.[21] An important feature of the (TP$^{i\mathrm{Pr}}$B)Fe-system is the presence of a flexible Fe-B interaction.[15,25] This flexibility may facilitate the formation of intermediates featuring Fe-N_x π-bonding (e.g., Fe=NNH$_2$, Fe≡N, Fe=NH) during catalysis. Whether the aforementioned hypothesis concerning a hemi-labile role for the interstitial C-atom of FeMoco is correct or not, these inorganic model studies lend credibility to the idea so far as the principles of coordination chemistry are concerned.

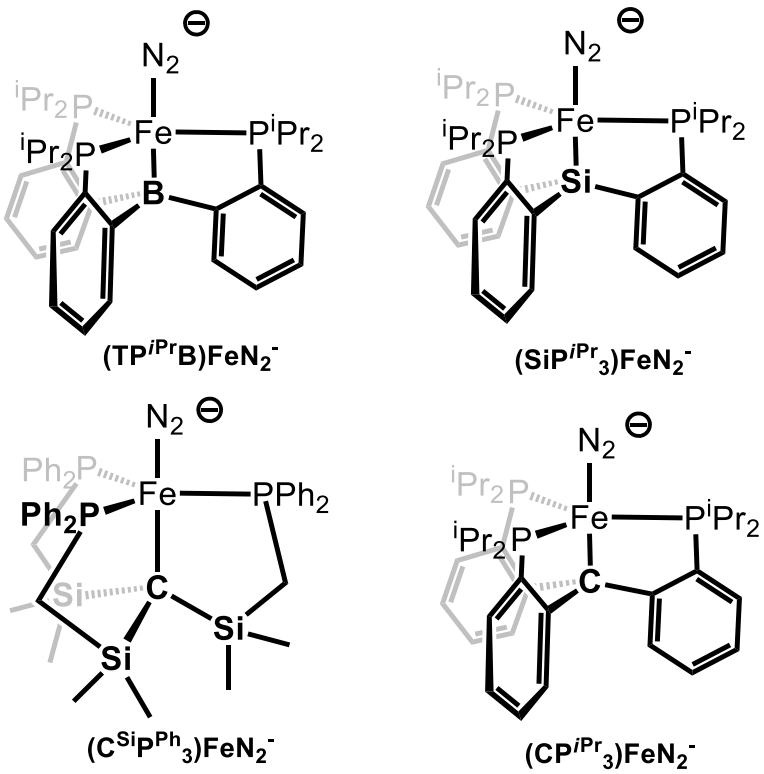

Figure 2.2. Select trigonal bipyramidal scaffolds previously studied by our lab, and the present (CP$^{i\mathrm{Pr}}_3$)FeN$_2^-$ system.

To extend our studies to systems that place a C-atom in a position trans to an Fe-N_2 binding site we have sought related ligand scaffolds that feature a C-atom anchor. In designing these scaffolds we have hypothesized that the proposed flexibility of the Fe-C linkage in the FeMo cofactor may be facilitated by the ability of the environment around the interstitial carbide—five additional electropositive Fe atoms—to stabilize developing negative charge on the carbon. With this in mind we have previously reported iron complexes of a tris(phosphino)alkyl ligand whose axial carbon binding site is flanked by three electropositive silyl groups (Figure 2.2) which may play a role in stabilizing the substantial ionic character of this Fe-C_{alkyl} bond (Figure 2.1).[22]

Herein we report a new tris(phosphino)alkyl ligand, (CP^{iPr}_3), featuring aryl linkers bound to the axial carbon. We reasoned that possible delocalization of negative or positive charge buildup into the aryl π-system would allow for increased flexibility in the Fe-C bond; this flexibility is expected to facilitate possible catalytic N_2 functionalization and reduction, as discussed above. Additionally, as this ligand is closely structurally related to the SiP_3, TPB, and NP_3 ligands whose iron coordination chemistry we have extensively explored, Fe complexes of CP_3^{iPr} are of obvious comparative interest and would be particularly beneficial with regard to considering the role an Fe-$C_{interstitial}$ interaction might play in facilitating N_2 binding and reduction within the cofactor. To this end, we embarked on the synthesis of the new ligand (CP^{iPr}_3)H and the development of its Fe-N_2 chemistry.

2.2 Results and Discussion

2.2.1 Ligand Synthesis

Whereas the ligands (SiP^{iPr}_3)H and $TP^{iPr}B$ are straightforward to synthesize by the addition of lithiated o-phosphinophenyl precursors to $HSiCl_3$ and BCl_3,[24,26] the preparation of (CP^{iPr}_3)H via an analogous method by addition of phosphinoaryllithium moieties to a C_1 source (e.g., triple addition to dimethylcarbonate followed by deoxygenation of the resultant triarylmethanol product) has proven ineffective in our hands. However, an orthogonal synthetic approach based on elaboration of an initially formed triarylmethane scaffold afforded a viable approach to the preparation of (CP^{iPr}_3)H on a multigram scale and in reasonable yields. This synthesis of (CP^{iPr}_3)H follows an approach inspired by a previously reported synthesis of $Ph_2P(o\text{-}C_6H_4CH_2C_6H_4\text{-}o)PPh_2$,[27] and hinges on the sequential formation and cleavage of two diaryliodonium ions to give the tris(2-halophenyl)methane precursor (**2.5**) (Scheme 2.1).

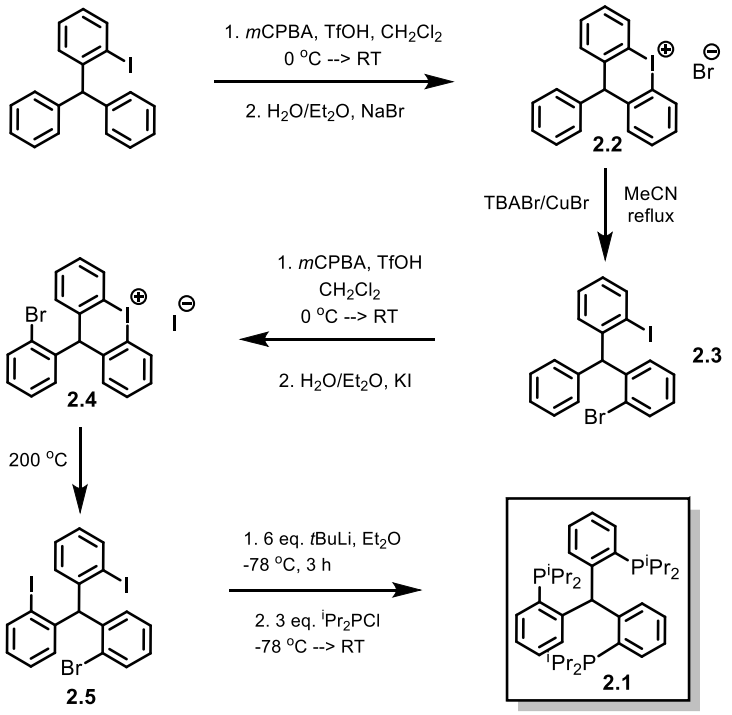

Scheme 2.1. Synthesis of (CP^{iPr}_3)H (**2.1**).

The synthesis of *o*-iodotriphenylmethane has been previously reported[28] and is readily effected in three steps from commercially available 2-nitrobenzaldehyde on a 20-gram scale. Cyclization of this species to the diaryliodonium bromide salt (**2.2**) is accomplished by a previously reported technique.[29] Slow but clean ring-opening of **2.2** by CuBr and [TBA][Br] in acetonitrile gives 2-bromo-2'-iodotriphenylmethane (**2.3**). The 2-bromo-2'-iodotriphenylmethane species was targeted rather than 2,2'-diiodotriphenylmethane in order to mitigate the possibility of complications from excessive oxidation in the next step.

Formation of a second diaryliodonium cation as its iodide salt follows *via* an analogous procedure to regioselectively generate **2.4**, which can be straightforwardly decomposed to 2-bromo-2',2''-diiodotriphenylmethane (**2.5**) by heating to 200 ^{o}C for 15 minutes under an inert atmosphere. Each step in the synthesis of **2.5** from o-iodotriphenylmethane can be accomplished in 75% yield or more (overall yield: 38% over five steps).

Lithiation of **2.5** with six equiv of *tert*-butyllithium at -78 ^{o}C followed by treatment with three equiv of diisopropylphosphine chloride gives the desired tris(*o*-diisopropylphosphinophenyl)methane, (CP^{iPr}_3)H (**2.1**) in 67% yield (Scheme 2.1). The protonated form of the ligand, **2.1**, is characterized by a single peak in its phosphorus NMR spectrum at -9.1 ppm. The ^{1}H NMR spectrum, while indicative of three-fold symmetry, also shows features suggestive of a rigid ligand scaffold where rotation about the phosphine-carbon bonds is hindered; in particular, four magnetically inequivalent sets of resonances are observed for the isopropyl methyl hydrogens. Additionally, the central C-H methine proton is shifted markedly downfield (8.15 ppm) and manifests as a quartet due to through-space coupling to the three phosphorus atoms. Similar NMR properties

were observed for the central methine proton in a related trisphosphine ligand based on a tris(indolyl)methane scaffold.[30]

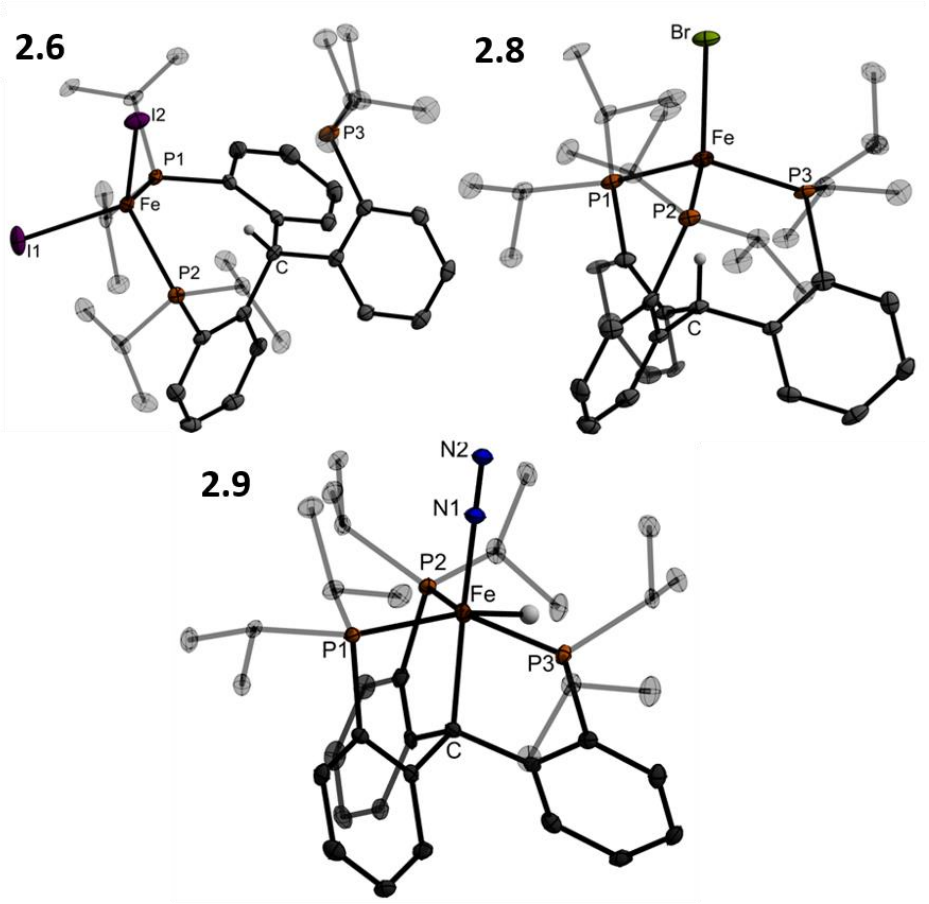

Figure 2.3. Crystal structures of {(CP$^{iPr}_3$)H}FeI$_2$ (**2.6**, top left), {(CP$^{iPr}_3$)H}FeBr (**2.8**, top right), and (CP$^{iPr}_3$)Fe(H)(N$_2$) (**2.9**, bottom). Ellipsoids shown at 50% probability; hydrogen atoms (except the triarylmethine C-H and Fe-H hydride) and solvent molecules omitted for clarity.

2.2.2 Metallation at iron and precursor complexes.

We initially hoped to effect metallation of **2.1** by first deprotonating it to give an alkali metal complex followed by transmetallation with an iron (II) halide or other transition

metal precursor. To our frustration, **2.1** proved unexpectedly difficult to deprotonate even with very strong bases such as benzyl potassium and Schlosser's base,[31] perhaps due in part to the steric protection of the methine proton; additionally, the acidity of this proton is likely not as high as for bare triphenylmethane since the ligand bulk limits the extent to which the aryl rings can approach a coplanar configuration to afford resonance stabilization of a resulting carbanion.[32] Furthermore, the strategy used for metallation of the $(SiP^{iPr}_3)H$ ligand on iron—using methyl Grignard with $FeCl_2$ to generate a methyl iron complex which then eliminates methane with concomitant formation of the iron-silicon bond[24]—was not effective for $(CP^{iPr}_3)H$. It appeared to instead result in reduction of iron without the formation of the desired iron-carbon bond. Thus, it was necessary to develop a different protocol for the formation of a (CP^{iPr}_3)Fe-complex featuring an iron-carbon bond.

Combining **2.1** and iron(II) iodide in toluene cleanly affords the tetracoordinate, κ_2-bisphosphine diiodide high-spin iron(II) complex (**2.6**) as a yellow powder (Scheme 2.2). Its solid-state structure (Figure 2.3) shows a tetrahedral environment at the iron center and a bidentate binding mode for the ligand. One-electron reduction of **2.6** in benzene or toluene using a range of reagents including sodium amalgam, potassium graphite, or alkylmagnesium/lithium reagents, results in the formation of the deep brick-red four-coordinate iron(I) complex $\{(CP^{iPr}_3)H\}FeI$ (**2.7**). The bromide congener, $\{(CP^{iPr}_3)H\}FeBr$ (**2.8**), is analogously prepared and has been crystallographically characterized (Figure 2.3); its most notable feature is the *endo* orientation of the unactivated methine C-*H*. This proton is located within the ligand cage pointed nearly linearly towards the iron center. Both **2.7** and **2.8** are unstable with respect to disproportionation to Fe(0), $(CP^{iPr}_3)H$, and

{(CP$^{iPr}_3$)H}FeX$_2$ (X = I, Br), especially in coordinating solvents. However, if appropriate conditions are employed, **2.7** is sufficiently long-lived to be generated and used without further purification for subsequent reactions.

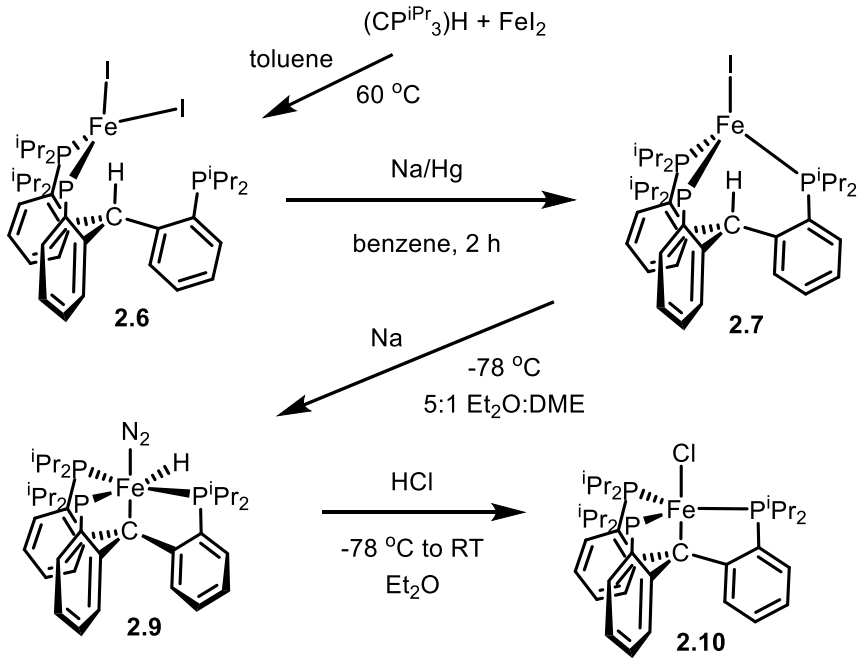

Scheme 2.2. Synthesis of iron complexes of (CP$^{iPr}_3$)H.

Further reduction of **2.7** with sodium metal in a 5:1 mixture of Et$_2$O and DME at -78 °C causes formal insertion of the Fe center into the C-H bond of the (CP$^{iPr}_3$)H ligand and uptake of atmospheric N$_2$ to give yellow, diamagnetic (CP$^{iPr}_3$)Fe(H)(N$_2$) (**2.9**). The position of the iron hydride is identifiable in the XRD difference map of **2.9**, as is the presence of an Fe-C bond at 2.155(2) Å (Figure 2.3). IR data for **2.9** show a strong N-N vibration at 2046 cm^{-1} and an Fe-H vibration at 1920 cm^{-1}.' The properties of **2.9** can be compared to the isostructural (SiP$^{iPr}_3$)Fe(H)(N$_2$) and

$[(NP^{iPr}_3)Fe(H)(N_2)]^+$ complexes[23,33] and other closely related species such as $\{[P(CH_2CH_2P^iPr_2)_3]Fe(H)(N_2)\}^+$;[34] the vibrational and metrical properties of the N_2 ligand suggest a more activated dinitrogen moiety in **2.9** relative to its congeners.

Deprotonation of **2.9** to afford $(CP^{iPr}_3)FeN_2^-$ was canvassed but proved unsuccessful. A more circuitous but ultimately effective route to $(CP^{iPr}_3)FeN_2^-$ proceeded via treatment of **2.9** with anhydrous HCl in Et_2O to afford dark red-orange $(CP^{iPr}_3)FeCl$ (**2.10**) in good yield (Scheme 2.2). The crystal structure of **2.10** was not reliably determined due to its propensity to crystallize in a cubic space group with extensive whole molecule disorder. Complex **2.10** is paramagnetic and its room temperature solution magnetic moment of 4.9 μ_B is suggestive of a high-spin, $S = 2$ ground state. A lower spin state might have been reasonably anticipated to arise from a presumably strong-field ligand set comprised of three diisopropylarylphosphines and an alkyl group. For comparison, $(SiP^{iPr})_3FeCl$ exhibits an intermediate $S = 1$ ground state.[24] The C_{alkyl} anchor in **2.10** thereby appears to be a weaker-field donor than the silyl anchor in $(SiP^{iPr}_3)FeCl$.

Metallation of $(CP^{iPr}_3)H$ on cobalt has also been established. Coordination of the ligand to CoX_2 generates a tetracoordinate cobalt(II) species analogous to **2.6**, which can be reduced by treatment with one equivalent of methylmagnesium bromide in THF at -78 ^oC to give, e.g., $\{(CP^{iPr}_3)H\}CoCl$, which, like the analogous **2.8**, is thermally unstable with respect to disproportionation, decomposing over the course of hours at room temperature in THF solution (Figure 2.4). Further reduction with additional equivalents of methylmagnesium bromide results in C-H bond activation, formal methane loss, and generation of a diamagnetic $(CP^{iPr}_3)CoN_2$ species, whose reactivity has been reported elsewhere.[35]

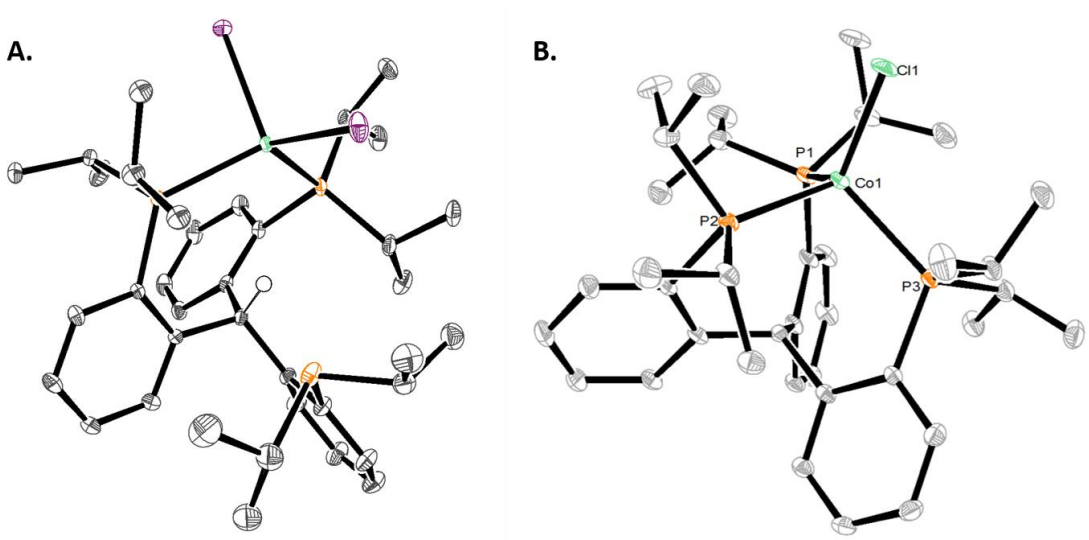

Figure 2.4. Crystal structures of and {(CP$^{iPr}_3$)H}CoI$_2$ (A) and{(CP$^{iPr}_3$)H}CoCl (B). Thermal ellipsoids shown at 50% probability.

2.2.3 Synthesis and characterization of the {(CP$^{iPr}_3$)FeN$_2$}^{n} (n = 0, -1, +1) series.

Reduction of the chloride precursor **2.10** affords entry into the desired series of trigonal bipyramidal iron dinitrogen complexes. Stirring **2.10** over sodium metal in THF produces the neutral low-spin Fe(I) complex (CP$^{iPr}_3$)FeN$_2$ (**2.11**) (υ(NN) = 1992 cm^{-1}) (Scheme 2.3). Complex **2.11** is low-spin and paramagnetic (S = 1/2); it has been crystallographically characterized (Figure 2.5) and shows a distortion from trigonal symmetry with one widened P-Fe-P angle (132.5^o), as expected due to the Jahn-Teller active ground state. The N$_2$ vibrational frequency and N-N bond length (1.134(4) Å) show that the dinitrogen ligand in this complex is somewhat more activated than that in the isoelectronic (SiP$^{iPr}_3$)FeN$_2$ complex (υ(NN) = 2003 cm^{-1}, N-N = 1.1245(2) Å) or in the neutral Fe(0) complex (TP^{iPr}B)FeN$_2$ (υ(NN) = 2011 cm^{-1}).[17,25] These differences are relatively small and as such are difficult to reliably interpret. But given the fact that (CP$^{iPr}_3$) appears to

have a weaker-field donor set than (SiP^{iPr}_3) according to the observed ground spin states of (CP^{iPr}_3)FeCl (S = 2) and (SiP^{iPr}_3)FeCl (S = 1), one might have reasonably anticipated (SiP^{iPr}_3)FeN_2 to have a lower υ(NN) than (CP^{iPr}_3)FeN_2.

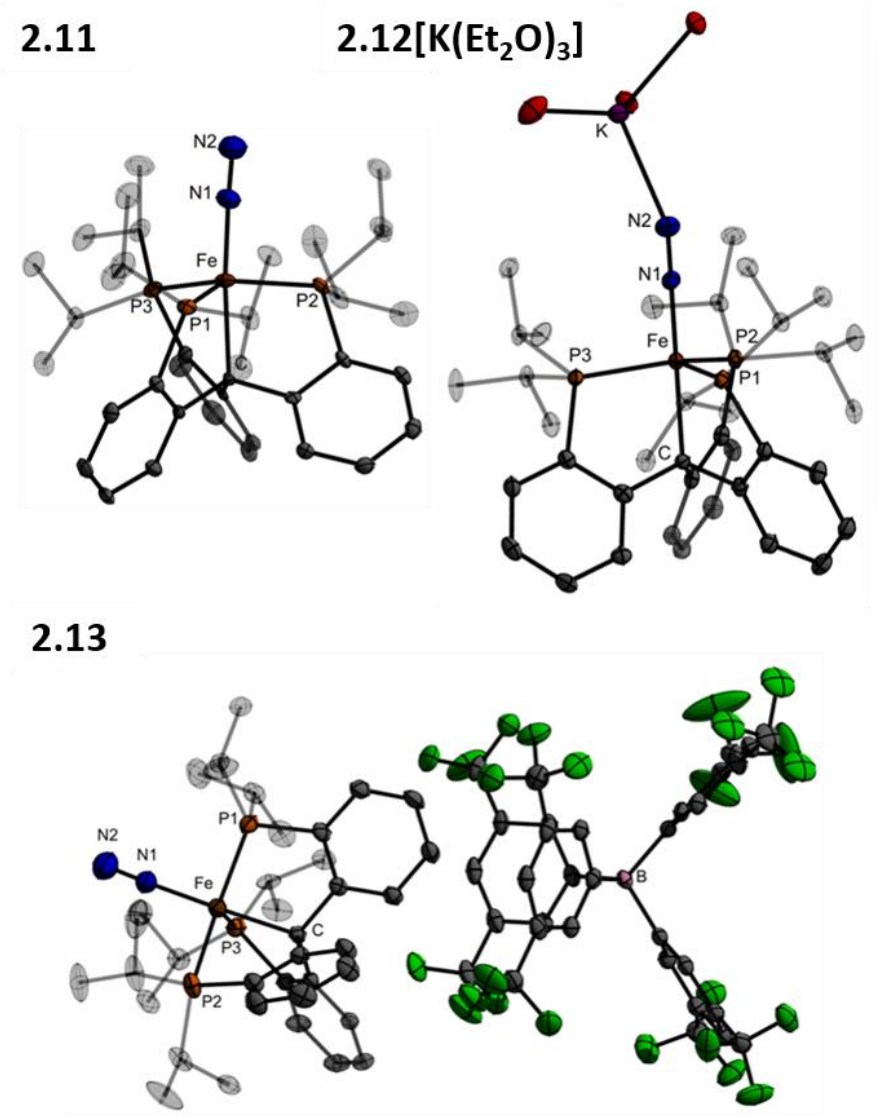

Figure 2.5. Crystal structures of (CP^{iPr}_3)FeN_2 (**2.11**, top left), (CP^{iPr}_3)FeN_2^- (**2.12**[$K(Et_2O)_3$], top right, ethyl groups of coordinated Et_2O molecules omitted), and (CP^{iPr}_3)FeN_2^+ (**2.13**, bottom). Ellipsoids are shown at 50% probability and hydrogen atoms are omitted for clarity.

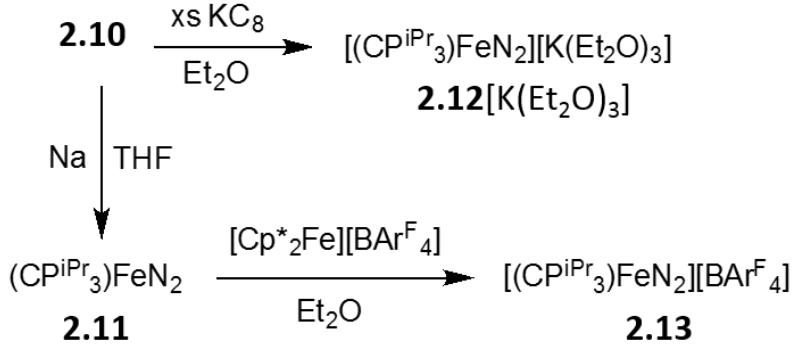

Scheme 2.3. Synthesis of the dinitrogen adduct series $(CP^{iPr}_3)FeN_2$ (**2.11**), $(CP^{iPr}_3)FeN_2^-$ (**2.12**), and $(CP^{iPr}_3)FeN_2^+$ (**2.13**).

Both a one-electron oxidation and a one-electron reduction of **2.11** are accessible (Figure 2.6). The Fe(II/I) couple appears at -1.20 V (vs Fc/Fc^+) and is quasi-reversible; the current in the cathodic wave is diminished and an irreversible reduction wave appears at -1.65 V. This is very similar electrochemical behavior to what has been documented for $(SiP^{iPr}_3)FeN_2$ and suggests that the same phenomenon is responsible for the observations in this system[17]—that is, N_2 coordinates reversibly to the $\{(CP^{iPr}_3)Fe\}^+$ complex; partial loss of N_2 upon oxidation of $(CP^{iPr}_3)FeN_2$ is likely responsible for the quasi-reversibility of the (II/I) couple, and the reduction at -1.65 V is most reasonably attributed to the cationic species $\{(CP^{iPr}_3)Fe(L)\}^+$ (where L may be THF, or may be a vacant site), which then takes up N_2 upon reduction. The Fe(I/0) couple is fully reversible, consistent with the formation of a stable $(CP^{iPr}_3)FeN_2^-$ anion. This reduction occurs at an unusually negative potential (-2.55 V vs Fc/Fc^+). For comparison, the reduction of $(SiP^{iPr}_3)FeN_2$ to $(SiP^{iPr}_3)FeN_2^-$ occurs at -2.2 V.[17]

The Fe-N_2 adduct triad $\{(CP^{iPr}_3)FeN_2\}^n$ (n = 0 (**2.11**), -1 (**2.12**), +1 (**2.13**)) proved synthetically accessible. Treatment of **2.10** with an excess of potassium graphite (KC_8) in Et_2O results in immediate reduction to the very dark brown-blue $CP^{iPr}_3FeN_2^-$ anion (**2.12**). The IR spectrum of a thin film deposited from diethyl ether solution shows a υ(NN) vibration at 1870 cm^{-1}, suggestive of a close ion pair with the potassium ion capping the N_2 moiety. Accordingly, treatment of the potassium complex with two equivalents of 12-crown-4 results in the formation of $[(CP^{iPr}_3)FeN_2][K(12\text{-crown-}4)_2]$ (**2.12**[K(12-crown-4)$_2$]) with a shift of the υ(NN) vibration to 1905 cm^{-1}. The anion has been crystallographically characterized (Figure 2.5) as its $K(Et_2O)_3$ salt, $[(CP^{iPr}_3)FeN_2][K(Et_2O)_3]$ (**2.12**[$K(Et_2O)_3$]; the bulk material after drying is solvated by 0.5 molecules of Et_2O per anion, **2.12**[$K(Et_2O)_{0.5}$]).

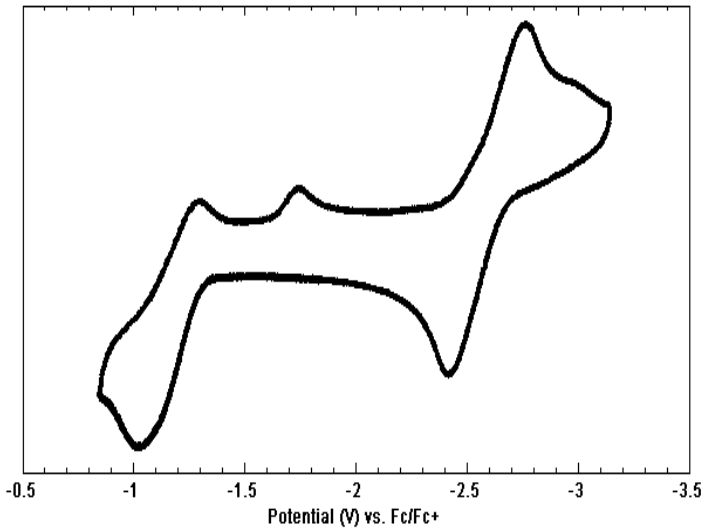

Figure 2.6. Cyclic voltammogram of **2.11**; scan rate 0.5 V/s.

Oxidation of **2.11** with one equivalent of $[Cp^*_2Fe][BAr^F_4]$ (Ar^F = 3,5-trifluoromethylphenyl; Cp* = pentamethylcyclopentadienide) in Et_2O gives rise to

[(CP^{iPr}_3)FeN_2][BAr^F_4] (**2.13**) as an orange crystalline solid, which has also been structurally characterized (Figure 2.5). The dinitrogen ligand in **2.13** (υ(NN) = 2128 cm^{-1}), is labile and in solution under an N_2 atmosphere appears to be in equilibrium with a solvated or vacant cation [(CP^{iPr}_3)Fe(L)]$^+$; in addition to the electrochemical properties discussed above, evidence from UV-vis spectroscopy is consistent with the loss of coordinated N_2 under vacuum.

Whereas a related series was accessible for the silyl-anchored {(SiP^{iPr}_3)FeN_2}^{n} system (n = 0, +1, -1),[17] only the anion ($C^{Si}P^{Ph}_3$)FeN_2^- proved accessible for the previously reported C_{alkyl}-anchored system.[22] Thus, the present {(CP^{iPr}_3)FeN_2}^{n} series allows for a direct comparison of how the anchoring atom (Si vs C) responds across three redox states when positioned trans to an N_2 ligand of an isostructural trigonal bipyramidal framework.

In the case of the {(SiP^{iPr}_3)FeN_2}^{n} series, the Fe-Si bond distance *decreases* upon reduction from 2.298(7) Å in the (SiP^{iPr}_3)FeN_2^+ cation to 2.2526(9) Å in the (SiP^{iPr}_3)FeN_2^- anion. In direct contrast, the Fe-C bond distance in {(CP^{iPr}_3)FeN_2}^{n} *increases* upon reduction, from 2.081(3) Å in **2.13** to 2.152(3) Å in **2.11** to 2.1646(17) Å in **2.12**. The different responses manifest in these two systems may be due to the electropositive silicon atom binding more strongly to the more electron-rich iron, whereas the more electronegative C_{alkyl} binds more strongly to the higher-valent, more electron-deficient iron center.

Notably, the overall change in the bond length is greater in the CP^{iPr}_3 case (0.084 Å from **2.13** to **2.12**) than for the more covalent SiP^{iPr}_3 system, where the overall change is only 0.045 Å despite the longer total bond length. This suggests a greater degree of flexibility in the Fe-C_{alkyl} interaction. A similar conclusion was drawn for the

$\{(C^{Si}P^{Ph}_3)Fe(CO)\}^n$ (n = +1, 0, -1) series, where an even more pronounced Fe-C lengthening was observed upon reduction.[22]

Table 2.1. Select characterization data for the Fe-N_2 adducts $\{(CP^{iPr})_3FeN_2\}^n$ and $\{(SiP^{iPr}_3)FeN_2\}^n$ (n = -1, 0, 1).

X = C, Si[a]	[X-Fe-N2]$^{-}$[b]	X-Fe-N2	[X-Fe-N2]$^{+}$
Fe-C (Å)	2.1646(17)	2.152(3)	2.081(3)
Fe-Si (Å)	2.2526(9)	2.2713(6)	2.298(7)
Fe-$N_{X = C}$ (Å)	1.7397(16)	1.797(2)	1.864(7)
Fe-$N_{X = Si}$ (Å)	1.763(3)	1.8191(1)	1.914(2)
$\nu(N_2)_{X = C}$ (cm^{-1})	1870	1992	2128
$\nu(N_2)_{X = Si}$ (cm^{-1})	1891	2003	2143
spin state	S = 0	S = 1/2	S = 1

[a]All data tabulated for X = Si is taken from reference 17. [b]For X = C, data provided is for the $[K(Et_2O)_3]^+$ salt (Figure 2.5). For X = Si, data provided is for the $[Na(THF)_3]^+$ salt.

In the case of the $(TP^{iPr}B)Fe$ system, a highly flexible Fe-B interaction has been observed as a function of the ligand positioned trans to the B-atom that may be important to its success in activating N_2 in both stoichiometric and catalytic reactions.[15,21,36] However, an analogous series of N_2 complexes has not been characterized to allow for direct comparison. Whereas the anion $[(TP^{iPr}B)]FeN_2]^-$ has been studied by X-ray crystallography (Fe-B = 2.311(2) Å), the $[(TP^{iPr}B)Fe]^+$ cation does not coordinate N_2 at atmospheric pressure, and attempts to obtain the crystal structure of neutral $(TP^{iPr}B)FeN_2$ have been unsuccessful.[25,36] Nonetheless, our chemical intuition is that the Fe-B linkage in $(TP^{iPr}B)Fe$ will be appreciably more flexible than the Fe-C linkage in $(CP^{iPr}_3)Fe$.

The C_{alkyl}-Fe interactions in both $(CP^{iPr}_3)FeN_2^-$ (**2.12**) and $(C^{Si}P^{Ph}_3)FeN_2^-$ reflect a higher degree of ionic character than in a prototypical Fe-C_{alkyl} bond, with $(C^{Si}P^{Ph}_3)FeN_2^-$ being most striking in this context.[22] Comparative DFT studies of $(C^{Si}P^{Ph}_3)FeN_2^-$ and $(CP^{iPr}_3)FeN_2^-$ including NBO analyses, support this view,[22,37] predicting strong polarization of the σ-bond pair towards the C-atom (23% Fe/ 77% C in $(C^{Si}P^{Ph}_3)FeN_2^-$; 27% Fe/ 73% C in $(CP^{iPr}_3)FeN_2^-$) (Figure 2.7). As expected, the Fe-C bond in **2.12** is slightly more covalent than that in $(C^{Si}P^{Ph}_3)FeN_2^-$, where the axial carbon is flanked by electropositive silicon atoms. Comparative NBO analyses for $(C^{Si}P^{Ph}_3)FeN_2^-$, $(SiP^{iPr}_3)FeN_2^-$, and simplified model systems were discussed at greater length in a previous report.[22]

Second-order perturbation analysis from an NBO calculation indicates the presence of stabilizing donor-acceptor interactions between filled and virtual orbitals, representing deviations from a simple Lewis structure description due to electronic delocalization.[37] In the case of **2.12**, significant interactions between the filled Fe-C_{alkyl} σ bond and π* orbitals of the aryl rings (C_{ipso}-C_{ortho}) are evident (Figure 2.7). Three primary donor-acceptor interactions (one to each ring) are located, representing stabilizations of 6.70 kcal/mol, 5.99 kcal/mol, and 5.95 kcal/mol. This result suggests that stabilization of the negative charge on carbon by delocalization onto the aryl rings is at least partially responsible for the observed ionic character of the Fe-C bond, and hence for its increased flexibility. We suggest that a similar stabilization of ionic character at an N_2-Fe-$C_{interstitial}$ site of the cofactor may facilitate N_2 binding.

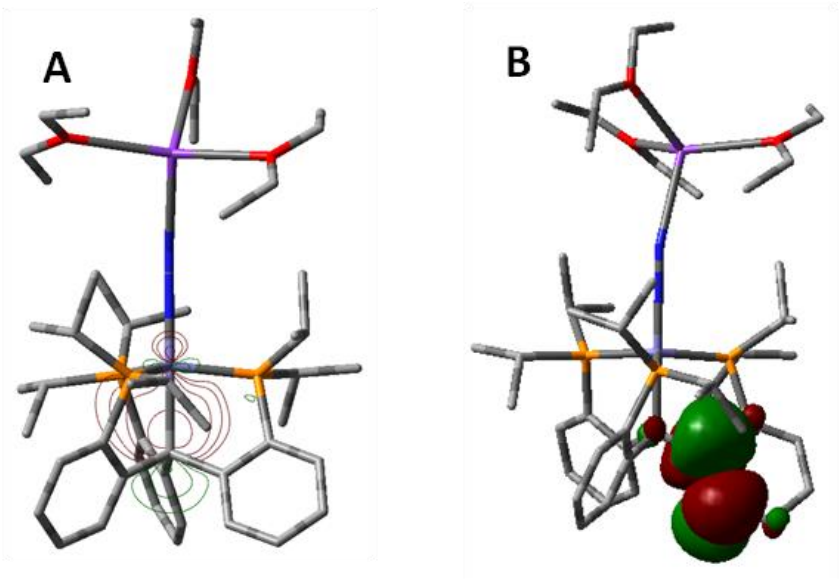

Figure 2.7. (A) Isocontour plot of the Fe-C_{alkyl} σ bond of **2.12**[$K(Et_2O)_3$] located from NBO analyses. (B) Contour plot of one of the C_{aryl} π* orbitals which accepts delocalized electron density from the Fe-C_{alkyl} σ bond.

2.2.4 Reactivity studies.

To compare the reactivity of $(CP^{iPr}_3)FeN_2^-$ at the bound N_2 ligand with $(SiP^{iPr}_3)FeN_2^-$, $(C^{Si}P^{Ph}_3)FeN_2^-$, and $(TP^{iPr}B)FeN_2^-$, treatment of **2.12** with TMSCl at -78 °C was examined and afforded the diamagnetic diazenido complex $(CP^{iPr}_3)FeN_2SiMe_3$ (**2.14**) (υ(NN) = 1736 cm^{-1}). This product, though it has not been structurally characterized, is spectroscopically similar to those obtained for the structurally related Si- and B-anchored systems.[15,17]

More interesting is the comparative behavior of $(CP^{iPr}_3)FeN_2^-$ on treatment with proton/electron equivalents at low temperature. Numerous studies have explored the possibility of Fe-N_2 protonation/reduction to release ammonia,[3,4,5,6,38] which in all but one

case[21] afforded low chemical yields of NH_3 (ca. ≤ 10% per Fe in one step; 35% per Fe overall in two independent synthetic steps[14]). The previously described C-anchored system $(C^{Si}P^{Ph}_3)FeN_2^-$ (Figure 2.2) follows a similar trend, affording negligible NH_3 on treatment at low temperature with $[H(Et_2O)_2][BAr^F_4]$ and KC_8. The Si-anchored system $(SiP^{iPr}_3)FeN_2^-$ also affords sub-stoichiometric NH_3 yields (35% per Fe) when similarly treated, and instead produces some N_2H_4 (~45% per Fe) when $H(Et_2O)BF_4$ and $CrCl_2$ are employed.[24]

By contrast, cooling a solution of **2.12**$[K(Et_2O)_{0.5}]$ in Et_2O at -78 °C followed by the addition of 40 equiv KC_8 and then 38 equiv $[H(Et_2O)_2][BAr^F_4]$ leads to the formation of 4.6 ± 0.8 equiv NH_3 (230% per Fe; average of 8 runs; Eq. 2.1), a yield that establishes a modest degree of N_2 reduction catalysis at low temperature. No N_2H_4 is observed. With **2.12**$[K(12\text{-crown-}4)_2]$ as the catalyst, the NH_3 yield is slightly lower at 3.5 ± 0.3 equiv. NH_3 quantification was carried out by UV-Vis using the indophenol protocol[39] as recently described in detail for the $(TP^{iPr}B)FeN_2^-$ catalyst system.[21] The total NH_3 product yield is lower for $(CP^{iPr}_3)FeN_2^-$ than that which was obtained for $(TP^{iPr}B)FeN_2^-$ when acid was added prior to the reductant. The significance of these modest differences is unclear, especially given the extreme air-sensitivity of the catalysts and the low turnover numbers. The order of addition of reagents has a minor effect; reversing the order and adding first acid, then reductant to **2.12**$[K(Et_2O)_{0.5}]$ decreases the yield to 3.8 ± 0.6 equiv. NH_3 per Fe. In side-by-side comparisons using the same batches of reagents (KC_8 and $[H(Et_2O)_2][BAr^F_4]$) and the same order of addition (*reductant added first*), **2.12**$[K(Et_2O)_{0.5}]$ afforded 4.4 ± 0.2 equiv. NH_3 per Fe, as compared to 5.0 ± 1.1 for $(TP^{iPr}B)FeN_2^-$ and 0.8 ± 0.4 for $(SiP^{iPr}_3)FeN_2^-$.

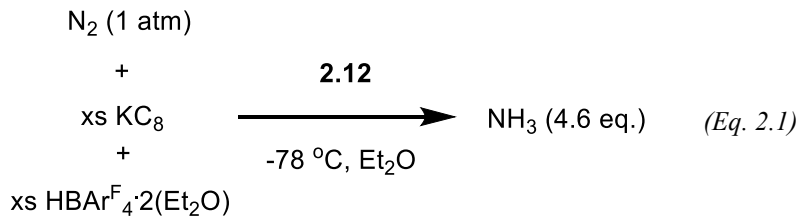

(Eq. 2.1)

Treatment of **2.12**[$K(Et_2O)_{0.5}$] with 10 equivalents of [$H(Et_2O)_2$][BAr^F_4] in the absence of added reductant generates negligible ammonia (<0.05 equivalents), verifying that both acid and reductant are necessary for the production of substantial amounts of NH_3.

In order to examine possible reasons for the limited turnover for ammonia production with this system, we sought to determine the fate of the precatalyst over the course of the experiment. An analysis of the iron-containing products of a reaction mixture using 10 equivalents of [$H(Et_2O)_2$][BAr^F_4] and 12 equivalents of KC_8 (Figure 2.8) identified the major iron-containing product as (CP^{iPr}_3)FeN_2 (**2.11**), which is readily reduced by KC_8 even at low temperature to reform the precatalyst **2.12**. However, a significant amount of (CP^{iPr}_3)Fe(N_2)(H) (**2.9**) is also present; **2.9** is not catalytically competent, generating no detectable ammonia when subjected to the catalytic conditions, and its formation is likely an important limiting factor in the catalyst performance. Another identifiable species by ^{1}H NMR is (CP^{iPr}_3)FeCl (**2.10**). Despite our efforts to remove all Cl^- in the preparation of [$H(Et_2O)_2$][BAr^F_4], the large excess of acid employed in this experiment likely ensures a non-negligible Cl^- impurity that may also attenuate catalyst activity. The identity of another diamagnetic hydride-bearing species apparent in the ^{1}H NMR is not currently known.

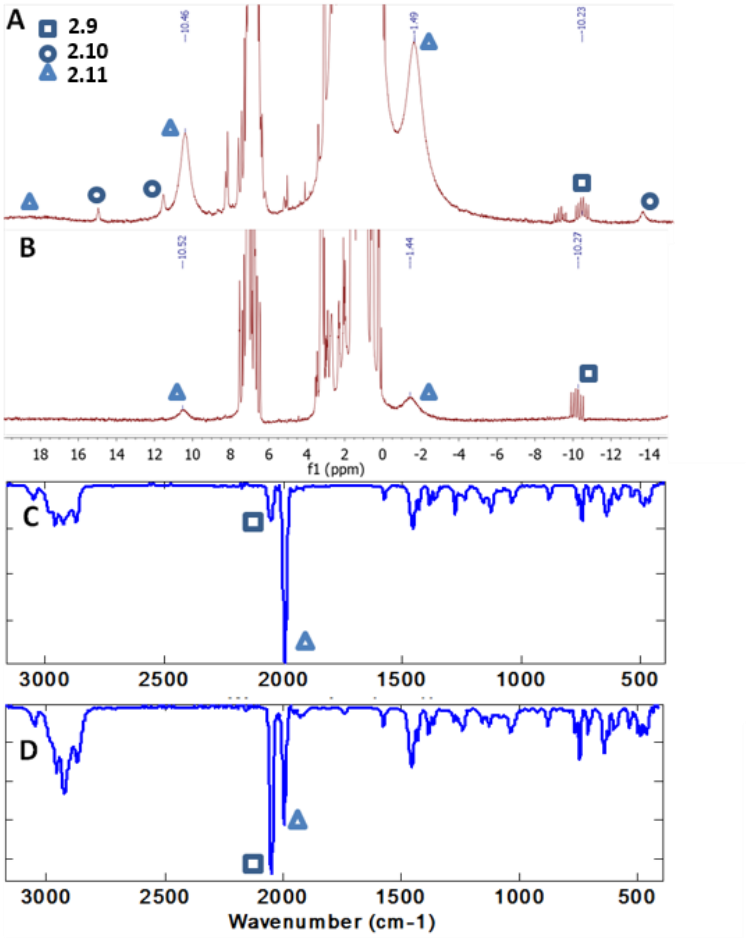

Figure 2.8. Spectroscopic analyses of reaction mixtures following the catalytic production of NH_3 using **2.12**[$K(Et_2O)_{0.5}$] as a catalyst. Symbols indicate characteristic resonances attributed to **2.9**, **2.10**, and **2.11**. (A),(C) ^1H NMR and IR spectra of a post-catalytic reaction mixture using 10 equiv. of $[H(Et_2O)_2][BAr^F{}_4]$ and 12 equiv. of KC_8. (B),(D) ^1H NMR and IR spectra of a post-catalytic reaction mixture using 38 equiv. of $[H(Et_2O)_2][BAr^F{}_4]$ and 40 equiv. of KC_8.

Further product analysis using the full catalytic conditions (38 equivalents of $[H(Et_2O)_2][BAr^F{}_4]$ and 40 equivalents of KC_8 with respect to the catalyst) showed that increasing amounts of $(CP^{iPr}{}_3)Fe(N_2)(H)$ (**2.9**) are formed as the system goes through

more turnovers, corroborating the idea that this species serves as a catalytically inactive sink which builds up throughout the reaction. Integration of the NMR spectrum of such a reaction mixture against an internal standard suggests that approximately 70% of the catalyst has been converted to **2.9**; even at this point, however, some active catalyst remains in the form of **2.11 (**Figure 2.8). The unknown hydride species present in the aforementioned reaction mixture derived from fewer equivalents of acid and reductant is no longer observed.

Notably, in neither of these experiments was any free ligand **2.1** (nor any ligand decomposition product) detected; it appears that all of the iron present remains ligated by the CP^{iPr}_3 ligand. This lack of degradation is promising, and suggests that improvements to the N_2 reduction catalysis, in terms of turnover number, may yet prove possible if the formation of terminal hydride **2.9** can be limited by modification of either the ligand scaffold and/or the catalytic conditions. Indeed, it may be that biological nitrogenases are designed to avoid catalytically inactive hydride sinks by being themselves modest hydrogenases.[40] A cluster approach would be a particularly good design in this context.[41]

2.3 Conclusions

To conclude, we have synthetically introduced the tripodal $(CP^{iPr}_3)H$ ligand and have prepared and structurally compared its $\{(CP^{iPr}_3)FeN_2\}^n$ complexes (n = 0, -1, +1) with those of the isostructural series $\{(SiP^{iPr}_3)FeN_2\}^n$. The $\{(CP^{iPr}_3)FeN_2\}^n$ complexes feature an axial N_2 ligand bound trans to an axial C-atom in a trigonal bipyramidal geometry, a design meant to crudely model one plausible geometry for a single Fe-N_2 binding site in the iron-molybdenum cofactor (FeMoco). The C_{alkyl}-Fe interaction in the $(CP^{iPr}_3)Fe$ system exhibits a substantially higher degree of ionic character, and is more flexible, than for

the related Si_{silyl}-Fe interaction in the isostructural and isoelectronic $(SiP^{iPr}_3)Fe$ system.[17] We suggest that this type of Fe-C flexibility crudely models the flexibility one can intuit for an N_2-Fe-$C_{interstitial}$ interaction within FeMoco. Whereas the N_2 anion $(SiP^{iPr}_3)FeN_2^-$ does not effectively facilitate the delivery of H-atoms to N_2 to produce NH_3 via proton/reductant equivalents, an Et_2O solution of $(CP^{iPr}_3)FeN_2^-$ under 1 atm of N_2 releases ca. 4.6 equiv NH_3 relative to Fe. The modest catalytic N_2 reduction behavior of $(CP^{iPr}_3)FeN_2^-$ at -78 °C is comparable to $(TP^{iPr}B)FeN_2^-$.[21]

It is noteworthy that amongst the isostructural SiP^{iPr}_3, $TP^{iPr}B$, and CP^{iPr}_3 series, the system with the most flexible axial linkage, $(TP^{iPr}B)Fe$, gives the greatest catalytic yield under a common set of reaction conditions, while the least flexible, $(SiP^{iPr}_3)Fe$, gives only substoichiometric yields of ammonia; the $(CP^{iPr}_3)Fe$ system falls in between the two both in terms of flexibility and catalytic competence. While we emphasize caution in interpreting these differences given the low overall turnover numbers, they are consistent with the previously advanced hypothesis that a flexible Fe-$C_{interstitial}$ interaction might facilitate N_2 binding and reduction at a single Fe site within FeMoco. Our structural and DFT studies[22] demonstrate that, in the right environment, a carbon atom can serve as a modestly flexible ligand trans to an Fe-N_2 binding site, and that this flexibility is enhanced by the ability of the carbon to accommodate a significant ionic charge. It seems likely to us that the inorganic carbide ligand in FeMoco is similarly, and likely more, able to stabilize substantial ionic character in the Fe-$C_{interstitial}$ bond (Figure 2.1), resulting in a flexible interaction that initially exposes an N_2 binding site that can be further modulated as a function of the N_xH_y reduction state.

At this stage reliable conclusions concerning the influence of the carbon atom on the intimate step-wise mechanism of nitrogen reduction are premature. Even within our synthetic series, it may be that different catalysts follow different mechanistic pathways (distal vs. alternating, or some hybrid path);[21,42] for instance, the most flexible system, (TP$^{i\mathrm{Pr}}$B)Fe, may be better suited to facilitate a distal pathway that samples strongly pi-bonded intermediates, while (CP$^{i\mathrm{Pr}}{}_3$)Fe, which we presume is less flexible, could instead be dominated by an alternating or hybrid pathway. Whether these structurally related iron systems mediate nitrogen reduction by a common or different mechanism will be challenging to determine but is a fascinating question. The work presented here adds to the context needed for further mechanistic studies on both synthetic and biological iron systems for catalytic nitrogen fixation.

2.4 Experimental Methods

2.4.1 General.

All manipulations were carried out using standard Schlenk or glovebox techniques under an N_2 atmosphere. Unless otherwise noted, solvents were deoxygenated and dried by thoroughly sparging with N_2 followed by passage through an activated alumina column in a solvent purification system by SG Water, USA LLC. Non-halogenated solvents were tested with a standard purple solution of sodium benzophenone ketyl in tetrahydrofuran in order to confirm effective moisture removal. *O*-iodotriphenylmethane,[28] $H(OEt_2)_2[B(3,5\text{-}(CF_3)_2\text{-}C_6H_3)_4]$,[43] KC_8,[44] $[(TPB)FeN_2][Na(12\text{-crown-}4)_2]$,[25] $[(SiP^{i\mathrm{Pr}}{}_3)FeN_2][Na(12\text{-crown-}4)_2]$[17] and $[(C^{\mathrm{Si}}P^{\mathrm{Ph}}{}_3)FeN_2][K(18\text{-crown-}6)_2]$[22] were prepared according to literature procedures. [Decamethylferrocenium][$B(3,5\text{-}(CF_3)_2\text{-}C_6H_3)_4$] was prepared by treating [ferrocenium][$B(3,5\text{-}(CF_3)_2\text{-}C_6H_3)_4$][45] with decamethylferrocene and

used without purification. $FeI_2(THF)_2$ was prepared by treating Fe powder with I_2 in THF,[46] and was dried to FeI_2 by heating under vacuum at 80°C for 6 hours. All other reagents were purchased from commercial vendors and used without further purification unless otherwise stated.

2.4.2 Physical methods.

Elemental analyses were performed by Robinson Microlit Laboratories (Ledgewood, NJ). Deuterated solvents were purchased from Cambridge Isotope Laboratories, Inc., degassed, and dried over active 3-Å molecular sieves prior to use. ^{1}H and ^{13}C chemical shifts are reported in ppm relative to tetramethylsilane, using residual proton and ^{13}C resonances from solvent as internal standards. ^{31}P and ^{19}F chemical shifts are reported in ppm relative to 85% aqueous H_3PO_4 and $CFCl_3$, respectively. Solution phase magnetic measurements were performed by the method of Evans.[47] Optical spectroscopy measurements were taken on a Cary 50 UV-Vis spectrophotometer using a 1-cm two-window quartz cell. Electrochemical measurements were carried out in a glovebox under a dinitrogen atmosphere in a one compartment cell using a CH Instruments 600B electrochemical analyzer. A glassy carbon electrode was used as the working electrode and platinum wire was used as the auxiliary electrode. The reference electrode was $Ag/AgNO_3$ in THF. The ferrocene couple Fc+/Fc was used as an internal reference. Solutions (THF) of electrolyte (0.2 M tetra-*n*-butylammonium hexafluorophosphate) and analyte were also prepared under an inert atmosphere.

2.4.3 X-ray Crystallography.

XRD studies were carried out at the Beckman Institute Crystallography Facility on a Bruker Kappa Apex II diffractometer (Mo Kα radiation). Structures were solved using

SHELXS and refined against F^2 on all data by full-matrix least squares with SHELXL.[48] The crystals were mounted on a wire loop. Methyl group hydrogen atoms not involved in disorder were placed at calculated positions starting from the point of maximum electron density. All other hydrogen atoms, except where otherwise noted, were placed at geometrically calculated positions and refined using a riding model. The isotropic displacement parameters of the hydrogen atoms were fixed at 1.2 (1.5 for methyl groups) times the U_{eq} of the atoms to which they are bonded.

2.4.4 Computations

A single-point calculation and Natural Bond Orbital (NBO) analysis was carried out on $[(CP^{iPr}{}_3)FeN_2][K(Et_2O)_3]$ (**2.12**) using the crystallographically determined atomic coordinates at the B3LYP/6-31++G(d,p) level of theory using the Gaussion03 suite of programs.[49] NBO analysis located a polarized σ interaction between Fe and the C-atom anchor (C01).

2.4.5 Syntheses

10-phenyl-10*H*-dibenzo[*b,e*]iodininium bromide (2.2). The procedure for the generation of **2.2** and **2.4** (below) was adapted from a reported method for the generation of diaryliodonium salts.[29] 3-chloroperoxybenzoic acid (9.0 g, ~70% by mass, ~0.037 mol) was dissolved in dichloromethane (150 mL) and cooled to 0 ^oC. 2-iodotriphenylmethane (11.7 g, 0.0316 mol) was added as a solid in portions over the course of 10 minutes, during which time there was no observable change to the reaction mixture. This mixture was stirred at 0 ^oC for 10 minutes and then neat trifluoromethanesulfonic acid (8.74 mL, 0.0990 mol) was added via syringe over the course of 5 minutes. The reaction mixture turned dark brown. After an additional 20 minutes, the reaction mixture was allowed to

warm to room temperature and stirred for one hour, and then the solvent was removed *in vacuo*. The solid material was suspended in 200 mL of diethyl ether and 200 mL of water, and then solid sodium bromide (14 g, 0.136 mol) was added and the mixture was shaken vigorously for 5 minutes, during which time a fine off-white precipitate developed. The precipitate was collected atop a sintered glass frit and washed copiously with water and diethyl ether (14.2 g, 0.0316 mol, quant). ^{1}H NMR ($(CD_3)_2S=O$, 300 MHz, 298 K, δ): 8.27 (dd, J = 8 Hz, 1 Hz, 2H), 7.68 (td, J = 8 Hz, 1 Hz, 2H), 7.46 (td, J = 8 Hz, 1 Hz), 7.27 (m, 3H), 6.78 (dm, J = 8 Hz, 2H), 6.09 (s, 1H) ppm. ^{13}C NMR ($(CD_3)_2S=O$, 75.4 MHz, 298 K, δ): 140.3 (s), 138.3 (s), 135.0 (s), 132.7 (s), 131.7 (s), 129.6 (s), 128.9 (s), 127.9 (s), 127.4 (s), 117.4 (s), 57.7 (s) ppm. ESI-MS (positive ion, amu): Calc. 370.0; Found 370.0.

2-bromo-2'-iodotriphenylmethane (2.3). 10-phenyl-10*H*-dibenzo[*b*,*e*]iodininium bromide (16.11 g, 0.0358 mol) was suspended in dry, degassed acetonitrile (250 mL), and solid tetrabutylammonium bromide (25 g, 0.078 mol) and copper(I) bromide (8 g, .06 mol) were added. The mixture was heated to a vigorous reflux and stirred at reflux for five days. The dark brown reaction mixture was then concentrated to dryness *in vacuo*, extracted with toluene, and filtered through a silica plug. The pale yellow filtrate was concentrated to dryness and the resulting material was recrystallized from methanol to give the desired product as an off-white powder which was collected atop a sintered glass frit and washed with cold methanol (12.7 g, 0.0282 mol, 79%). ^{1}H NMR ($CDCl_3$, 300 MHz, 298 K, δ): 7.90 (dd, J = 8 Hz, 1 Hz, 1H), 7.60 (dd, J = 8 Hz, 1 Hz, 1H), 7.34-7.18 (m, 5H), 7.13 (td, J = 8 Hz, 1 Hz, 1H), 7.03 (dd, J = 8 Hz, 1 Hz, 2H), 6.95 (td, J = 8 Hz, 1 Hz, 1H), 6.79 (dd, J = 8 Hz, 1 Hz, 2H), 6.02 (s, 1H) ppm. ^{13}C NMR ($CDCl_3$, 75.4 MHz,

298 K, δ): 145.2 (s), 142.2 (s), 141.1 (s), 140.1 (s), 133.1 (s), 131.2 (s), 130.7 (s), 130.0 (s), 128.5 (s), 128.3 (s), 128.2 (s), 128.0 (s), 127.2 (s), 126.7 (s), 126.3 (s), 102.9 (s), 60.8 (s) ppm. MS (amu): Calc. 449.9, 447.9; Found 449.9, 447.9.

10-(2-bromophenyl)-10*H*-dibenzo[*b,e*]iodininium iodide (2.4). 3-chloroperoxybenzoic acid (5 g, ~70% by mass, ~0.0203 mol) was dissolved in dichloromethane (200 mL) and cooled to 0 ^{o}C. 2-bromo-2'-iodotriphenylmethane (8.2 g, 0.0182 mol) was added as a solid in portions over the course of 10 minutes, during which time there was no observable change in the reaction mixture. This mixture was stirred at 0 ^{o}C for 10 minutes and then neat trifluoromethanesulfonic acid (5.04 mL, 0.0571 mol) was added via syringe over the course of 5 minutes. The reaction mixture turned dark brown. After an additional 30 minutes, the reaction mixture was allowed to warm to room temperature and stirred for 30 minutes, and then the solvent was removed *in vacuo*. The solid material was suspended in 200 mL of diethyl ether and 200 mL of water, and then solid potassium iodide (15 g, 0.090 mol) was added and the mixture was shaken vigorously for 5 minutes, during which time a fine yellow precipitate developed. The precipitate was collected atop a sintered glass frit and washed copiously with water and diethyl ether (9.95 g, 0.0173 mol, 95%). ^{1}H NMR ($(CD_3)_2S=O$, 300 MHz, 298 K, δ): 8.20 (dd, J = 8 Hz, 1 Hz, 2H), 7.83 (dd, J = 8 Hz, 1 Hz, 2H), 7.72 (dd, J = 8 Hz, 1 Hz, 1H), 7.60 (td, J = 8 Hz, 1 Hz, 2H), 7.47-7.39 (m, 3H), 7.33 (td, J = 8 Hz, 1 Hz, 1H), 7.23 (dd, J = 8 Hz, 1 Hz, 1H), 6.02 (s, 1H) ppm. ^{13}C NMR ($(CD_3)_2S=O$, 75.4 MHz, 298 K, δ): 138.9 (s), 135.4 (s), 135.1 (s), 135.0 (s), 133.4 (s), 132.8 (s), 131.7 (s), 130.7 (s), 130.0 (s), 128.0 (s), 117.2 (s), 110.0 (s), 58.8 (s) ppm. ESI-MS (positive ion, amu): Calc. 446.9, 448.9; Found 446.9, 448.9.

2-bromo-2',2''-diiodotriphenylmethane (2.5): Solid 10-(2-bromophenyl)-10*H*-dibenzo[*b,e*]iodininium iodide (4.54 g, 7.88 mmol) was sealed inside a Schlenk tube under N_2 and heated to 200^o C for 15 minutes, and then cooled to room temperature. The resulting dark violet residue was taken up in dichloromethane (50 mL) and washed with saturated aqueous sodium thiosulfate (50 mL) and then water (30 mL) and saturated aqueous sodium chloride (30 mL), then dried over magnesium sulfate, filtered, and concentrated to dryness *in vacuo*. The resulting off-white residue was recrystallized from methanol to give the desired product as a fine white powder, which was collected atop a sintered glass frit and washed with cold methanol (3.4 g, 5.90 mmol, 75%). ^{1}H NMR ($CDCl_3$, 300 MHz, 298 K, δ): 7.93 (d, J = 8 Hz, 2H), 7.64 (d, J = 8 Hz, 1H), 7.30-7.16 (m, 4H), 7.00 (t, J = 8 Hz, 2H), 6.72 (d, J = 8 Hz, 3H), 6.04 (s, 1H) ppm. ^{13}C NMR ($CDCl_3$, 75.4 MHz, 298 K, δ): 144.1 (s), 141.1 (s), 140.2 (s), 133.3 (s), 131.1 (s), 130.7 (s), 128.6 (s), 128.5 (s), 127.3 (s), 126.7 (s), 103.6 (s), 65.4 (s) ppm. MS (amu): Calc. 573.8, 575.8; Found 446.9, 448.9 ([M-I]+), 368.1 ([M-I-Br]+), 320.1, 322.1 ([M-2I]+).

Tris(2-(diisopropylphosphino)phenyl)methane ("($C^{iPr}P_3$)H") (2.1): 2-bromo-2',2''-diiodotriphenylmethane (2.00 g, 3.48 mmol) was dissolved in diethyl ether (100 mL) and cooled to -78 ^{o}C while stirring. Solid *t*-butyllithium (1.36 g, 21.23 mmol) was added in portions over the course of 10 minutes and the reaction mixture was stirred at low temperature for 3 hours. Then chlorodiisopropylphosphine (1.96 g, 12.8 mmol) was dissolved in 10 mL of diethyl ether and added to the reaction mixture. The reaction mixture was allowed to warm slowly to room temperature overnight, resulting in the precipitation of a fine white solid. The reaction mixture was filtered through silica and the pale yellow-orange filtrate was concentrated to a sticky yellow solid which was triturated with

acetonitrile to give an off-white powder. The solid was washed copiously with acetonitrile and then dried under vacuum, giving 1.4 g (2.36 mmol, 68%) of the desired product. ^{1}H NMR (C_6D_6, 300 MHz, 298 K, δ): 8.15 (q, J = 6 Hz, 1H), 7.44 (d, J = 7 Hz, 3H), 7.06 (td, J = 7 Hz, 2 Hz, 3H), 7.00-6.93 (m, 6H), 2.27 (septet of doublets, J = 4 Hz, 7 Hz, 3H), 1.73 (septet of doublets, J = 3 Hz, 7 Hz, 3H), 1.40 (dd, J = 7 Hz, 13 Hz, 9H), 1.32 (dd, J = 7 Hz, 12 Hz, 9H), 0.88 (dd, J = 7 Hz, 13 Hz, 9H), 0.44 (dd, J = 7 Hz, 12 Hz, 9H) ppm. ^{13}C NMR (C_6D_6, 75.4 MHz, 298 K, δ): 159.0 (d, J = 29 Hz), 144.8 (d, J = 17 Hz), 140.0 (s), 139.3 (s), 132.4 (s), 59.1 (m), 32.7 (m), 30.0 (m), 29.4 (s), 27.3 (m), 21.0 (s) ppm. ^{31}P NMR (C_6D_6, 121.4 MHz, 298 K, δ): -9.1 ppm. Anal. Calcd. for $C_{37}H_{55}P_3$: C, 74.97; H, 9.35. Found: C, 74.73; H, 9.49.

{(CP$^{i\mathrm{Pr}}_3$)H}FeI$_2$ (2.6): (CP$^{i\mathrm{Pr}}_3$)H (500 mg, 0.843 mmol) was added to FeI_2 (350 mg, 1.13 mmol) in 15 mL of toluene and stirred at 60 ^{o}C for 2 hours, at which point the reaction mixture was filtered through Celite and the yellow filtrate was concentrated to give a yellow powder (761 mg, 0.843 mmol, quant). Crystals suitable for X-ray diffraction were grown by layering of pentane over a saturated toluene solution. ^{1}H NMR (C_6D_6, 300 MHz, 298 K, δ): 179.69, 26.00, 18.60, 14.92, 14.28, 13.62, 12.74, 9.96, 9.00, 8.29, 6.76, 6.16, 5.72, 5.48, 4.97, 4.28, 3.78, 0.30, 0.13, -0.48, -0.91, -2.02, -3.68, -5.09, -9.45 ppm. μ_{eff} (C_6D_6, Evans' method, 298 K): 4.85 μ_B.

(CP$^{i\mathrm{Pr}}_3$)Fe(N$_2$)H (2.9): {(CP$^{i\mathrm{Pr}}_3$)H}FeI$_2$ (370 mg, 0.410 mmol) was suspended in benzene (10 mL) and stirred vigorously over an excess of 0.7 % sodium/mercury amalgam (25 mg Na, 1.1 mmol) for two hours. The initially yellow suspension turned a deep brick red color during this time due to the formation of {(CP$^{i\mathrm{Pr}}_3$)H}FeI (**7**). The reaction mixture was filtered through Celite and concentrated to dryness *in vacuo*. The deep red resi-

due was then suspended in diethyl ether (15 mL) at -78 °C and 3 mL of dimethoxyethane was added; this solution was vigorously stirred over excess sodium mirror for 4 hours at -78 °C, during which time the color lightened to orange. The reaction mixture was then filtered through Celite and concentrated to dryness. The residue was extracted into pentane and again filtered through Celite, giving a lighter yellow-orange filtrate which was concentrated to dryness again. This residue could be recrystallized from diethyl ether by slow evaporation to give yellow crystalline solids. These solids were washed with hexamethyldisiloxane and minimal cold diethyl ether, and then dried *in vacuo* to give 155 mg (0.229 mmol, 56%) of the desired product. Crystals suitable for X-ray diffraction were grown by evaporation of a concentrated pentane solution into hexamethyldisiloxane. ^{1}H NMR (C_6D_6, 300 MHz, 298 K, δ): 7.57 (t, J = 6 Hz, 1H), 7.34 (m, 1H), 7.08 (m, 2H), 6.96 (m, 2H), 6.83-6.75 (m, 4H), 6.65 (m, 1H), 6.50 (m, 1H), 2.94 (septet, J = 8 Hz, 1H), 2.75 (m, 2H), 2.36 (septet, J = 6 Hz, 1H), 2.05 (septet, J = 7 Hz, 1H), 1.75-1.17 (m, 25H), 1.02 (dd, J = 7 Hz, 11 Hz, 3H), 0.65 (dd, J = 7 Hz, 15 Hz, 3H), 0.56 (dd, J = 7 Hz, 10 Hz, 3H), 0.27 (dd, J = 8 Hz, 13 Hz, 3H), -10.2 (ddd, J = 38 Hz, 53 Hz, 50 Hz) ppm. ^{31}P NMR (C_6D_6, 121.4 MHz, 298 K, δ): 90.1 (dt, J = 100 Hz, 17 Hz, 1P), 67.0 (m, 1P), 63.4 (dt, J = 100 Hz, 17 Hz, 1P) ppm. IR (thin film; cm^{-1}): 2046 (N-N), 1920 (Fe-H). Anal. Calcd. for $C_{37}H_{55}FeP_3N_2$: C, 65.68; H, 8.19; N, 4.14. Found: C, 65.91; H, 7.89; N, 3.94.

{(CP$^{i\mathrm{Pr}}{}_3$)H}FeBr (2.8): {(CP$^{i\mathrm{Pr}}{}_3$)H}$FeBr_2$ (5.0 mg, 0.0070 mmol, generated by treating CP_3H with anhydrous $FeBr_2$ in toluene) was dissolved in toluene, cooled to -78 °C, and treated with isopropyl magnesium chloride (3.5 μL, 2.0M in Et_2O). The reaction mixture rapidly turned dark brick-red. It was stirred at low temperature for one hour and then allowed to warm to room temperature for thirty minutes before being filtered and concen-

trated. The dark red powder was not purified, but was analyzed by NMR in C_6D_6, and X-ray quality crystals were grown by layering pentane over a filtered benzene solution.

(CP$^{iPr}_3$)FeCl (2.10): (CP$^{iPr}_3$)Fe(N_2)H (61 mg, 0.0901 mmol) was dissolved in diethyl ether (8 mL) and cooled to -78 ^oC. HCl in diethyl ether (1.0 M, 108 μL, 0.108 mmol) was added to the solution in one portion. The reaction mixture was stirred at low temperature for one hour and then warmed to room temperature and stirred overnight. The color darkened to deep red-orange, and the reaction mixture was filtered through Celite and concentrated to dryness. The red residue was recrystallized by evaporation of a pentane solution into hexamethyldisiloxane and the resulting dark red crystals were washed sparingly with cold pentane and dried *in vacuo,* giving 46 mg (0.0673 mmol, 75%) of (CP$^{iPr}_3$)FeCl. Crystals suitable for X-ray diffraction were grown by evaporation of a concentrated pentane solution into hexamethyldisiloxane. ^{1}H NMR (C_6D_6, 300 MHz, 298 K, δ): 179.93, 26.47, 23.05, 17.44, 17.22, 15.03, 11.66, 1.52, -10.27, -13.36, -16.82 ppm. μ_{eff} (C_6D_6, Evans' method, 298 K): 4.92 μ_B. Anal. Calcd. for $C_{37}H_{54}FeP_3Cl$: C, 65.06; H, 7.97. Found: C, 64.96; H, 8.01.

(CP$^{iPr}_3$)FeN$_2$ (2.11): (CP$^{iPr}_3$)FeCl (82 mg, 0.120 mmol) was dissolved in THF (2 mL) and stirred over sodium mirror for 20 minutes, or until NMR analysis showed complete consumption of the starting material, and then filtered and concentrated. The residue was extracted with pentane and filtered through Celite, and concentrated to a brownish-orange residue which was recrystallized by evaporation of a pentane solution into hexamethyldisiloxane. The dark brown-orange crystals were washed with hexamethyldisiloxane and cold pentane and dried *in vacuo* to give 39 mg (0.0581 mmol, 48 %) of (CP$^{iPr}_3$)FeN_2. Crystals suitable for X-ray diffraction were grown by evaporation of a concentrated pen-

tane solution into hexamethyldisiloxane. ^{1}H NMR (C_6D_6, 300 MHz, 298 K, δ): 19.3 (very broad), 10.4, 6.8, 3.0, 2.0, 0.6, -1.4 ppm. μ_{eff} (C_6D_6, Evans' method, 298 K): 1.75 μ_B. IR (thin film; cm^{-1}): 1992 (N-N). Anal. Calcd. for $C_{37}H_{54}FeP_3N_2$: C, 65.78; H, 8.06; N, 4.15. Found: C, 66.03; H, 8.01; N, 3.86.

[(CP$^{iPr}_3$)FeN$_2$][K(Et$_2$O)$_{0.5}$] (2.12[K(Et$_2$O)$_{0.5}$]): (CP$^{iPr}_3$)FeCl (40 mg, 0.0586 mmol) was dissolved in diethyl ether(5 mL) at room temperature and an excess of potassium graphite (KC_8, 25 mg) was added. The reaction mixture was stirred for 10 minutes and then filtered through Celite. The dark brown solution was concentrated to about 2 mL and then pentane was layered over the ether solution and it was allowed to stand overnight during which time dark bluish-brown crystals formed. The supernatant was decanted and the crystals were washed thoroughly with pentane and thoroughly dried under vacuum, giving 26 mg of the desired product (0.0277 mmol, 47%). NMR analysis indicates the presence of 0.5 ether solvent molecules per anion. Crystals suitable for X-ray diffraction were grown by vapor diffusion of pentane into a diethyl ether solution; in these crystals the potassium cation is solvated by three diethyl ether molecules. ^{1}H NMR (d_8-THF, 300 MHz, 298 K, δ): 7.04 (s, 3H), 6.67 (s, 3H), 6.47 (s, 6H), 3.38 (q, J = 7 Hz, 2H, diethyl ether (CH_3CH_2)$_2$O), 2.99 (br s, 3H), 2.14 (br s, 3H), 1.42 (d, J = 6 Hz, 9H), 1.36 (d, J = 5 Hz, 9H), 1.12 (t, J = 7 Hz, 3H, diethyl ether (CH_3CH_2)$_2$O), 1.01 (d, J = 5 Hz, 9H), 0.12 (d, 9H) ppm. ^{31}P NMR (5:1 C_6D_6/d_8-THF, 121.4 MHz, 298 K, δ): 68.1 ppm. IR (thin film deposited from Et_2O; cm^{-1}): 1870 (N-N).

[(CP$^{iPr}_3$)FeN$_2$][K(12-c-4)$_2$] (2.12[K(12-c-4)$_2$]). A sample of **2.12** (15 mg, 0.020 mmol) was dissolved in diethyl ether (1 mL) and 12-crown-4 (8.8 mg, 0.050 mmol) was added as a solution in diethyl ether (1 mL). The resulting solution was layered with pen-

tane and allowed to stand overnight, resulting in the crystallization of **12**[K(12-crown-4)$_2$] as a very dark blue solid. The crystals were washed with pentane and dried under vacuum, giving 10 mg of material (53% yield). ^{1}H NMR (d_8-THF, 300 MHz, 298 K, δ) 6.86 (br s, 6H), 6.47 (s, 6H), 3.62 (s, 36H, 12-crown-4), 1.43 (s, 9H), 1.30 (s, 9H), 0.91 (s, 9H), 0.16 (s, 9H) ppm. ^{31}P (C_6D_6, 121.4 MHz, 298 K, δ): 66 ppm. IR (thin film; cm^{-1}) 1905 (N-N).

[(CP$^{iPr}_3$)FeN$_2$][B(3,5-(CF$_3$)$_2$-C$_6$H$_3$)$_4$] (2.13): (C^{iPr}P$_3$)FeN$_2$ (7.3 mg) was dissolved in diethyl ether (1 mL) and a solution of [Fe(C$_5$Me$_5$)$_2$][B(3,5-(CF$_3$)$_2$-C$_6$H$_3$)$_4$] in diethyl ether (1 mL) was added dropwise while stirring at room temperature. The reaction mixture was then concentrated to give an orange solid which was washed with benzene and then dried *in vacuo*. Crystals suitable for X-ray diffraction were grown by slow evaporation of a diethyl ether solution into hexamethyldisiloxane. ^{1}H NMR (4:1 C_6D_6/THF-d_8 under N_2, 300 MHz, 298 K, δ): 16.65, 14.48, 8.15, 7.60, 2.71 ppm. (Note: the exact position of the paramagnetically shifted NMR peaks varies with the composition of the solvent due to the likely exchange of the N_2 ligand with THF). μ_{eff} (d_8-THF, Evans' method, 298 K): 4.3 μ_B. IR (thin film; cm^{-1}): 2128 (N-N). Satisfactory elemental analysis could not be obtained due to the lability of the coordinated N_2 ligand.

(CP$^{iPr}_3$)FeN$_2$SiMe$_3$ (2.14): [(CP$^{iPr}_3$)FeN$_2$][K(Et$_2$O)$_{0.5}$] (35 mg, 0.0465 mmol) was dissolved in diethyl ether (2 mL) and cooled to -78 ºC. Trimethylsilyl chloride (6 µL, 0.0473 mmol) was dissolved in diethyl ether (1 mL) and added dropwise to the stirring reaction mixture. The reaction was stirred at low temperature for one hour and then warmed to room temperature for one hour, concentrated to dryness, taken up in pentane, filtered through Celite, and concentrated. The red-orange residue was recrystallized by

slow evaporation of a pentane solution into hexamethyldisiloxane, and the resulting red solids were washed with cold hexamethyldisiloxane and dried *in vacuo* to give 21 mg (0.0280 mmol, 60%) of solid material, which was contaminated with a small amount of CP_3FeN_2 (**2.11**) which we were unable to remove by repeated recrystallization. **2.14** decomposes slowly to **2.11** over time. ^{1}H NMR (C_6D_6, 300 MHz, 298 K, δ) 7.33 (br m, 3H), 6.80 (t, J = 4 Hz, 6H), 6.63 (m, 3H), 2.67 (septet, J = 7 Hz, 3H), 1.97 (septet, J = 7 Hz, 3H), 1.45 (m, 18H), 0.96 (q, J = 7 Hz, 9H), 0.72 (q, J = 7 Hz, 9H), 0.12 (s, 3H) ppm. ^{31}P (C_6D_6, 121.4 MHz, 298 K, δ): 80.1 ppm. IR (thin film; cm^{-1}) 1736 (N-N).

2.4.6 Reactions

Ammonia Quantification. A Schlenk tube was charged with HCl (4 mL of a 1.0 M solution in Et_2O, 4 mmol). Reaction mixtures were vacuum transferred into this collection flask. Residual solid in the reaction vessel was treated with a solution of [Na][O-*t*-Bu] (40 mg, 0.4 mmol) in 1,2-dimethoxyethane (1 mL) and sealed. The resulting suspension was allowed to stir for 10 minutes before all volatiles were again vacuum transferred into the collection flask. After completion of the vacuum transfer, the flask was sealed and warmed to room temperature. Solvent was removed *in vacuo* and the remaining residue was dissolved in H_2O (1 mL). An aliquot of this solution (20 μL) was then analyzed for the presence of NH_3 (trapped as [NH_4][Cl]) *via* the indophenol method.[38] Quantification was performed with UV-Vis spectroscopy by analyzing absorbance at 635 nm.

Standard catalytic procedure with [(CP$^{iPr}_3$)FeN$_2$][K(Et$_2$O)$_{0.5}$] (2.12): [(CP$^{iPr}_3$)FeN$_2$][K(Et$_2$O)$_{0.5}$] (1.9 mg, 0.0025 mmol) was dissolved in Et_2O (0.5 mL) in a small Schlenk tube equipped with a stir bar. This solution was cooled to -78 °C in a cold well inside of the glove box. A suspension of KC_8 (14 mg, 0.100 mmol) in Et_2O (0.75

mL) was cooled to -78 ^{o}C and added to the reaction mixture with stirring. After five minutes, a similarly cooled solution of $HBAr^{F}_{4} \cdot 2\ Et_2O$ (93 mg, 0.092 mmol) in Et_2O (1.0 mL) was added to the suspension in one portion with rapid stirring. Any remaining acid was dissolved in cold Et_2O (0.25 mL) and added subsequently, and the Schlenk tube was sealed. The reaction was allowed to stir for 60 minutes at -78 °C before being warmed to room temperature and stirred for 15 minutes.

2.5 References

1. Smil, V. *Enriching the Earth* (MIT Press, Cambridge, 2001).

2. (a) Burgess, B. K.; Lowe, D. J. *Chem. Rev.* **1996**, **96**, 2983-3011. (b) Eady, R. R. *Chem. Rev.* **1996**, *96*, 3013-3030.

3. Peters, J.C.; Mehn, M.P. in *Activation of Small Molecules: Organometallic and Bio-inorganic Perspectives* ed. Tolman, W.B.) 81-119 (Wiley-VCH, 2006).

4. Hazari, N. *Chem. Soc. Rev.* **2010**, *39*, 4044.

5. MacLeod, K. C.; Holland, P.L. *Nature Chem.* **2013**, *5*, 559.

6. Crossland, J.L.; Tyler, D.R. *Coord. Chem. Rev.* **2010**, *254*, 1883.

7. Yandulov, D.V.; Schrock, R.R. *Science* **2003**, *301*, 76.

8. Arashiba, K.; Miyake, Y.; Nishibayashi, Y. *Nature Chem.* **2011**, *3*, 120.

9. Weare, W.W.; Dai, X.; Byrnes, M.; Chin, J.-M.; Schrock, R.R.; Muller, P. *Proc. Natl. Acad. Sci.* **2006**, *103*, 17099.

10. (a) Saouma, C.T.; Lu, C.C.; Peters, J.C. *Inorg. Chem.* **2012**, *51*, 10043. (b) Saouma, C.T.; Kinney, R. A.; Hoffman, B.M.; Peters, J.C. *Angew. Chem. Int. Ed.* **2011**, *50*, 1. (c) Saouma, C.T.; Muller, P.; Peters, J.C. *J. Am. Chem. Soc.* **2009**, *131*, 10358.

11. Smith, J.M. Lachiotte, R.J.; Pittard, K.A.; Cundari, T.R.; Lukat-Rodgers, G.; Holland, P.L. *J. Am. Chem. Soc.* **2001**, *123*, 9222.

12. Field, L.D.; Li, H.; Magill, A.M. *Inorg. Chem.* **2001**, *48*, 5.

13. Li, Y.; Li, Y.; Wang, B.; Luo, Y.; Yang, D.; Tong, P.; Zhao, J.; Luo, L.; Zhou, Y.; Chen, S.; Cheng, F.; Qu, J. *Nature Chem.* **2013**, *5*, 320.

14. Rodriguez, M. M.; Bill, E.; Brennessel, W.W.; Holland, P.L. *Science* **2011**, *334*, 780.

15. Moret, M.E.; Peters, J.C.; *J. Am. Chem. Soc*, **2011**, *133*, 18118.

16. Yuki, M.; Tanaka, H.; Sasaki, K.; Miyake, Y.; Yoshizawa, K.; Nishibayashi, Y. *Nature Comm.* **2012**, *3*, 1254.

17. Lee, Y.; Mankad, N.P., Peters, J.C. *Nature Chem.* **2012**, *2*, 558.

18. (a)Leigh, G.J.; Jimenez-Tenorio, M. *J. Am. Chem. Soc.* **1991**, *113*, 5862. (b) Hall, D.A.; Leigh, G.J. *J. Chem. Soc. Dalton Trans.* **1996**, 3539. (c) Gilbertson, J.D.; Szymczak, N.K.; Tyler, D.R. *J. Am. Chem. Soc.* **2005,** *127*, 10184. (d) Yamamoto, A.; Miura, Y.; Ito, T.; Chen, H. L.; Iri, K.; Ozawa, F.; Miki, K.; Sei, T.; Tanaka, N.; Kasai, N. *Organometallics* **1993,** *2*, 1429. (e) George, T.A.; Rose, D.J.; Chang, Y.; Chen, Q.; Zubieta, J. *Inorg. Chem.* **1995**, *34*, 1295. (f) Borodko, Y.G.; Broitman, M.O.; Kachapina, L.M.; Shilov, A.E.; Ukhin, L.Y. *J. Chem. Soc. D*, **1971**, 1185.

19. Einsle, O.; Tezcan, A.; Andrade, S.L.A.; Schmid, B.; Yoshida, M.; Howard, J.B.; Reese, D.C. *Science* **2002**, *297*, 1696.

20. (a) Spatzal, T.; Aksoyoglu, M.; Zhang, L.; Andrade, S.L.A.; Schleicher, E.; Weber, S.; Rees, D.C.; Einsle, O. *Science* **2011**, *334*, 940. (b) Lancaster, K.M.; Roemelt, M.; Ettenhuber, P.; Hu, Y.; Ribbe, M.W.; Neese, F.; Bergmann, U.; DeBeer, S. *Science* **2011**, *334*, 974-7. (c) Lancaster, K.M.; Hu, Y.; Bergmann, U.; Ribbe, M.W.; DeBeer,

S. *J. Am. Chem. Soc.* **2013**, *135*, 610-2. (d) Wiig, J.A.; Hu, Y.; Lee, C.C.; Ribbe, M.W. *Science* **2012**, *337*, 1672-1675.

21. Anderson, J.S.; Rittle, J.; Peters, J.C. *Nature* **2013**, *501*, 84.

22. Rittle, J.; Peters, J.C. *Proc. Natl. Acad. Sci. U.S.A.* [Online early access]**.** DOI: 10.1073/pnas.1310153110. Published Online: Sept 16, 2013.

23. Macbeth, C.E.; Harkins, S.B.; Peters, J.C. *Can. J. Chem.* **2005**, *83*, 332.

24. Mankad, N.P.; Whited, M.T.; Peters, J.C. *Angew. Chem. Int. Ed.* **2007**, *46*, 5768.

25. Moret, M.-E.; Peters, J.C. *Angew. Chem. Int. Ed.* **2011**, *50*, 2063.

26. Bontemps, S.; Bouhadir, G.; Dyer, P.W.; Miqueu, K.; Bourissou, D. *Inorg. Chem.* **2007**, *46*, 5149.

27. Lesueur, W.; Solari, E.; Floriani, C.; Chiesi-Villa, A.; Rizzoli, C. *Inorg. Chem.* **1997**, *36*, 3354.

28. Bickelhaupt, F.; Jongsma, C.; de Koe, P.; Lourens, R.; Mast, N.R.; van Mourik, G.L.; Vermeer, H.; Weustink, R.J.M. *Tetrahedron* **1976,** *32*, 1921.

29. Bielawski, M.; Olofsson, B. *Chem. Commun.* **2007,** 2521.

30. Ciclosi, M.; Lloret, J.; Estevan, F.; Lahuerta, P.; Sanau, M.; Perez-Prieto, J. *Angew. Chem. Int. Ed.* **2006**, *45*, 6741.

31. Schlosser, M. *Pure Appl. Chem.* **1988**, *60*, 1627.

32. Hoffmann, R.; Bissel, R.; Farnum, D. G. *J. Phys. Chem.* **1969**, *73*, 1789.

33. Lee, Y.; Kinney, R. A.; Hoffman, B.M.; Peters, J.C. *J. Am. Chem. Soc.* **2011**, *133*, 16366.

34. Field, L.D.; Guest, R.W.; Vuong, K.Q.; Dalgarno, S.J. Jensen, P. *Inorg. Chem.* **2009**, *48*, 2246.

35. Del Castillo, T. J.; Thompson, N. B.; Suess, D. L.; Ung, G.; Peters, J. C. *Inorg. Chem.* **2015**, *54*, 9256.

36. Anderson, J.S.; Moret, M.-E.; Peters, J.C. *J. Am. Chem. Soc.* **2013**, *135*, 534.

37. Weinhold, F.; Landis, C. (2005) *Valency and Bonding: A Natural Bond Orbital Donor-Acceptor Perspective* (Cambridge, Univ. Press, Cambridge).

38. Hills, A.; Hughes, D. L.; Jimenez-Tenorio, M.; Leigh, G. F.; Rowley, A. T. *J. Chem. Soc. Dalton Trans*. **1993**, *25*, 3041.

39. Weatherburn, M.W. *Anal. Chem.* **1967**, *39*, 971.

40. (a) Yang, Z.-Y.; Khadka, N.; Lukoyanov, D.; Hoffman, B.M.; Dean, D. R.; Seefeldt, L.C. *Proc. Natl. Acad. Sci. U.S.A.* **2013**, *110*, 16327. (b) Simpson, F.B.; Burris, R.H. *Science* **1984**, *224*, 1095.

41. (a) Tard, C.; Liu, X.; Ibrahim, S.K.; Maurizio, B.; DeGioia, L.; Davis, S.C.; Yang, X.; Wang, L.-S.; Sawers, G.; Pickett, C.J. *Nature* **2005**, *433*, 610. (b) Gloaguen, F.; Rauchfuss, T.B. *Chem. Soc. Rev.* **2009**, *38*, 100. (c) Darensbourg, M.Y.; Lyon, E.J.; Smee, J.J. *Coord. Chem. Rev.* **2000**, *206-207*, 533. (d) Peters, J.W.; Lanzilotta, W.N.; Lemon, B.J.; Seefeldt, L.C. *Science* **1998**, *282*, 1853. (e) Volbeda, A.; Charon, M.-H.; Piras, C.; Hatchikian, E.C.; Frey, M.; Fontecilla-Camps, J.C. *Nature* **1995,** *373*, 580. (f) Vincent, K.A.; Parkin, A.; Armonstrong, F.A. *Chem. Rev.* **2007**, *107*, 4366.

42. (a) Chatt, J.; Dilworth, J.R.; Richards, R. L. *Chem. Rev.* **1978**, *78*, 589. (b) Seefeldt, L.; Hoffman, B.M.; Dean, D.R. *Annu. Rev. Biochem.* **2009**, *78*, 701. (c) Lukoyanov, D.; Dikanov, S.A.; Yang, Z.-Y.; Barney, B.M.; Samoilova, R.I.; Narasimhulu, K.V.; Dean, D.R.; Seefeldt, L.C.; Hoffman, B.M. *J. Am. Chem. Soc.* **2011**, *133*, 11655.

43. Brookhart, M.; Grant, B.; Volpe, A.F. Jr. *Organometallics*, **1992**, *11*, 3920.

44. Wietz, I.S.; Rabinovitz, M.J. *J. Chem. Soc. Perkin Trans.*, **1993**, *1*, 117.

45. Chavez, I.; Alvarez-Carena, A.; Molins, E.; Roig, A.; Maniukiewicz, W.; Arancibia, A.; Arancibia, V.; Brand, H.; Manriquez, J.M. *J. Organomet. Chem.* **2000**, *601*, 126.

46. Job, R.; Earl, R. *Inorg. Nuc. Chem. Lett.* **1979**, *15*, 21.

47. Evans, D.F. *J. Chem. Soc.* **1959**, 2003.

48. Sheldrick, G.M. *Acta Cryst. A.* **2008**, *82*, 169.

49. Gaussian 03, Revision C.02, Frisch, M. J.; Trucks, G. W.; Schlegel, H. B.; Scuseria, G. E.; Robb, M. A.; Cheeseman, J. R.; Montgomery, Jr., J. A.; Vreven, T.; Kudin, K. N.; Burant, J. C.; Millam, J. M.; Iyengar, S. S.; Tomasi, J.; Barone, V.; Mennucci, B.; Cossi, M.; Scalmani, G.; Rega, N.; Petersson, G. A.; Nakatsuji, H.; Hada, M.; Ehara, M.; Toyota, K.; Fukuda, R.; Hasegawa, J.; Ishida, M.; Nakajima, T.; Honda, Y.; Kitao, O.; Nakai, H.; Klene, M.; Li, X.; Knox, J. E.; Hratchian, H. P.; Cross, J. B.; Bakken, V.; Adamo, C.; Jaramillo, J.; Gomperts, R.; Stratmann, R. E.; Yazyev, O.; Austin, A. J.; Cammi, R.; Pomelli, C.; Ochterski, J. W.; Ayala, P. Y.; Morokuma, K.; Voth, G. A.; Salvador, P.; Dannenberg, J. J.; Zakrzewski, V. G.; Dapprich, S.; Daniels, A. D.; Strain, M. C.; Farkas, O.; Malick, D. K.; Rabuck, A. D.; Raghavachari, K.; Foresman, J. B.; Ortiz, J. V.; Cui, Q.; Baboul, A. G.; Clifford, S.; Cioslowski, J.; Stefanov, B. B.; Liu, G.; Liashenko, A.; Piskorz, P.; Komaromi, I.; Martin, R. L.; Fox, D. J.; Keith, T.; Al-Laham, M. A.; Peng, C. Y.; Nanayakkara, A.; Challacombe, M.; Gill, P. M. W.; Johnson, B.; Chen, W.; Wong, M. W.; Gonzalez, C.; and Pople, J. A.; Gaussian, Inc., Wallingford CT, 2004.

Chapter 3. Diiron bridged-thiolate complexes that bind N_2 at the $Fe^{II}Fe^{II}$, $Fe^{II}Fe^{I}$, and $Fe^{I}Fe^{I}$ redox states

Reproduced in part with permission from:

Creutz, S. E.; Peters, J. C. *J. Am. Chem. Soc.* **2015**, *137*, 7310.

3.1 Introduction

Although biological nitrogen fixation mediated by the iron-molybdenum cofactor (FeMoco) of MoFe-nitrogenase enzymes has inspired a wealth of synthetic model studies,[1-4] the modeling field is marked by a sharp dichotomy between functional and structural models of the FeMoco cluster. In the crystallographically characterized state of the biological Fe_7MoS_9 cluster, the "belt" irons that are hypothesized to be likely initial binding site(s) for N_2[5] are in an FeS_3C coordination environment consisting of three sulfides bridged to either one or two additional metal centers (Fe or Mo) and the interstitial carbide (C^{4-}) ligand (Figure 3.1).[6] In contrast, synthetic iron complexes for which spectroscopically and/or structurally characterized N_2 complexes are known are dominated by ligands composed primarily of phosphorus and nitrogen donors.

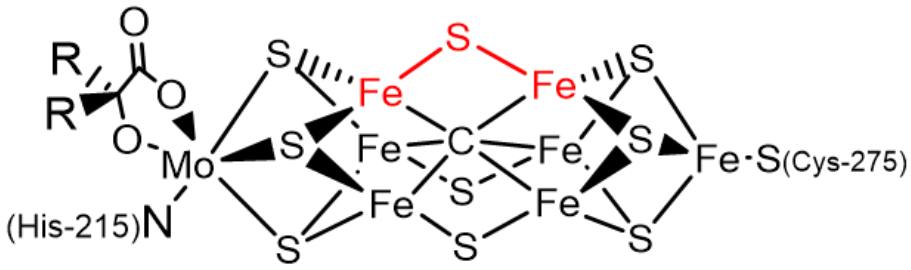

Figure 3.1. Representation of the nitrogenase iron-molybdenum cofactor, highlighting one candidate Fe-S-Fe substrate binding site.[7]

Sulfur-supported transition metal complexes that bind N_2 remain very uncommon.[8] This state of affairs is particularly noteworthy for iron, especially in the context of nitrogenase model chemistry: reported examples of iron centers ligated to a sulfur donor ligand of any kind (e.g., S^{2-}, SR^-, SR_2) and at the same time an N_2 ligand are few in number,

limited to several $Fe(N_2)$(thioether) derivatives.[9] No examples of $Fe(N_2)$ complexes involving anionic sulfur donors (sulfides or thiolates) have ever been reported,[10] despite numerous examples of synthetic iron-sulfide and iron-thiolate complexes and clusters.[11] This is perhaps not surprising: sulfides and thiolates/thioethers typically act as weak-field ligands that do not give rise to the types of low-spin and low-valent iron centers that are well-suited to bind N_2.[8b,12] The few examples of low-valent, low-coordinate diiron bridged-sulfide complexes (Fe(μ-S)Fe) that are known have not yet been observed to bind N_2.[12]

Herein we pursue a strategy to overcome these challenges via a binucleating ligand scaffold designed with a mixed phosphine-thiolate coordination environment that places iron in a trigonal geometry. This strategy affords a bridging Fe(μ-SAr)Fe moiety with high affinity Fe-N_2 binding sites across three redox states.

3.2 Results and Discussion

Scheme 3.1. Synthesis of protected ligand 3.4

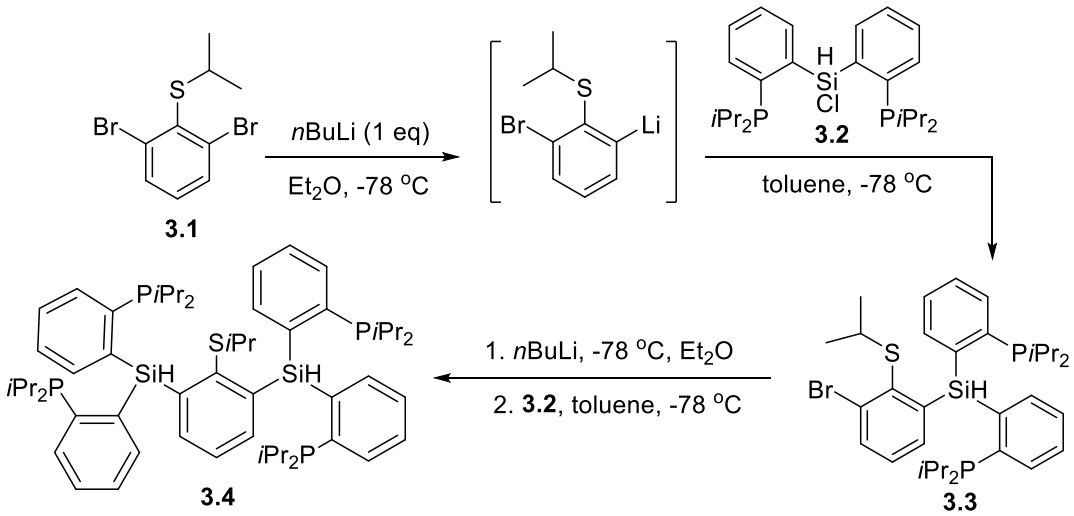

The binucleating ligand of choice and its synthesis are shown in Schemes 3.1 and 3.2. Monolithiation of thioether **3.1** followed by reaction with chlorosilane electrophile **3.2** gives the diphosphine-thioether product **3.3**; a second lithiation and electrophile addition affords the protected ligand **3.4** in good yield. Deprotection of the isopropyl thioether with sodium naphthalenide provides the thiolate ligand **3.5** which, when stirred with two equivalents of $FeCl_2$, generates a metalated brown paramagnetic solid product formulated as **3.6** (Scheme 3.2).

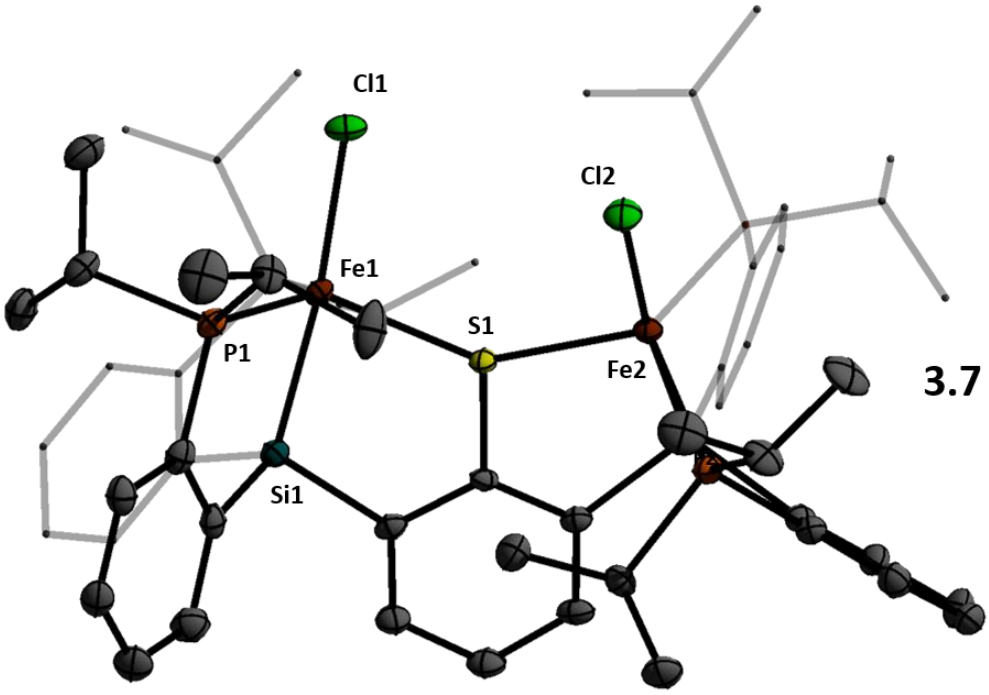

Figure 3.2. Structure of **3.7** with countercation and solvent molecules omitted. One of two equivalent anions in the asymmetric unit shown. Ellipsoids at 50% and hydrogen atoms omitted.

Treating **3.6** with two equivalents of methyl Grignard followed by [PPN]Cl (PPN = bis(triphenylphosphine)iminium) results in formal loss of two equivalents of methane and concomitant installation of the Fe-Si bonds to provide an anionic diiron(II) dichloride complex, **3.7**, as its PPN salt (Scheme 3.2). Complex **3.7** is a paramagnetic, bright red solid and has been crystallographically characterized; its structure shows two trigonal bi-pyramidal Fe-Cl sites within a bis(phosphine)silyl binding pocket (axial chloride *trans* to axial silyl) that are symmetrically bridged by the arylthiolate. The two SiP_2FeCl subunits are canted with respect to the central arene ring; the Cl-Fe-Fe-Cl dihedral angle is 36°.

Scheme 3.2. Synthesis of 3.6 and 3.7

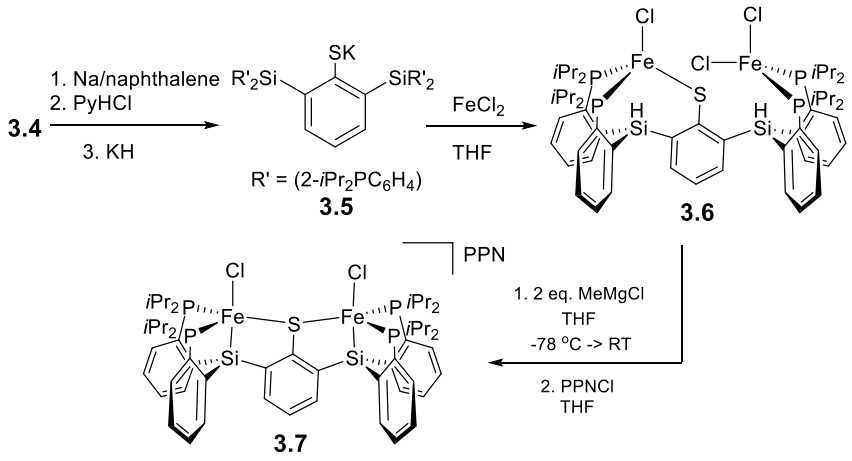

Entry to the desired series of diiron N_2 adduct complexes was next pursued. Treatment of **3.7** with $NaBPh_4$ gives a putative intermediate monochloride complex (with loss of NaCl and $[PPN][BPh_4]$) which, when followed by reduction with excess sodium amalgam in THF, affords the anion $\{N_2\text{-}Fe^{I}(\mu\text{-}SAr)Fe^{I}\text{-}N_2\}^-$ **3.8** as a $\{Na(THF)_x\}^+$ salt (Scheme 3.3). Treatment of this salt with 12-crown-4 sequesters the sodium countercation to give $\{N_2\text{-}Fe^{I}(\mu\text{-}SAr)Fe^{I}\text{-}N_2\}\{Na(12\text{-crown-}4)_2\}$, ($\{$**3.8**$\}\{Na(12\text{-crown-}4)_2\}$). The solid-state structure of $\{$**3.8**$\}\{Na(12\text{-crown-}4)_2\}$ shows coordination of a terminally bound N_2

ligand at each of the two iron centers at the axial position *trans* to the silyl donor and *cis* to the bridging arylthiolate linker (Figure 3.3). Anion **3.8** displays two infrared absorption features corresponding to the symmetric and asymmetric stretches arising from the two chemically equivalent N_2 ligands.[14] These shift from 1978 and 1928 cm^{-1} in the ion-paired $\{Na(THF)_x\}^+$ salt $\{\mathbf{3.8}\}\{Na(THF)_x\}$ (thin film deposited from THF) to 2017 and 1979 cm^{-1} in $\{\mathbf{3.8}\}\{Na(12\text{-crown-4})_2\}$. Both salts of the formally diiron(I) anion **3.8** are deep green in color and diamagnetic due to strong coupling.

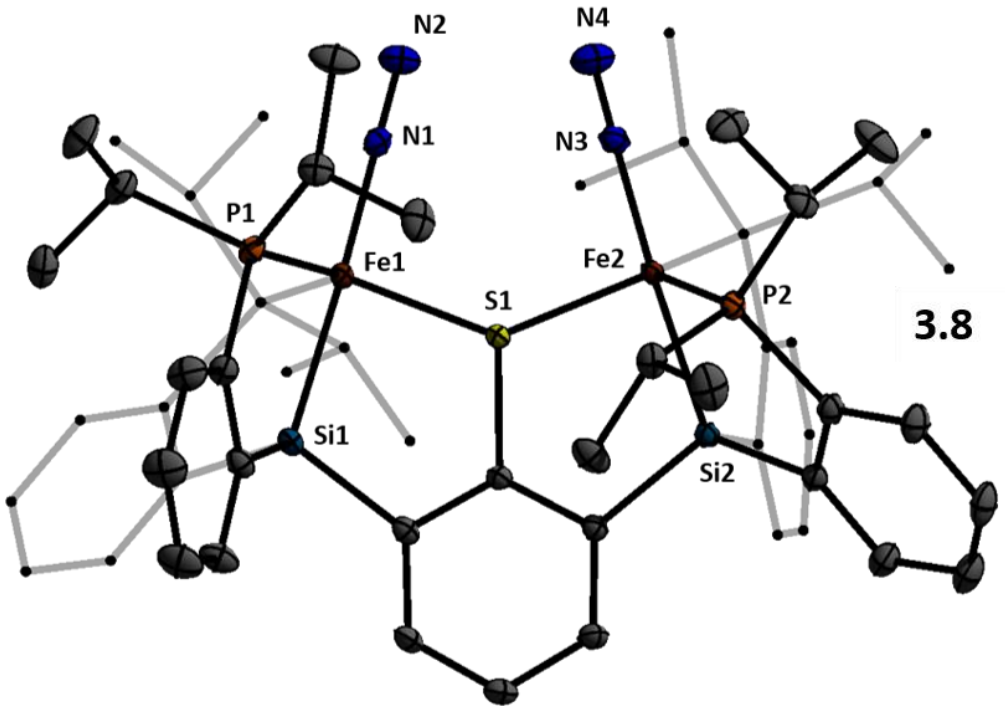

Figure 3.3. Crystal structure of $\{\mathbf{3.8}\}\{Na(12\text{-crown-4})_2\}$. The countercation ($Na(12\text{-crown-4})_2$), solvent molecules, and hydrogen atoms are omitted for clarity. Thermal ellipsoids shown at 50% probability.

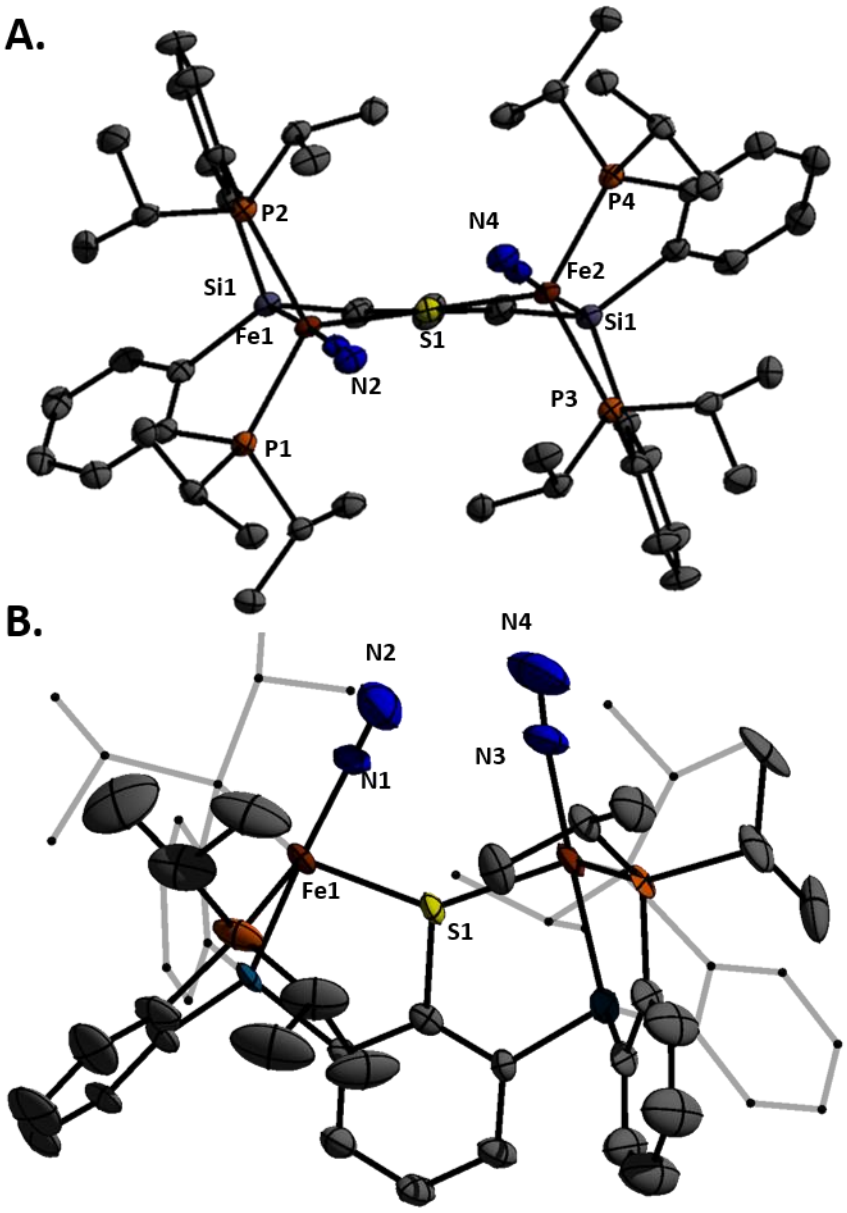

Figure 3.4. Crystal structure of **3.9** (A) and **3.10** (B). Thermal ellipsoids shown at 50% probability; hydrogen atoms and BAr^F_4 counteranion of **10** omitted for clarity.

Stepwise oxidation of **3.8** with $FcPF_6$ followed by $FcBAr^F_4$ gives the mixed-valent N_2-$Fe^{II}(\mu\text{-SAr})Fe^{I}$-$N_2$ complex **3.9** and then the cationic $\{N_2\text{-}Fe^{II}(\mu\text{-SAr})Fe^{II}\text{-}N_2\}^+$ complex **3.10**, respectively; both complexes have also been crystallographically characterized

(Scheme 3.3, Figure 3.4). Electrochemical characterization of mixed-valent **3.9** by cyclic voltammetry (Figure 3.5) shows a reversible oxidation (generating **3.10**) at -1.3 V (vs Fc/Fc^{+}) and reversible reductions at -1.9 V and -3.3 V. The first reduction (-1.9 V) gives the anion **3.8**, while the second reduction apparently generates a more highly reduced, dianionic $\{N_2\text{-}Fe^{I}(\mu\text{-}SAr)Fe^{0}\text{-}N_2\}^{2-}$ species that has not been isolated.

Scheme 3.3. Synthesis of Fe-N_2 adducts $\{3.8\}^{-}$, 3.9, and 3.10

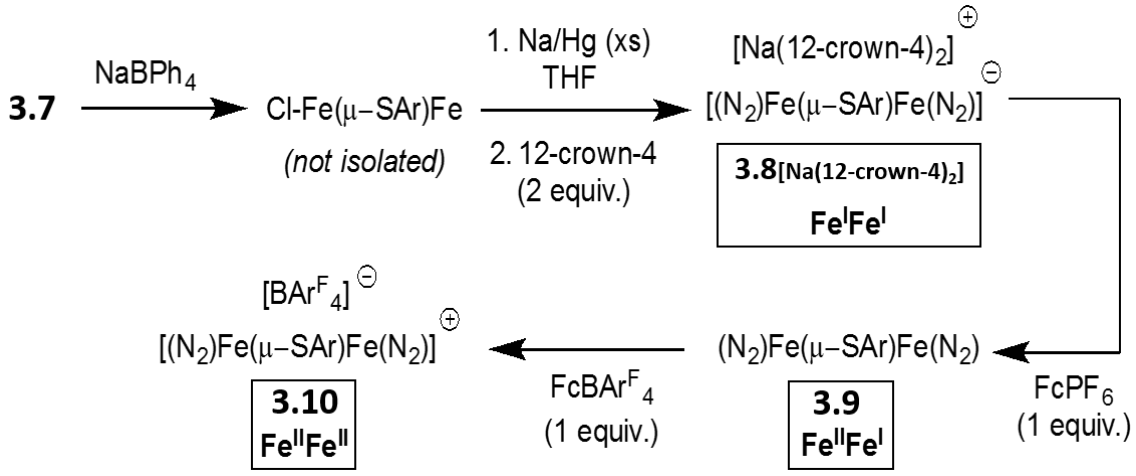

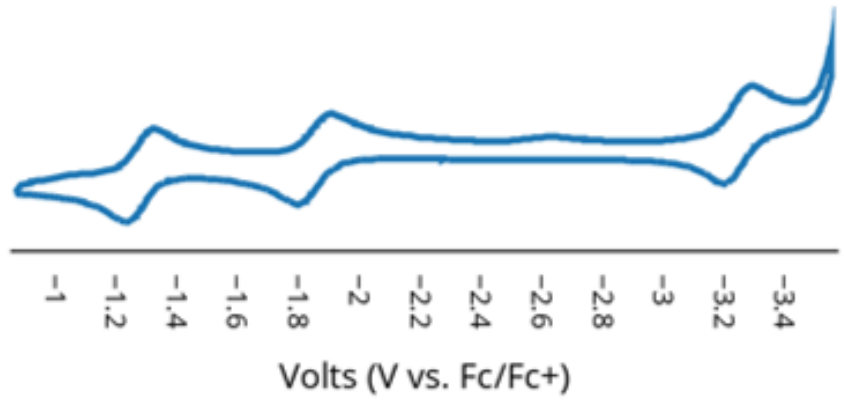

Figure 3.5. Cyclic voltammogram of **3.9**. Cyclic voltammogram was measured in 0.4 M [TBA][PF_6] in THF at 100 mV/s and internally referenced to Fc/Fc^{+}.

Compounds **3.8**, **3.9**, and **3.10** have very similar overall solid-state structures despite minor changes in the bond lengths of the immediate iron coordination environment (Table 3.1), consistent with the reversible CV data described above. The Fe-P bond lengths within **3.8** - **3.10** show little variation and the Fe-S bonds are nearly symmetrical; only average bond lengths are therefore shown in Table 3.1.

Table 3.1. Comparison of selected bond lengths and spectroscopic parameters for complexes **3.8** -**3.12**.

	Fe-P (Å, avg)	Fe-S (Å, avg)	Fe-S-Fe (°)	ν(NN) (cm^{-1})
8	2.226	2.184	137.098(15)	2017, 1979
9	2.291	2.208	135.52(5)	2070, 1983
10	2.341	2.244	138.02(4)	2129
11	2.264	2.189	136.562(15)	2036, 2093
12	2.219	2.332	140.42(3)	2044, 1981

Studies on nitrogen reduction by FeMoco suggest that iron hydride species may play an important mechanistic role and access to EPR active models of such species can help to constrain spectroscopic parameters (e.g., EPR/ENDOR) for potential hydride intermediate assignments.[15,16] Synthetic access to N_2/hydride species within the present iron thiolate-N_2 model system proved viable. When complex **3.6** is reduced with excess sodium amalgam in benzene, a new hydride product, {$(N_2)Fe^{II}(\mu\text{-}SAr)Fe^{II}N_2(H)$} (**3.11**), is produced cleanly (Scheme 3.4).

Scheme 3.4. Synthetic access to hydrides 3.11 and 3.12

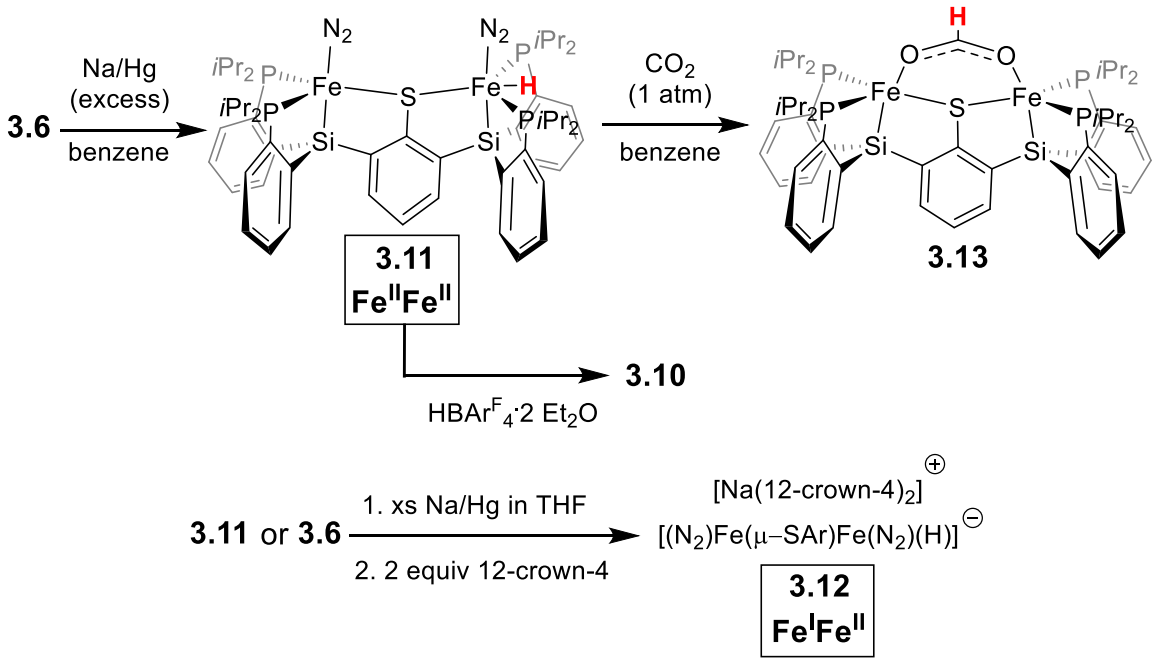

Complex **3.11** is an orange-brown, diamagnetic solid featuring two uncoupled ^{31}P NMR resonances in a 1:1 ratio at 84 and 94 ppm. The ^{1}H NMR spectrum of **3.11** shows a triplet at -13 ppm that integrates to a single hydride and is coupled only to the more downfield phosphorus resonance. These data allow the position of the hydride to be assigned as *trans* to the thiolate ligand between two phosphine ligands at one of the two iron centers. Additionally, the infrared spectrum of **3.11** shows two sharp and strong peaks at 2036 and 2096 cm^{-1}, corresponding to two inequivalent N≡N stretches (Figure 3.6). The Mossbauer spectrum of **3.11** also indicates inequivalent iron centers with two quadrupole doublets in a 1:1 ratio. Complex **3.11** has been crystallographically characterized, but the hydride position could not be located from the data and, as the molecule sits on a crystallographically imposed 2-fold rotation axis, its position could not be indirectly inferred. Curiously, **3.11** is in fact isostructural to **3.9**, but IR, NMR, Mossbauer, and

UV-Vis data unambiguously confirm the differing identities of crystals of the two species; nor are **3.11** and **3.9** readily interconverted by any known reaction or decomposition.

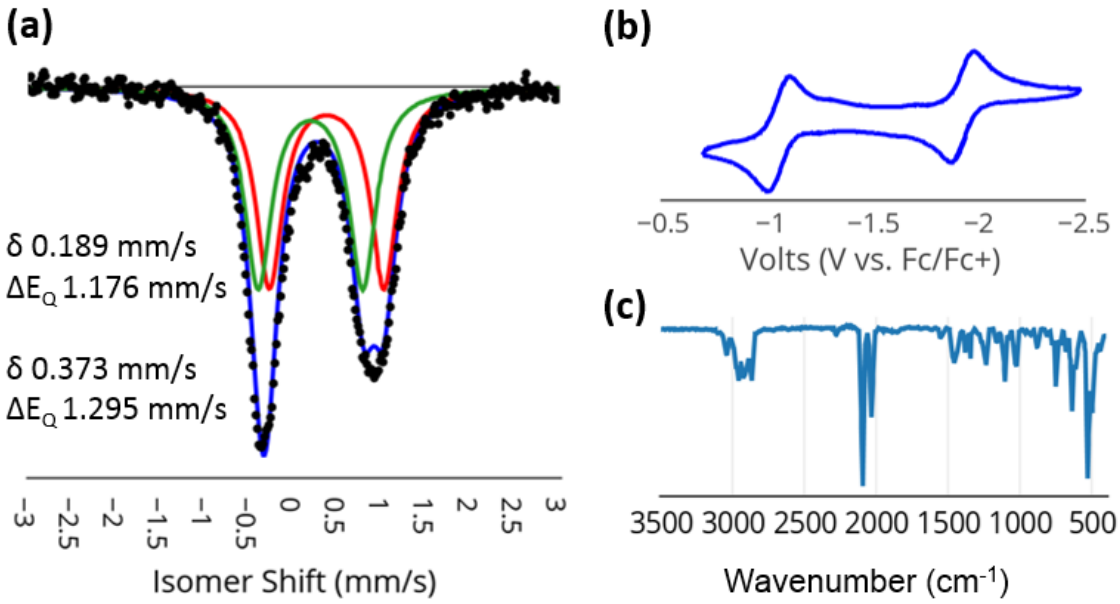

Figure 3.6. Spectroscopic characterization of **3.11**. (a) Mossbauer spectrum of microcrystalline **3.11** (80 K, suspended in boron nitride matrix). Parameters for the displayed fit are shown. (b) Cyclic voltammogram measured in 0.4 M [TBA][PF_6] in THF at 100 mV/s and internally referenced to Fc/Fc^+. (c) IR spectrum of **3.11** as a thin film deposited from benzene solution.

To chemically confirm the presence of the hydride ligand, **3.11** was exposed to an atmosphere of CO_2 in benzene. This reaction quantitatively affords the product of CO_2 insertion into the Fe-H bond (**3.13**, Scheme 3.4). Bright red, paramagnetic diiron(II) **3.13** has been crystallographically characterized, showing a bridged formate that is κ^1 with respect to each Fe center. The structure of **3.13** suggests that this diiron platform may be

interesting to pursue in the context of bimetallic CO_2 reduction catalysis. Treatment of **3.11** with one equivalent of $HBAr^F_4{\cdot}2Et_2O$ cleanly generates **3.10** via loss of H_2.

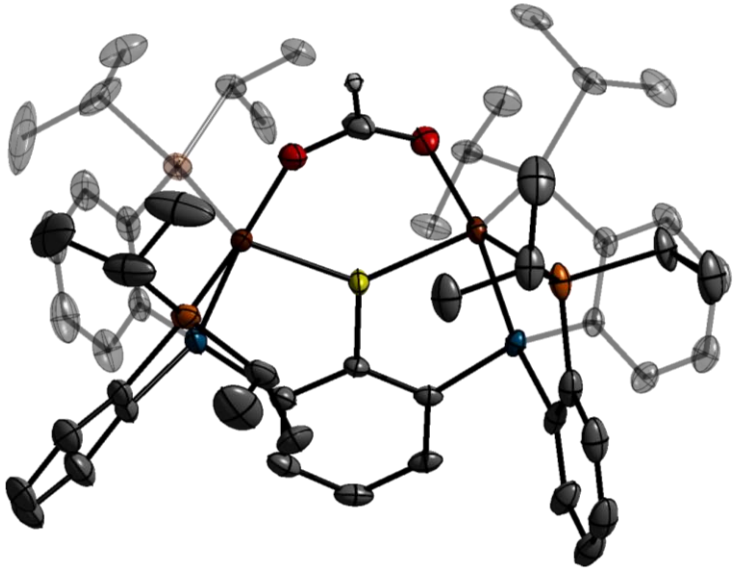

Figure 3.7. Crystal structure of **3.13**; hydrogen atoms except for the formate hydrogen are omitted for clarity, and thermal ellipsoids shown at 50% probability.

The cyclic voltammogram of hydride **3.11** shows reversible oxidation (-1.1 V) and reduction (-2.0 V) events (Figure 3.6b). The anionic $\{(N_2)Fe^{II}(\mu\text{-}SAr)Fe^{I}N_2(H)\}^-$ reduction product, **3.12**, can be isolated and crystallographically characterized. This is achieved by stirring **3.11** (or **3.6**) over sodium amalgam in THF followed by treatment with 12-crown-4 (Scheme 3.4). Complex **3.12** is a paramagnetic brown solid with sharp, strong IR absorbance features at 2044 and 1981 cm^{-1} (shifted from 1999 and 1928 cm^{-1} prior to treatment with 12-crown-4). Its crystal structure (Figure 3.8) shows a wide P-Fe-P angle at Fe1 (147.72(4)^o) compared to that at Fe2 (113.06(3)^o). This variation reflects the presence of a hydride ligand at Fe1, apparently in a position *trans* to the bridged thiolate donor as assigned to the solution structure of diamagnetic **3.11**. By contrast to the solid-state struc-

tures of **3.8** - **3.10** that show symmetric or near-symmetric coordination of the bridged-thiolate ligand (Table 3.1), the two iron sites of **3.12** have distinct Fe-S bond lengths: an elongated Fe-S bond of 2.3744(7) Å to the hydride-bound Fe1 site compared with a shorter Fe-S bond of 2.2893(7) Å at the Fe2 site. The difference presumably reflects a *trans* influence from the hydride ligand at Fe1.

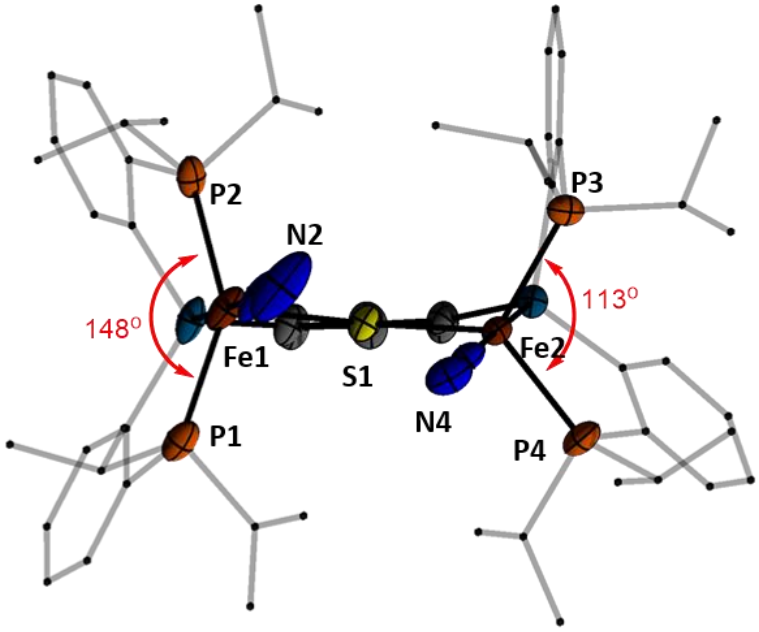

Figure 3.8. Crystal structure of **3.12** highlighting differing P-Fe-P angles due to the presence of a hydride ligand on Fe1 between P1 and P2. Countercation ($Na(12\text{-crown-}4)_2$), solvent molecules, and hydrogen atoms (including hydride, which was not crystallographically located) omitted for clarity; thermal ellipsoids shown at 50% probability.

Biomimetic reactivity of the Fe-(μ-SAr)-Fe subunit in the present scaffold has been explored *via* the reduction or decomposition of the nitrogenase substrates N_2 and N_2H_4; in both these cases cleavage of the N-N bond has been demonstrated. For instance, treatment of **3.8**$\{Na(12\text{-crown-}4)_2\}$ with an excess (100 equivalents) of KC_8 and $HBAr^F{}_4{\cdot}2$

Et_2O in the presence of an N_2 atmosphere (Et_2O, -78 °C, 2 h) produces 1.8 ± 0.3 equivalents of NH_3; this yield is comparable to that achieved by the related monometallic silyl-anchored iron complex, $\{[SiP^{iPr}_3]FeN_2\}\{Na(12\text{-crown-}4)_2\}$ (Scheme 3.5).[17] The comparatively low yield of NH_3 production from **3.8**$\{Na(12\text{-crown-}4)_2\}$ may reflect rapid generation of H_2 instead. No ammonia is produced when **3.8**$\{Na(12\text{-crown-}4)_2\}$ is treated with acid in the absence of added reductant.

Scheme 3.5. NH_3 generation from N_2 or N_2H_4

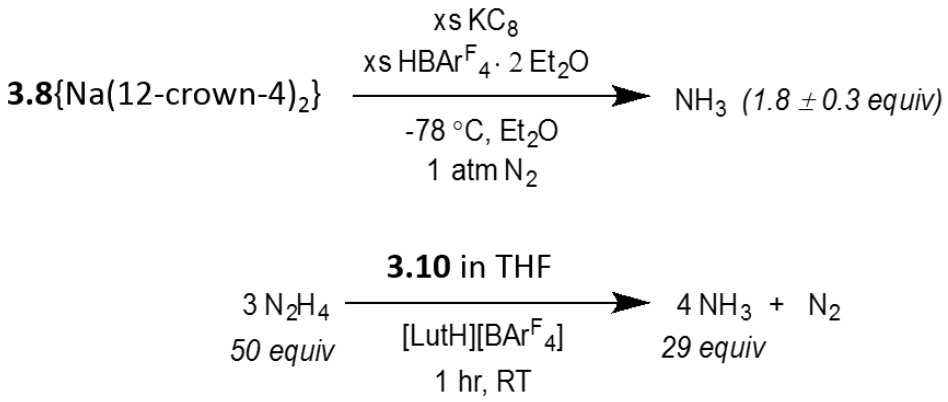

By contrast to its modest N_2-reducing capacity, the cationic complex **3.10** serves as an effective precatalyst for hydrazine disproportionation to NH_3 and N_2 with a turnover number that is significantly higher than previously reported for any iron complex.[18] Reproducible yields of ammonia were only achieved in the presence of an acid co-catalyst (Scheme 3.5). Thus, treatment of **3.10** in THF with one equivalent of $[LutH][BAr^F_4]$ and 50 equivalents of N_2H_4 produced 29 equivalents of NH_3 during the course of one hour at room temperature (LutH = lutidinium). The turnover number appears to be limited by catalyst decomposition; neither longer reaction times nor higher concentrations of N_2H_4 resulted in higher yields of ammonia. For comparison, a related monometallic iron complex of a silyl-anchored bisphosphine thioether ligand, $\{[SiP^{iPr}_2S^{Ad}]FeN_2\}\{BAr^F_4\}$,[9b] pro-

duced less than two equivalents of ammonia under the same reaction conditions, even with longer reaction times (8 hours); this comparison suggests the possibility that some degree of bimetallic cooperativity and/or the presence of the bridging thiolate as a proton shuttle may be important in facilitating the N-N bond cleavage of hydrazines catalyzed by **3.10**. Mechanistic studies will be interesting in this context since hydrazine has been suggested as a possible intermediate in dinitrogen reduction where the N-N bond is cleaved at a late stage; it can be converted to ammonia either by further reduction or by a disproportionation pathway that also produces N_2.[19]

3.3 Concluding Remarks

To conclude, a paradox in inorganic synthesis is the dichotomy between the sulfur-rich coordination environment of the iron and molybdenum centers of the FeMoco, and the dearth of well-defined N_2 adducts for these metals (and all transition metals) featuring sulfur donor ligands.[20] The synthetic work described here has provided the first examples[10] of thiolate-ligated Fe-N_2 species via a bimetallic Fe-(μ-SAr)-Fe subunit benefiting from a combination of phosphine and silyl donors. This subunit moreover shows that the N_2 ligands are retained across at least three redox states ($Fe^{II}Fe^{II}$, $Fe^{II}Fe^{I}$, $Fe^{I}Fe^{I}$) in the presence of the thiolate donor. This is significant because formally low-valent iron sites in the presence of S^{2-} or SH^- are plausible intermediates of biological nitrogen fixation but are not well represented in the synthetic literature. Synthetic access to terminally bonded iron hydrides in the presence of the bridging thiolate and N_2 ligands has also been established.[21] Finally, the ability of the present scaffold to mediate the stoichiometric and catalytic cleavage of N-N bonds has been briefly explored. Ongoing work will further

examine the reactivity patterns of these $(N_2)Fe$-(μ-SAr)-$Fe(N_2)$ subunits in the context of nitrogen fixation and reduction catalysis (e.g., H^+, CO_2) more generally.

3.4 Experimental Procedures

3.4.1 General considerations.

All syntheses and measurements, unless otherwise stated, were carried out under an inert atmosphere (N_2) in a glovebox or using standard Schlenk techniques, and solvents were dried and degassed by thoroughly sparging with N_2 and then passing through an activated alumina column in a solvent purification system supplied by SG Water, LLC. Combustion analyses were carried out by Midwest Microlabs (Indianapolis). Non-halogenated solvents were tested with a standard purple solution of sodium benzophenone ketyl in tetrahydrofuran in order to confirm effective moisture removal. **3.2**,[9b] $Fc[BAr^F_4]$,[22] $HBAr^F_4{\cdot}2Et_2O$ (Ar^F = 3,5-bistrifluoromethylphenyl),[23] and $\{[SiP^{iPr}_2S^{Ad}]FeN_2\}Bar^F_4$[9b] were prepared according to literature procedures. All other reagents were purchased from commercial vendors and used without further purification unless otherwise stated.

3.4.2 Physical methods.

Optical spectroscopy measurements were taken on a Cary 50 UV-vis spectrophotometer using a 1-cm two-window quartz cell. Electrochemical measurements were carried out in a glovebox under a dinitrogen atmosphere in a one compartment cell using a CH Instruments 600B electrochemical analyzer. A glassy carbon electrode was used as the working electrode and a graphite rod was used as the auxiliary electrode. A silver pseudoreference electrode was used. The ferrocene couple Fc+/Fc was used as an internal reference. Solutions (THF) of electrolyte (0.4 M tetra-n-butylammonium hexafluorophos-

phate) and analyte were also prepared under an inert atmosphere. Fourier transform infrared ATR spectra were collected on a Thermo Scientific Nicolet iS5 Spectrometer with diamond ATR crystal (utilized iD5 ATR insert). Solution phase magnetic measurements were performed by the method of Evans.[24] Mossbauer spectra were recorded on a spectrometer from SEE Co. (Edina, MN) operating in the constant acceleration mode in a transmission geometry. The sample was kept in an SVT-400 cryostat from Janis (Wilmington, MA). The quoted isomer shifts are relative to the centroid of the spectrum of a metallic foil of α-Fe at room temperature. Solid samples were prepared by grinding polycrystalline material into a fine powder and then mounted in a Delrin cup fitted with a screw-cap as a boron nitride pellet. Data analysis was performed using the program WMOSS (www.wmoss.org) and quadrupole doublets were fit to Lorentzian lineshapes.

3.4.3 Syntheses and characterization data

Scheme 3.6. Synthesis of 3.1 from 2,6-dibromoaniline

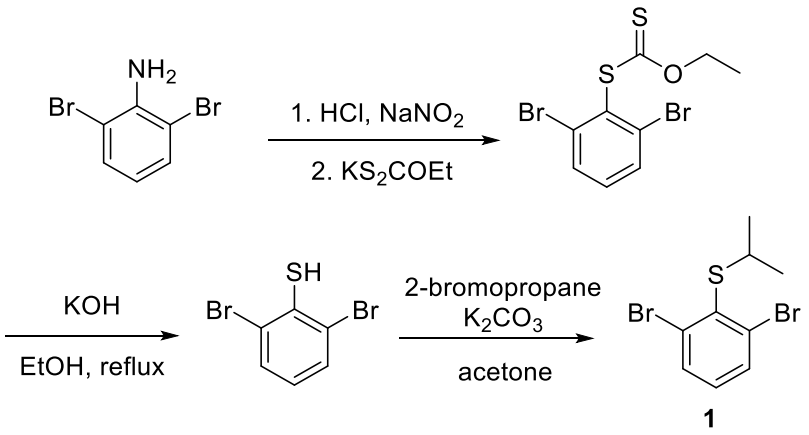

(2,6-dibromophenyl)ethyl xanthate. 2,6-dibromoaniline (24.5 g, 0.0976 mol) was slurried in 15 mL of H_2O and 16.3 mL of concentrated (35%) aqueous HCl and ~15 g of ice were added, and the resulting mixture was cooled to 0 ^oC in an ice-water bath. A solution

of $NaNO_2$ (6.71 g, 0.0973 mol in 30 mL H_2O) was added slowly over 40 minutes. After the addition was complete the mixture was stirred for an additional 30 minutes at 0 °C, and was then added slowly over 20 minutes to a solution of potassium ethyl xanthate (18.77 g, 0.117 mol) in H_2O (100 mL) at 60 °C. After the addition was complete the reaction was stirred for an additional 30 minutes at 60 °C, then cooled to room temperature, extracted with dichloromethane (2 x 200 mL), dried over magnesium sulfate, filtered, and concentrated to a yellowish solid. This solid residue was recrystallized from methanol to give the desired product as a crystalline white solid (23.1 g, 0.0649 mol, 67%). ^{1}H NMR ($CDCl_3$, 300 MHz, 298 K): δ 7.67 (d, *J* = 8 Hz, 2H, 3,5-C*H*$_{Ar}$), 7.14 (t, *J* = 8 Hz, 1H, 4-C*H*$_{Ar}$), 4.61 (q, *J* = 8 Hz, 2H, -OC*H*$_2$CH$_3$), 1.32 (t, *J* = 8 Hz, 3H, -OCH$_3$C*H*$_3$) ppm. This species has been previously reported via a similar synthetic route.[25]

2,6-dibromothiophenol. (2,6-dibromophenyl)ethyl xanthate (23.1 g, .0649 mol) was dissolved in 200 mL of ethanol and KOH pellets (100g, 1.78 mol) were added. The mixture was heated to reflux while stirring overnight, and then the reaction mixture was concentrated to dryness, extracted into H_2O (200 mL), and washed with diethyl ether (2 x 200 mL). The aqueous layer was then acidified with HCl and extracted with EtOAc (2 x 200 mL). The organic layers from this second extraction were combined, dried over magnesium sulfate, filtered through a silica plug, and then concentrated to dryness. The resulting material (16.5 g, 0.0616 mol, 95%) was used without further purification for the subsequent step. ^{1}H NMR ($CDCl_3$, 300 MHz, 298 K): δ 7.49 (d, *J* = 8 Hz, 2H, 3,5-C*H*$_{Ar}$), 6.85 (t, *J* = 8 Hz, 1H, 4-C*H*$_{Ar}$), 5.00 (s, -S*H*) ppm. This species has been previously reported via a similar synthetic route.[25]

(2,6-dibromophenyl)isopropyl thioether (3.1). 2,6-dibromothiophenol (16.5 g, 0.0616 mol) was dissolved in acetone (200 mL) with 2-bromopropane (7.6 g, 0.062 mol) and powdered potassium carbonate (13.2 g, 0.0955 mol) was added. This mixture was heated to reflux while stirring overnight. The reaction was then cooled to room temperature and concentrated to dryness. The residue was taken up in dichloromethane (200 mL) and washed with water (2 x 100 mL). The organic layers were dried over magnesium sulfate, filtered, and concentrated to give a yellow oil. This oil was distilled at reduced pressure to give the desired product as a clear oil (16.8 g, 0.0542 mol, 88%). ^{1}H NMR ($CDCl_3$, 300 MHz, 298 K): δ 7.62 (d, J = 8 Hz, 2H, 3,5-CH_{Ar}), 7.00 (t, J = 8 Hz, 1H, 4-CH_{Ar}), 3.59 (septet, J = 8 Hz, 1H, -SCH(CH_3)$_2$), 1.28 (d, J = 8 Hz, 6H, -SCH(CH_3)$_2$) ppm.

(3-bromo-2-(isopropylthio)phenyl)(bis(2-diisopropylphenylphosphino)silane (3.3). **3.1** (1.81 g, 5.84 mmol) was dissolved in diethyl ether (50 mL) and cooled to -78 ^{o}C. *N*-butyllithium (3.84 ml, 1.6 M in hexane, 6.1 mmol) was added in one portion and the reaction mixture was stirred at low temperature for one hour and then allowed to warm to room temperature for one hour before being concentrated to dryness. The white residue was taken up in toluene (50 mL) and again cooled to -78 ^{o}C, and then bis(diisopropylphenylphosphino)chlorosilane (**3.2**) (2.628 g, 5.95 mmol) was added dropwise as a solution in toluene (10 mL). This was stirred at low temperature for three hours and then allowed to warm to room temperature for one hour; the cloudy gray mixture was then filtered through Celite and the filtrate was concentrated to dryness and washed with pentane to give the product as a white powder (2.38 g, 3.68 mmol, 63%). ^{1}H NMR (C_6D_6, 300 MHz, 298 K): δ 7.51 (d, J = 8 Hz, 1H, CH_{ArS}), 7.39 (d, J = 8 Hz, 2H, CH_{ArP}), 7.20-7.15 (m, 4H, CH_{ArP}), 7.07 (d, J = 8 Hz, 1H, CH_{ArS}), 6.95 (t, J = 8 Hz,

2H, C*H*$_{ArP}$), 6.59 (t, *J* = 8 Hz, 1H, 4-C*H*$_{ArS}$), 3.99 (septet, *J* = 6 Hz, 1H, -SC*H*(CH$_3$)$_2$), 2.02 (m, 4H, -P[C*H*(CH$_3$)$_2$]$_2$), 1.35 (d, *J* = 6 Hz, 6H, -SCH(C*H*$_3$)$_2$), 1.13 (dd, *J* = 6, 13 Hz, 12H, -P[CH(C*H*$_3$)$_2$]$_2$), 0.93 (m, 12H, -P[CH(C*H*$_3$)$_2$]$_2$) ppm. ^{31}P NMR (C$_6$D$_6$, 121.4 MHz, 298 K): 1.0 (s) ppm.

2,6-bis[bis(2-diisopropylphenylphosphino)silyl)]phenyl isopropyl thioether (3.4). **3.3** (6.70 g, 10.2 mmol) was dissolved in diethyl ether (100 mL) and cooled to -78 ^{o}C. *N*-butyllithium (6.51 mL, 1.6 M in hexane, 10.4 mmol) was added in one portion and the mixture was allowed to stir at low temperature for one hour and then warmed to room temperature for one hour before being concentrated to dryness. The white residue was redissolved in toluene (100 mL), cooled back to -78 ^{o}C, and then bis(diisopropylphenylphosphino)chlorosilane (**3.2**) (4.70 g, 10.4 mmol) was added as a solution in toluene (15 mL). The reaction was allowed to stir at low temperature over-night and slowly warmed to room temperature. The yellow suspension was then filtered through Celite and the filtrate was concentrated to dryness. The yellow residue was washed with pentane to give the desired product as a white solid (6.4 g, 63%). ^{1}H NMR (C$_6$D$_6$, 300 MHz, 298 K): δ 7.42 (d, *J* = 7 Hz, 4H, C*H*$_{Ar}$), 7.32 (d, *J* = 7 Hz, 4H, C*H*$_{Ar}$), 7.27-7.15 (m, 6H, C*H*$_{Ar}$), 7.11 (t, *J* = 7 Hz, 4H, C*H*$_{Ar}$), 6.81 (t, *J* = 7 Hz, 1H, 4-C*H*$_{ArS}$), 4.47 (br m, 1H, -SC*H*(CH$_3$)$_2$), 2.02 (m, 8H, -P[C*H*(CH$_3$)$_2$]$_2$), 1.57 (d, *J* = 6 Hz, 6H, -SCH(C*H*$_3$)$_2$), 1.15 (m, 24H, -P[CH(C*H*$_3$)$_2$]$_2$), 0.90 (m, 24 H, -P[CH(C*H*$_3$)$_2$]$_2$) ppm. ^{31}P NMR (C$_6$D$_6$, 121.4 MHz, 298 K): 0.9 (s) ppm.

[HSiP$^{i\mathrm{Pr}}{}_2$]$_2$Fe$_2$Cl$_3$ (3.6). Protected ligand **3.4** (1.0 g, 1.02 mmol) was dissolved in 15 mL of THF with naphthalene (160 mg, 1.25 mmol) and vigorously stirred over sodium (60 mg, 2.61 mmol) for two hours; the solution took on a deep orange-brown color. This step

serves to cleave the S-*i*Pr bond. The solution was then decanted from the remaining sodium and quenched by stirring over excess pyridinium chloride (300 mg) for four hours until the suspension was colorless, giving the deprotected thiol. The mixture was then concentrated to dryness *in vacuo*, extracted with benzene, filtered through Celite, and again concentrated. The residue was taken up in THF and stirred over KH (110 mg, 2.8 mmol) for one hour, resulting in the evolution of H_2, and the reaction mixture was again filtered through Celite to give a colorless solution of the potassium salt of the thiolate ligand. To this solution was added $FeCl_2$ (285 mg, 2.25 mmol), resulting in an immediate color change to deep blue followed by a slower color change to dark brown. This was vigorously stirred overnight, and then the reaction mixture was concentrated to dryness. The brown residue was extracted with benzene and filtered through Celite; the filtrate was concentrated to a volume of 2 mL and then layered with 15 mL of pentane and allowed to stand overnight, resulting in the precipitation of a brown microcrystalline solid; the supernatant was decanted and the solids were washed with pentane to give the desired product (770 mg, 0.67 mmol, 61%). ^{1}H NMR (C_6D_6, 300 MHz, 298 K): δ 116.7, 76.7, 30.0, 18.0, 15.1, 14.2, 10.0, 9.3, 8.3, 5.1, 3.9, 2.7, -1.0, -10.4, -66.8 ppm.

{[SiP$^{iPr}_2$]$_2$Fe$_2$Cl$_2$}{PPN} (3.7). Complex **3.6** (1.004 g, 0.846 mmol) is dissolved in THF (30 mL) and cooled to -78 ºC. A solution of methylmagnesium chloride (0.564 mL, 3.0 M in THF, 1.69 mmol) in 10 mL of THF was added dropwise over 15 minutes, and the reaction, which turned reddish-orange, was stirred at low temperature for two hours. It was then allowed to warm to room temperature for two hours, resulting in a color change to reddish brown. Then 20 mL of dioxane were added, the reaction was stirred for an additional 20 minutes, and 60 mL of pentane were added. The resulting mixture was fil-

tered through Celite and the filtrate was concentrated to dryness. The red-brown residue was extracted with benzene and filtered through Celite again, then concentrated to dryness again. This product mixture appears to contain a mixture of dichloride and monochloride species which coordinate various donors likely including THF and bridging $MgCl_2$; isolation of a clean product is facilitated by treating with an additional chloride source to give the anionic dichloride. Accordingly, the red-brown solid residue is taken up in THF (40 mL) with 10 mL of dioxane and combined with [PPN]Cl (500 mg, 0.871 mmol), and the resulting suspension was stirred overnight. The resulting bright red mixture was concentrated to dryness, extracted with benzene, and filtered through Celite. The filtrate was concentrated to 10 mL, and then pentane (20 mL) was added, resulting in the precipitation of dark red solids. The supernatant is decanted and the solids are washed with pentane and then dried *in vacuo* to give the desired product as a red solid (1.2 g, 0.72 mmol, 86%). Crystals suitable for x-ray diffraction were grown by allowing a supersaturated benzene solution to sit at room temperature overnight. ^{1}H NMR (C_6D_6, 300 MHz, 298 K): δ 27.6, 16.4, 12.2, 7.8, 7.7, 7.5, 4.2, 2.8, 1.9, 0.8, -0.8, -3.3, -18.9 ppm. μ_{eff} (C_6D_6, Evans method, 298 K): 3.3 μ_B. Anal. Calcd. For $C_{90}H_{105}Cl_2Fe_2NP_6SSi_2$: C, 65.22; H, 6.39; N, 0.85. Found: 64.81; H, 6.58; N, 0.98. UV-vis (THF, 298 K, nm {cm^{-1} M^{-1}}): 503 {7200}.

{[SiP$^{iPr}_2$]$_2$Fe$_2$(N$_2$)$_2$}{Na(12-crown-4)$_2$} (3.8{Na(12-crown-4)$_2$)). Compound **3.7** (100 mg, 0.0603 mmol) is dissolved in THF and stirred with sodium tetraphenylborate (22 mg, 0.0643 mmol) overnight in order to generate a putative monochloride intermediate with precipitation of sodium chloride and [PPN][BPh_4]. The orange reaction mixture is concentrated to dryness and extracted with 1:2 benzene:pentane (10 mL) and filtered through

Celite. The filtrate is dried to a light orange powder; NMR analysis confirms the formation of a new product. A crystal grown by slow evaporation of an Et_2O solution of this material was analyzed by X-ray crystallography, and though the resulting structure was not of sufficient quality for publication, it was consistent with a diiron complex with a single coordinated chloride disordered over the two axial iron sites. This material is stirred over excess sodium amalgam (1% Na in Hg) in THF overnight, resulting in a color change to deep green. The solution is decanted from the remaining amalgam, concentrated to dryness, extracted with 1:1 THF:diethyl ether, and filtered through Celite. The filtrate is layered with a solution of two equivalents of 12-crown-4 in diethyl ether and allowed to sit overnight, resulting in the formation of dark green crystals. The supernatant is decanted and the crystals are washed with pentane and diethyl ether and then dried *in vacuo* to give the product as dark green crystals (56 mg, 0.0379 mmol, 63%). Crystals suitable for x-ray diffraction were grown by allowing pentane to diffuse into a concentrated solution of **3.8**{Na(12-crown-4)$_2$) in 2:1 Et_2O:THF. ^{1}H NMR (2:1 C_6D_6:d_8-THF, 300 MHz, 298 K): 8.40 (d, J = 7 Hz, 4H, CH_{Ar}), 8.05 (d, J = 7 Hz, 2H, CH_{Ar}), 7.27 (d, J = 7 Hz, 4H, CH_{Ar}), 7.10 (t, J = 7 Hz, 4H, CH_{Ar}), 6.97 (t, J = 7 Hz, 4H, CH_{Ar}), 3.26 (s, 32H, 12-crown-4), 2.42 (br s, 4H, -P[CH(CH$_3$)$_2$]$_2$), 2.07 (br s, 4H, -P[CH(CH$_3$)$_2$]$_2$, 1.07 (br s, 12 H, -P[CH(CH_3)$_2$]$_2$), 0.97-0.90 (m, 32H, -P[CH(CH_3)$_2$]$_2$) ppm. ^{31}P NMR (2:1 C_6D_6:d_8-THF, 121.4 MHz, 298 K): 88.2 (br s) ppm. IR (thin film from THF): ν(N-N) = 2017, 1979 cm^{-1}. Anal. Calcd. for **3.8**{Na(12-crown-4)$_2$}·3THF, $C_{82}H_{128}Fe_2N_4NaO_{11}P_4SSi_2$: C, 58.18; H, 7.62; N, 3.31. Found: C, 58.41; H, 7.77; N, 3.49. UV-vis (THF, 298 K, nm {cm^{-1} M^{-1}}): 385 {12100}, 506 {7800}, 627 {12300}, 756 {3200}.

[SiP$^{iPr}_2$]$_2$Fe$_2$(N$_2$)$_2$ (3.9). Compound **3.8**{Na(12-crown-4)$_2$} (50 mg, 0.0338 mmol) was dissolved in THF (10 mL) and combined with ferrocenium hexafluorophosphate (12.3 mg, 0.0372 mmol) and stirred at room temperature for 6 hours. The reaction mixture, which had turned brownish-green, was then concentrated to dryness, extracted with benzene, filtered through Celite, and concentrated. The product was recrystallized from cold diethyl ether and thoroughly washed with pentane and cold Et_2O to give **3.9** as a brownish-green powder (14 mg, 0.0127 mmol, 38%). Crystals suitable for X-ray diffraction were grown by evaporation of an ether solution. ^{1}H NMR (C_6D_6, 300 MHz, 298 K): δ 15.7, 7.8, 6.9, 6.4, 4.8, 4.0, 2.4, 1.2, -3.0, -6.7 ppm. μ_{eff} (C_6D_6, Evans method, 298 K): 2.2 μ_B. IR (thin film from benzene): ν(N-N) = 2070, 1983 cm^{-1}. UV-vis (THF, 298 K, nm {cm^{-1} M^{-1}}): 368 {25200}, 770 {12600}, 930 {8800}. We were unable to obtain satisfactory CHN analysis on this compound, likely due to some lability of the coordinated N_2 ligand(s).

[SiP$^{iPr}_2$]$_2$Fe$_2$(N$_2$)$_2$H (3.11). Complex **3.6** (334 mg, 0.288 mmol) was dissolved in benzene and stirred over excess sodium amalgam (1% Na in Hg) for four hours. The reaction is then filtered through Celite and concentrated to dryness to give **3.11** as an orange-brown solid residue (286 mg, 0.259 mmol, 90%). This material appeared spectroscopically pure and was used for further reactions without further purification. Single crystals suitable for x-ray diffraction were grown by evaporation of an Et_2O solution. ^{1}H NMR (C_6D_6, 300 MHz, 298 K): δ 8.21 (d, *J* = 7 Hz, 2H, C*H*$_{Ar}$), 8.15 (d, *J* = 7 Hz, 2H, C*H*$_{Ar}$), 8.12 (d, *J* = 7 Hz, 1H, C*H*$_{Ar}$), 7.84 (d, *J* = 7 Hz, 1H, C*H*$_{Ar}$), 7.19 (t, *J* = 8 Hz, 4H, C*H*$_{Ar}$), 7.14-6.99 (m, 8H, C*H*$_{Ar}$), 6.83 (t, *J* = 7 Hz, 1H, C*H*$_{Ar}$), 2.61 (septet, *J* = 7 Hz, 2H, -P[C*H*(CH$_3$)$_2$]$_2$), 2.26 (septet, *J* = 7 Hz, 2H, -P[C*H*(CH$_3$)$_2$]$_2$), 2.03 (m, 4H, -

P[C*H*(CH_3)$_2$]$_2$), 1.37 (br s, 6H, -P[CH(C*H*$_3$)$_2$]$_2$), 1.15 (br s, 6H, -P[CH(C*H*$_3$)$_2$]$_2$), 0.96 (m, 18H, -P[CH(C*H*$_3$)$_2$]$_2$), 0.78 (br d, *J* = 6 Hz, 6H, -P[CH(C*H*$_3$)$_2$]$_2$), 0.66 (br s, 6H, -P[CH(C*H*$_3$)$_2$]$_2$), 0.46 (br s, 6H, -P[CH(C*H*$_3$)$_2$]$_2$) ppm. ^{31}P NMR (C_6D_6, 121.4 MHz, 298 K): δ 93.7 (s), 84.2 (s) ppm. IR (thin film from benzene): ν(N-N) 2093, 2036 cm^{-1}. UV-vis (THF, 298 K, nm {cm^{-1} M^{-1}}): 395 {13900}, 720 {2800}, 980 {15600}.

{[SiP$^{iPr}_2$]$_2$Fe$_2$(N$_2$)$_2$}{BAr$^F_4$} (3.10). Method A: Complex **3.11** (63 mg, 0.0570 mmol) was dissolved in diethyl ether (5 mL) and cooled to -35 ºC. A similarly cooled solution of HBAr$^F_4$·2Et$_2$O (58 mg, 0.0572 mmol) in diethyl ether (5 mL) was then added in one portion, resulting in an immediate color change to dark blue. The reaction mixture was allowed to warm to room temperature, resulting in a further color change to brown. After stirring at room temperature for three hours the solution was filtered, concentrated to a volume of 2 mL, and layered with pentane (10 mL). This mixture was allowed to stand overnight resulting in the precipitation of brown solids. The supernatant was decanted and the solid residue was washed with pentane and 1:1 benzene:pentane and then dried *in vacuo*, giving **3.10** as a dark brown powder (82 mg, 0.0496 mmol, 87%). Single crystals suitable for X-ray diffraction were grown by vapor diffusion of pentane into an Et$_2$O solution. **Method B:** Complex **3.9** (8.9 mg, 0.0081 mmol) was dissolved in Et$_2$O and an ether solution of FcBAr$^F_4$ (8.5 mg, 0.0081 mmol) was added in one portion. After stirring for one hour at room temperature the reaction mixture was analyzed by NMR and IR, and the spectroscopic properties were consistent with those of complex **3.10** as synthesized by method A. ^{1}H NMR (5:1 C_6D_6:d_8-THF, 300 MHz, 298 K): δ 10.6, 8.8, 8.3, 8.1, 7.8, 7.6, 6.5, 6.3, 5.5, 5.1, 4.5, 2.3, 1.9, 0.6, -6.0 ppm. IR (thin film from THF): ν(N-N) 2129 cm^{-1}. UV-vis (THF, 298 K, nm {cm^{-1} M^{-1}}): 378 {11000}, 426 {8900}, 503

{7200}, 589 {5100}. We were unable to obtain satisfactory CHN analysis on this compound, likely due to lability of the coordinated N_2 ligand(s).

{[SiP$^{iPr}_2$]$_2$Fe$_2$(N$_2$)$_2$H}{Na(12-crown-4)$_2$} (3.12). Method A. Complex **3.6** (120 mg, 0.104 mmol) was stirred over excess sodium amalgam (1% Na in Hg) in THF (10 mL). After stirring for 7 hours, the solution is decanted from the remaining amalgam and concentrated to dryness. The residue is extracted with diethyl ether, filtered through Celite, and concentrated to a volume of 5 mL and then layered with a solution of 12-crown-4 (39 mg, 0.22 mmol) in ether (5 mL). Brown crystals formed after sitting for several hours. The supernatant was decanted and the crystals were washed with pentane and diethyl ether and then dried *in vacuo*, giving the desired product **3.12** (110 mg, 0.0743, 71%). Single crystals suitable for x-ray diffraction were grown by dissolving **3.12** in 2:1 Et_2O:THF and allowing pentane vapors to diffuse in slowly. **Method B.** Complex **3.11** (50 mg, 0.0452 mmol) was stirred over excess sodium amalgam in THF (5 mL). Workup and purification were carried out as for method A and the spectroscopic parameters of the isolated product were identical. ^{1}H NMR (1:1 C_6D_6:d_8-THF, 300 MHz, 298 K): δ 11.2, 8.2, 7.8, 7.6, 7.1, 6.6, 4.7, 3.4, 2.8, 1.2, 0.7 ppm. μ_{eff} (d_8-THF, Evans method, 298 K): 2.2 μ_B. IR (thin film from THF): ν(N-N) 2044, 1981 cm^{-1}; ν(Fe-H) 1881 cm^{-1}. Anal. Calcd. for **3.12**·THF, $C_{74}H_{115}Fe_2N_4NaO_9P_4SSi_2$: C, 57.29; H, 7.47; N, 3.61. Found: C, 57.59; H, 7.56; N, 3.43. UV-vis (THF, 298 K, nm {cm^{-1} M^{-1}}): 367 {3300}, 504 {1800}, 631 {900}.

[SiP$^{iPr}_2$]$_2$Fe$_2$(μ-O$_2$CH) (3.13). Complex **3.11** (32.2 mg, 0.029 mmol) was dissolved in benzene (5 mL). The orange-brown solution was freeze-pump-thawed three times and then exposed to CO_2 (1 atm). The color rapidly changed to bright red and was stirred for

one hour at room temperature. The reaction mixture was lyophilized to give the desired product as a bright red powder (31.9 mg, 0.029 mmol, quant.). Single crystals suitable for x-ray diffraction were grown by slow evaporation of a diethyl ether solution. ^{1}H NMR (C_6D_6:d_8, 300 MHz, 298 K): δ 36.6, 25.1, 9.9, 7.9, 7.4, 3.5, 2.4, 1.9, -0.7, -2.1, -35.3 ppm. μ_{eff} (C_6D_6, Evans method, 298 K): 3.2 μ_B. IR (thin film from benzene): ν(C-O) 1547 cm^{-1}.

3.4.4 Reactivity studies

Conversion of N_2 to NH_3 by 3.8{Na(12-crown-4)$_2$}. **3.8**{Na(12-crown-4)$_2$} (1.8 mg, 0.0012 mmol) was dissolved in Et_2O (2 mL) in a Schlenk tube under an N_2 atmosphere and cooled to -78 °C. KC_8 (16 mg, 0.12 mmol) was added as a cooled suspension in Et_2O (1 mL) followed by $HBAr^F_4{\cdot}2Et_2O$ (100 mg, 0.10 mmol) in Et_2O. This was stirred at low temperature for two hours and then allowed to warm to room temperature for one hour. Volatiles were then vac-transferred onto an ethereal solution of HCl (4 mL, 2 M). The solid residue was treated with a solution of KO^{t}Bu in THF and again vac transferred onto the HCl solution. The resulting ammonium chloride was analyzed by the indophenol method.[26] This experiment was repeated twice, giving 1.5 and 2.1 equivalents of ammonia. In a separate experiment, the same conditions were used except that KC_8 was omitted from the reaction; no detectable ammonia was formed.

Conversion of N_2H_4 to NH_3 by 3.10. In a standard run, **3.10** (3.0 mg, 0.0015 mmol) was dissolved in THF (4 mL) in a Schlenk tube then a solution of N_2H_4 (2.5 mg, 0.08 mmol) and [LutH][BAr^F_4] (1.5 mg, 0.0015 mmol) in 4 mL THF was added and the tube was sealed and stirred at room temperature for one hour. After one hour, the volatiles were vac-transferred onto ethereal HCl (4 mL, 2M) and the resulting ammonium chloride

was analyzed via the indophenol method.[26] A table of representative conditions and results is given below; all reactions were run in THF at room temperature (Table 3.2). While modest yields of NH_3 were sometimes achieved without added acid it was highly irreproducible. An attempted catalysis reaction was run using $\{[SiP^{iPr}_2S^{Ad}]FeN_2\}BAr^F_4$ using the same conditions as entry **B**, and only 1.5 equivalents of NH_3 were produced.

Table 3.2 Ammonia production by hydrazine disproportionation

	[**10**], mM	[N_2H_4], mM	Equiv. N_2H_4	Equiv. [LutH][BAr^F_4]	Time (h)	Yield (equiv. NH_3)
A	0.19	19	100	1	8	29
B	0.19	10	50	1	8	34
C	0.19	10	50	1	1	29
D	0	10	50	1	8	0

3.5 References

1. (a) MacKay, B. A.; Fryzuk, M. D. *Chem. Rev.* **2004**, *104*, 385. (b) Peters, J. C.; Mehn, M. P. in *Activation of Small Molecules* (Ed.: W. B. Tolman), Wiley-VCH, Weinheim, **2006**, p. 81.
2. MacLeod, K. C.; Holland, P. L. *Nat. Chem*. **2013**, *5*, 559.
3. Crossland, J. L.; Tyler, D. R. *Coord. Chem. Rev*. **2010**, *254*, 1883.
4. Barriere, F. in Biosinspired Catalysis: *Metal-Sulfur Complexes*, Ch. 9 (Wiley, **2015**).
5. Lukoyanov, D.; Dikanov, S. A.; Yang, Z.-Y.; Barney, B. M.; Samoilova, R. I.; Narasimhulu, K. V.; Dean, D. R.; Seefeldt, L. C.; Hoffman, B. M. *J. Am. Chem. Soc.* **2011**, *133*, 11655.

6. (a) Einsle, O.; Tezcan, A.; Andrade, S. L. A.; Schmid, B.; Yoshida, M.; Howard, J. B.; Rees, D. C. *Science* **2002**, *297*, 1696. (b) Spatzal, T.; Aksoyoglu, M.; Zhang, L.; Andrade, S. L. A.; Schleicher, E.; Weber, S.; Rees, D. C.; Einsle, O. *Science* **2011**, *334*, 940. (c) Lancaster, K. M.; Roemelt, M.; Ettenhuber, P.; Hu, Y.; Ribbe, M. W.; Neese, F.; Bergmann, U.; DeBeer, S. *Science* **2011**, *334*, 974. (d) Lancaster, K. M.; Hu, Y.; Bergmann, U.; Ribbe, M. W.; DeBeer, S. *J. Am. Chem. Soc.* **2013**, *135*, 610. (e) Wiig, J. A.; Hu, Y.; Lee, C. C.; Ribbe, M. W. *Science* **2012**, *337*, 1672.

7. (a) Lee, H. I.; Igarashi, R. Y.; Laryukhin, M.; Doan, P. E.; Dos Santos, P. C.; Dean, D. R.; Seefeldt, L. C.; Hoffman, B. M. *J. Am. Chem. Soc.* **2004**, *126*, 9563. (b) Spatzal, T.; Perez, K. A.; Einsle, O.; Howard, J. B.; Rees, D. C. *Science*, **2014**, *345*, 1620.

8. (a) Yoshida, T.; Adachi, T.; Kaminaka, M.; Ueda, T.; Higuchi, T. *J. Am. Chem. Soc.* **1988**, *110*, 4872. (b) Pombeiro, A. J. L.; Hitchcock, P. B.; Richards, R. L. *J. Chem. Soc., Dalton Trans.* **1987**, 319. (c) Cruz-Garritz, D.; Torrens, H.; Leal, J.; Richards, R. L. *Transition Met. Chem.* **1983**, 8, 127. (d) Morris, R. H.; Ressner, J. M.; Sawyer, J. F.; Shiralian, M. *J. Am. Chem. Soc.* **1984**, *106*, 3683. (e) Dilworth, J. R.; Hu, J.; Thompson, R. M.; Hughes, D. L. *Chem. Commun*. **1992**, 551. (f) Seymore, S. B.; Brown, S. N. *Inorg. Chem*. **2006**, *45*, 9540. (g) Mori, H.; Seino, H.; Hidai, M.; Mizobe, Y. *Angew. Chem. Int. Ed*. **2007**, *46*, 5431. (h) Sellmann, D.; Hautsch, B.; Rosler, A.; Heinemann, F. W. *Angew. Chem. Int. Ed.* **2001**, *40*, 1505. (i) Sellmann, D.; Hille, A.; Rosler, A.; Heinemann, F. W.; Moll, M. *Inorg. Chim. Acta* **2004**, *357*, 3336. (j) Fernandez, P.; Sousa-Pedrares, A.; Romero, J.; Duran, M. L.; Sousa, A.; Perez-Lourido, P.; Garcia-Vazquez, J. A. *Eur. J. Inorg. Chem*. **2010**, 814.

9. (a) Bart, S.; Lobkovsky, E.; Bill, E.; Wieghardt, K.; Chirik, P. J. *Inorg*. *Chem*. **2007**, *46*, 7055. (b) Takaoka, A.; Mankad, N. P.; Peters, J. C. *J. Am. Chem. Soc*. **2011**, *133*, 8440.

10. After our initial publication on this topic, an example of an iron bis(thiolate) dinitrogen complex was published by Holland *et al.*: Coric, I.; Mercado, B. Q.; Bill, E.; Vinyard, D. J.; Holland, P. L. *Nature* **2015,** *526*, 96.

11. (a) Lee, S. C.; Lo, W.; Holm, R. H. *Chem. Rev.* **2014**, *114*, 3579. (b) Rao, P. V.; Holm, R. H. *Chem. Rev.* **2004**, *104*, 527. (c) Malinak, S. M.; Coucouvanis, D. *Progress in Inorganic Chemistry*, **2001**, *49* , 599.

12. (a) Lane, R. W.; Ibers, J. A.; Frankel, R. B.; Papaeftymiou, G. C.; Holm, R. H. *J. Am. Chem. Soc.* **1977**, *99*, 84. (b) Lee, S. C.; Holm, R. H. *Chem. Rev.* **2004**, *104*, 1135. (c) Malianak, S. M.; Coucouvanis, D. *Prog. Inorg. Chem.* **2001**, *49*, 599.

13. (a) Anderson, J. S.; Peters, J. C. *Angew. Chem. Int. Ed.* **2014**, *53*, 5978. (b) Rodriguez, M. M.; Stubbert, B. D.; Scarborough, C. C.; Brennessel, W. W.; Bill, E.; Holland, P. L. *Angew. Chem. Int. Ed.* **2012**, *51*, 8247.

14. Rittle, J.; McCrory, C.; Peters, J. C. *J. Am. Chem. Soc.* **2014**, *136*, 13853.

15. (a) Hoffman, B. M.; Lukoyanov, D.; Yang, Z.-Y.; Dean, D. R.; Seefeldt, L. C. *Chem. Rev.* **2014**, *114*, 4041. (b) Hoffman, B. M.; Dean, D. R.; Seefeldt, L. C. *Acc. Chem. Res.* **2009**, *42*, 609.

16. Kinney, R. A.; Saouma, C. T.; Peters, J. C.; Hoffman, B. M. *J. Am. Chem. Soc.* **2012**, *134*, 12637.

17. Anderson, J. S.; Rittle, J.; Peters, J. C. *Nature* **2013**, *501*, 84.

18. (a) Chen, Y.; Zhou, Y.; Chen, P.; Tao, Y.; Li, Y.; Qu, J. *J. Am. Chem. Soc*. **2008**, *130*, 15250. (b) Chang, Y.-H.; Chan, P.-M.; Tsai, Y.-F.; Lee, G.-H.; Hsu, H.-F. *Inorg. Chem.*

2014, *53*, 664. (c) Umehara, K.; Kuwata, S.; Ikariya, T. *J. Am. Chem. Soc.* **2013**, *135*, 6754.

19. Davis, L. C. *Arch. Biochem. Biophys.* **1980**, *204*, 270.

20. Sellmann, D.; Sutter, J. *Acc. Chem. Res*. **1997**, *30*, 460.

21. Diiron thiolate-bridged iron hydrides are also structurally relevant to hydrogenases. See for example: Wang, W.; Rauchfuss, T. B.; Zhu, L. *J. Am. Chem. Soc.* **2014**, *136*, 5773.

22. Chavez, I.; Alvarez-Carena, A.; Molins, E.; Roig, A.; Maniukiewicz, W.; Arancibia, A.; Arancibia, V.; Brand, H.; Manriquez, J. M. *J. Organomet. Chem*. **2000**, *601*, 126.

23. Brookhart, M.; Grant, B.; Volpe, A. F., Jr. *Organometallics* **1992**, *11*, 3920.

24. Evans, D. F. *J. Chem. Soc*. **1959**, 2003.

25. Stoyanovich, F. M.; Marakatkina, M. A.; Goldfarb, Y. L. *Bulletin of the Academy of Sciences of the USSR, Division of Chemical Science (English Translation).* **1976,** *25*, 2362.

26. Weatherburn, M. W. *Anal. Chem.* **1967**, *39*, 971.

Chapter 4. Incorporating secondary-sphere interactions into Fe complexes relevant to N_2 fixation

4.1 Introduction

The inorganic chemistry community has long been interested in modelling both the structure and function of metalloenzyme active sites using synthetic, small-molecule systems.[1] Frustratingly, structural models of these metal-containing active sites which faithfully model the primary coordination sphere have frequently met with little success in mimicking the catalytic activity of these enzymes. In most cases, these model complexes lack the peripheral secondary sphere interactions present in biological systems. Structural, computational, and mechanistic studies on metalloenzymes show that the vast majority of known examples likely benefit from the presence of secondary sphere interactions such as hydrogen bonds in facilitating catalytic reactivity at the metal center—both by stabilizing intermediates and by orchestrating the necessary arrangement of reactants.[2]

Increasingly, inorganic chemists have worked to incorporate secondary sphere interactions, especially hydrogen bonding, in structural and functional models of metalloenzyme active sites. In a number of cases, especially in the context of proton reduction and oxygen activation, these approaches have been markedly successful both in engendering superior reactivity and in stabilizing reactive intermediates such as terminal metal oxo complexes.[3]

A role for secondary sphere interactions in nitrogen fixation is less well established. Biological nitrogen fixation is a fascinatingly complex process that is catalysed by iron-containing active sites of which the most well-studied is the Fe_7MoS_9C cluster in the iron-molybdenum cofactor (FeMoco). Very little is

known conclusively about the mechanism of this reaction in these biological systems, including the potential presence or importance of hydrogen bonding interactions around the active site.[4-7]

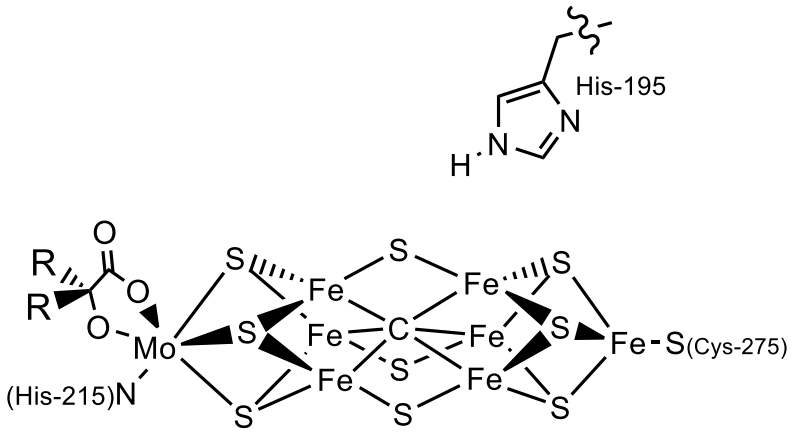

Figure 4.1. Schematic of the nitrogenase FeMo cofactor; His-195 may interact *via* hydrogen-bonding with the active site.

In the nitrogenase enzyme of *Azotobacter vinelandii*, a highly conserved histidine residue is poised over the "beltway" irons on one face of the cluster. Based on computations and biological studies of mutant enzymes, it is hypothesised that one or more of these iron centers may be the binding site for N_2 and the locus of catalytic reduction to ammonia (Figure 4.1).[5] Removing this histidine residue *via* site-directed mutagenesis shuts down N_2 fixation, suggesting that it may play a role in the reaction, perhaps *via* hydrogen bonding or simply by acting as a proton shuttle to the active site.[8] Intriguingly, a recent crystal structure of a CO-bound form of FeMoCo appears consistent with the

presence of a hydrogen bond between the terminal oxygen atom of a bridging CO ligand and the N-H moiety of this histidine residue.[9]

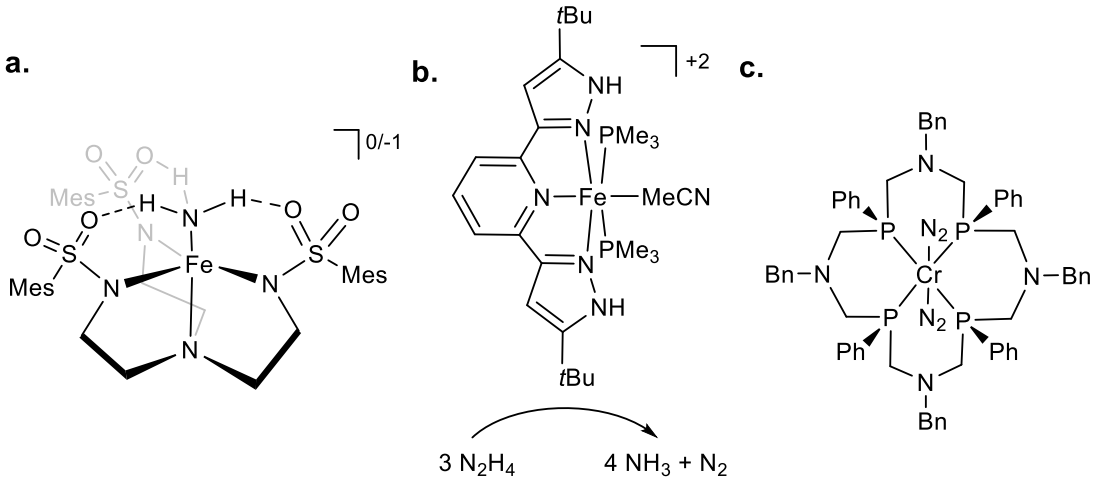

Figure 4.2. Select previously reported systems incorporating hydrogen-bonding or proton-responsive moieties for the binding and/or conversion of nitrogenous substrates. **a.** Fe(II) and Fe(III) complexes of ammonia show multiple hydrogen-bonding interactions with ligand.[14] **b.** The participation of a proton-responsive ligand is invoked in the disproportionation of hydrazine by Fe(II).[13] **c.** Treatment of a Cr(0)-$(N_2)_2$ complex within a scaffold bearing tertiary amines with acid produces ammonia and hydrazine.[16]

There have been relatively few efforts to incorporate secondary sphere interactions into synthetic systems for N_2 fixation, although several recent studies have examined the influence of pendant amine groups on the protonation of Mo- and W-N_2 complexes.[10] While catalytic N_2 fixation has now been established on synthetic molecular Mo platforms, and, more recently, Fe platforms, none of these systems explicitly invoke any secondary sphere interactions in their

reactivity.[11,12] However, secondary sphere participation has been shown to be involved in one iron system for catalytic hydrazine disproportionation, a reaction of possible relevance to N_2 fixation (Figure 4.2b).[13] Fe(II)-NH_3 and Fe(III)-NH_3 complexes with secondary-sphere hydrogen-bonding interactions have been characterised by the Borovik group (Figure 4.2a),[14] while select other examples of secondary sphere interactions with possible metal-bound N_2 reduction intermediates including hydrazine and diazene are known.[15] Recently, the first example of N_2 reduction to ammonia by a Cr-N_2 species was reported; this complex is supported by a ligand containing pendant tertiary amines, but it is not clear what role, if any, these play in the N_2 functionalization reaction (Figure 4.2c).[16] Further exploration of the role of secondary sphere interactions in facilitating N_2 fixation and in stabilizing potential N_2 reduction intermediates, especially on iron, seems desirable.

Our lab has extensively studied a series of tetradentate trisphosphine ligands with apical N, Si, B, or C donors in the context of N_2 activation and reduction, including catalytic fixation to ammonia.[12a-b,17] We therefore sought to explore the potential applicability of secondary-sphere interactions to these ligand platforms, and to determine if incorporating pendant functionalities could either enhance catalytic reactivity or stabilize reactive intermediates such as amides, imides, diazenes, diazenidos, or hydrazides. Towards that end, we report here the synthesis of new ligands incorporating tertiary amines as hydrogen bond acceptors and their interaction with various N_xH_y ligands of relevance to catalytic

N_2 reduction. The influence of the pendant amine groups on the reactivity of the Fe-N_2 complexes with protons is also examined.

4.2 Results and Discussion

4.2.1 Ligand Design and Synthesis

We initially targeted modification of the (SiP_3)[M] tris(phosphino)silyl ligand platform that our group has used extensively to explore the structures and reactivity of Fe-N_xH_y species relevant to N_2 fixation. Tertiary amines were targeted as the secondary-sphere functionality due to their anticipated stability towards the highly reducing conditions required for N_2 fixation on synthetic iron systems. In order to provide sufficient rigidity to position the hydrogen-bonding groups around the substrate binding cavity, while still allowing sufficient flexibility to adjust for the presence of different substrates in the metal binding pocket, we chose to incorporate the pendant groups into six-membered heterocyclic rings (Scheme 4.1).

Scheme 4.1. Synthesis of ligand arm **L_0**

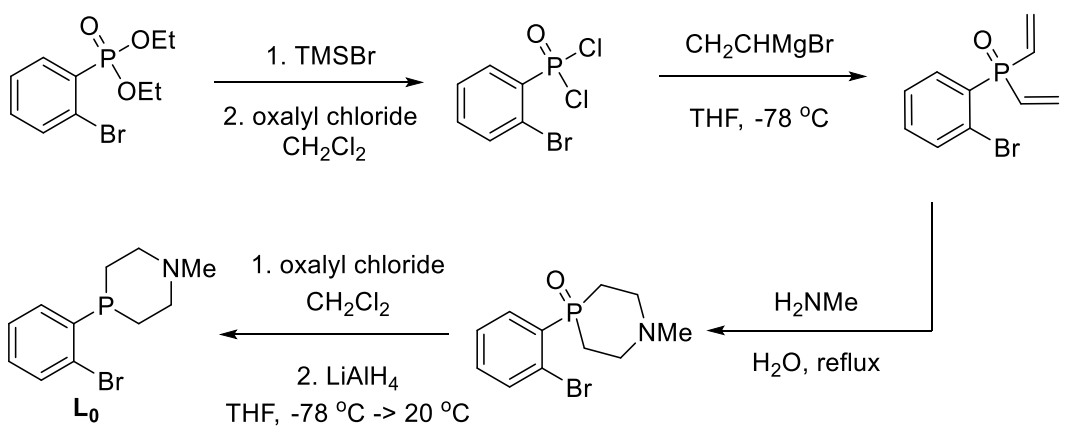

Scheme 4.2. Synthesis of ligands $\mathbf{L_1}$ and $\mathbf{L_2}$

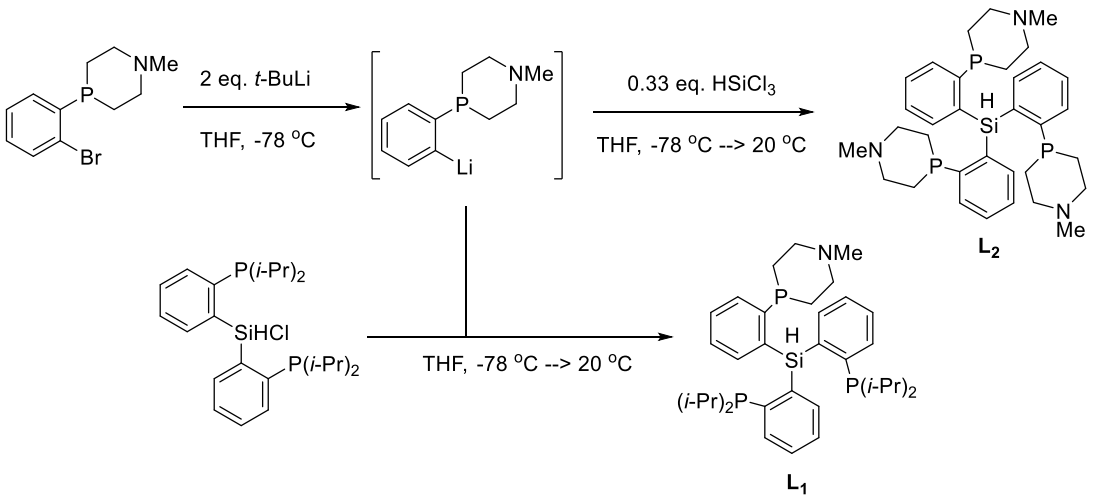

Thus, we pursued a modified phosphine ligand arm incorporating a tertiary amine into a six-membered heterocycle that would position the amines around the apical binding pocket of the metal center. Synthesis of the ligand arm (**L_0**) involves first generating *o*-bromophenyldivinylphosphine oxide followed by cyclization with methylamine *via* a double Michael-type addition.[18] The resulting phosphine oxide azacycle can then be reduced to the desired phosphine (Scheme 4.1). The ligand arm can then be lithiated and added to the appropriate electrophile to assemble symmetric or unsymmetric tris(phosphino)silyl tetradentate ligands. In this manner, two tris(phosphine)silyl ligands have been assembled—one asymmetric azaphosphine-bis(diisopropylphenylphosphine)-silyl ligand (**L_1**) and one symmetric tris(azaphosphine)silyl ligand (**L_2**) (Scheme 4.2).

Scheme 4.3. Synthesis of Fe(II) and Fe(I) precursor complexes.

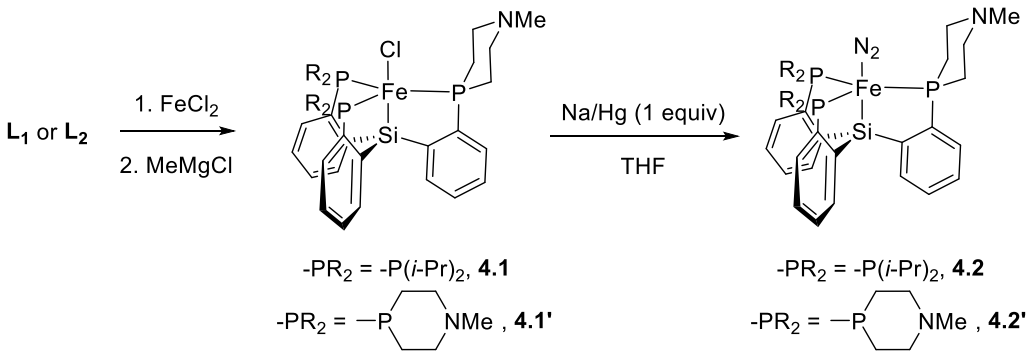

4.2.2 Synthesis of Precursor Iron Complexes of L_1 and L_2

Metallation of the new ligands **L_1** and **L_2** on iron follows procedures similar to those used previously for $HSiP^{iPr}_3$, using methylmagnesium chloride to putatively generate a transient Fe-Me species which loses methane with concomitant activation of the Si-H bond to give a trigonal bipyramidal Fe(II) chloride complex.[17d] Subsequent reduction of these complexes under an N_2 atmosphere with one equivalent of sodium amalgam generates the corresponding Fe(I) complex with loss of sodium chloride and uptake of N_2 (Scheme 4.3, Figure 4.3).

Comparison of the spin states and IR parameters for these complexes to the parent (SiP^{iPr}_3)[Fe] complexes suggests that the electronic properties and donicity of the azacyclic phosphine are not substantially different from those of other dialkylaryl phosphine ligands, which will facilitate interpretation of the effects of secondary sphere interactions on the properties of these complexes (Table 4.1).[17b-d]

Table 4.1. Comparison data for [Fe]Cl and [Fe]N_2 complexes[17b,c]

	4.1	**4.1'**	SiP^{iPr}_3FeCl	**4.2**	**4.2'**	$(SiP^{iPr}_3)FeN_2$
μ_B (B.M.)	3.0	3.0	3.3	2.1	2.1	2.2
$\nu(N_2)$ (cm^{-1})	--	--	--	2005	2007	2008

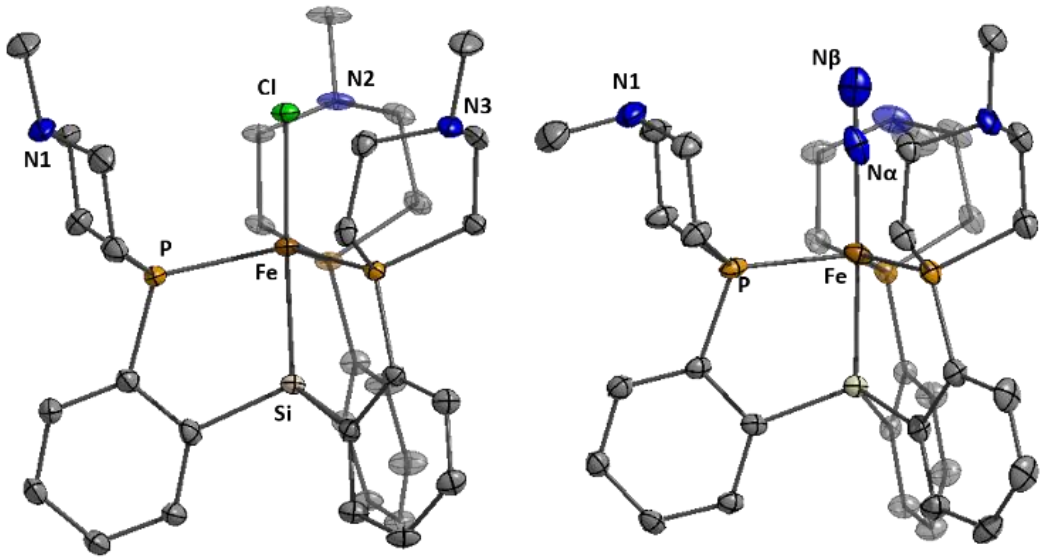

Figure 4.3. Structures of **4.1'** and **4.2'**. Solvent molecules and hydrogen atoms omitted for clarity. Thermal ellipsoids are shown at 50% probability.

As expected for a saturated six-membered ring, the phosphaazacycles in these complexes—in which no hydrogen bonding is present—adopt a chair conformation, with the N-Me group adopting either a pseudo-axial or pseudo-equatorial conformation. In these conformations, the tertiary amine is not well positioned for hydrogen bonding to a substrate bound axially to iron. Therefore, as will be shown below, hydrogen bonding requires the ring to adopt the less favourable boat or twist-boat conformation, which will serve as a useful structural diagnostic for the presence of hydrogen bonding.

4.2.3 Synthesis and characterization of Fe-N_xH_y complexes

In order to probe the impact of pendant hydrogen-bonding moieties on the activation of N_2 or the stabilization of N_2 reduction intermediates, we sought to structurally characterise complexes of various N_xH_y ligands including ammonia, hydrazine, and amide ($-NH_2$).

Access to the hydrazine and ammonia adducts proceeds *via* oxidation of **4.2** or **4.2'** with ferricenium BAr^F_4 (Ar^F = 3,5-bistrifluoromethylphenyl) to generate *in situ* an (**L**$_1$)[Fe(II)] or (**L**$_2$)[Fe(II)] complex which is treated with hydrazine or gaseous ammonia to give the desired complex (Scheme 4.4). The resulting complexes **4.3**, **4.3'**, and **4.4** are stable to vacuum and have been isolated in pure form and crystallographically characterized. Complex **4.4'** is not sufficiently stable to be isolated (*vide infra*).

Scheme 4.4. Synthesis of cationic NH_3 and N_2H_4 adducts of (L)Fe(II).

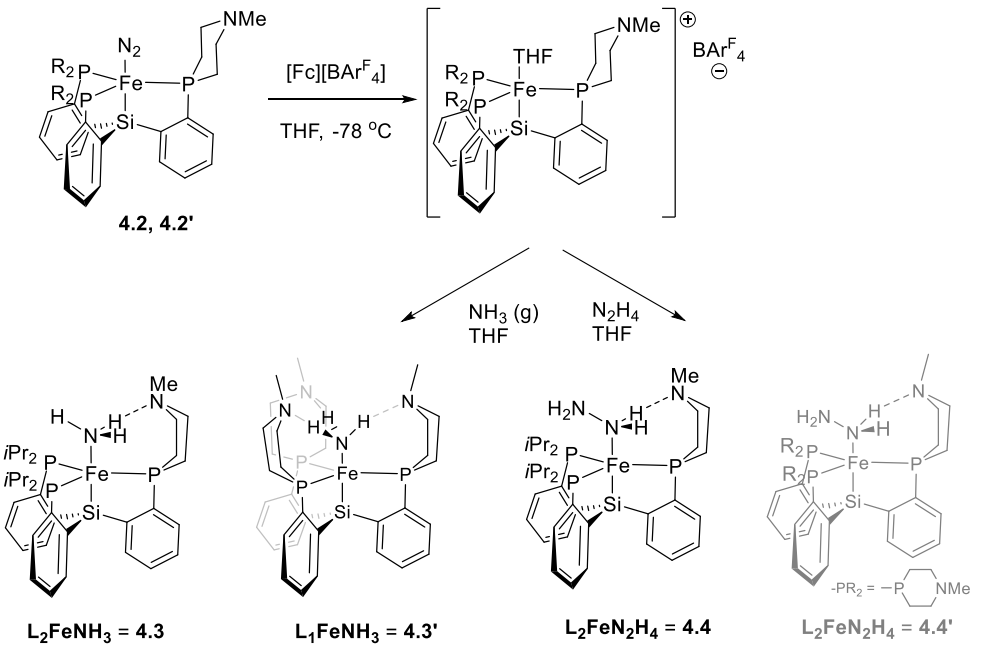

Structural analysis of **4.3**, **4.3'**, and **4.4** clearly illustrate the presence of hydrogen bonding interactions between the tertiary amines in the ligand and the N-H bonds of the iron-bound substrates (Figure 4.4). The boat-type conformations of the six-membered azaphosphine rings are diagnostic for the presence of at least moderately strong hydrogen bonds, as the energetic benefit of the hydrogen bonds must be sufficient to overcome the energetic penalty of adopting the disfavoured boat conformation rather than the chair conformations which are observed in all structures lacking hydrogen bonds.

In the structures of complexes **4.3**, **4.3'**, and **4.4**, the N-bound hydrogen atoms could be located from the density difference map and their positions were allowed to refine freely. In all cases where hydrogen bonds were apparent from the conformation of the azaphosphacycles, hydrogen atoms were located in the expected position, bound to the Fe-coordinated nitrogen atom and appropriately oriented for interaction with the tertiary amine acceptors. In the case of ammonia complex **4.3'**, two independent molecules are present in the asymmetric unit. In one of these molecules, all three ligand azaphosphacycles occupy a boat conformation indicative of hydrogen bonding interactions with the three ammonia hydrogen atoms. In the second molecule, two of the ligand arms are engaged in hydrogen bonding, while the third is disordered (3:2) between boat and chair conformations. The shortest donor-acceptor bond lengths between N_{α} and N^{Me} are 2.994 Å, 2.984 Å, and 3.074 Å in **4.3**, **4.3'**, and **4.4**, respectively. The donor-acceptor distances for the hydrogen bonds are in the regime of what has been classified as a "moderate" strength hydrogen bond.[19]

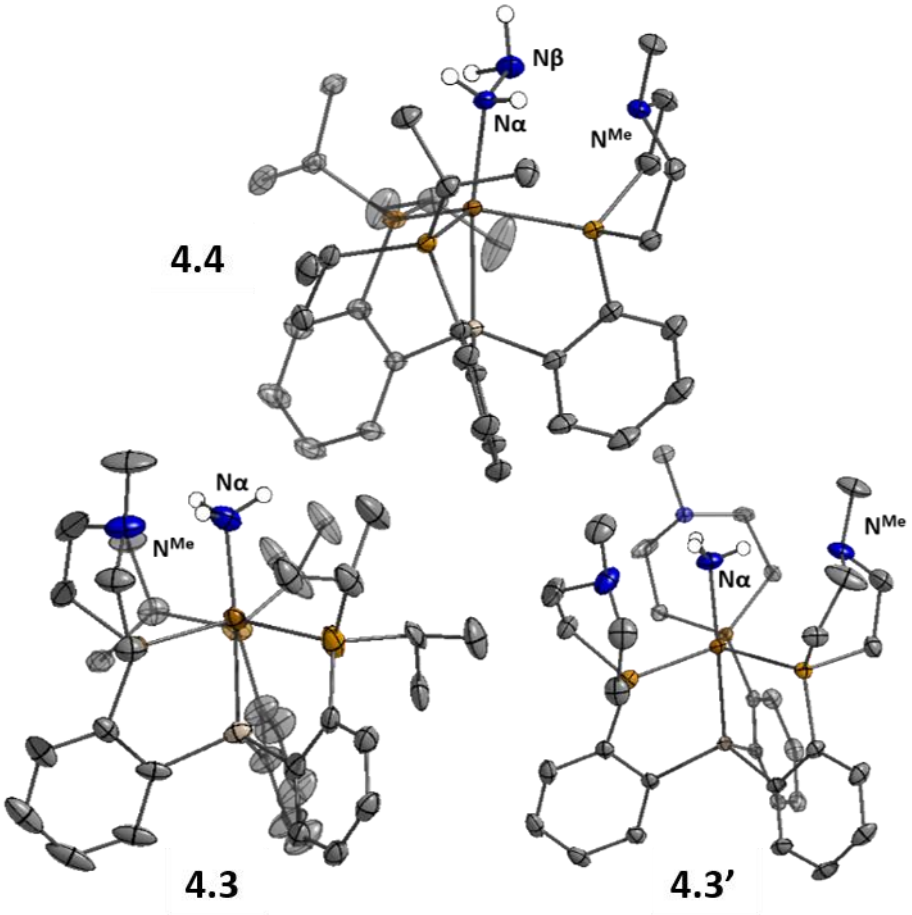

Figure 4.4. Structure of ammonia and hydrazine complexes **4.3, 4.3',** and **4.4**. BAr^F_4 counteranions, solvent molecules, and carbon-bound hydrogen atoms omitted for clarity. Thermal ellipsoids are shown at 50% probability.

Since engaging in hydrogen bonding with a coordinated substrate requires the six-membered rings of the ligand to adopt a higher-energy conformation (boat rather than chair), a lower limit for the strength of the hydrogen bonds can be obtained if the difference in energy between these two conformations is known. In order to approximate this energy difference, DFT computations on a truncated model ligand, $HSiP^{Me}_2P^{NMe}$ (**4.8**), an analogue where the isopropyl groups have

been replaced by methyls, were carried out with the azaphophine ring in the chair (as in the structure of **4.1'** or **4.5**, *vide infra*) or boat (as in the structure of **4.3**) conformation. The energy difference between the conformers was calculated to be approximately 17 kJ/mol, again consistent with a hydrogen of at least moderate strength.

Both **4.4** and **4.4'** are unstable, decomposing to give ammonia complexes **4.3** and **4.3'**, respectively. While **4.4** decomposes fully over the course of several hours at 60 °C, **4.4'** decomposes with sufficient rapidity in solution that it has not been possible to isolate this complex in pure form, and full conversion to **4.3'** is observed typically within several minutes at room temperature. The parent complex $[(SiP^{iPr}_3)FeN_2H_4][BAr^F_4]$ is also susceptible to a similar decomposition process; however, in this case full conversion to the ammonia complex requires heating at 60 °C for several days. The kinetics of these decomposition reactions show complex behaviour characteristic of autocatalytic reactions, similar to that observed for the metalloboratrane complex $[(TPB)FeN_2H_4][BAr^F_4]$. The nature of the autocatalyst has not yet been identified, complicating any detailed quantitative kinetic analysis.[20] However, qualitatively, it appears that the rate of the decomposition reaction is increased by the presence of hydrogen bond acceptors in the secondary coordination sphere. Similar trends have previously been observed in another iron system which was able to catalytically disproportionate hydrazine.[13]

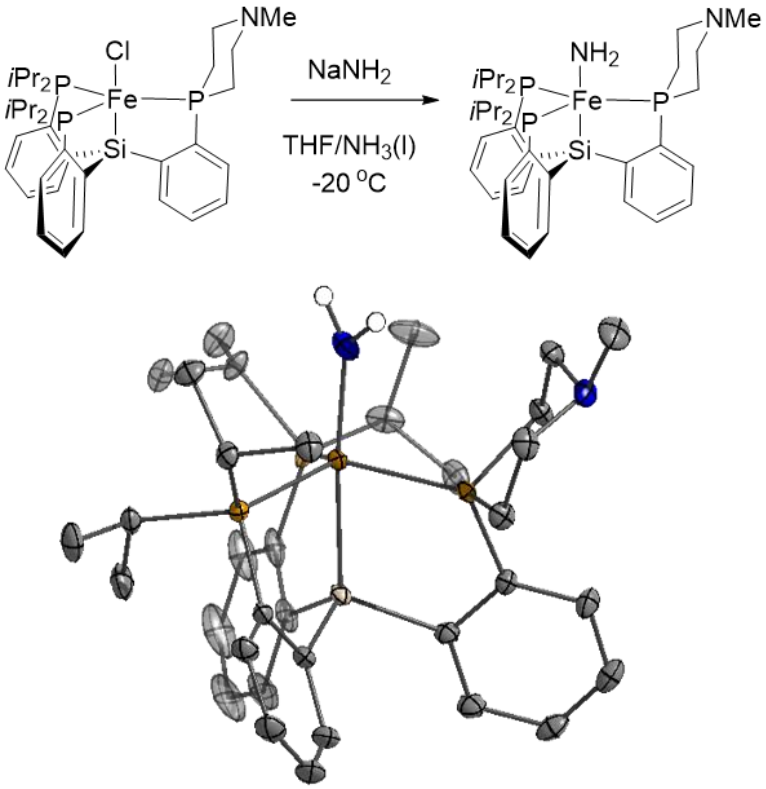

Figure 4.5. Synthesis of a parent amide complex. Crystal structure of **4.5** is shown with thermal ellipsoids at 50% probability; carbon-bound hydrogens are omitted for clarity.

Terminal parent amide (-NH_2) complexes of iron are relatively rare despite their relevance as a possible intermediate in N_2 fixation to ammonia on iron, with only two examples previously structurally characterised.[20,21] We have found that an Fe(II) amide complex, (**L**$_2$)Fe-NH_2 (**4.5**) is readily synthesised by treating (**L**$_2$)FeCl (**4.1**) with excess $NaNH_2$ in 1:1 THF/NH_3(l) solvent (Figure 4.5). The identity of the –NH_2 ligand was confirmed by digesting the complex with HCl and then analysing the resulting solution for ammonia using the indophenol method, which showed quantitative generation of ammonia. Complex **4.5** has

been structurally characterised and does not show any hydrogen bonding to the ligand in the solid state. This is not unexpected as the $–NH_2$ moiety in **4.5** is more electron-rich than the NH_3 ligand in cationic complexes **4.3** and **4.3'**, and therefore further stabilization of the partial positive charge of the $–NH_2$ hydrogens by hydrogen bonding is not energetically favourable enough to overcome the conformational flip of the azaphosphacycle to the boat conformation.

Attempted oxidation of **4.5** with $[Fc][BAr^F_4]$ (Ar^F = 3,5-bis(trifluoromethyl)phenyl) gave ammonia complex **4.3** as the primary detectable product. This suggests that while an Fe(III)-NH_2 or imide complex may be transiently formed, it is unstable and reacts further, e.g. by hydrogen atom abstraction from solvent and/or disproportionation, to give the observed products. Carrying out the reaction in thawing 2-MeTHF allows for the detection of a new *S*=1/2 species by EPR at 77 K which disappears upon warming. However, attempts to capture this intermediate, e.g. by reaction with phosphines generate phosphinimines, were not successful.

4.2.4 Synthesis and reactivity of reduced Fe-N_2 complexes

In the systems studied by our lab that generate ammonia from N_2 in a catalytic or stoichiometric manner, the precatalyst or precursor is typically the anionic $[(L)Fe\text{-}N_2]^-$ complex.[12] Therefore, we synthesised and characterised $[(\mathbf{L_1})FeN_2]^-$ and $[(\mathbf{L_2})FeN_2]^-$ as their sodium salts by reduction of **4.2** and **4.2'** with excess sodium amalgam in THF (Figure 4.6a). The solid state structure of **4.6'** (ν(NN) = 1878 cm^{-1}) illustrates that, in addition to acting as a hydrogen-bond acceptor,

the tertiary amine in the secondary coordination sphere can interact with a Lewis acidic countercation such as $[Na(THF)_3]^+$ (Figure 4.7).

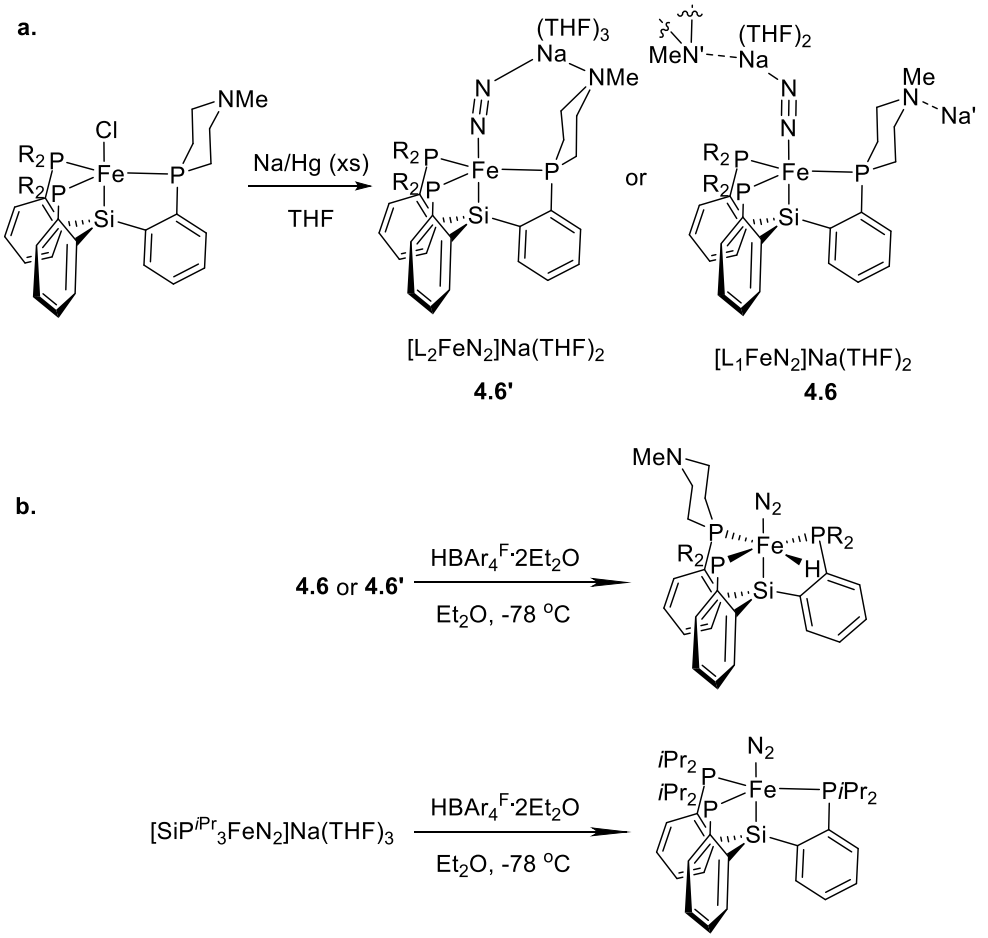

Figure 4.6. Synthesis of anions and differing protonation reactivity. **a.** Reduction of **4.1** or **4.1'** to give **4.6** or **4.6'** respectively. **4.6'** shows intramolecular coordination of the sodium counteraction to the tertiary amine in the solid state, while **4.6** shows intermolecular coordination of the sodium to the tertiary amine (N'Me) of a neighboring molecule. **b.** Differing protonation reactivities of **4.6**, **4.6'**, and parent complex $[(SiP^{iPr}_3)FeN_2][Na(THF)_3]$.

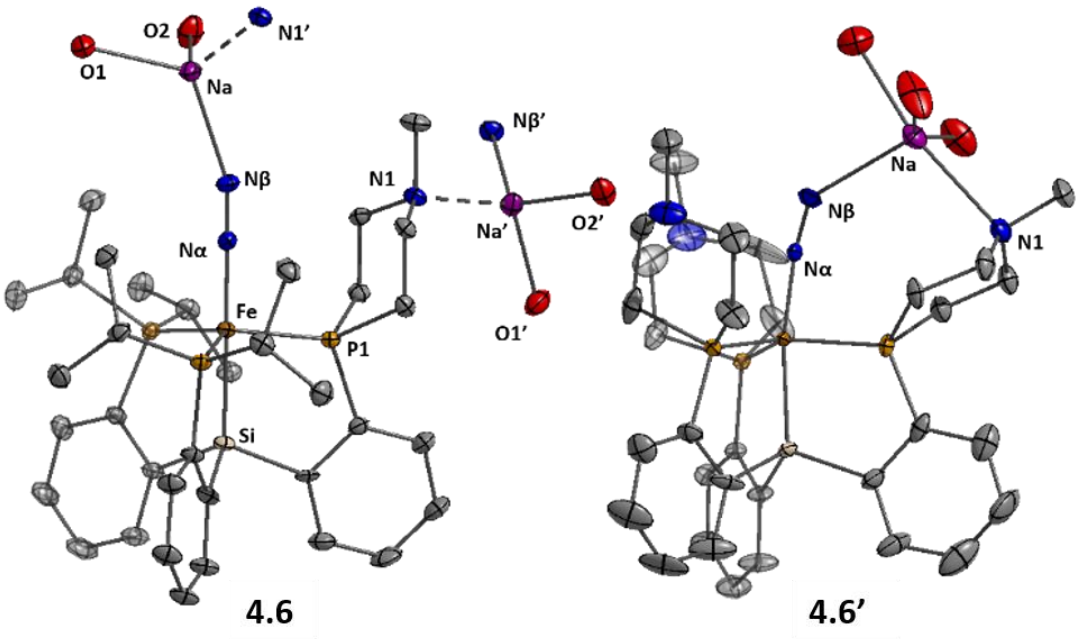

Figure 4.7. Structures of complexes **4.6** and **4.6'**. For **4.6**, the intermolecular interaction (dashed lines) between the sodium cation and the tertiary amine group of a neighboring molecule (N1') is shown, as well as the interaction with the sodium countercation of another neighbour (Na'). Thermal ellipsoids are shown at 50% probability, and hydrogen atoms and uncoordinated solvent are omitted for clarity. Coordinated THF molecules are truncated to show only the oxygen atom bound to Na.

In the case of **4.6'**, the N-Na bonds are sufficiently long that the six-membered azacycle can maintain a distorted chair conformation while still supporting this interaction. In the solid state, the Fe-N-N angle, which is typically very close to 180° in terminal Fe-N_2 complexes, is distorted to 171.7° due to the interaction with the Na cation whose position is constrained by coordination to the pendant

amine in the ligand. In contrast, the crystal structure of **4.6** (ν(NN) = 1874 cm^{-1}) shows intermolecular coordination of the sodium cation to the amine of a neighbouring molecule, forming an infinite chain structure; in this case the azacycle adopts a chair conformation and the Fe-N-N angle does not significantly deviate from linearity (Figure 4.7).

While treatment of $[(SiP^{iPr}_3)FeN_2]^-$ in an N_2 atmosphere with an excess (50 equivalents) of protons and electrons ($HBAr^F_4{\cdot}2Et_2O$ and KC_8, respectively) generated 0.8 ± 0.4 equivalents of ammonia, performing the same reaction with **4.6** or **4.6'** resulted in no detectable ammonia formation.[12a] The stoichiometric reactions of these anions with acid provides some clues as to the reason for this difference (Figure 4.6b). In the case of $[(SiP^{iPr}_3)FeN_2]^-$, treatment with either stoichiometric (one equiv.) $HBAr^F_4{\cdot}2Et_2O$ or the tertiary ammonium acid $[HN^iPr_2Et][BAr^F_4]$ at -78 °C results in clean oxidation to $(SiP^{iPr}_3)FeN_2$, a reaction which is believed to proceed with formal loss of ½ H_2 from a transient [Fe]NNH intermediate. However, with **4.6** or **4.6'**, the same reactions result in immediate generation of the hydride complexes ($\mathbf{L_1}$)Fe(N_2)(H) and ($\mathbf{L_2}$)Fe(N_2)(H). Given that formation of the transient [Fe]NNH species is believed to be a necessary step in the transformation of N_2 to NH_3 on these complexes, the failure of **4.6** and **4.6'** to facilitate the formation of this species is likely a primary reason for their inability to mediate N_2 fixation.

This difference can be rationalized by considering the kinetically and thermodynamically preferred sites of protonation in these complexes. In the absence of an exposed basic site on the ligand, the kinetic site of protonation is

the terminal N-atom of the N_2 ligand, which transiently generates an –NNH ligand which can undergo further reactivity. However, when the tertiary amine is present, this becomes the kinetic site of protonation; the amine then acts as a stable proton shuttle which can deliver the proton to the metal center to form the hydride complex, which tends to be a thermodynamic sink in these systems (Figure 4.8). A similar effect has been observed in the case of protonation of anionic tungsten N_2 complexes with and without pendant amines in the ligand.[10b]

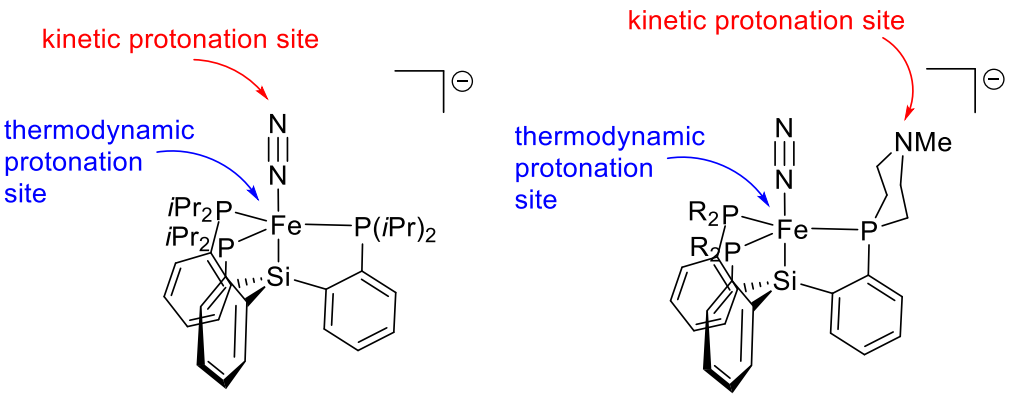

Figure 4.8. Kinetic and thermodynamic protonation sites of $[(SiP^R_3)FeN_2]^-$ anions.

4.2.5 Complexes of a zwitterionic ligand—effect of Coulombic interactions

In addition to hydrogen bonding, several other types of secondary sphere interactions have been recognised; one which may be particularly important in modulating reduction potentials is the Coulombic interaction with charged species which are proximal, but not directly electronically coupled, to the metal site. There are a number of examples of systems where incorporation of a metal

center into a zwitterionic framework using a charged fragment in the ligand backbone can substantially alter the properties of the metal relative to their non-zwitterionic congeners. Properties such as acidity/basicity and reduction potentials can depend strongly on overall molecular charge.[22] Given that synthetic systems for nitrogen reduction on iron typically require accessing very reducing potentials to functionalise N_2, modifying the ligand scaffolds in a way that alters the redox potential without altering the primary coordination sphere of the metal may be desirable.

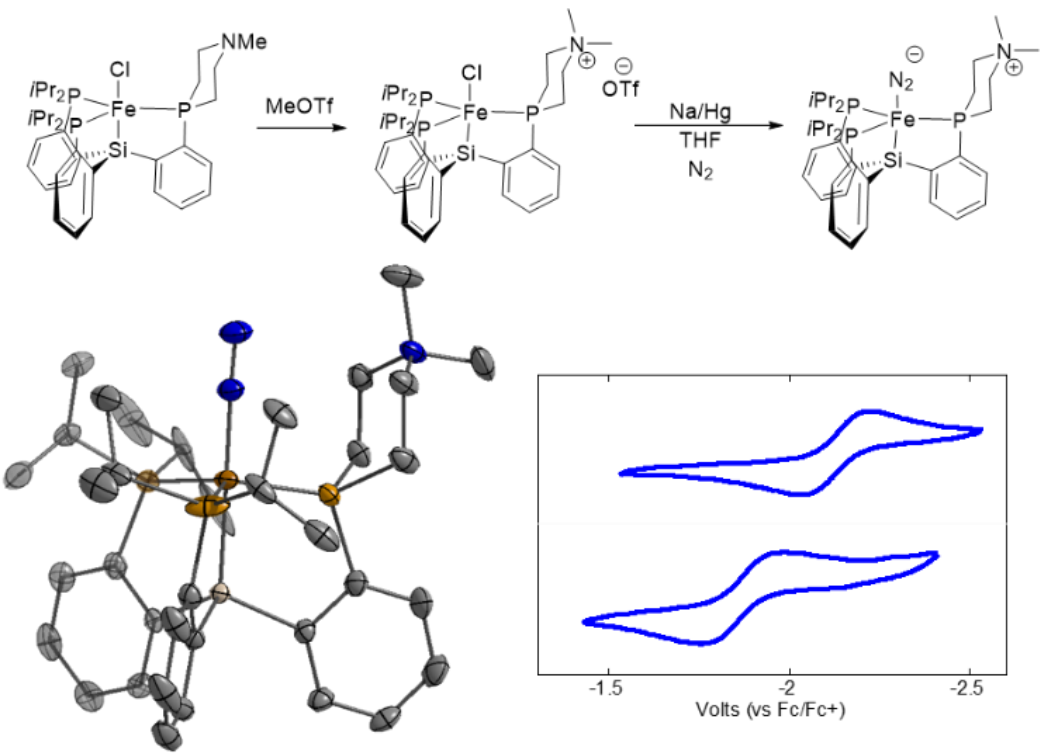

Figure 4.9. Synthesis and characterization of zwitterionic complex **4.7**. Thermal ellipsoids are shown at 50% probability and hydrogen atoms and solvent are omitted for clarity. Cyclic voltammagrams of **4.6** (top) and **4.7** (bottom) show the Fe(0)/Fe(I) couple.

The present ligand platform provides an opportunity for entry into a system where this idea can be explored simply by quaternization of the pendant amine group. This allows for the synthesis of an overall neutral, zwitterionic Fe(0)-N_2 complex (**4.7**) which is isoelectronic to the anionic complexes **4.6** or **4.6**' or parent anion $[(SiP^{iPr}_3)FeN_2]^-$ (Figure 4.9). As might be expected, the N_2 stretching frequency of **7** (1917 cm^{-1}) is very close to that of the $[(SiP^{iPr}_3)FeN_2][Na(12\text{-crown-}4)_2]$ complex (1920 cm^{-1}) where the sodium countercation is encapsulated by crown ethers and therefore does not interact directly with the dinitrogen ligand. Despite the overall neutral charge of **4.7**, the β nitrogen of the N_2 ligand still bears substantial negative charge, as demonstrated by the calculated Mulliken atomic charges and the electrostatic potential map for this molecule. Based on other systems our group has studied, it seems that a concentration of negative charge at this position is important for facilitating functionalization at this position with electrophilic reagents, including protons.[12,17]

The electrochemical properties of **4.7** illustrate that the incorporation of a positive charge into the ligand does significantly alter the Fe(0)/Fe(I) reduction potential as compared to **4.6** – from -2.2 V (vs Fc/Fc^+) for the Fe(0)/Fe(I) couple of **4.6** to -1.9 V for **4.7**. This is a significant shift which may allow more facile access to the Fe(0) state required in order to effect functionalization—while a strong reductant such as sodium amalgam is required to access **4.6**, **4.7** should be accessible using milder reagents.

Since a pendant Lewis basic site is no longer present, the reactivity of **4.7** is more similar to that of $[(SiP^{iPr}_3)FeN_2]^-$ than to **4.6** or **4.6'**. Treatment of **4.7** at -78 °C with one equivalent of $HBAr^F_4{\cdot}2Et_2O$ results in clean oxidation to a cationic Fe(I) complex, $[(SiP^{iPr}_2P^{NMe2})FeN_2]BAr^F_4$, rather than formation of a metal hydride as in the case of **4.6** and **4.6'**. As in the case of $[(SiP^{iPr}_3)FeN_2]^-$, significant but substoichiometric amounts of ammonia (~0.5 equiv.) are generated when **4.7** is subjected to standard catalytic conditions with KC_8 and $HBAr^F_4{\cdot}2Et_2O$ in the presence of N_2.

These results illustrate a promising strategy for substantially improving the redox properties of an N_2 fixation system without significantly compromising either its ability to activate N_2 (as judged by the vibrational frequency of coordinated N_2) or its reactivity towards ammonia production.

4.2.6 Synthesis of a boratrane ligand variant

Scheme 4.5. Synthesis of tris(phosphine) borane ligands with three (a) or one (b) pendant amines.

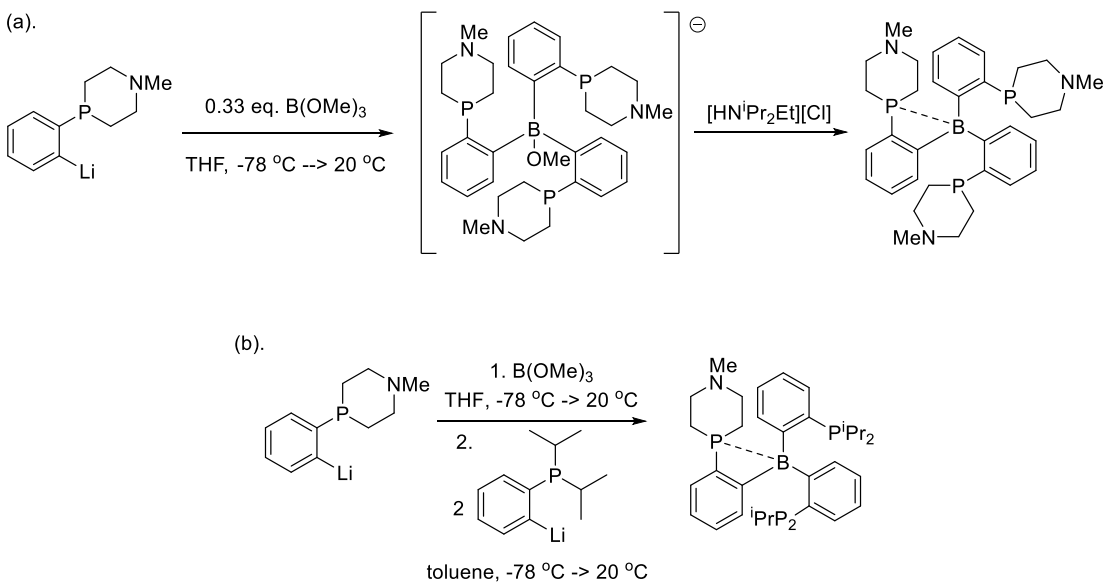

While the silane-anchored ligands **L**$_1$ and **L**$_2$ were initially targeted in part due to the relative facility of their synthesis, we are also interested in pursuing borane-anchored ligands with pendant amine groups (analogous to the tris(phosphine)borane, TP$^{i\text{Pr}}$B), as iron complexes on such a scaffold would provide a more direct comparison to the best known molecular iron catalyst for N_2 fixation, [(TP$^{i\text{Pr}}$B)FeN$_2$]$^-$, and may facilitate different reactivity. While work on this scaffold is still in its early stages, we have successfully assembled both symmetric and unsymmetric boratrane ligand variants with either three or one pendant amines, respectively (Scheme 4.5) through the use of B(OMe)$_3$ as the borane source, rather than the more Lewis acidic BCl_3 or $BF_3{\cdot}Et_2O$, which resulted in decomposition of the ligand precursors. Metallation of these scaffolds has been achieved, as illustrated by the crystallographically characterized (TP$^{\text{NMe}}$B)FeBr complex (Figure 4.10).

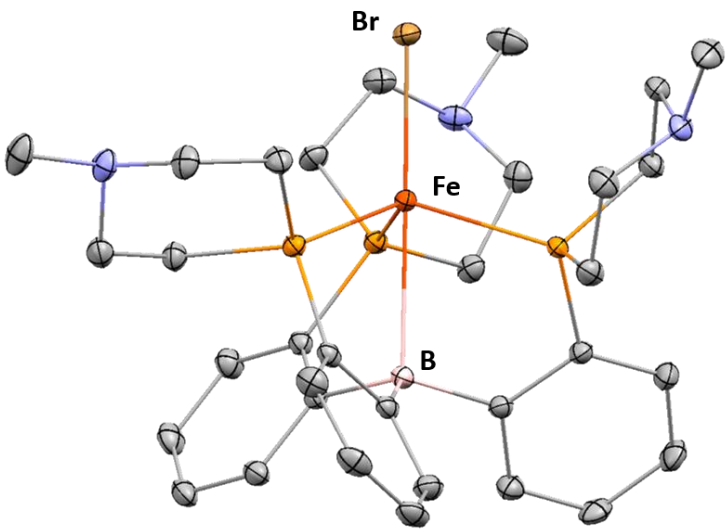

Figure 4.10. Crystal structure of (TP$^{\text{NMe}}$B)FeBr, with thermal ellipsoids at 50% probability. Hydrogen atoms and solvent omitted for clarity.

4.3 Conclusions

We have demonstrated the incorporation of secondary-sphere interactions into iron-phosphine scaffolds relevant to synthetic nitrogen fixation. While the incorporation of hydrogen bond acceptors did not improve the properties of these iron complexes as catalysts for N_2 reduction, instead functioning to facilitate the formation of metal hydride species, the presence of modestly strong hydrogen bonds between pendant ligand functionalities and possible N_2 reduction products, ammonia and hydrazine, has been demonstrated. Additionally, the secondary coordination sphere is shown to organise cation binding to an anionic Fe-N_2 complex in such a way as to alter the N_2 coordination geometry; and the incorporation of an intramolecular positive charge in the secondary ligand sphere functions to allow access to an Fe(0)-N_2 complex at substantially less negative potentials. These findings may parallel analogous functions for secondary sphere interactions around the active site of biological metalloenzymes, including the FeMoco cluster of nitrogenase.

4.4 Experimental Methods

4.4.1 General considerations.

All syntheses and measurements, unless otherwise stated, were carried out under an inert atmosphere (N_2) in a glovebox or using standard Schlenk techniques, and solvents were dried and degassed by thoroughly sparging with N_2 and then passing through an activated alumina column in a solvent purification system supplied by SG Water, LLC. Combustion analyses were carried out by Midwest Microlabs (Indianapolis). Non-

halogenated solvents were tested with a standard purple solution of sodium benzophenone ketyl in tetrahydrofuran in order to confirm effective moisture removal. Diethyl (2-bromophenyl)phosphonate,[23] $Fc[BAr^F_4]$ (Ar^F = 3,5-trifluoromethylphenyl),[24] $HBAr^F_4{\cdot}2Et_2O$ (Ar^F = 3,5-bistrifluoromethylphenyl),[25] KC_8,[26] $[(SiP^{iPr}_3)FeN_2][Na(12\text{-crown-}4)_2]$[27], and bis(o-diisopropylphosphino-phenyl)chlorosilane were prepared according to literature procedures. All other reagents were purchased from commercial vendors and used without further purification unless otherwise stated.

4.4.2 Physical methods.

Optical spectroscopy measurements were taken on a Cary 50 UV−vis spectrophotometer using a 1-cm two-window quartz cell. Electrochemical measurements were carried out in a glovebox under a dinitrogen atmosphere in a one compartment cell using a CH Instruments 600B electrochemical analyzer. A glassy carbon electrode was used as the working electrode and a graphite rod was used as the auxiliary electrode. A silver pseudoreference electrode was used. The ferrocene couple Fc+/Fc was used as an internal reference. Solutions (THF) of electrolyte (0.4 M tetra-n-butylammonium hexafluorophosphate) and analyte were also prepared under an inert atmosphere. Fourier transform infrared ATR spectra were collected on a Thermo Scientific Nicolet iS5 Spectrometer with diamond ATR crystal. Solution phase magnetic measurements were performed by the method of Evans.[29] ^1H and ^{13}C chemical shifts are reported in ppm relative to tetramethylsilane, using residual solvent resonances as internal standards. ^{31}P chemical shifts are reported in ppm relative to 85%

aqueous H_3PO_4. X-band EPR spectra were obtained on a Bruker EMX spectrometer; solutions were prepared as frozen glasses in 2-MeTHF.

4.4.3 Synthetic Procedures and Characterization Data

(2-bromophenyl)-divinylphosphine oxide. Diethyl (2-bromophenyl)phosphonate (15.1 g, 0.0515 mol) was transferred to a 1L roundbottom Schlenk flask under N_2 with a large stir bar. TMSBr (17.2 mL, 0.130 mol, neat) was added by syringe at room temperature and the resulting solution was stirred at room temperature for three hours. The reaction was then concentrated *in vacuo* with mild heating (50 ^oC) until a pale yellow oil remained. This oil was redissolved in 80 mL of dry dichloromethane and then 20 drops of dry DMF were added. Oxalyl chloride (17.6 mL, 0.205 mol, neat) was added via syringe; vigorous bubbling was observed and the color of the reaction mixture darkened slightly. This mixture was stirred for one hour at room temperature and then concentrated *in vacuo* with mild heating (50 ^oC). The resulting residue was redissolved in 300 mL of dry, degassed THF and cooled to -78 ^oC. Vinyl magnesium bromide (1.0 M in THF, 102.9 mL, 0.103 mol) was diluted with an additional 150 mL of dry, degassed THF in an addition funnel and added slowly over the course of four hours to the cold reaction mixture. After the addition was completed the reaction mixture, still at -78 ^oC, was stirred for an additional 2 hours. Then the reaction was quenched by swiftly pouring it into a stirring mixture of ~150 mL of HCl and ~300 mL of ice. After reaching room temperature the quenched solution was extracted with dichloromethane (2 x 300 mL). The organic washings were combined and washed with 2 M NaOH and then saturated brine solution. The organic fraction was dried over magnesium sulfate, filtered, and concentrated to give a pale, sometimes cloudy oil (10.6 g, 0.0440 mol,

85%). This material was typically of sufficient purity to be used in the next step without further purification; however, if desired, analytically pure material can be obtained by column chromatography on silica gel (2% MeOH in ethyl acetate). ^{1}H NMR ($CDCl_3$, 300 MHz, 298 K): δ 8.14 (ddd, *J* = 12, 8, 2 Hz, 1H, C*H*$_{Ar}$), 7.63 (ddd, *J* = 8, 4, 1 Hz, 1H, C*H*$_{Ar}$), 7.44 (m, 2H, C*H*$_{Ar}$), 6.83 (ddd, *J* = 27.4, 18.7, 12.6 Hz, 2H, C*H*$_{vinyl}$), 6.31 (m, 4H, C*H*$_{vinyl}$). ^{31}P NMR ($CDCl_3$, 121 MHz, 298 K): δ 17.8 ppm.

4-(2-bromophenyl)-1-methyl-1,4-azaphosphinane-4-oxide. (2-bromophenyl)-divinylphosphine oxide (10.6 g, 0.0440 mol) was transferred (using a small amount of THF) to a 500 mL round bottom flask with a stir bar and 200 mL of water were added. Then 4.0 mL of 40 wt% aqueous solution of methylamine (1.2 equiv) were added. This mixture was refluxed for 4 hours, and then cooled to room temperature and extracted with dichloromethane. The dichloromethane portions were dried over sodium sulfate, filtered, and concentrated to give an off-white solid. This residue was purified by column chromatography on silica gel using 2% NEt_3 in 5:1 DCM:MeOH. The desired product was isolated as a white solid (8.5 g, 0.0295 mmol, 67%). ^{1}H NMR ($CDCl_3$, 400 MHz, 298 K): δ 7.91 (m, 1H, C*H*$_{Ar}$), 7.49 (m, 1H, C*H*$_{Ar}$), 7.33 (t, 1H, C*H*$_{Ar}$), 7.24 (t, 1H, C*H*$_{Ar}$), 2.6-3.0 (m, 6H, azaphosphinane-C*H*$_2$), 2.27 (s, 3H, N-C*H*$_3$), 1.87 (m, 2H, azaphosphinane-C*H*$_2$) ppm. ^{31}P NMR ($CDCl_3$, 161.9 MHz, 298 K): δ 28.6 ppm. ^{13}C NMR ($CDCl_3$, 100.6 MHz, 298 K): δ 135.3 (d, J_{CP} = 7.3 Hz, *C*$_{Ar}$), 134.3 (d, J_{CP} = 7.8 Hz, *C*$_{Ar}$), 133.5 (d, J_{CP} = 2.5 Hz, *C*$_{Ar}$), 131.9 (d, J_{CP} = 94.8 Hz, *C*$_{Ar}$), 127.4 (d, J_{CP} = 9.9 Hz, *C*$_{Ar}$), 124.2 (d, J_{CP} = 6.0 Hz, *C*$_{Ar}$), 51.2 (d, J_{CP} = 7.4 Hz, P-(CH_2CH_2)$_2$NCH_3), 46.3 (s, P-(CH_2CH_2)$_2$N*C*H$_3$), 26.7 (d, J_{CP} = 66.5 Hz, P-(*C*H$_2$CH$_2$)$_2$NCH$_3$) ppm.

4-(2-bromophenyl)-1-methyl-1,4-azaphosphinane (L_0). 4-(2-bromophenyl)-1-methyl-1,4-azaphosphinane-4-oxide (2.16 g, 7.50 mmol) was dissolved in 80 mL of dry, degassed DCM to give a clear, homogeneous solution. Then neat oxalyl chloride (629 μL, 1.0 equiv) was added by syringe in one portion. Over the next few minutes an off-white precipitate developed and the solution color changed to pale yellow. This reaction mixture was stirred for one hour and then concentrated to dryness *in vacuo*. Then, 80 mL of dry, degassed THF was added; the resulting suspension was stirred vigorously and cooled to -78° C. Lithium aluminum hydride (1.0 M solution in THF, 7.56 mL, 1.0 equiv) was added *via* syringe over 5 minutes. Bubbling was observed. After 30 minutes the reaction was transferred to a 0 °C bath and stirred for an additional one hour, at which point the solution is pale yellow and homogeneous. The reaction is allowed to warm to room temperature for one hour, and then quenched with 3 mL of degassed ethyl acetate; a precipitate slowly develops. After about 20 minutes the volume is reduced *in vacuo* to 20 mL. Under continued anaerobic conditions, this mixture is diluted with 200 mL of DCM and washed with 100 mL of 1.0 M aqueous NaOH. The organic fraction is dried over sodium sulfate, filtered, and concentrated to a pale orange, cloudy oil. This is extracted into pentane (2 x 30 mL) and filtered through Celite, removing some orange and white solids. The filtrate is concentrated to a white powder (1.72 g, 6.32 mmol, 84%). The material thus obtained is typically spectroscopically pure and is used in subsequent steps without additional purification, but can be further recrystallized from cold pentane if needed. ^{1}H NMR (C_6D_6, 400 MHz, 298 K): δ 7.34 (dd, J = 8.0, 3.0 Hz, 1H, CH_{Ar}), 7.06 (d, J = 8 Hz, 1H, CH_{Ar}), 6.92 (t, J = 8 Hz, 1H, CH_{Ar}), 6.70 (t, J = 7.6 Hz, 1H, CH_{Ar}), 2.63 (m, 2H, azaphosphinane-

C*H*$_2$), 2.33 (m, 2H, azaphosphinane-C*H*$_2$), 2.035 (s, 3H, N-C*H*$_3$), 2.00 (m, 4H, azaphosphinane-C*H*$_2$) ppm. ^{31}P NMR (C_6D_6, , 161.9 MHz, 298 K): δ -41.2 ppm. ^{13}C NMR (C_6D_6, 100.6 MHz, 298 K): δ 140.7 (d, J_{CP} = 22.7 Hz, C_{Ar}), 132.9 (s, C_{Ar}), 131.4 (s, C_{Ar}), 129.0 (s, C_{Ar}), 128.9 (d, J_{CP} = 26.2 Hz, C_{Ar}), 126.948 (s, C_{Ar}), 53.5 (s, P-(CH_2CH_2)$_2$NCH$_3$), 46.6 (s, P-(CH_2CH_2)$_2$N*C*H$_3$), 23.7 (d, J_{CP} = 12.5 Hz, P-(*C*H_2CH_2)$_2$NCH$_3$) ppm.

HSiP$_2^{iPr}$P^{NMe} (L$_1$). 4-(2-bromophenyl)-1-methyl-1,4-azaphosphinane (1.511 g, 5.56 mmol) was dissolved in THF (20 mL) and cooled to -78 ºC. *t*BuLi (1.7 M in pentane, 6.527 mL, 11.12 mmol) was added over 5 minutes and the resulting mixture was stirred at low temperature for 1.5 hours. Bis(2-diisopropylphosphinophenyl)chlorosilane (2.505 g, 5.56 mmol) was added over five minutes as a solution in THF (10 mL). This reaction mixture was allowed to stir overnight while slowly warming to room temperature. The resulting yellow-orange solution was concentrated to dryness, extracted with benzene, and filtered through Celite. The filtrate was concentrated to give a white powder which was washed with pentane, giving 2.61 g of the desired product (4.29 mmol, 77%). ^{1}H NMR (C_6D_6, 300 MHz, 298 K): δ 7.60 (m, 1H, C*H*$_{Ar}$), 7.38 (m, 6H, C*H*$_{Ar}$), 7.18 (m, 2H, C*H*$_{Ar}$), 7.02 (t, *J* = 7 Hz, 3H, C*H*$_{Ar}$), 2.74 (m, 2H, azaphosphine-C*H*$_2$), 1.9-2.3 (m, 11H, -NC*H*$_3$, azaphosphine-C*H*$_2$, and –C*H*$(CH_3)_2$), 1.82 (m, 2H, azaphosphine-C*H*$_2$), 1.16 (m, 12H, -CH(C*H*$_3)_2$), 0.97 (m, 12H, -CH$(CH_3)_2$) ppm. ^{13}C NMR (C_6D_6, 100.6 MHz, 298 K): δ 146.3 (d, J_{CP} = 52 Hz), 144.54 (d, J_{CP} = 17 Hz), 143.9 (d, J_{CP} = 42 Hz), 138.7 (d, J_{CP} = 13 Hz), 138.4 (d, J_{CP} = 14 Hz), 132.2 (s), 130.5 (s), 129.6 (s), 128.9 (s), 54.9 (s), 47.0 (s), 25.5 (m), 20.7 (d, J_{CP} = 17 Hz), 20.3 (m) ppm. NMR (C_6D_6, 121 MHz, 298 K): δ 0.8 (s, 2P), -48.4 (s, 1P) ppm.

$HSiP_3^{NMe}$ (L_2). 4-(2-bromophenyl)-1-methyl-1,4-azaphosphinane (3.13 g, 11.5 mmol) was dissolved in THF (20 mL) and cooled to -78 °C. *t*BuLi (1.7 M in pentane, 13.53 mL, 23.0 mmol) was added over 5 minutes and the resulting mixture was stirred at low temperature for 1.5 hours. Trichlorosilane (380 µL, 3.76 mmol) was added in one neat portion. This reaction mixture was allowed to stir overnight while slowly warming to room temperature. The resulting yellow-orange solution was concentrated to dryness, extracted with benzene, and filtered through Celite. The filtrate was concentrated to give a white powder which was washed with pentane, giving 2.19 g of the desired product (3.61 mmol, 94%). ^{1}H NMR (C_6D_6, 300 MHz, 298 K): δ 7.65 (dd, *J* = 7.4, 3.3 Hz, 3H, C*H*$_{Ar}$), 7.44 (t, *J* = 6.2 Hz, 3H, C*H*$_{Ar}$), 7.22 – 7.12 (m, 3H, C*H*$_{Ar}$), 7.02 (t, *J* = 7.4 Hz, 3H, C*H*$_{Ar}$), 2.85 – 2.61 (m, 6H, azaphosphine-C*H*$_2$), 2.24 – 2.06 (m, 12H, azaphosphine-C*H*$_2$), 2.01 (s, 9H, -NC*H*$_3$), 1.73 (t, *J* = 12.1 Hz, 6H, azaphosphine-C*H*$_2$) ppm. ^{31}P NMR (C_6D_6, 121 MHz, 298 K): δ -49.4 (s) ppm. ^{13}C NMR (C_6D_6, 100.6 MHz, 298 K): δ 146.3 (d, J_{CP} = 16.8 Hz, C_{Ar}), 137.8 (d, J_{CP} = 13.6 Hz, C_{Ar}), 130.5 (s, C_{Ar}), 129.4 (s, C_{Ar}), 128.2 (C_{Ar}), 54.4 (s, P-(CH_2CH_2)$_2$NCH$_3$), 46.7 (s, P-(CH_2CH_2)$_2$NCH$_3$), 25.4 (d, J_{CP} = 11.6 Hz, P-(CH_2CH_2)$_2$NCH$_3$) ppm.

($SiP^{iPr}_2P^{NMe}$)FeCl (4.1). $HSiP_2^{iPr}P^{NMe}$ (2.61 g, 4.29 mmol) was combined with $FeCl_2$ (1.10 g, 8.68 mmol) in 50 mL of THF and vigorously stirred overnight to give a homogeneous yellow solution. This reaction mixture was cooled to -78 °C, and MeMgBr (2.86 mL, 3.0 M in THF, 8.58 mmol) was diluted with 18 mL of THF and added dropwise over 20 minutes to the reaction mixture. The reaction was allowed to warm slowly overnight with stirring. To the resulting dark brown reaction mixture was added dioxane (20 mL) and pentane (20 mL) and the mixture was stirred for an hour at

room temperature and then filtered through Celite. The bright orange-yellow filtrate was concentrated to dryness, extracted with benzene, and filtered again. This was concentrated to give a yellow-orange solid which was washed with pentane to give **4.1** (2.57 g, 3.68 mmol, 85%). ^{1}H NMR (C_6D_6, 300 MHz, 298 K): δ 127.9, 80.1, 55.0, 26.7, 13.1, 10.9, 6.6, 6.3, 5.7, 5.3, 5.0, 2.9, 3.0, -1.4, -2.6 ppm. μ_{eff} (Evans Method, C_6D_6, 298 K): 3.0 μ_β. Anal. Calcd. for $C_{35}H_{51}ClFeNP_3Si$: C, 60.22; H, 7.36; N, 2.01. Found: C, 59.92; H, 7.27; N, 2.11.

(SiP$^{NMe}_3$)FeCl (4.1'). $HSiP_3^{NMe}$ (2.19 g, 3.62 mmol) was combined with $FeCl_2$ (917 mg, 7.23 mmol) in 50 mL of THF and vigorously stirred overnight to give a homogeneous yellow solution. This reaction mixture was cooled to -78 ^{o}C, and MeMgBr (2.41 mL, 3.0 M in THF, 7.23 mmol) was diluted with 18 mL of THF and added dropwise over 20 minutes to the reaction mixture. The reaction was allowed to warm slowly overnight with stirring. To the resulting dark brown reaction mixture was added dioxane (20 mL) and pentane (20 mL) and the mixture was stirred for an hour at room temperature and then filtered through Celite. The bright orange-yellow filtrate was concentrated to dryness, extracted with benzene, and filtered again. This was concentrated to give a yellow-orange solid which was washed with pentane to give **4.1'** (0.910 g, 1.31 mmol, 36%). Crystals suitable for X-ray diffraction were grown by vapor diffusion of pentane into a concentrated benzene solution. ^{1}H NMR (C_6D_6, 300 MHz, 298 K): δ 158, 33.9, 17.1, 10.6, 5.9, 5.3, 2.6, -1.1 ppm. μ_{eff} (Evans Method, C_6D_6, 298 K): 3.0 μ_β. Anal. Calcd. for $C_{33}H_{45}ClFeN_3P_3Si$: C, 56.95; H, 6.52; N, 6.04. Found: C, 56.28; H, 6.43; N, 5.76.

($SiP^{iPr}_2P^{NMe}$)FeN_2 (4.2). (SiP_2P^{NMe})FeCl (245 mg, 0.351 mmol) was dissolved in THF (10 mL) and stirred over 1% sodium-mercury amalgam (9.7 mg Na, 0.422 mmol, 1.2 equiv.) for three hours. The reaction mixture was concentrated to dryness, extracted into benzene, filtered through Celite, and concentrated to dryness. The residue was taken up in pentane and again filtered through Celite, then concentrated to give an orange powder which was recrystallized from cold pentane to give an orange microcrystalline solid which was washed with cold pentane (141 mg, 0.204 mmol, 58%). ^{1}H NMR (C_6D_6, 300 MHz, 298 K): δ 69.1, 26.9, 19.3, 8.3, 8.0, 6.4, 5.9, 4.7, 3.9, 3.2, 2.4, 1.8, -2.1, -13.9 ppm. μ_{eff} (Evans Method, C_6D_6, 298 K): 2.1 μ_β. IR (thin film deposited from C_6D_6): 2005 cm^{-1} (ν(N-N)). We were unable to obtain satisfactory EA after several attempts, likely due to some lability of the coordinated N_2 ligand.

(SiP^{NMe}_3)FeN_2 (4.2'). (SiP^{NMe}_3)FeCl (500 mg, 0.716 mmol) was dissolved in THF (10 mL) and stirred over 1% sodium-mercury amalgam (18.2 mg Na, 0.791 mmol, 1.1 equiv.) for three hours. The reaction mixture was concentrated to dryness, extracted into benzene, filtered through Celite, and concentrated to dryness. The residue was taken up in 1:1 benzene:pentane and again filtered through Celite, then concentrated to give a yellow-orange powder which was washed with pentane to give spectroscopically clean product (245 mg, 50%). Single crystals suitable for X-ray diffraction were grown by cooling a concentrated Et_2O solution in a -35 ^oC freezer overnight. ^{1}H NMR (C_6D_6, 300 MHz, 298 K): δ 85.1, 19.9, 10.6, 8.31, 7.20, 6.95, 6.38, 5.58, 3.03 ppm. μ_{eff} (Evans Method, C_6D_6, 298 K): 2.1 μ_β. IR (thin film deposited from C_6D_6): 2007 cm^{-1} (ν(N-N)). We were unable to obtain satisfactory EA after several attempts, likely due to some lability of the coordinated N_2 ligand.

[(SiP$^{iPr}_2$P^{NMe})FeNH$_3$][BAr$^F_4$] (4.3). (SiP$^{iPr}_2$P^{NMe})FeN$_2$ (100 mg, 0.145 mmol) was dissolved in THF (5 mL) and a solution of [Fc][BAr$^F_4$] (144 mg, 0.95 equiv) in THF (5 mL) was added. The orange solution darkened to brown and the reaction mixture was allowed to stir at room temperature for one hour before being transferred to a Schlenk tube and degassed by briefly exposing to dynamic vacuum. This solution was exposed at room temperature to 1 atm of NH_3 (which had been dried by stirring over sodium at -78 ^oC). The color changed from brown to bright orange. The reaction mixture was concentrated to dryness and the orange residue was extracted with ether and filtered through Celite. The ether solution was concentrated to 3 mL, layered with pentane, and allowed to stand overnight, resulting in the formation of orange crystals which were thoroughly washed with pentane (162 mg, 70%). Crystals suitable for X-ray analysis were grown by vapor diffusion of pentane into an ether solution. ^{1}H NMR (5:1 C_6D_6:d_8-THF, 300 MHz, 298 K): δ 91.2, 59.9, 46.0, 29.0, 10.34, 8.32 (BAr$^F_4$), 7.70 (BAr$^F_4$), 5.89, 5.59, 5.28, 3.79, -0.35, -2.72, -3.28 ppm. ^{19}F NMR (5:1 C_6D_6:d_8-THF, 282 MHz, 298 K): δ -62 ppm. μ_{eff} (Evans Method, 4:1 C_6D_6:d_8THF, 298 K): 3.3 μ_β. Anal. Calcd. for $C_{67}H_{66}BF_{24}FeN_2P_3Si{\cdot}Et_2O$: C, 52.74; H, 4.74; N, 1.73. Found: C, 52.64; H, 4.54; N, 1.42.

[(SiP$^{NMe}_3$)FeNH$_3$][BAr$^F_4$] (4.3'). (a) (SiP$^{NMe}_3$)FeN$_2$ (42 mg, 0.061 mmol) was dissolved in THF (5 mL) and a solution of [Fc][BAr$^F_4$] (61 mg, 0.95 equiv) in THF (5 mL) was added. The orange solution darkened to brown and the reaction mixture was allowed to stir at room temperature for one hour before being transferred to a Schlenk tube and degassed by briefly exposing to dynamic vacuum. This solution was exposed at room temperature to 1 atm of NH_3 (which had been dried by stirring over sodium at

-78 °C). The color changed from brown to bright orange. The reaction mixture was concentrated to dryness and the orange residue was extracted with ether and filtered through Celite. The ether solution was concentrated to 3 mL, layered with pentane, and allowed to stand overnight, resulting in the formation of orange crystals which were thoroughly washed with pentane (69 mg, 73%). (b) (SiP^{NMe}_3)FeN_2 (45 mg, 0.065 mmol) was dissolved in THF (5 mL) and a solution of $FcBAr^F_4$ (62 mg, 0.9 equiv) in THF (5 mL) was added. The orange solution darkened to brown and the reaction mixture was allowed to stir at room temperature for two hours before being cooled to -78 °C; excess hydrazine (100 μL) was then added. The reaction was allowed to warm to room temperature for 10 minutes during which time it turned bright orange; it was then concentrated *in vacuo*, extracted with Et_2O, filtered through Celite, and concentrated down to 2 mL of a bright orange Et_2O solution. This solution was layered with pentane and stored at -35 °C overnight, resulting in the formation of feathery orange crystals; the supernatant was decanted and the crystals were washed with pentane and dried to give the desired product as an orange crystalline solid (37 mg, 41%). Crystals suitable for X-ray analysis were grown by vapor diffusion of pentane into an ether solution. ^{1}H NMR (5:1 C_6D_6:d_8-THF, 300 MHz, 298 K): δ 122 (v.b.), 41 (v.b.), 13.1, 8.37 (BAr^F_4), 7.74 (BAr^F_4), 5.69, 4.54, 3.46, -0.68, -1.78 ppm. ^{19}F NMR (5:1 C_6D_6:d_8-THF, 282 MHz, 298 K): δ -62 ppm. μ_{eff} (Evans Method, 4:1 C_6D_6:d_8THF, 298 K): 3.2 μ_β. Anal. Calcd. for $C_{65}H_{66}BF_{24}FeN_4P_3Si$: C, 50.67; H, 3.93; N, 3.64. Found: C, 50.11; H, 3.86; N, 3.40.

[($SiP^{iPr}_2P^{NMe}$)FeN_2H_4][BAr^F_4] (4.4). [Fc][BAr^F_4] was added to ($SiP^{iPr}_2P^{NMe}$)FeN_2 (130 mg, 0.188 mmol) in THF (10 mL) and the resulting brown-orange solution was stirred

at room temperature for 2 hours before cooling to -78 °C. Excess neat hydrazine (100 μL) was added and then the solution was allowed to warm to room temperature while stirring for 30 minutes then concentrated *in vacuo*. The orange residue was taken up in Et_2O (5 mL) and filtered through Celite, and then layered with pentane (10 mL) and allowed to stand overnight. The resulting dark red crystals were washed copiously with pentane and then dried *in vacuo* to give the desired product (200 mg, 68%). ^{1}H NMR (4:1 C_6D_6:d_8THF, 300 MHz, 298 K): δ 46.8, 36.8, 34.6, 4.7, 11.6, 8.23, 7.62, 6.24, 5.84, 5.39, 2.97, 1.91, -2.4 (br), -2.94, -3.39, -3.92 ppm. ^{19}F NMR (4:1 C_6D_6:d_8THF, 282 MHz, 298 K): δ -62 ppm. μ_{eff} (Evans Method, 4:1 C_6D_6:d_8THF, 298 K): 3.3 μ_β. Anal. Calcd. for $C_{67}H_{67}BF_{24}FeN_3P_3Si{\cdot}2Et_2O$: C, 52.80; H, 5.14; N, 2.46. Found: C, 53.37; H, 4.53; N, 2.09.

[(SiP$^{iPr}_2$P^{NMe})FeN$_2$][Na(THF)$_2$] (4.6). (SiP$^{iPr}_2$P^{NMe})FeCl (214 mg, 0.307 mmol) was dissolved in THF (10 mL) and stirred over an excess of sodium amalgam (37 mg Na, 1 wt% in Hg) overnight. The dark red solution was then decanted from the excess mercury, dried *in vacuo*, extracted with Et_2O, filtered through Celite, and again dried *in vacuo* to give a dark red residue. This residue was taken up in 2:1 Et_2O:THF, layered with pentane, and allowed to stand overnight to give dark crystals of the desired product (115 mg, 44%). Single crystals suitable for X-ray diffraction were grown by vapor diffusion of pentane into a concentrated 2:1 Et_2O:THF solution. ^{1}H NMR (d_8-THF, 300 MHz, 298 K): δ 7.95 (m, 3H, C*H*$_{Ar}$), 7.51 (m, 1H, C*H*$_{Ar}$), 7.20 (m, 2H, C*H*$_{Ar}$), 6.93-6.80 (m, 6H, C*H*$_{Ar}$), 3.25 (m, 2H, azaphosphine-C*H*$_2$), 2.78 (m, 4H, -C*H*(CH$_3$)$_2$), 2.32 (m, 7H, -NC*H*$_3$ and azaphosphine-C*H*$_2$), 1.07 (m, 18H, -CH(C*H*$_3$)$_2$), 0.63 (m, 6H, -CH(C*H*$_3$)$_2$) ppm. ^{31}P NMR (d_8-THF, 121 MHz, 298 K): δ 92 (br s, 2P, -P^{iPr2}), 37 (br s,

1P, -P(CH_2CH_2)$_2$NMe) ppm. IR: solid powder on ATR, 1874 cm^{-1} (ν(N-N)); thin film deposited from THF, 1880 cm^{-1} (ν(N-N)): . Anal. Calcd. for $C_{43}H_{65}FeN_3NaO_2P_3Si$: C, 60.35; H, 7.66; N, 4.91. Found: C, 60.30; H, 7.69; N, 5.00.

[(SiP$^{NMe}_3$)FeN$_2$][Na(THF)$_3$] (4.6'). (SiP$^{NMe}_3$)FeCl (203 mg, 0.292 mmol) was dissolved in THF (10 ml) and stirred vigorously over an excess of sodium amalgam (30 mg Na in 4.0 g Hg) overnight. The dark red reaction mixture was then filtered through Celite and concentrated to a volume of 2 mL. This was layered with 5 mL of Et_2O and 10 mL of pentane and allowed to stand overnight to allow the formation of dark crystalline solids. The supernatant was decanted and the crystals were washed with pentane, benzene, and additional pentane and then dried *in vacuo* to give the desired product (175 mg, 65%). ^{1}H NMR (d_8-THF, 400 MHz, 298 K): δ 8.083 (d, 3H, *J* = 7 Hz, C*H*$_{Ar}$), 7.52 (d, 3H, *J* = 7 Hz, C*H*$_{Ar}$), 7.03 (t, 3H, *J* = 7 Hz, C*H*$_{Ar}$), 6.94 (t, 3H, *J* = 7 Hz, C*H*$_{Ar}$), 3.46 (m, 6H, azaphosphine-C*H*$_2$), 2.91 (m, 6H, -C*H*(CH_3)$_2$), 2.38 (s, 9H, -NC*H*$_3$) ppm. ^{31}P NMR (d_8-THF, 161 MHz, 298 K): δ 44 (br s) ppm. IR: solid powder on ATR, 1878 cm^{-1} (ν(N-N)); thin film deposited from THF, 1870 cm^{-1} (ν(N-N)). Anal. Calcd. for $C_{45}H_{66}FeN_5NaO_3P_3Si$: C, 58.44; H, 7.19; N, 7.57. Found: C, 57.79; H, 6.96; N, 7.42.

(SiP$^{iPr}_2$P^{NMe})FeNH$_2$ (4.5). (SiP$^{iPr}_2$P^{NMe})FeCl (148 mg, 0.217 mmol) was dissolved in THF (5 mL) in a Schlenk bomb and excess sodium amide (65 mg) was added. The reaction mixture was frozen at 77 K and the headspace was evacuated. Liquid ammonia (~2 mL), which had been previously dried by stirring over excess sodium metal, was condensed onto the reaction mixture which was then thawed to give a homogeneous

yellow-orange mixture which was stirred at -20 °C for one hour until the color darkened to red-orange. The solvent was then removed *in vacuo* and the residue was extracted with pentane and filtered through Celite. The red-orange residue was recrystallized by slow evaporation of pentane, and the resulting red crystals were washed with cold pentane to give the desired product (110 mg, 0.162 mmol, 75%). ^{1}H NMR (C_6D_6, 300 MHz, 298 K): δ 134.6, 87.8, 70.2, 27.8, 8.72, 7.05, 6.46, 6.19, 4.88, 4.24, 2.04, 1.88, 0.54, -0.46, -2.5 ppm. μ_{eff} (Evans Method, C_6D_6, 298 K): 3.1μ_β. The identity of the $-NH_2$ ligand was further confirmed by treating an Et_2O solution of the product with excess HCl in Et_2O and then subjecting the resulting solution to a standard workup and indophenol test for ammonia (see below). Quantitative ammonia (1.0 equiv.) was detected.

[(SiP$^{i\mathrm{Pr}}_2$P$^{\mathrm{NMe2}}$)FeCl][OTf]. (SiP$_2$P$^{\mathrm{NMe}}$)FeCl (168 mg, 0.246 mmol) was dissolved in THF (5 mL) and cooled to -78 °C; MeOTf (30 μL, 1.1 eq) was added and the reaction mixture was allowed to warm to room temperature. After stirring for one hour the reaction mixture was concentrated to dryness and the resulting yellow residue was washed with Et_2O and dried *in vacuo*, giving the product as a yellow powder (156 mg, 0.184 mmol, 64%). This material was used for subsequent reactions without further purification. ^{1}H NMR (C_6D_6, 300 MHz, 298 K): δ 73.1, 64.7, 56.7, 31.9, 6.1, 5.9, 2.1, 1.7, -1.0, -1.4, -2.8 ppm. ESI/MS: 712.2 amu ([(SiP$^{i\mathrm{Pr}}_2$P$^{\mathrm{NMe2}}$)FeCl]$^+$).

(SiP$^{i\mathrm{Pr}}_2$P$^{\mathrm{NMe2}}$)FeN$_2$ (4.7). [(SiP$^{i\mathrm{Pr}}_2$P$^{\mathrm{NMe2}}$)FeCl][OTf] (103 mg, 0.119 mmol) was dissolved in THF and stirred over excess sodium amalgam overnight, resulting in a color change to deep red. The solution as decanted from the remaining mercury,

concentrated to dryness, extracted with benzene, and filtered through Celite. The product was recrystallized by layering a concentrated benzene solution with pentane and allowing it to stand overnight. The resulting dark red crystals were washed with pentane and dried *in vacuo* to give the desired product (60 mg, 71%). ^{31}P NMR (C_6D_6, 121 MHz, 298 K): δ 94.3 (d, J = 76 Hz, 2P, -P^{iPr2}), 33.4 (t, J = 76 Hz, 1P, -P(CH_2CH_2)$_2$NMe) ppm. IR (thin film deposited from benzene): 1917 cm^{-1} (ν(N-N)).

4.4.4 Reactivity studies

Ammonia quantification. Reaction mixtures were analyzed for the presence of ammonia according to the following procedure. Upon completion of the reaction, volatiles were vac-transferred onto an ethereal solution of HCl (4 mL, 2 M). The solid residue was treated with a solution of KO^{t}Bu in THF and again vac transferred onto the HCl solution. The resulting ammonium chloride was analyzed by the indophenol method as previously reported.[30,12a]

Representative procedure for ammonia generation: attempted NH_3 production from [(SiP$_2$P^{NMe})FeN$_2$][Na(THF)$_2$] (4.6). [(SiP$_2$P^{NMe})FeN$_2$][Na(THF)$_2$] (1.6 mg, 0.0019 mmol) was dissolved in Et_2O (1 mL) and cooled to -78 ^{o}C. Similarly cooled solutions of KC_8 (15 mg, 55 eq, in 1 mL Et_2O) and $HBAr_4^F$.2Et_2O (93 mg, 46 eq, in 1 mL Et_2O) were added rapidly and sequentially. The resulting reaction mixture was allowed to stir at low temperature for 2 hours before being allowed to warm to room temperature for one hour. The reaction mixture was then analyzed for ammonia production; no detectable ammonia was present.

Representative procedures for protonation: Stoichiometric protonation of [(SiP$^{iPr}_2$P^{NMe})FeN$_2$][Na(THF)$_2$] (4.6). (a) [(SiP$^{iPr}_2$P^{NMe})FeN$_2$][Na(THF)$_2$] (54 mg, 0.063 mmol) was dissolved in Et$_2$O (2 mL) and cooled to -78 ^{o}C. A similarly cooled solution of HBAr$_4^F$.2Et$_2$O (63 mg, 0.062 mmol) in 2 mL Et$_2$O was added in one portion with stirring, resulting in an immediate color change to yellow. The reaction was stirred at room temperature for 30 minutes and then allowed to warm to room temperature for one hour before concentrating to dryness. The resulting yellow residue was analyzed by NMR, which was consistent with formation of an iron hydride ((SiP$^{iPr}_2$P^{NMe})Fe(N$_2$)(H)) as the main product. The NMR analysis demonstrates the *trans* disposition of the hydride ligand relative to the amine-bearing ligand arm, which is further confirmed crystallographically. X-ray quality crystals were grown by slow evaporation of a concentrated pentane solution of the crude reaction product. (b) [(SiP$^{iPr}_2$P^{NMe})FeN$_2$][Na(THF)$_2$] (10 mg, 0.012 mmol) was dissolved in Et$_2$O (2 mL) and cooled to -78 ^{o}C. A similarly cooled solution of [HNEt^{i}Pr$_2$][BAr$_4^F$] (12.8 mg, 0.012 mmol) in 2 mL Et$_2$O was added in one portion with stirring, resulting in an immediate color change to yellow. The reaction was stirred at room temperature for 30 minutes and then allowed to warm to room temperature for one hour before concentrating to dryness. The resulting yellow residue was analyzed by NMR, which was again consistent with formation of an iron hydride ((SiP$^{iPr}_2$P^{NMe})Fe(N$_2$)(H)) as the main product.

4.5 References

1. (a) A. S. Borovik. *Acc. Chem. Res.*, **2005**, *38*, 54. (b) D. Natale and J. C. Mareque-Rivas. *Chem. Comm.*, 2008, 425. (c) R. L. Shook and A. S. Borovik. *Chem.*

Comm., **2008**, 6095. (d) R. L. Shook and A. S. Borovik. *Inorg. Chem.*, **2010**, *49*, 3646.

2. (a) R. H. Holm, P. Kennepohl and E. I. Solomon. *Chem. Rev.*, **1996**, *96*, 3523. (b) Y. Lu and J. S. Valentine. *Curr. Opin. Struct. Biol.*, **1997**, *7*, 495.
3. Selected examples: (a) A. Dutta, J. A. S. Roberts and W. J. Shaw. *Angew. Chem. Int. Ed.*, **2014**, *53*, 6487. (b) R. M. Henry, R. K. Shoemaker, D. L. Dubois and M. Rakowski DuBois. *J. Am. Chem. Soc.*, **2006**, *128*, 3002. (c) C. E. Macbeth, A. P. Golombek, V. G. Young, C. Yang, K. Kuczera, M. P. Hendrich, A. S. Borovik. *Science*, **2000,** *289*, 938. (d) C. E. MacBeth, R. Gupta, K. Mitchell-Koch, V. G. Young, G. Lushington, W. H. Thompson, M. P. Hendrich, A. S. Borovik. *J. Am. Chem. Soc.*, **2004**, *126*, 2556. (e) R. L. Lucas, D. R. Powell, A. S. Borovik. *J. Am. Chem. Soc.*, **2005**, *127*, 11596. (f) D. C. Lacy, R. Gupta, K. L. Stone, J. Greaves, J. W. Ziller, M. P. Hendrich, A. S. Borovik. *J. Am. Chem. Soc.*, **2010**, *132*, 12188. (g) C. T. Carver, B. D. Matson and J. M. Mayer. *J. Am. Chem. Soc.*, **2012**, *134*, 5444. (h) C. Costentin, S. Drouet, M. Robert and J.-M. Saveant. *Science*, **2012**, *388*, 90.
4. (a) B. M. Hoffman, D. R. Dean and L. C. Seefeldt. *Acc. Chem. Res.*, **2009**, *42*, 609. (b) B. M. Hoffman, D. Lukoyanov, D. R. Dean and L. C. Seefeldt. *Acc. Chem. Res.*, **2013**, *46*, 587.
5. (a) B. M. Barney, R. Y. Igarashi, P. C. Dos Santos, D. R. Dean and L. C. Seefeldt. *J. Biol. Chem.*, **2004**, *279*, 53621. (b) L. C. Seefeldt, I. G. Dance and D. R. Dean. *Biochemistry*, **2004**, *43*, 1401.
6. J. B. Howard and D. C. Rees. *Proc. Natl. Acad. Sci.*, **2006**, *103*, 17088.
7. I. Dance. *Dalton Trans.*, **2012**, *41*, 7647.

8. C.-H. Kim, W. E. Newton and D. R. Dean. *Biochemistry*, **1995**, *34*, 2798.

9. T. Spatal, K. A. Perez, O. Einsle, J. B. Howard and D. C. Rees. *Science*, **2014**, *345*, 1620.

10. (a) Labios, L. A., Heiden, Z.M. and Mock, M. T. *Inorg. Chem.* **2015**, *54*, 4409. (b) C. J. Weiss, J. D. Egbert, S. Chen, M. L. Helm, R. M. Bullock and M. T. Mock. *Organometallics*, **2014**, *33*, 2189.

11. (a) D. V. Yandulov and R. R. Schrock. *Science*, **2003**, *301*, 76. (b) K. Arashiba, Y. Miyake and Y. Nishibayashi. *Nat. Chem.*, **2011**, *3*, 120. (c) S. Kuriyama, K. Arashiba, K. Nakajima, H. Tanaka, N. Kamaru, K. Yoshizawa and Y. Nishibayashi. *J. Am. Chem. Soc.*, **2014**, *136*, 9719.

12. (a) J. S. Anderson, J. Rittle and J. C. Peters. *Nature*, **2013**, *501*, 84. (b) S. E. Creutz and J. C. Peters. *J. Am. Chem. Soc.*, **2013**, *136*, 1105. (c) G. Ung and J. C. Peters. *Angew. Chem. Int. Ed.*, **2015**, *54*, 532.

13. K. Umehara, S. Kuwata and T. Ikariya. *J. Am. Chem. Soc.*, **2013**, *135*, 6754.

14. N. Sickerman, S. M. Peterson, J. W. Ziller and A. S. Borovik. *Chem. Comm.*, **2014**, *50*, 2515.

15. (a) M. Reiher, O. Salomon, D. Selmann and B. A. Hess. *Chem. Eur. J.*, **2001**, *7*, 5195. (b) O. Tutusaus, C. Ni and N. K. Szymczak. *J. Am. Chem. Soc.*, **2013**, *135*, 3403.

16. M. T. Mock, S. Chen, M. O'Hagan, R. Rousseau, W. G. Dougherty, S. W. Kassel and M. R. Bullock. *J. Am. Chem. Soc.*, **2013**, *135*, 11493.

17. (a) C. E. MacBeth, S. B. Harkins and J. C. Peters. *Can. J. Chem.*, **2005**, *83*, 332. (b) N. P. Mankad, M. T. Whited and J. C. Peters. *Angew. Chem. Int. Ed.*, **2007**, *46*,

5768. (c) M. T. Whited, N. P. Mankad, Y. Lee, P. F. Oblad and J. C. Peters. *Inorg. Chem.*, **2009**, *48*, 2507. (d) Y. Lee, N. P. Mankad and J. C. Peters. *Nat. Chem.*, **2010**, *2*, 558. (e) M.-E. Moret and J. C. Peters. *Angew. Chem. Int. Ed.*, **2011**, *50*, 2063. (f) M.-E. Moret and J. C. Peters. *J. Am. Chem. Soc.* **2011**, *133*, 18118 (g) J. Rittle and J. C. Peters. *Proc. Natl. Acad. Sci.*, **2013**, *110*, 15898.

18. D. J. Collins, L. E. Rowley and J. M. Swan. *Aust. J. Chem.*, **1974**, *27*, 841.
19. Steiner, T. *Angew. Chem. Int. Ed.* **2002**, *41*, 48.
20. J. S. Anderson, M.-E. Moret and J. C. Peters. *J. Am. Chem. Soc.*, **2012**, *135*, 534.
21. D. J. Fox and R. G. Bergman. *J. Am. Chem. Soc.*, **2003**, *125*, 8984.
22. R. H. Morris. *J. Am. Chem. Soc.*, **2014**, *136*, 1948.
23. Bonnaventure, I.; Charette, A. B. *J. Org Chem.* **2008**, *73*, 6330.
24. Chavez, I.; Alvarez-Carena, A.; Molins, E.; Roig, A.; Maniukiewicz, W.; Arancibia, A.; Arancibia, V.; Brand, H.; Manriquez, J. M. *J. Organomet. Chem*. **2000**, *601*, 126.
25. Brookhart, M.; Grant, B.; Volpe, A. F., Jr. *Organometallics* **1992**, *11*, 3920.
26. Weitz, I. S.; Rabinovitz, M. *J. Chem. Soc., Perkin Trans. 1* **1993**, 117.
27. Lee, Y.; Mankad, N. P.; Peters, J. C. *Nature Chem.* **2010**, *2*, 558.
28. Takaoka, A.; Peters, J. C. *J. Am. Chem. Soc.* **2011**, *133*, 8440.
29. Evans, D. F. *J. Chem. Soc*. **1959**, 2003.
30. Weatherburn, M. W. *Anal. Chem.* **1967**, *39*, 971.

Chapter 5. Development of photoinduced, copper-mediated and copper-catalyzed C-N coupling reactions

5.1 Introduction

Arylamines (anilines) are a commonly encountered subunit in organic compounds, important in fields ranging from pharmaceuticals to materials science.[1-3] Because many aryl halides and amines are readily available, coupling these two reactants provides a particularly attractive, convergent approach to the synthesis of arylamines. Thus, the discovery by Ullmann in 1903 that this C–N bond construction can be accomplished by heating these partners in the presence of a stoichiometric amount of copper was a landmark achievement in organic chemistry (Fig. 5.1A).[4-5] During the past century there have been numerous important advances in C–N coupling reactions, ranging from the discovery of milder, copper-*catalyzed* processes to the development of methods based on palladium and other transition metals.[6-11]

Despite the tremendous importance of copper-based Ullmann C–N coupling reactions, understanding of the mechanism of these processes has evolved only slowly.[6-9,12] It is believed that Ullmann couplings generally begin with Cu–N bond formation; however, a variety of pathways for the subsequent cleavage of the Ar–X bond have been proposed, including a concerted oxidative addition[13,14] and a single-electron transfer (SET, which encompasses halogen-atom transfer) mechanism with radical intermediates[15] (Fig. 5.1B). It is likely that different pathways may be operative under different conditions.

Currently, there is virtually no direct experimental evidence for the viability of an SET mechanism (*12*), although Buchwald and Houk have recently described a computational study in support of this pathway for certain Ullmann C–N couplings (*15–16*). In this report, we address this deficiency by providing an array of experimental data for the reaction of aryl halides with a well-defined copper(I) amido complex (**5.1**), all of which

are consistent with an SET/radical mechanism for C–N bond construction. In addition to furnishing the strongest evidence to date for the viability of an SET pathway for copper-based Ullmann C–N bond formation, this study affords the first examples of a photoinduced variant of this powerful transformation.

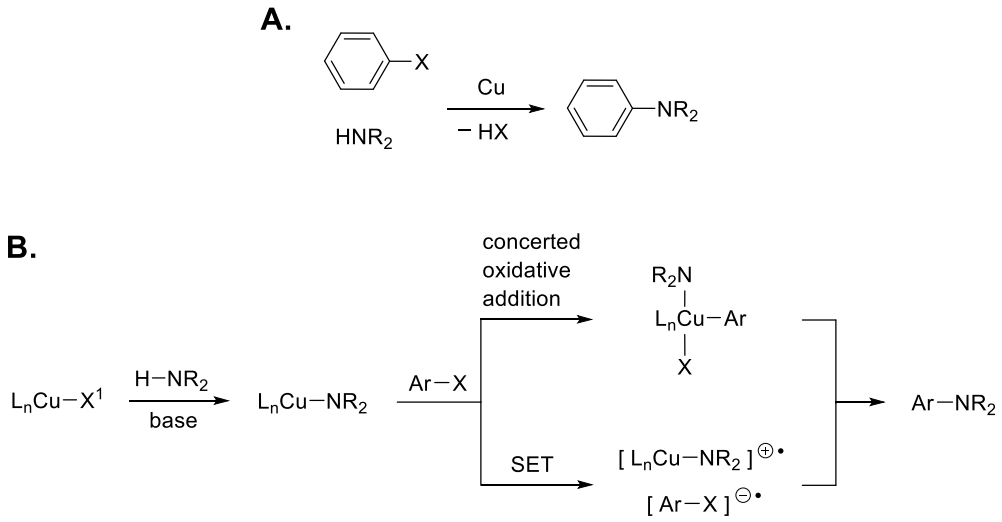

Figure 5.1. (**A**) Generalized equation for an Ullmann coupling to form an arylamine. (**B**) Outline of two of the possible mechanisms for Ullmann C–N bond formation.

5.2 Results and discussion

5.2.1 Stoichiometric C_{aryl}-N coupling reactivity

During the past several years, we have explored the chemistry of copper(I) amido complexes,[17-18] and we have determined that adducts such as carbazolide complex $(Ph_3P)_2Cu$(carbazolide) (**5.2**) are photoluminescent.[19] We envisioned that we could capitalize on the photophysical properties of this family of complexes as a mechanistic tool to examine the viability of an SET/radical pathway for Ullmann C–N bond formation (Fig. 5.2). Thus, photolysis of a copper–carbazolide complex could lead to electron

transfer to the aryl halide to afford a radical anion, which would rapidly fragment to form an aryl radical and a halide anion (top of Fig. 5.2).[20] This aryl radical could then react with the copper complex to furnish the C–N coupling product. Alternatively, the aryl radical could be generated directly through halogen atom transfer from the aryl halide to the excited copper–carbazolide complex (inner-sphere electron-transfer; bottom of Fig. 5.2). Regardless of which pathway is followed, this would represent, to our knowledge, the first example of a photoinduced Ullmann coupling to form a C–N bond.

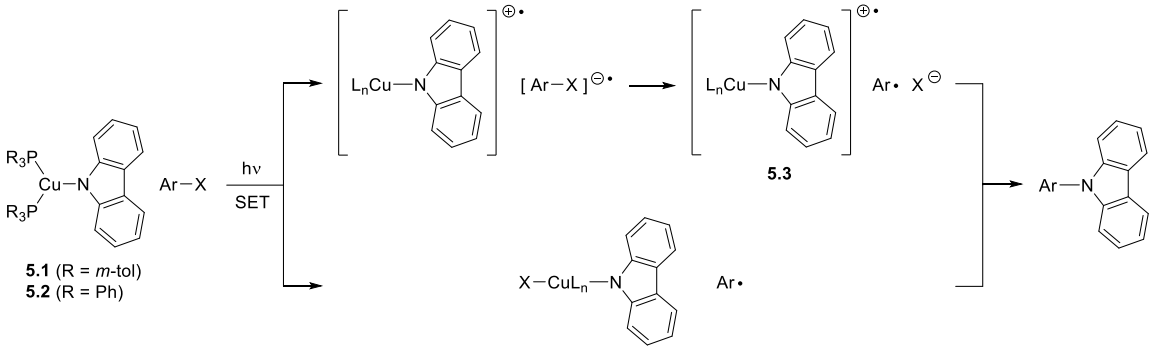

Figure 5.2 Outline of a possible pathway for photoinduced Ullmann C–N bond formation via a copper–carbazolide complex.

In a preliminary investigation, photolysis of PPh_3 adduct **5.2** in the presence of iodobenzene did indeed result in C–N bond formation; however, the solubility properties of complex **5.2** led us to synthesize a new, related copper complex wherein the PPh_3 ligands are replaced with P(*m*-tol)$_3$. A single-crystal X-ray diffraction study confirmed that the copper–carbazolide complex **5.1** maintains a three-coordinate trigonal-planar geometry in the solid state (Fig. 5.3). Complex **5.1** is colorless and is not visibly luminescent in acetonitrile; however, emission and excitation spectra confirm that it has accessible excitations available in the near ultraviolet (Fig. 5.4A).

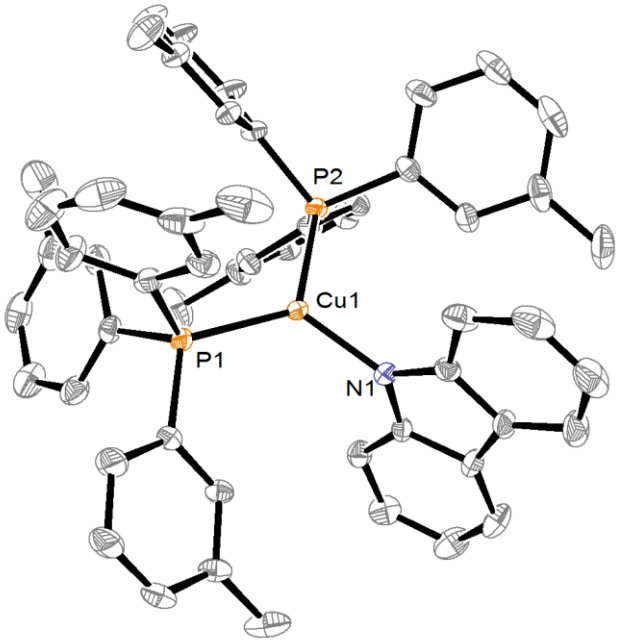

Figure 5.3. X-ray structure of copper complex **5.1** (thermal ellipsoids drawn at 50% probability).

When a solution of copper–carbazolide complex **1** and iodobenzene in CH_3CN is irradiated with a standard 13-watt compact fluorescent light bulb (CFL) at room temperature for 10 hours, C–N bond formation proceeds in good yield (77%; Table 1, entry 1); an even higher yield is obtained in CD_3CN (84%; entry 2). Under otherwise identical conditions in the absence of light, no *N*-phenylcarbazole is observed (<1%; entry 3), and negligible coupling occurs in the dark even upon heating at 65 °C for 12 hours. Finally, irradiation of a mixture of carbazole and iodobenzene (without **1**) leads to no detectable *N*-phenylcarbazole (<1%).

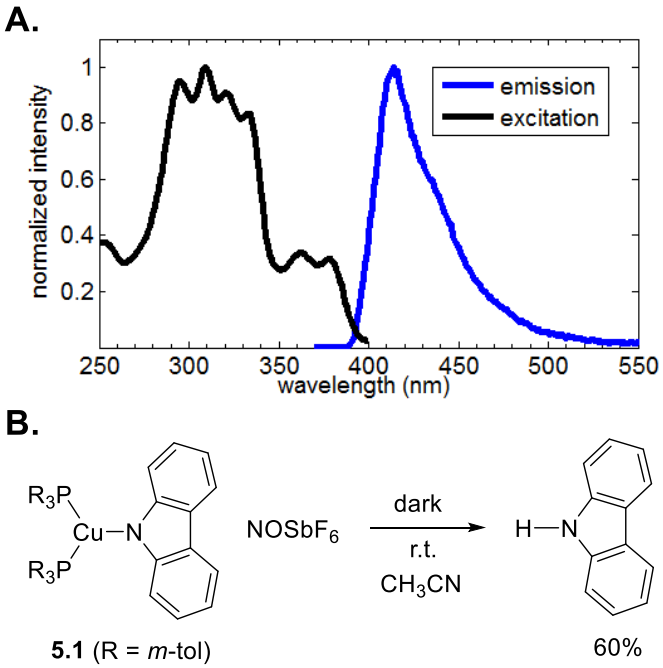

Figure 5.4. (**A**) Emission and excitation spectra of copper complex **5.1** in CH_3CN. (**B**) Chemical oxidation of copper complex **5.1**.

Photolysis of a solution of copper–carbazolide complex **5.1** and iodobenzene with a 100-watt mercury lamp results in C–N bond formation even at –40 °C (Table 5.1, entry 4). This observation is noteworthy because previously described couplings of carbazole with iodobenzene in the presence of copper have employed temperatures of at least 90 °C.[21]

Table 5.1. Photoinduced Ullmann C–N coupling reactions of copper–carbazolide complex **5.1** with PhX (X = I, Br, Cl).

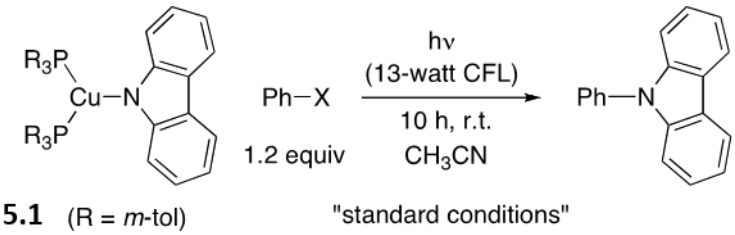

5.1 (R = *m*-tol) "standard conditions"

Coupling with iodobenzene (X = I)		
Entry	Conditions	Yield (%)[a]
1	standard conditions	77 (74)
2	CD_3CN instead of CH_3CN	84 (82)
3	dark	<1
4	–40 °C, 100-watt Hg lamp	69 (68)
Coupling with bromobenzene (X = Br)		
Entry	Conditions	Yield (%)[a]
5	standard conditions	40
6	100-watt Hg lamp	76 (72)
7	–40 °C, 100-watt Hg lamp, 5 equiv PhBr	59
8	dark	<1
Coupling with chlorobenzene (X = Cl)		
Entry	Conditions	Yield (%)[a]
9	standard conditions	5
10	100-watt Hg lamp, 24 h, 5 equiv PhCl	68 (66)
11	–40 °C, 100-watt Hg lamp, 5 equiv PhCl	11
12	dark	<1

[a] Yields were determined by GC analysis versus a calibrated internal standard (4,4'-di-*t*-butylbiphenyl) and are the average of at least two experiments; yields of purified product are in parentheses.

For these photoinduced Ullmann C–N coupling reactions, we postulate that upon irradiation an excited state of copper complex **5.1** transfers an electron to iodobenzene to

produce a radical ion pair (Fig. 5.2). The higher yield obtained in CD_3CN (Table 5.1, entry 2) compared with CH_3CN (entry 1) can be attributed to a kinetic isotope effect for undesired abstraction of a hydrogen/deuterium from the solvent by the phenyl radical or by radical cation **5.3** (Fig. 5.2). Consistent with this hypothesis, we observe benzene and unsubstituted N*H* carbazole as side products in these photoinduced couplings, and we have established that, when we independently generate radical cation **5.3** via chemical oxidation of **5.1** in CH_3CN, the unsubstituted N*H* carbazole is formed (Fig. 5.4B).[22]

Bromobenzene also undergoes Ullmann coupling when irradiated with a 13-watt CFL in the presence of copper–carbazolide complex **5.1**. As would be expected on the basis of relative reduction potentials (PhI: –1.91 V; PhBr: –2.43 V; PhCl: –2.76 V (vs. SCE in DMF on a platinum electrode)),[23] photoinduced C–N bond formation is considerably slower for bromobenzene (Table 5.1, entry 5) than for iodobenzene (entry 1). Nevertheless, a good yield of the desired product can be obtained at room temperature if a 100-watt mercury lamp is used (entry 6), and a moderate yield is observed even at –40 °C (entry 7). In the absence of light, no Ullmann coupling occurs (entry 8).

We are not aware of previous reports of Ullmann couplings of carbazole with chlorobenzene. We estimate the excited-state reduction potential of copper–carbazolide complex **5.1** to be ~ –2.6 V (vs. SCE in CH_3CN; based on the electrochemistry of **5.1** and its approximate value of E^{00} = 3.1 eV (obtained from the intersection of the emission and excitation profiles of **5.1**)), which suggests that electron transfer to chlorobenzene is viable. Under the standard conditions for the reaction of copper–carbazolide complex **5.1** with iodobenzene, chlorobenzene undergoes cross-coupling in low yield (5%; Table 5.1, entry 9). However, irradiation by a 100-watt mercury lamp in the presence of excess

chlorobenzene leads to efficient photoinduced Ullmann coupling at room temperature (entry 10).

5.2.2 Mechanistic probes

A variety of data are consistent with radical intermediates in these photochemical Ullmann reactions. For example, we detect benzene as a side product (vide supra); furthermore, monodeuterated arene is generated when the reaction is conducted in CD_3CN, along with a small amount of succinonitrile due to dimerization of the resulting cyanomethyl radical.[24] Finally, we observe the formation of iodobiphenyls when a large excess of iodobenzene is used.

Low-temperature (77 K) EPR data are consistent with photoinduced generation of a copper-containing radical when copper–carbazolide complex **5.1** and iodobenzene are irradiated with a 100-watt mercury lamp at –40 °C for 15 minutes in a 4:5 mixture of proprionitrile/butyronitrile (Fig. 5.5); this species and the deep-blue color of the reaction mixture rapidly disappear upon warming. The EPR spectrum has nearly axial symmetry. Coupling to $^{63/65}$Cu is too small relative to the broadness of the signal to be observed;[25] nevertheless, the strongly anisotropic g-values suggest that this species has at least partial metalloradical (Cu(II)) character. The same EPR spectrum is produced when complex **5.1** is treated at –78 °C with 0.3 equivalents of the oxidant Magic Blue (tris(4-bromophenyl)aminium hexachloridoantimonate), indicating that the same radical species can be generated by chemical and by photoinduced oxidation. We speculate that, rather than being radical cation **5.3** itself (Fig. 5.2), the detected radical is likely a more stable derivative, such as $Cu_2(P(m\text{-tol})_3)_4(\text{carbazolide})_2^{+\bullet}$, formed via trapping of radical cation **5.3** by complex **5.1**. The lack of resolved $^{63/65}$Cu hyperfine coupling in the EPR signal is

consistent with such a species,[26] as is our observation that this signal is absent when one equivalent of Magic Blue is used.

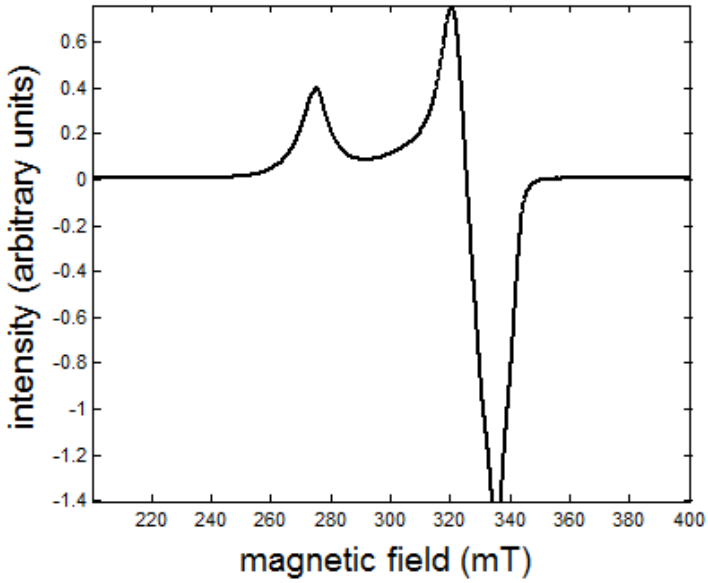

Figure 5.5. X-band EPR spectrum of a frozen (77 K) reaction mixture. Parameters: g = [2.440, 2.055, 1.990].

To provide further support for radical intermediates in these photoinduced Ullmann reactions, we examined the coupling of copper–carbazolide complex **5.1** with 2-(allyloxy)iodobenzene (**5.4**), a radical probe (Fig. 5.6). Because radical **5.5** is known to cyclize very rapidly ($k = 9.6 \times 10^9$ s^{-1} in DMSO),[27] the consistent failure to observe cyclized products in other studies of Ullmann C–N bond-forming reactions with this substrate has been cited as evidence against a radical pathway.[12-15] In contrast, in the case of our photoinduced Ullmann coupling, we observe exclusive formation of cyclized compounds (**5.6** and 3-methyl-2,3-dihydrobenzofuran; Fig. 5.6).

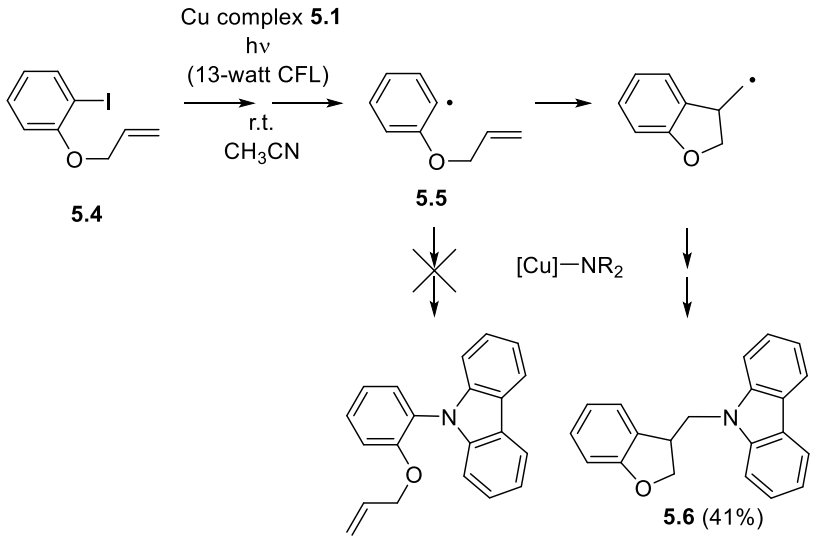

Figure 5.6. Cyclization, followed by C–N bond formation, in a photoinduced Ullmann reaction of an aryl iodide bearing a pendant olefin.

Control reactions establish that copper complex **1** does not couple with **4** in the dark, even upon heating to 65 °C. Furthermore, no cyclized products are detected when compound **4** is photolyzed in the absence of complex **1**.

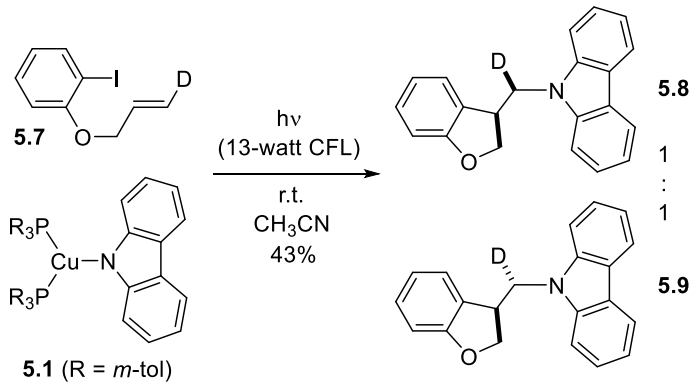

Figure 5.7. Stereochemical study of a photoinduced Ullmann reaction.

In fact, the formation of dihydrobenzofuran **5.6** does not conclusively support a radical pathway, since it could in principle be generated via concerted oxidative addition of **5.4** to form an arylcopper reagent, followed by *β*-migratory insertion and reductive elimination. However, our observation that deuterium-labeled aryl iodide **5.7** furnishes a 1:1 mixture of diastereomers (Fig. 5.7) is fully consistent with a radical pathway, whereas the oxidative-addition/syn-insertion/reductive-elimination sequence should only produce diastereomer **5.8**.

A control experiment established that olefin **5.7** does not undergo cis/trans isomerization under the reaction conditions. We have also performed this stereochemical study with the bromo analogue of **5.7**; again, a 1:1 mixture of diastereomers is generated, and no uncyclized products are observed.

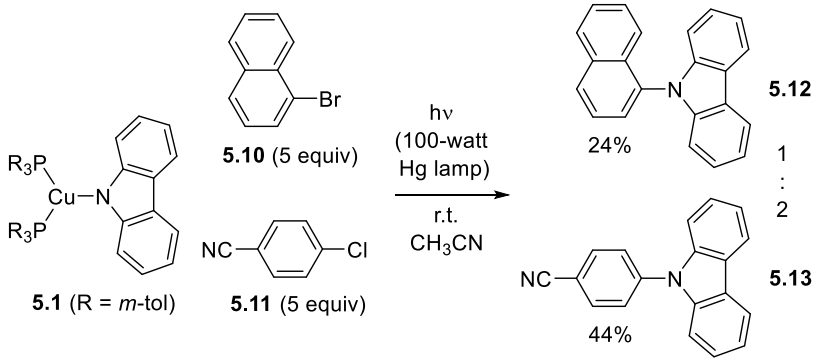

Figure 5.8. Competition study of a photoinduced Ullmann reaction.

An additional mechanistic probe that has been employed to distinguish between concerted oxidative addition of Ar–X and a pathway involving SET to the haloarene is the relative reactivity of 1-bromonaphthalene (**5.10**) and 4-chlorobenzonitrile (**5.11**) (Fig. 5.8).[13] According to this analysis, if C–X cleavage proceeds via concerted oxidative addition, then preferential coupling of 1-bromonaphthalene is expected, whereas, if the

reaction occurs via an SET mechanism, then 4-chlorobenzonitrile should react more rapidly, due to its more favorable reduction potential (–2.03 V for **5.11**; –2.17 V for **5.10** (vs. SCE in DMF)).[23]

When copper–carbazolide complex **5.1** is photolyzed in the presence of a 1:1 mixture of 1-bromonaphthalene and 4-chlorobenzonitrile, Ullmann coupling product **5.13**, derived from 4-chlorobenzonitrile, is predominant (Fig. 5.8). This observation is consistent with a radical-based SET pathway for C–N bond formation, and it stands in sharp contrast with a previous investigation wherein only the bromoarene was reactive, which was interpreted as supporting a concerted mechanism for oxidative addition under those conditions.[13]

5.2.3 Catalytic C_{aryl}-N coupling reactivity

Because copper-*catalyzed* Ullmann C–N couplings are of substantial interest,[6-9] we have pursued preliminary studies to ascertain if turnover can be achieved in these photoinduced processes. We have determined that irradiation of iodobenzene and lithium carbazolide in the presence of 10 mol% of copper–carbazolide complex **5.1** does indeed furnish the C–N coupling product in 64% yield, thereby establishing the viability of copper catalysis in this photochemical reaction manifold (Table 5.2, entry 1). In the absence of light, no detectable coupling is observed (entry 5.2), and photolysis of the coupling partners in the absence of complex **5.1** leads to very little *N*-phenylcarbazole (3%; entry 3). Notably, these copper-catalyzed photoinduced Ullmann couplings can even be effected at –40 ^{o}C (entry 4). In the presence of 1.5 mol% of copper–carbazolide complex **5.1**, a turnover number of ~20 can be achieved (entry 5). CuI also serves as a

catalyst for photoinduced Ullmann C–N couplings, likely via electron transfer from a luminescent copper–carbazolide complex generated in situ (entries 6 and 7).

Table 5.2. Photoinduced Ullmann C-N coupling reactions catalyzed by copper–carbazolide complex **5.1**.

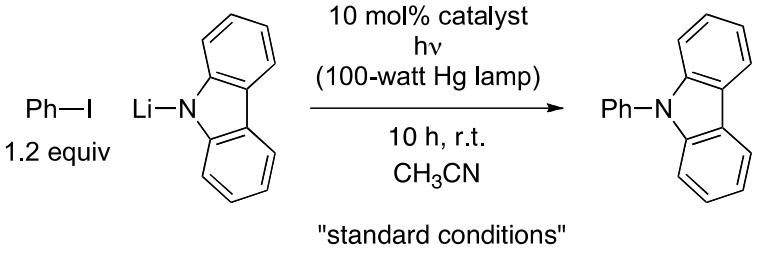

Entry	Catalyst	Conditions	Yield (%)[a]
1	**5.1**	standard conditions	64 (52)
2	**5.1**	dark	<1
3	none	standard conditions	3
4	**5.1**	–40 °C	45
5	1.5 mol% **5.1**	standard conditions	30
6	CuI	standard conditions	65 (58)
7	CuI	dark	<1

[a] Yields were determined by GC analysis versus a calibrated internal standard (4,4'-di-*t*-butylbiphenyl) and are the average of at least two experiments; yields of purified product are in parentheses.

Finally, when aryl iodide **5.7** (Fig. 5.7) and lithium carbazolide are employed as coupling partners in the presence of copper–carbazolide complex **5.1** under the catalytic conditions outlined in Table 5.2, a 1:1 mixture of diastereomers **5.8** and **5.9** is formed (and no uncyclized products). This observation is consistent with a common radical-based SET pathway for catalyzed and uncatalyzed Ullmann couplings effected by complex **5.1**.

5.2.4 Photoinduced, copper-catalyzed C_{alkyl}-N coupling and mechanistic studies

Encouraged by the successful coupling of an alkyl electrophile and carbazolide nucleophile as illustrated in Figure 5.6, we chose to target C_{alkyl}-N coupling as the initial focus of further studies on a *catalytic*, photoinduced coupling reaction. While the formation of C_{alkyl}-N bonds *via* an S_N2 reaction between an amine and an alkyl halide is a classic "textbook" reaction[28] (Figure 5.9A) that still plays an important role in organic synthesis,[29] it typically requires elevated reaction temperatures for hindered primary electrophiles and unactivated secondary electrophiles. To our knowledge, there were virtually no prior examples of transition-metal-catalyzed variants of this method, which should enable carbon-nitrogen bond formation to proceed under milder conditions.[30]

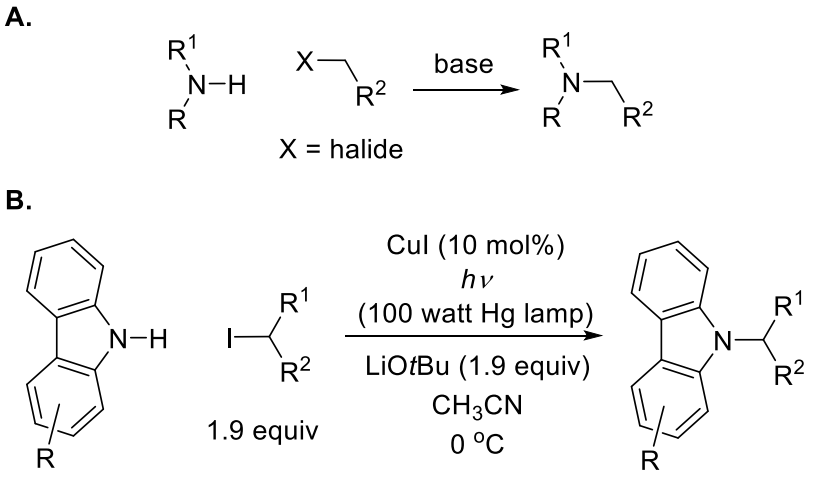

Figure 5.9. (A) Reaction of an amine and an alkyl halide to form a C_{alkyl}-N bond. (B) Optimized conditions for the photoinduced, copper-catalyzed coupling reaction between a carbazole and a secondary alkyl iodide.

Collaborative work in the Fu group established an optimized protocol for the photoinduced, copper-catalyzed coupling of carbazoles with a suite of secondary alkyl

iodides which proceeds under very mild conditions (0 °C); little or no product formation occurs in the absence of copper and/or light (Figure 5.9B).[31] The catalyst for these reactions is simply CuI; no added ligands are necessary.

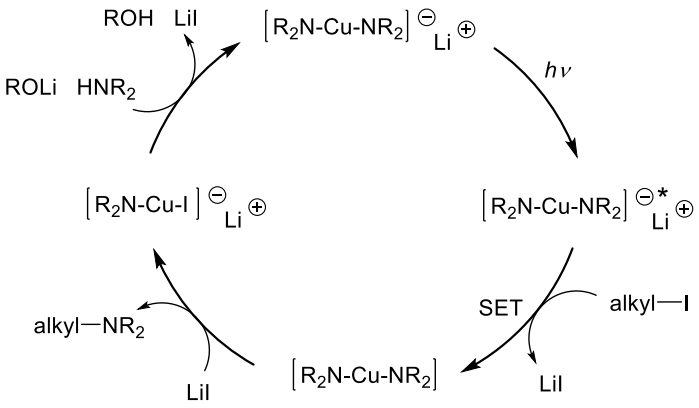

Figure 5.10. A possible pathway for photoinduced, copper-catalyzed N-alkylation of carbazole.

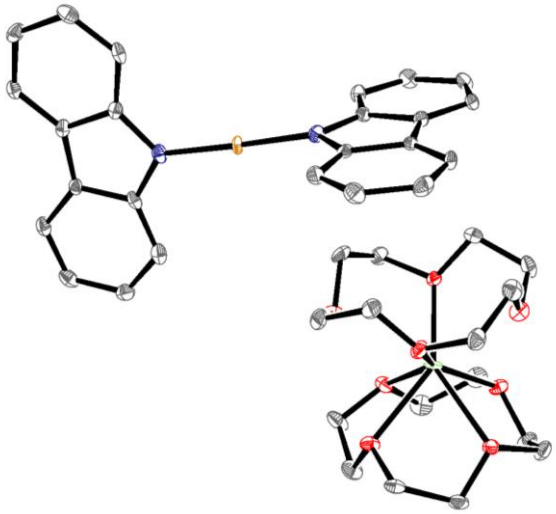

Figure 5.11. Crystal structure of **5.11**, thermal ellipsoids shown at 50% probability and hydrogen atoms omitted for clarity.

We hypothesized that Li[Cu(carbazolide)$_2$] is formed under the reaction conditions and may be an intermediate in the alkylation pathway (Figure 5.10).[32] When we examined

the electrospray mass spectra of coupling reactions in progress, we did indeed detect substantial quantities of ions with molecular weights of 395 and 397 amu (and the ratio stays approximately constant), which correspond to the masses of $[^{63}Cu(carbazolide)_2]^-$ and $[^{65}Cu(carbazolide)_2]^-$. We were able to synthesize $[Cu(carbazolide)_2]^-$ as its $[Li(CH_3CN)_4]^+$ (**5.10**) and $[Li(12\text{-crown-}4)_2]^+$ (**5.11**) salts, and we obtained an X-ray crystal structure of the latter (Figure 5.11). In the solid state, this two-coordinate copper complex adopts a linear geometry (N-Cu-N = 178°) with a dihedral angle of 89° between the two carbazolide planes. We have demonstrated that **5.10** is competent both as a catalyst for C-N coupling under the conditions established above, and also for stoichiometric C-N bond formation (Figure 5.12). Thus, the data that we have accumulated to date are consistent with the suggestion that $Li[Cu(carbazolide)_2]$ may be an intermediate in this metal-catalyzed N-alkylation reaction.

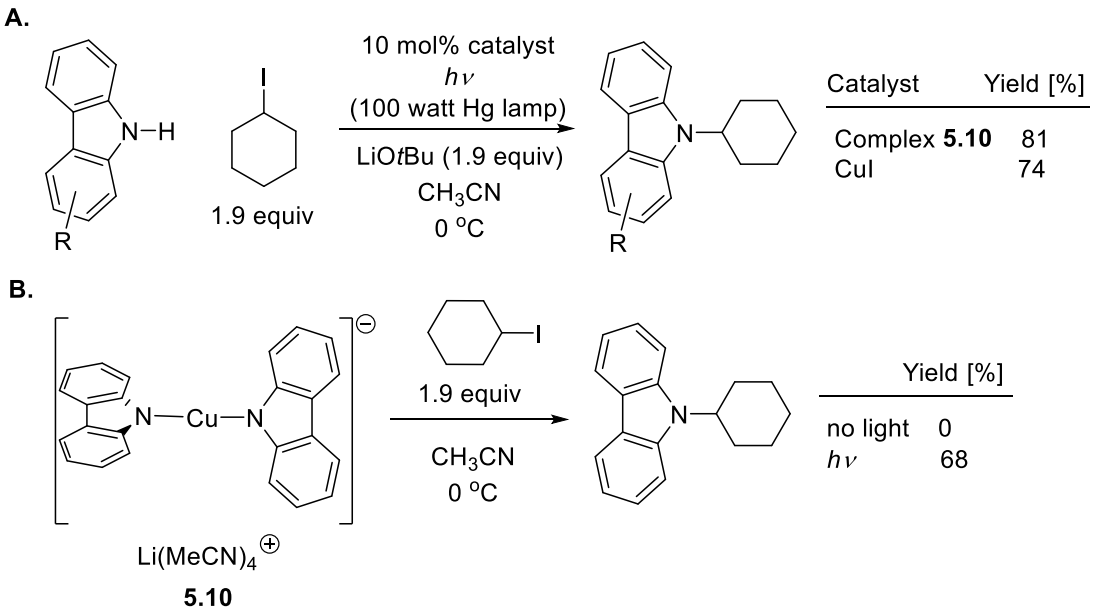

Figure 5.12. (A) Demonstration of catalytic competence of **5.10**. (B) Stoichiometric photoinduced C-N bond formation with **5.10**.

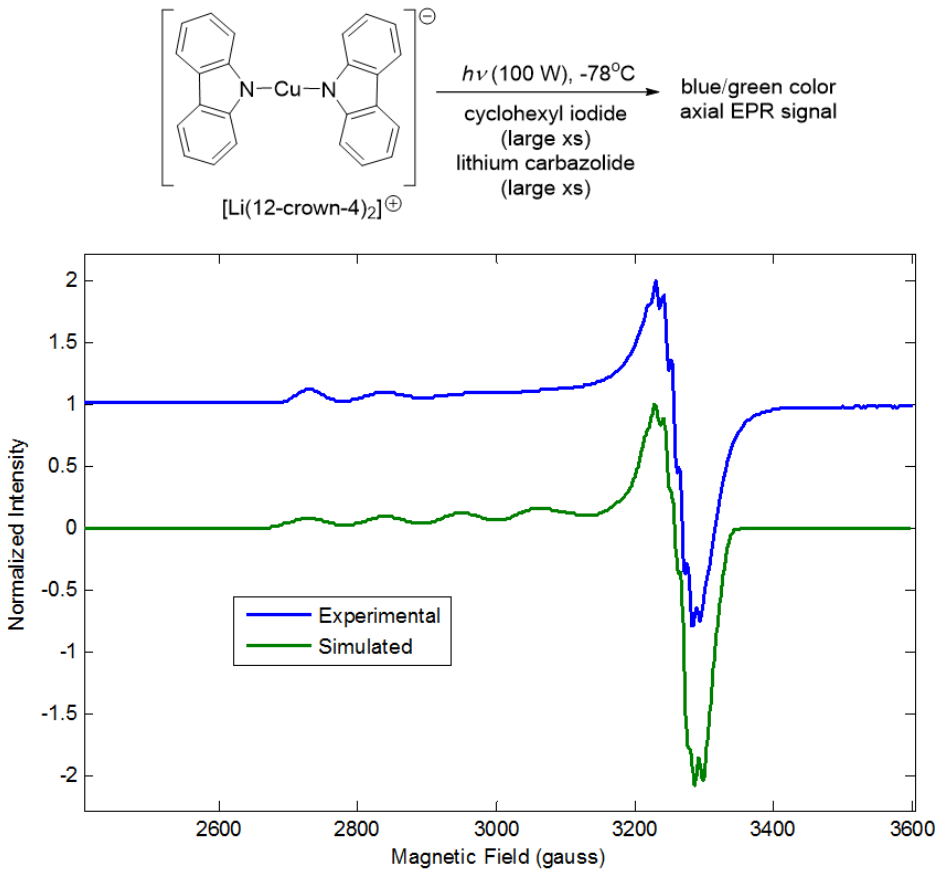

Figure 5.13. EPR signal (and corresponding simulation) generated by low-temperature photolysis of a mixture of **5.11**, cyclohexyl iodide, and lithium carbazolide. (Simulation parameters: g=[2.3175, 2.0580, 2.0500]; HStrain=[120, 5, 5]; coupling to copper with A=[350, 25, 21]; coupling to three equivalent nitrogen atoms all with A=[50, 35, 35]).

We also sought to probe the possible formation of a Cu^{II} species during the catalytic reaction, similar to that established for the photoinduced reaction of **5.1** with iodobenzene (Figure 5.4), which would help support a radical pathway for the mechanism of this reaction. Accordingly, photolysis (100 W Hg lamp) of a solution of either **5.11** or CuI with a large excess of cyclohexyl iodide and a large excess of lithium carbazolide in 4:5 proprionitrile:butyronitrile at -78 °C for 10 minutes generated a deep blue-green solution

which was analyzed by EPR. The EPR spectrum showed an axial signal with apparent coupling to a copper nucleus (Figure 5.13). The spectrum could be well simulated by coupling to copper as well as three equivalent nitrogen nuclei—i.e., a $[Cu^{II}(carbazolide)_3]^-$ anion. This species is thermally unstable, and both the blue-green color and the corresponding EPR signal decay rapidly upon warming to room temperature.

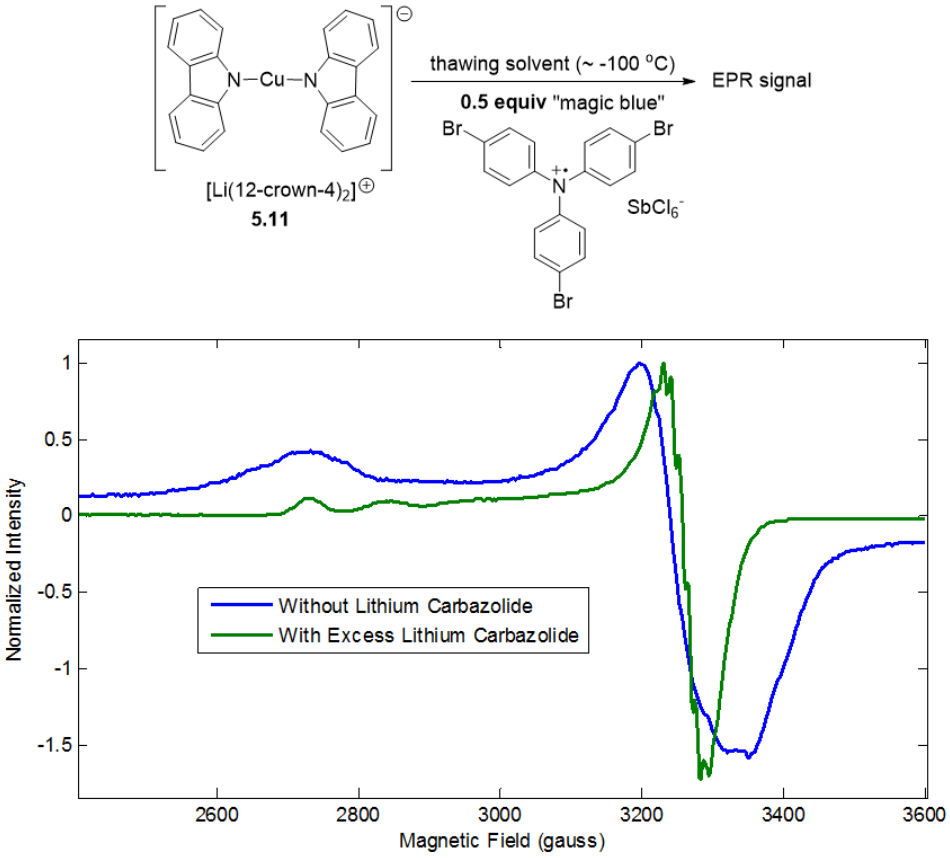

Figure 5.14. EPR signals generated by chemical oxidation of **5.11** in the presence or absence of an excess of lithium carbazolide.

An identical spectrum to the above is generated by chemical oxidation of **5.11** with 0.5 equivalents of Magic Blue in the presence of an excess of lithium carbazolide in thawing

4:5 proprionitrile:butyronitrile solvent. In contrast, chemical oxidation of **5.11** with 0.5 equivalents of magic blue *without* added carbazolide generates a different, broad axial EPR spectrum qualitatively similar to that shown in Figure 5.4, accompanied by a pale blue color (Figure 5.14).

The above results suggest that a reactive $[Cu^{II}(carbazolide)_3]^-$ is formed by oxidation of the copper(I) catalyst precursor during the course of the photoinduced C_{alkyl}-N coupling reaction, and this species may play an important role in the C-N bond forming step of the reaction mechanism.

5.3 Conclusion

In summary, due to the frequent occurrence in organic molecules of the amine subunit, considerable effort has been dedicated to the development of milder and more versatile methods for the synthesis of C–N bonds, especially C_{aryl}-N bonds, and impressive progress has been achieved, including for Ullmann couplings. On the other hand, our understanding of the possible mechanisms by which Ullmann reactions may proceed has advanced more slowly. An array of potential pathways for cleavage of the aryl–X bond has been proposed, ranging from concerted oxidative addition to single-electron transfer (SET). With regard to the latter (SET) mechanism, there has been computational, but virtually no direct experimental, support for its viability. Herein, we have provided the most substantial evidence to date that Ullmann C–N couplings can be achieved via an SET pathway. Specifically, we have exploited the photophysical properties of a new copper complex to develop the first examples of *photoinduced* Ullmann C–N bond formation. Thus, irradiation of $[(m\text{-tol})_3P]_2Cu(carbazolide)$ (**5.1**) in the presence of an aryl iodide, bromide, or chloride leads to C–N bond formation under unusually mild

conditions (room temperature); indeed, the coupling of an aryl iodide or bromide can even be accomplished at –40 °C. An array of data, including a cyclization/stereochemical investigation and a reactivity study, are consistent with an SET pathway for Ullmann C–N bond formation. These photoinduced couplings are not limited to stoichiometric processes: Ullmann reactions can also be achieved with a *catalytic* amount of copper–carbazolide complex **5.1** or even simple copper salts (CuI). We have furthermore extended this reactivity to the formation of C_{alkyl}-N bonds and identified possible Cu^{I} and Cu^{II} intermediates in this catalytic reaction.

Ongoing work has since expanded the substrate scope for photoinduced, copper-catalyzed coupling reactions to a wide range of N, O, S, and C nucleophiles.[33] Mechanistic studies on these systems likewise continue, and it is becoming clear that, in catalytic systems, the mechanism is highly substrate-dependent and likely more complex than our original working hypothesis (Figure 5.10). In particular, photoelectron transfer from the nucleophile (e.g., lithium carbazolide) to the electrophile substrate likely plays a significant role under catalytic conditions. Further synthetic and mechanistic explorations will likely lead to a better understanding of this complex reaction manifold, and will aid in expanding the chemistry to new classes of reaction partners.

5.4 Experimental details.

5.4.1 General.

All manipulations of air-sensitive materials were carried out using standard Schlenk or glovebox techniques under an N_2 atmosphere. Benzene and acetonitrile were deoxygenated and dried by sparging with inert gas followed by passage through an activated alumina column in the solvent purification system by SG Water, USA LLC and

stored over 4 Å molecular sieves. All reagents were purchased from commercial vendors and used without further purification unless otherwise stated. Lithium carbazolide,[19] $(Ph_3P)_2Cu(cbz)$ (**5.2**),[19] 2-allyloxyiodobenzene,[34] 2-propargyloxyiodobenzene,[35] and Cp_2ZrHCl[36] were synthesized according to published procedures. The synthesis of E-(3-deuterioallyl)oxy-2-iodobenzene was adapted from reference 37. Elemental analyses were performed by Midwest Microlab, LLC., Indianapolis, IN. Deuterated solvents were purchased from Cambridge Isotope Laboratories, Inc., degassed, and dried over activated 4 Å molecular sieves before use. Proprionitrile, butyronitrile, and deuterated acetonitrile were dried over calcium hydride prior to use. The lamps used for photolysis were either a 13W compact fluorescent lamp (Wespointe model #WP13MSLT2), or a 100W mercury lamp (Blak-Ray Long-Wave Ultraviolet Lamp, Model B). ^{1}H, ^{2}D, and ^{13}C chemical shifts are reported in ppm relative to tetramethylsilane, using residual solvent proton, deuterium, and ^{13}C resonances as internal standards. ^{31}P chemical shifts are reported in ppm relative to 85% aqueous H_3PO_4. X-band EPR spectra were obtained on a Bruker EMX spectrometer and simulated using Easyspin.[38] Emission and excitation spectra were measured at room temperature with a Jobin Yvon Spex Fluorolog®-3 at the Beckman Institute Laser Resource Center. An excitation wavelength of 310 nm was employed for the emission spectra, and emission at 458 nm was monitored for the excitation spectra.

5.4.2 X-ray crystallography

XRD studies were carried out at the Beckman Institute Crystallography Facility on a Bruker Kappa Apex II diffractometer (Mo Kα radiation). Structures were solved using

SHELXS[39] and refined against F^2 on all data by full-matrix least squares with SHELXL. The crystals were mounted on a glass fiber.

5.4.3 Syntheses, characterization data, and reactions

Synthesis of [P(*m*tol$_3$)]$_2$Cu(cbz) (5.1): CuBr(Me_2S) (393 mg, 1.91 mmol) was suspended in 3 mL of benzene. Tris(2-methylphenyl)phosphine (1.162 g, 3.82 mmol) was added as a solution in 20 mL of benzene, and the resulting clear and colorless solution as diluted to a total volume of 50 mL. Lithium carbazolide (340 mg, 1.96 mmol) was added as a solid in small portions over 40 minutes. The reaction mixture became cloudy and developed a green-yellow color over the course of the addition. After four hours, the reaction mixture was filtered through Celite to remove lithium bromide. The filtrate was concentrated to dryness to give a sticky green foam, which was redissolved in minimal 5:1 diethyl ether:pentane, and then stored at -40^o C for 30 minutes until a green-yellow precipitate formed. The yellow supernatant was decanted, and the solids were washed with cold diethyl ether and dried under vacuum, giving 1.048 g of **5.1** (65%). Single crystals suitable for x-ray diffraction were grown *via* slow evaporation of a diethyl ether solution of **5.1** into methylcyclohexane. ^{1}H NMR (C_6D_6, 300 MHz): δ 8.51 (d, 2H, NAr-*H*), 7.74 (d, 2H, NAr-*H*), 7.51 (d, 6H, P($CH_3C_6H_5$)$_3$), 7.39 (t, 2H, NAr-*H*), 7.29 (t, 2H, NAr-*H*), 7.22 (t, 6H, P($CH_3C_6H_5$)$_3$), 6.88-6.78 (m, 12H, P($CH_3C_6H_5$)$_3$), 1.75 (s, 18H, P($CH_3C_6H_5$)$_3$). ^{13}C NMR (C_6D_6, 100 MHz): δ 151.2 (s), 139.01 (d, J_{CP}=8.6 Hz), 135.36 (d, J_{CP}=18.5 Hz), 133.39 (d, J_{CP}=39.3 Hz), 130.99 (s), 130.84 (d, J_{CP}=9.6 Hz), 128.95 (d, J_{CP}=6.5 Hz), 128.59 (s), 126.37 (s), 123.73 (s), 120.34 (s), 115.22 (d, J_{CP}=9.4 Hz), 21.00 (s). ^{31}P NMR (C_6D_6, 121 MHz): δ -4 (s). Anal. Calcd. For $C_{54}H_{50}NP_2Cu$: C, 77.35; H, 6.01; N, 1.67; Found: C, 77.19; H, 6.39; N, 1.56.

Synthesis of N-phenylcarbazole from 5.1 and PhX, general procedure: PhX (1.2 equiv or 5 equiv) was dissolved in CH_3CN (10 mL) and added to solid **5.1** (200 mg, 0.24 mmol) to give a clear solution after stirring for ~10 minutes in the dark. The solution was transferred to a 500 mL Erlenmeyer flask equipped with a ground glass joint. The Erlenmeyer flask was sealed with a well-greased stopper and rubber bands. The reaction mixture was photolyzed from the bottom of the Erlenmeyer with either a 13W compact fluorescent lightbulb or a 100W mercury lamp for 10 hours while the temperature was maintained at either 28 ^oC by the use of cooling airflow, or at -40 ^oC in a dry ice/acetonitrile bath. At the end of the reaction time the reaction mixture was a clear, pale yellow-orange. The reaction mixture was then opened to air, diluted with diethyl ether (15 mL), and washed with distilled water (3X5 mL). The aqueous fractions were back-extracted with 5 mL of diethyl ether, and the combined organic layers were stirred with 5 mL of an aqueous 30% hydrogen peroxide solution for 20 minutes. The aqueous layer was then separated, and the organic layer was washed with water (2X5 mL); the aqueous layers were washed with 5 mL of diethyl ether, and then the combined organic layers were stirred with 10 mL of saturated aqueous ferrous sulfate for 30 minutes. Then the aqueous layer was removed, and the organic layer was washed with water (2X5 mL). The aqueous layers were washed with 5 mL of diethyl ether, then the combined organic layers were washed with 5 mL of saturated aqueous sodium chloride and then dried over magnesium sulfate, filtered, and concentrated. The resulting orange residue was filtered through a plug of silica, washing with hexanes, and the filtrate concentrated to a light orange residue (NOTE: unless otherwise stated, the above-described work-up procedure is used for all further coupling reactions detailed below). This residue was purified by

column chromatography on silica gel, eluting with hexanes, giving N-phenylcarbazole as a white solid. The identity of the product was confirmed by comparison of GC-MS and NMR data with those of a commercial sample.

Synthesis of N-phenylcarbazole with catalytic 5.1: Lithium carbazolide (100 mg, 0.58 mmol, 1.0 eq.), iodobenzene (142 mg, 0.70 mmol, 1.2 eq.), and **5.1** (48.8 mg, 0.058 mmol, 0.10 eq.) were combined in 2 mL of acetonitrile to give a clear yellow solution in a 20 mL scintillation vial, which was sealed with a PTFE-lined cap and electrical tape. This reaction mixture was photolyzed for 10 hours with a 100W mercury lamp at 28 ^{o}C, giving a dark brown mixture. The reaction mixture was worked up as described above. This residue was purified by column chromatography on silica gel, eluting with hexanes, giving N-phenylcarbazole as a white solid (73 mg, 52%). The identity of the product was confirmed by comparison of GC-MS and NMR data with those of a commercial sample.

Synthesis of N-phenylcarbazole with catalytic CuI: Lithium carbazolide (100 mg, 0.58 mmol, 1.0 eq.), iodobenzene (142 mg, 0.70 mmol, 1.2 eq.), and copper(I) iodide (10.6 mg, 0.058 mmol, 0.10 eq.) were combined in 2 mL of acetonitrile to give a clear yellow solution in a 20 mL scintillation vial, which was sealed with a PTFE-lined cap and electrical tape. This reaction mixture was photolyzed for 10 hours with a 100W mercury lamp at 28 ^{o}C, giving a dark brown mixture. The reaction mixture was then opened to air, diluted with diethyl ether (15 mL), and washed with distilled water (3X5 mL). The aqueous fractions were back-extracted with 5 mL of diethyl ether, and the combined organic layers were washed with 5 mL of saturated aqueous sodium chloride and then dried over magnesium sulfate, filtered, and concentrated. The resulting orange residue was filtered through a plug of silica, washing with hexanes, and the filtrate concentrated

to a light orange residue. This residue was purified by column chromatography on silica gel, eluting with hexanes, giving N-phenylcarbazole as a white solid (82 mg, 58%). The identity of the product was confirmed by comparison of GC-MS and NMR data with those of a commercial sample.

Synthesis of 5.6: 2-allyloxyiodobenzene (74 mg, 0.29 mmol, 1.2 equiv) was added to an acetonitrile solution (0.5 mL) of **5.1** (200 mg, 0.24 mmol). The reaction mixture was stirred in darkness for 20 minutes and then subjected to photolysis using a 13W CFL lightbulb at 28°C for 10 hours. The reaction mixture was worked up as described above. The yellow-orange residue was purified by silica gel chromatography (5% EtOAc:hexanes) to give **6** as a white solid (29.2 mg, 41%). ^{1}H NMR (C_6D_6, 300 MHz, 298 K): δ 8.04 (d, 2H, 4-*H*-cbz, J=8 Hz), 7.34 (t, 2H, 2-*H*-cbz, J=8 Hz), 7.23 (t, 2H, 2-*H*-cbz, J=8 Hz), 7.01 (d, 2H, 1-*H*-cbz, J=8 Hz), 6.98 (t, 1H, 6-*H*-dihydrobenzofuran, J=8 Hz), 6.87 (d, 1H, 4-*H*-dihydrobenzofuran, J=8 Hz, 6.59 (m, 2H, 7-*H*-dihydrobenzofuran and 5-*H*-dihydrobenzofuran), 4.03 (dd, 1H, 2-C*H*H-dihydrobenzofuran, J=9 Hz, 4 Hz), 3.73-3.91 (m, 3H, 2-CH*H*-dihydrobenzofuran and N(cbz)-CH_2-dihydrobenzofuran), 3.55 (m, 1H, 3-C*H*-dihydrobenzofuran) ppm. ^{13}C{^{1}H} (C_6D_6, 75 MHz, 298 K) δ 160.8 (7a-*C*-dihydrobenzofuran), 140.8 (*C*(Ar)), 129.4 (*C*(Ar)), 128.2 (*C*(Ar)), 127.9 (*C*(Ar)), 126.1 (*C*(Ar)), 125.3 (*C*(Ar)), 123.5 (*C*(Ar)), 120.8 (*C*(Ar)), 119.7 (*C*(Ar)), 110.2 (*C*(Ar)), 109.1 (*C*(Ar)), 74.4 (2-*C*H_2-dihydrobenzofuran), 46.6 (N-*C*H_2), 42.1 (3-*C*H-dihydrobenzofuran) ppm.

Synthesis of E-(3-deuterioallyl)oxy-2-iodobenzene (5.7): In the glovebox, 2-propargyloxyiodobenzene (1.019 g, 3.95 mmol) was dissolved in ~5 mL of THF and added dropwise to a white suspension of Cp_2ZrHCl (Schwartz's reagent, 1.2 g, 4.65

mmol, 1.18 eq.) in ~20 mL of THF. Within a few minutes the white suspension had turned clear dark orange-red. The reaction mixture was allowed to stir at room temperature for 4 hours, and then brought out of the glove box in a septum-covered round-bottomed flask. D_2O (1.5 mL) was added via syringe to the reaction, causing the red-orange color to immediately disappear, leaving a pale yellow solution. The solution was stirred at room temperature for 30 minutes. The reaction mixture was then diluted with ~100 mL of diethyl ether, causing white solids to crash out. The solution was dried over magnesium sulfate, filtered, concentrated, filtered through a plug of silica, and concentrated again. The remaining yellowish oil was distilled at reduced pressure to give E-(3-deuterioallyl)oxy-2-iodobenzene as a clear, colorless oil. The isolated material is approximately a 10:1 mixture of the desired isotopomer and (2-deuterioallyl)oxy-2-iodobenzene (370 mg, 36%). ^{1}H NMR (C_6D_6, 400 MHz, 298 K): δ 7.67 (d, 1H, 3-Ar-*H*, J=8 Hz), 6.91 (t, 1H, Ar-*H*, J=8 Hz), 6.38 (t, 1H, Ar-*H*, J=8 Hz), 6.31 (d, 1H, Ar-*H*, J=8 Hz), 5.70 (dt, 1H, -OCH$_2$C*H*CHD, J=17 Hz, 5 Hz), 5.32 (d, 1H, -OCH$_2$CHC*H*D, J=17 Hz), 4.01 (d, 2H, -OC*H*$_2$CHCHD, J=5 Hz) ppm. ^{13}C{^{1}H} NMR (C_6D_6, 100 MHz, 298 K): δ 157.2, 139.5, 132.5, 129.0, 122.3, 116.4 (1:1:1 t, J_{CD}=24 Hz), 112.2, 86.7, 69.0 ppm. ^{2}D{^{1}H} NMR (C_6H_6, 76 MHz, 298 K): δ 5.03 (s).

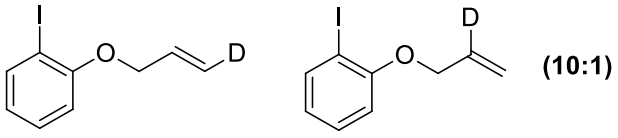

Chart 5.1. Isotopomers formed in synthesis of deuterated radical clock **5.7**.

Synthesis of 5.8 and 5.9: **5.7** (41 mg, 0.16 mmol, 1.1 eq.), as a mixture of isotopomers as detailed above, was added to **5.1** (119 mg, 0.14 mmol) in acetonitrile (5 mL) to give a clear, colorless solution. The reaction mixture was subjected to photolysis at room temperature under a 100W mercury lamp for 8 hours, resulting in a color change to pale orange. GC-MS confirmed the presence of the cyclized, deuterodehalogenation product 3-deuteriomethyl-2,3-dihydrobenzofuran as well as the carbazole coupling products **5.8** and **5.9** (m/z=300.1, 181.2). None of the uncyclized coupling product N-(2-allyloxyphenyl)carbazole was observed by GC-MS or by NMR. The reaction mixture was worked up as described above. The resulting orange residue was purified by column chromatography (5% EtOAc/hexanes) and then recrystallized from cold hexanes to give **5.8** and **5.9** as off-white crystals (19.1 mg, 45%). The isolated product is a mixture of the desired pair of diastereomers and the isomer derived from the minor isotopomer of the starting material. ^{1}H NMR ($CDCl_3$, 300 MHz, 298 K): δ 8.16 (d, 2H, 4-*H*-cbz, J=8 Hz), 7.50 (t, 2H, 2-*H*-cbz, J=8 Hz), 7.42 (d, 2H, 1-*H*-cbz, J=8 Hz), 7.30 (t, 2H, 2-*H*-cbz, J=8 Hz), 7.22 (t, 1H, 6-*H*-dihydrobenzofuran, J=8 Hz), 7.02 (dd, 1H, 4-*H*-dihydrobenzofuran, J=8 Hz, 3 Hz), 6.93 (d, 1H, 7-*H*-dihydrobenzofuran, J=8 Hz), 6.83 (t, 1H, 5-*H*-dihydrobenzofuran, J=8 Hz), 4.52-4.38 (m, 3H, N-C*H*D, 2-H_2-dihydrobenzofuran), 4.14 (m, 1H, 3-*H*-dihydrobenzofuran) ppm. ^{13}C{^{1}H} ($CDCl_3$, 126 MHz, 298 K) δ 160.1 (7a-*C*-dihydrobenzofuran), 140.4 (8a-*C*-cbz), 129.2 (6-*C*H-dihydrobenzofuran), 127.7 (3a-*C*-dihydrobenzofuran), 125.9 (2-*C*H-cbz), 125.1 (4-*C*H-dihydrobenzofuran), 123.0 (4a-*C*-cbz), 120.8 (5-*C*H-dihydrobenzofuran), 120.5 (4-*C*H-cbz), 119.4 (3-*C*H-cbz), 110.0 (7-*C*H-dihydrobenzofuran), 108.7 (1-*C*H-cbz), 74.6 (2-*C*H_2-dihydrobenzofuran), 46.47

(1:1:1 triplet, N-*C*HD, J_{CD}=21 Hz), 42.2 (3-*C*H-dihydrobenzofuran) ppm. $^{2}D\{^{1}H\}$ (C_6H_6, 76 MHz, 298 K) δ 3.84 (0.5D, N-CH*D*), 3.75 (0.5D, N-C*D*H) ppm.

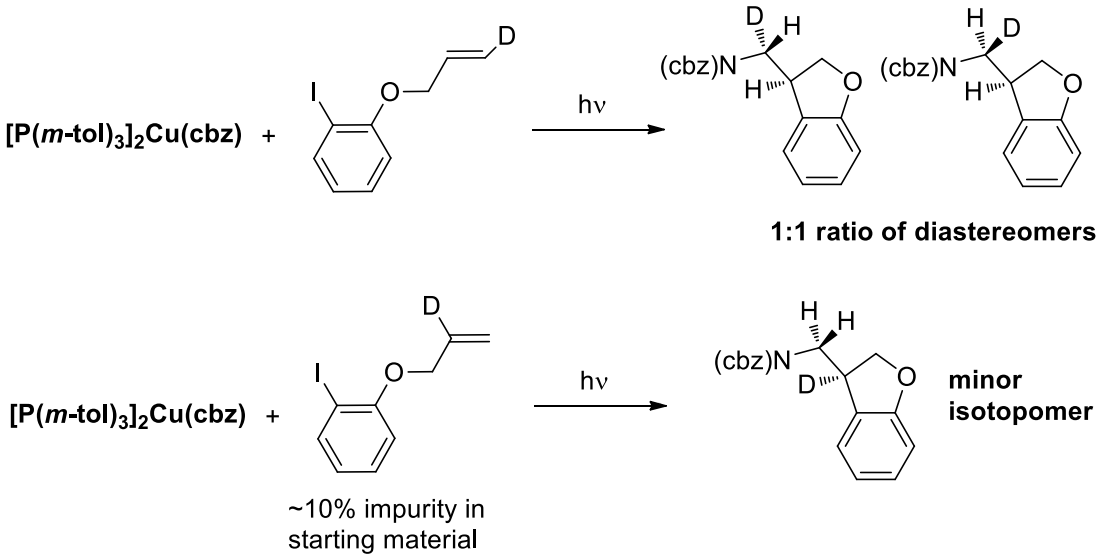

Scheme 5.1. Formation of isotopomers of the coupling product of **5.7** and **5.1**; NMR of the crude reaction shows a lack of isomerized starting material (Z-(3-deuterioallyl)oxy-2-iodobenzene), indicating that the double bond of the "radical trap" does not isomerize under the reaction conditions. The deuterium NMR peak for the isomerized material would be expected at 5.34 ppm.

Synthesis of N-(1-naphthyl)carbazole (5.12) from 1-bromonaphthalene and 5.1: 1-bromonaphthalene (59.3 mg, 0.29 mmol, 1.2 equiv.) was dissolved in CH_3CN (20 mL) and added to solid **5.1** (200 mg, 0.24 mmol) to give a clear solution after stirring for ~10 minutes in the dark. The solution was transferred to a 500 mL Erlenmeyer flask equipped with a ground glass joint. The Erlenmeyer flask was sealed with a well-greased stopper and rubber bands. The reaction mixture was photolyzed from the bottom of the

Erlenmeyer with a 100W mercury lamp for 10 hours while the temperature was maintained at 28-30 ^{o}C. At the end of the reaction time the reaction mixture was a clear, pale yellow. The reaction mixture was worked up as described above. This residue was purified by column chromatography on silica gel, eluting with hexanes, giving N-(1-naphthyl)carbazole as a white solid. The NMR parameters for the isolated material match those previously reported.[40] ^{1}H NMR ($CDCl_3$, 500 MHz): δ 8.27 (d, 2H, J=8 Hz), 8.07 (m, 2H), 7.69 (m, 2H), 7.58 (t, 1H, J=8 Hz), 7.41-7.34 (m, 6H), 7.06 (d, 2H, J=8 Hz) ppm. ^{13}C NMR ($CDCl_3$): δ 142.2, 134.9, 134.1, 131.0, 129.1, 127.0, 126.8, 125.9, 123.7, 123.3, 130.4, 119.8, 110.3 ppm.

Synthesis of N-(4-cyanophenyl)carbazole (5.13) from 4-chlorobenzonitrile and 5.1: 4-chlorobenzonitrile (39.4 mg, 0.29 mmol, 1.2 equiv.) was dissolved in CH_3CN (20 mL) and added to solid **5.1** (200 mg, 0.24 mmol) to give a clear solution after stirring for ~10 minutes in the dark. The solution was transferred to a 500 mL Erlenmeyer flask equipped with a ground glass joint. The Erlenmeyer flask was sealed with a well-greased stopper and rubber bands. The reaction mixture was photolyzed from the bottom of the Erlenmeyer with a 100W mercury lamp for 10 hours while the temperature was maintained at 28-30 ^{o}C. At the end of the reaction time the reaction mixture was a clear, pale pinkish-orange. The reaction mixture was worked up as described above. This residue was purified by column chromatography on silica gel, eluting with 2% ethyl acetate in hexanes, giving N-(1-naphthyl)carbazole as a white solid. The NMR parameters for the isolated material match those previously reported.[41] ^{1}H NMR ($CDCl_3$, 300 MHz): δ 8.15 (d, 2H, J=8 Hz), 7.9 (d, 2H, J=8Hz), 7.7 (d, 2H, J=8 Hz), 7.47 (m, 4H),

7.36 (t, 2H, J=8 Hz) ppm. ^{13}C NMR ($CDCl_3$): δ 142.0, 139.9, 133.9, 127.1, 136.4, 123.9, 121.0, 120.6, 118.4, 110.4, 109.5 ppm.

Competition reaction between 1-bromonaphthalene and 4-chlorocyanobenzene: 10 mg of **5.1** (0.0119 mmol) was combined with 5 eq. each of 1-bromonaphthalene and 4-chlorocyanobenzene in 1.0 mL of acetonitrile in a 20 mL glass scintillation vial, and sealed with a PTFE-lined cap and electrical tape. The vial was illuminated from the bottom with a 100W Hg lamp for 10 hours, then opened to the atmosphere, diluted with THF, and analyzed by GC against a calibrated internal standard (4,4'-di-*t*-butylbiphenyl). On average over two trials, **5.12** and **5.13** were formed in a 1:1.83 ratio (24% yield of **5.12**, 44% yield of **5.13**).

Synthesis of [Cu(carbazolide)$_2$][Li(12-crown-4)$_2$] (5.11). This synthesis was performed under inert atmosphere in a glovebox. Lithium carbazolide (200 mg, 1.13 mmol), prepared by treatment of carbazole with *n*-butyllithium at -78 ^oC in diethyl ether, was dissolved in acetonitrile (5 mL) and added to a suspension of copper(I) iodide (107 mg, 0.56 mmol) in acetonitrile (1 mL) at room temperature. The solution, which darkened to a greenish-yellow color, was stirred for 30 minutes and then filtered through Celite, giving a bright orange-yellow filtrate. 1,4,7,10-tetraoxacyclododecane (12-crown-4, 200 mg, 1.13 mmol) was dissolved in acetonitrile (1 mL) and added to the filtrate while stirring, resulting in the immediate precipitation of [Cu(carbazolide)$_2$][Li(12-crown-4)$_2$] as a white solid. This solid was collected atop a sintered glass frit and washed with acetonitrile (2 x 1 mL) and then with copious diethyl ether, giving 288 mg (68%) of the desired complex. Crystals suitable for x-ray diffraction were grown by layering diethyl ether over a saturated THF solution at room temperature. ^1H NMR (300 MHz, CD_2Cl_2,

298 K): δ 8.04 (d, 2H, J = 8 Hz), 7.87 (d, 2H, J= 8 Hz), 7.32 (t, 2H, J = 8 Hz), 6.99 (t, 2H, J = 8 Hz), 3.38 (s, 16H, 12-crown-4) ppm. ESI-MS (negative ion mode) *m/z*: 395.2, 397.2 $[Cu(carbazolide)_2]^-$. Anal. Calcd for $C_{40}H_{48}N_2O_8CuLi$: C, 63.61; H, 6.41; N, 3.71. Found: C, 62.85; H, 6.42; N, 3.71.

Synthesis of $[Cu(carbazolide)_2][Li(MeCN)_4]$ (5.10). Lithium carbazolide (364 mg, 2.10 mmol), prepared by treatment of carbazole with *n*-butyllithium at -78 ^oC in Et_2O, was dissolved in acetonitrile (10 mL) and added to a suspension of copper(I) iodide (200 mg, 1.05 mmol) in acetonitrile (1 mL) at room temperature. The solution, which took on a dark green appearance due to the formation of a fine black precipitate, was stirred for 30 minutes and then filtered through Celite, giving a bright orange-yellow filtrate. This filtrate was concentrated to a gooey orange solid which was dried under vacuum for two hours. This material was then taken up in benzene (1 mL) and pentane was added (2 mL) to precipitate a sticky yellow-white solid. The supernatant was then decanted from the sticky solid. This procedure (take up the solid in benzene, add pentane to precipitate a sticky mass, decant supernatant) is repeated 3-4 times until the solid no longer dissolves in benzene and instead forms a free-flowing, off-white powder. This powder was isolated atop a sintered glass frit and washed with benzene (3 x 5 mL) and pentane (3 x 5 mL), giving 240 mg of the title compound (45%). ^1H NMR (300 MHz, CD_2Cl_2, 298 K): δ 8.07 (d, 4H, J = 8 Hz), 7.86 (d, 4H, J = 8 Hz), 7.36 (t, 4H, J = 8 Hz), 7.06 (t, 4H, J = 8 Hz), 1.88 (s, 12H) ppm. ESI-MS (negative ion mode) *m/z*: 395.2, 397.2 $[Cu(carbazolide)_2]^-$.

5.5 References and Notes:

1. A. S. Travis, in *Chemistry of Anilines*, Z. Rapaport, Ed. (John Wiley & Sons, New York, 2007), Vol. 1, pp. 1–73.
2. A. S. Travis, in *Chemistry of Anilines*, Z. Rapaport, Ed. (John Wiley & Sons, New York, 2007), Vol. 2, pp. 715–782.
3. *Atorvastatin in the Management of Cardiovascular Risk: From Pharmacology to Clinical Evidence*, S. Grundy, Ed. (Kluwer, Auckland, New Zealand, 2007).
4. Ullmann, F. *Ber. Dtsch. Chem. Ges.* **1903**, *36*, 2382.
5. Goldberg, I. *Ber. Dtsch. Chem. Ges.* **1906**, *39*, 1691.
6. Monnier, F.; Taillefer, M. *Angew. Chem. Int. Ed.* **2009**, *48*, 6954.
7. Evano, G.; Blanchard, N.; Toumi, M. *Chem. Rev.* **2008**, *108*, 3054.
8. Beletskaya, I. P.; Cheprakov, A. V.; *Coord. Chem. Rev.* **2004**, *248*, 2337.
9. Ley, S. V.; Thomas, A. W. *Angew. Chem. Int. Ed.* **2003**, *42*, 5400.
10. L. Jiang, S. L. Buchwald, in *Metal-Catalyzed Cross-Coupling Reaction*s, A. De Meijere, F. Diederich, Eds. (Wiley–VCH, New York, 2004), Vol. 2, pp 699–760.
11. J. F. Hartwig, S. Shekhar, Q. Shen, F. Barrios–Landeros, in *Chemistry of Anilines*, Z. Rapaport, Ed. (John Wiley & Sons, New York, 2007), Vol. 1, pp. 455–536.
12. Sperotto, E.; van Klink, G. P. M.; van Koten, G.; de Vries, J. G. *Dalton Trans.* **2010**, *39*, 10338.
13. Tye, J. W.; Weng, Z.; Johns, A. M.; Incarvito, C. D.; Hartwig, J. F. *J. Am. Chem. Soc.* **2008**, *130*, 9971.
14. Giri, R.; Hartwig, J.F. *J. Am. Chem. Soc.* **2010**, *132*, 15860.

15. Jones G. O.; Liu, P.; Houk, K. N.; Buchwald, S. L. *J. Am. Chem. Soc.* **2010**, *132*, 6205.

16. Yu, H.-Z.; Jiang, Y.-Y.; Fu, Y.; Liu, L. *J. Am. Chem. Soc.* **2010**, *132*, 18078.

17. Harkins, S. B; Peters, J. C. *J. Am. Chem. Soc.* **2005**, *127*, 2030.

18. Deaton, J. C. *et al. J. Am. Chem. Soc.* **2010**, *132*, 9499.

19. Lotito, K. J.; Peters, J. C. *Chem. Commun.* **2010**, *46*, 3690.

20. Rossi, R. A. *Acc. Chem. Res.* **1982**, *15*, 164.

21. Xi, Z.; Liu, F.; Zhou, Y.; Chen, W. *Tetrahedron* **2008**, *64*, 4254.

22. Mankad, N. P.; Antholine, W. E.; Szilagyi, R. K.; Peters, J. C. *J. Am. Chem. Soc.* **2009**, *131*, 3878.

23. Enemaerke, R. J.; Christensen, T. B.; Jensen, H.; Daasbjerg, K. *J. Chem. Soc., Perkin Trans. 2* **2001**, 1620.

24. Keller, C. L.; Dalessandro, J. D.; Hotz, R. P.; Pinhas, A. R. *J. Org. Chem.* **2008**, *73*, 3616.

25. Solomon, E. I. *Inorg. Chem.* **2006**, *45*, 8012.

26. Hay, M.; Richards, J. H.; Lu, Y. *Proc. Natl. Acad. Sci.* **1996**, *93*, 461.

27. Annunziata, A.; Galli, C.; Marinelli, M.; Pau, T. *Eur. J. Org. Chem.* **2001**, 1323.

28. In introductory textbooks on organic chemistry, the alkylation of amines with alkyl halides is often the first reaction of amines that is described. For example, see: (a) M. Loudon in Organic Chemistry, 5th ed., Roberts & Company, Greenwood Village, 2009, chap. 23.7A. (b) J. McMurry, Organic Chemistry, Brooks/Cole, Belmont, 2012, chap. 24.7.

29. In a recent "Analysis of the reactions used for the preparation of drug candidate molecules" (Carey, J. S.; Laffan, D.; Thomson, C.; Williams, M. T. *Org. Biomol. Chem.* **2006**, *4*, 2337.), "Heteroatom alkylation & arylation" was the reaction category with the highest frequency use (19%; Table 2). Within this category, "N-substitution" was the most-often-used process (57%; Table 10), and, within N-substitution, "N-Alkylation with Alk-X" was the most frequently employed reaction (36%; Table 11).
30. There are isolated reports of N-alkylations of amines with unactivated alkyl halides that proceed in the presence of a substoichiometric quantity of a transition metal. For example, see: (a) Aydin, A.; Kaya, I. *Electrochim. Acta.* **2012**, *65*, 104. (165 ^{o}C; primary alkyl bromide); (b) Tu, X.; Fu, X.; Jiang, Q.; Liu, Z.; Chen, G. *Dyes Pigm.* **2011**, *88*, 39. (80 ^{o}C; primary alkyl bromide); (c) Kozuka, M.; Tsuchida, T.; Mitani, M. *Tetrahedron Lett.* **2005**, *46*, 4527. (83 ^{o}C; primary alkyl bromide).
31. Non-negligible product formation under irradiation in the absence of CuI (16% versus 76% for cyclohexyl iodide) may be due to the photophysical properties of lithium carbazolide itself. See: Vos, H. W.; Blom, H. H.; Velthorst, N. H.; MacLean, C. *J. Chem. Soc. Perkin Trans. 2* **1972**, 635.
32. We are not aware of previous investigations of $[Cu(carbazolide)_2]^-$ complexes. However, $[Cu(anilide)_2]^-$ complexes have been proposed as intermediates in nonphotochemical arylations of anilines; see reference 14 and Tsen, C.-K.; Lee, C.-R.; Han, C.-C.; Shyu, S.-G. *Chem. Eur. J.* **2011**, *17*, 2716.

33. (a) Ziegler, D.; Choi, J.; Munoz-Molina, J.; Bissember, A.; Peters, J. C.; Fu, G. C. *J. Am. Chem. Soc.* **2013**, *135*, 13107. (b) Uyeda, C.; Tan, Y.; Fu, G. C.; Peters, J. C. *J. Am. Chem. Soc.* **2013**, *135*, 9548. (c) Tan, Y.; Munoz-Molina, J. M.; Fu, G. C.; Peters, J. C. *Chem. Sci.* **2014**, *5*, 2831. (d) Do, H. Q.; Bachman, S.; Bissember, A. C.; Peters, J. C.; Fu, G. C. *J. Am. Chem. Soc.* **2014**, *136*, 2162. (e) Ratani, T.; Bachman, S.; Fu, G. C.; Peters, J. C. *J. Am. Chem. Soc.* **2015**, *137*, 13902.

34. Goering, H. L.; Jacobson, R. R. *J. Am. Chem. Soc.* **1958**, *80*, 3277.

35. Molander, G. A.; Harring, L. S. *J. Org. Chem.* **1990**, *55*, 6171.

36. Buchwald, S. L.; LaMaire, S. J.; Nielsen, R. B.; Watson, B. T.; King, S. M. *Org. Synth.* **1993**, *71*, 77.

37. Orain, D.; Guillemin, J.-C. *J. Org. Chem.* **1999**, *64*, 3563.

38. Stoll, S.; Schweiger, A. *J. Magn. Reson.* **2006**, *42*, 178.

39. Sheldrick, G. M. *Acta. Cryst.* **2008**, *A64*, 112.

40. Workup procedure adapted from Wolfe, J. P.; Buchwald, S. L. *J. Am. Chem. Soc.* **1997**, *119*, 6054.

41. Boisvert, G.; Giasson, R. *Tet. Lett.* **1992**, *33*, 6587.

42. Zhou, Y.; Verkade, J. G. *Adv. Synth. Catal.* **2010**, *351*, 616.

Chapter 6. Spin-state Tuning at Pseudotetrahedral d^6 Ions – Reversible Spin-Crossover in $[BP_3]Fe^{II}$-X Complexes

6.1 Introduction

Spin-crossover phenomena in molecular systems are of interest in part due to their potential applications in magnetic sensing and information storage.[1] Spin crossover complexes can act as a type of molecular switch, where properties such as color and magnetism undergo large changes when appropriate stimuli—for instance heat, pressure, or light—are applied. Such responsive behavior is desirable for materials applications, especially when the complexes exhibit abrupt spin transitions and/or bistability.[2-5] Spin-crossover molecules which exhibit gradual and non-hysteretic spin equilibria have also shown potential for applications in sensing.[6] More generally, spin-crossover has been implicated as an important factor in chemical processes that occur at and are facilitated by transition metal centers such as those in metalloenzymes.[7]

Direct and predictable structure-function correlations between magnetic properties and molecular structure that would allow for the rational design and synthesis of spin-crossover systems have yet to be fully realized. For this reason, chemists continue to pursue a more thorough understanding of the factors that govern the existence and properties of a spin-crossover transition both in solution and in the solid state.[8] One advantage of studying molecular systems is that, since the spin state of a transition metal complex is dependent on the balance between the ligand field stabilization energy and spin pairing energy of the valence d-electrons, spin crossover can serve as a sensitive reporter of the energetic landscape of the spin states and valence orbital manifold of a metal complex. Subtle changes in the primary coordination environment of a molecular system affect these properties and thus the energetics of the available spin manifold. Therefore, a molecular system that exhibits well-defined and tunable spin-crossover can

provide a great deal of information about the impact of small changes to the coordination environment of a metal ion on its electronic structure.

To date, the vast majority of known spin-crossover complexes are 6-coordinate, octahedral d^6 iron(II) complexes, typically with coordination spheres composed primarily of N, O, and C donors, due to the often favorable balance of ligand field strength and spin-pairing energy in these complexes.[9,10] Low-coordinate spin-crossover complexes are more rare. For example, earlier work in our own laboratory on pseudotetrahedral cobalt(II) complexes established for the first time the possibility of spin-crossover in pseudotetrahedral d^7 ions. This work capitalized on the electronic structure engendered by strong-field tripodal "$PhBP_3$" ligands, enabling spin-state tuning without severe geometric changes.[11-13] Five-coordinate spin-crossover complexes of iron have been known since the 1970s,[14] but the first pseudotetrahedral spin-crossover complex of iron(II) was reported only in 2011,[15] with several other four-coordinate examples having been characterized since then.[16,17] These pseudotetrahedral iron(II) spin-crossover complexes, and those that will be described herein, build on and expand the electronic structure framework that had been established for the $[PhBP_3]Co^{II}$-X systems.[11-13]

In 2004 our lab reported the partial N-atom transfer of a terminal iron(IV) nitride, $[PhBP^{iPr}_3]Fe(N)$, to triphenyl- and triethylphosphine to afford the iron(II) phosphiniminato complexes of the type $[PhBP^{iPr}_3]Fe\text{-}N{=}PR_3$.[18] During the course of more recent N-atom transfer studies we noted that several complexes of the general type $[PhBP^{R}_3]Fe\text{-}N{=}PR'_3$ are involved in spin equilibria at room temperature. These pseudotetrahedral d^6 complexes benefit from the electronic properties of the phosphiniminato ligand[15,16] to exhibit spin transitions between diamagnetic $S = 0$ states

and high-spin S = 2 states. Modifications to the ligand substituents, both on the trisphosphine borate chelate and on the phosphiniminato moiety, allow for multifaceted tuning of the spin states and crossover temperatures. They can range from complexes that are high-spin at all temperatures to those with a spin-crossover critical temperature (T_c) as high as 405 K. We introduce a versatile synthetic protocol for installing the phosphiniminato ligand that allows the spin-crossover system to be easily and rationally tuned across a wide range of temperatures, including near and above room temperature. This ease of tunability may be of interest for future applications.

6.2 Results

6.2.1 Synthesis of [PhBP$^{R}_3$]Fe(N=PR'$_3$) Complexes

Transition metal complexes of phosphiniminato (-N=PR_3) ligands are common, especially for early transition metals such as titanium and other group 4-6 metals, and are most typically synthesized either by reaction of an electrophilic metal nitride with a phosphine, or via metathesis between $Me_3SiN=PR_3$ and an M-Cl species via loss of Me_3SiCl.[19] The structurally characterized examples of phosphiniminato ligands on group 8 or 9 transition metals have generally been synthesized by reaction of terminal nitride complexes with phosphines (Scheme 6.1A).[15,16,18,20] We sought a more general synthetic pathway that would be applicable to systems where nitride species are not readily accessible.

We have determined that salt metathesis between previously reported [PhBP$^{R}_3$]FeCl precursors[21] and LiN=PR'$_3$ reagents affords the desired phosphiniminato complexes in good yields (Scheme 6.1B). The lithiated phosphiniminatos are generated in situ, first by double deprotonation of the phosphiniminium chlorides, [H_2NPR'$_3$]Cl, with *n*-

butyllithium, followed by addition to the iron(II) chloride precursors at low temperature in THF. This route was facilitated by the recent report of a synthesis of $[H_2NPPh_3]Cl$ by the sequential treatment of triphenylphosphine with hexachloroethane and ammonia gas; we have found that this synthetic route can be generalized to other phosphines, including trialkylphosphines, under anhydrous conditions.[22] The $[PhBP^{iPr}_3]Fe\text{-}N{=}PPh_3$ (**7**) and $[PhBP^{iPr}_3]Fe\text{-}N{=}PEt_3$ (**9**) complexes synthesized by this method show identical solution spectroscopic properties to those previously generated by reaction of the thermally unstable terminal nitride $[PhBP^{iPr}_3]Fe{\equiv}N$ with PPh_3 or PEt_3 (Scheme 6.1A).[18]

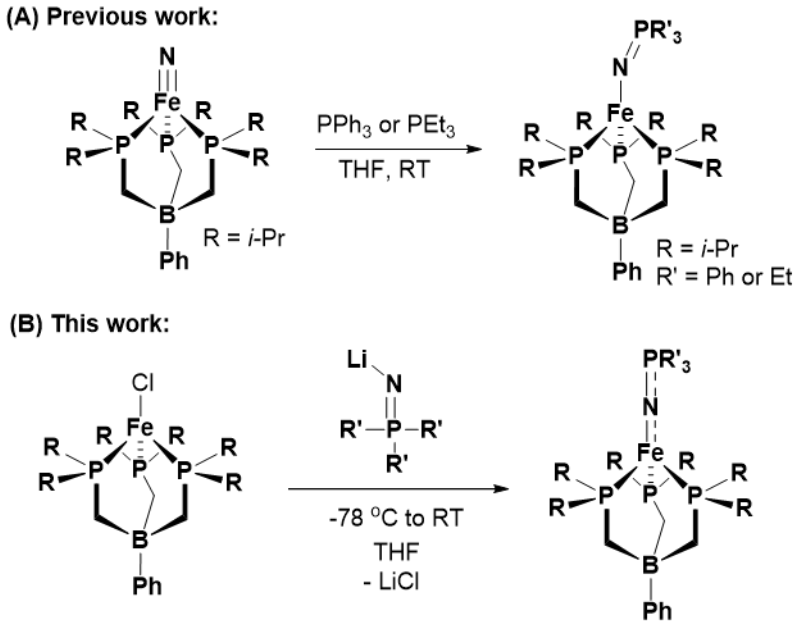

$[PhBP^{Ph}_3]Fe(NPPh_3)$	**6.1**	$[PhBP^{m\text{-}ter}_3]Fe(NPCy_3)$	**6.6**
$[PhBP^{Ph}_3]Fe(NPCy_3)$	**6.2**	$[PhBP^{iPr}_3]Fe(NPPh_3)$	**6.7**
$[PhBP^{CH2Cy}_3]Fe(NPPh_3)$	**6.3**	$[PhBP^{iPr}_3]Fe(NPCy_3)$	**6.8**
$[PhBP^{CH2Cy}_3]Fe(NPCy_3)$	**6.4**	$[PhBP^{iPr}_3]Fe(NPEt_3)$	**6.9**
$[PhBP^{m\text{-}ter}_3]Fe(NPPh_3)$	**6.5**		

Scheme 6.1. Synthesis and numbering scheme for complexes **6.1**-**6.9**.

6.2.2 Structural Characterization

Complexes **6.1**, **6.2**, **6.4**, **6.5**, and **6.7**-**6.9** have been structurally characterized by X-ray crystallography (Figure 6.1). Metrical parameters of interest are tabulated in Table 6.1. The Fe-P distances are strongly correlated with the spin state, lengthening by ~ 0.3 Å between the low-spin and high-spin forms, and the complexes can hence be readily divided into two categories (high- or low-spin) based on their structural parameters (pictorially represented in Figure 6.2). Indeed, the change in Fe-P distance in response to the spin state makes such assignments using the solid-state metrical parameters facile and unambiguous, as was observed for the previously [$PhBP_3$]CoX system where the Co-P distances are likewise highly responsive to spin state.[11-13] Accordingly, low-spin complexes **6.1**, **6.2**, **6.4**, and **6.5** display shorter Fe-P (avg ~ 2.15 Å) and Fe-N (~ 1.75 Å) bond lengths, a longer N-P bond (1.58 Å), and a nearly linear Fe-N-P angle. In contrast, the high-spin complexes **6.7**, **6.8**, and **6.9** feature long Fe-P bonds (avg ~ 2.45 Å), a longer Fe-N bond (1.85 Å), and a somewhat shorter N-P bond (1.53 Å), along with a moderately bent Fe-N-P bond angle (160° - 165°). The changes in Fe-N and N-P bond lengths are consistent with a higher degree of Fe-N multiple bonding in the low-spin state, concomitant with a shorter Fe-N bond. The high-spin species, by contrast, feature stronger and shorter N-P double bonds and likely minimal multiple bonding character between the Fe and N atoms.

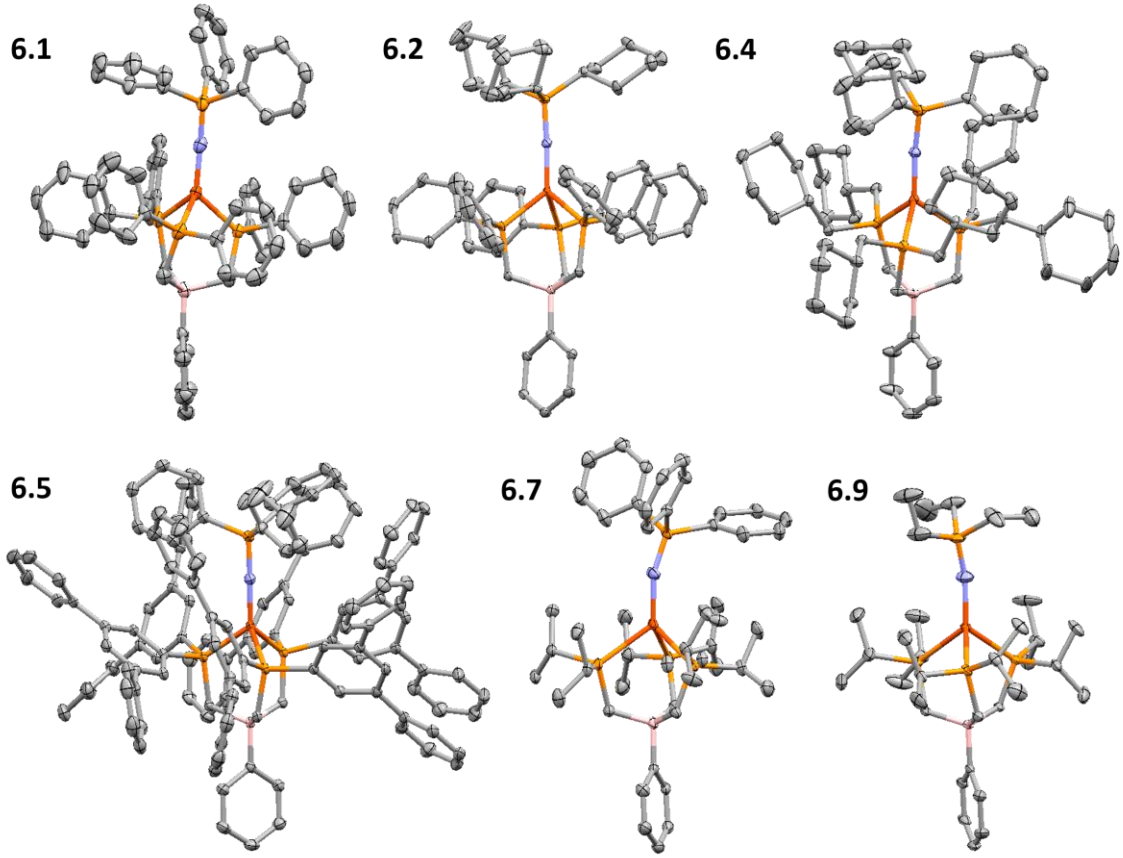

Figure 6.1. Crystal structures of complexes **6.1**, **6.2**, **6.4**, **6.5**, **6.7** and **6.9**. The structure of complex **6.8** is shown in Appendix B. Thermal ellipsoids represented at 50% probability; solvents and hydrogen atoms omitted for clarity.

	6.1[a]	***6.2***	***6.4***[a]	***6.5***	***6.7***	***6.8***	***6.9***
R, R'	Ph, Ph	Ph, Cy	CH_2Cy, Cy	*m*-ter, Ph	*i*Pr, Ph	*i*Pr, Cy	*i*Pr, Et
Fe-P (avg, Å)	2.1621(11)	2.1673 (5)	2.1682(2)	2.1560(7)	2.4629(13)	2.5085(10)	2.4368(5)
Fe-N (Å)	1.757(3)	1.7382 (16)	1.7446(17)	1.7360(18)	1.859(3)	1.842(5)	1.8325(17)
N-P (Å)	1.576(3)	1.5972 (16)	1.5815(17)	1.5866(19)	1.534(3)	1.559(6)	1.5192(17)
Fe-N-P (°)	174.8(2)	174.99 (11)	174.28(11)	177.48(14)	159.8(2)	163.0(9)	165.30(14)

Table 6.1. Metrical parameters for the solid-state structures of **6.1**, **6.2**, **6.4**, **6.5**, and **6.7-6.9**. All data was acquired at 100(2) K. [a]Parameters averaged over two independent molecules in the asymmetric unit.

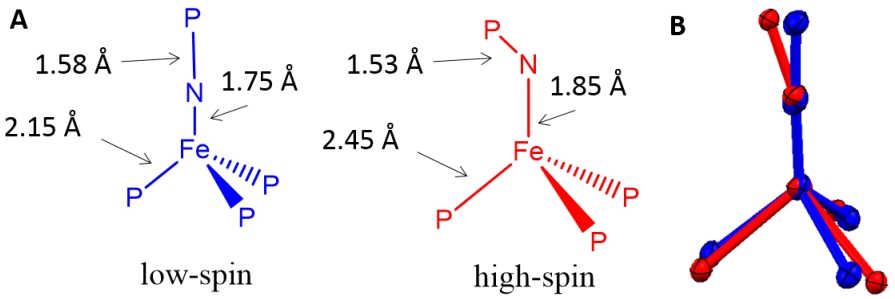

Figure 6.2. (**A**) Visually exaggerated representation of the changes in metrical parameters between structurally characterized low- and high-spin [PhBP$^{R}_{3}$]Fe(N=PR'$_{3}$) complexes, with representative approximate bond lengths. (**B**) Overlay of the representative core structures of **6.1** (low spin, blue) and **6.7** (high spin, red).

The changes in metrical parameters observed among complexes **6.1**-**6.9** are comparable to those observed by Smith *et al* for a series of tris(carbene)borate iron phosphiniminato complexes ([PhB(MesIm)$_3$]Fe(N=PR$_3$)); similarly, these complexes exhibit longer Fe-N and shorter N-P bonds in the respective high-spin complexes as compared to the low-spin complexes.[15,16]

6.2.3 UV-visible Spectroscopy

Spin crossover in complexes **6.1**-**6.6** and **6.9** is accompanied by a striking color change from deep blue or purple in the low-spin form, populated at low-temperature, to a pale yellow in the high-spin form at higher temperature. Notably, the high-spin states (including **6.7** and **6.8**, which do not undergo spin-crossover at any temperature examined) display completely featureless absorption spectra in the range from ~475 nm to 900 nm, whereas the low-spin states display three clear features in this region (Figure 6.3). The energies of these absorptions vary in each complex (Table 6.2) but the spectra show the most intense absorption at ~590 nm with a discernible shoulder around ~550

nm, and a slightly weaker, well-separated absorption at ~700 nm. In some cases, and most notably in complex **6.4** (Figure 6.3D), the high-spin state displays a discernible absorbance around ~400 nm that is not present in the low-spin state; this feature does not interfere with analysis of the longer-wavelength regime.

These properties make it possible to quantitatively model the spin-equilibria in these complexes based on the absorbance intensities, as the absorbance in the 475-900 nm range originates only from the low-spin states. This analysis can be carried out even if the absorption coefficients of the pure low-spin state are unknown. However, several corrections must be applied. First, due to the change in density of the solvent (toluene) with temperature, the effective concentration of the sample changes as the temperature is raised or lowered; the absorption must be multiplied by a simple scaling factor at each temperature to account for this change. Secondly, due to the change in absorption lineshapes with temperature, simply charting the absorbance at the maximum for a given peak is inadequate. Instead, the spectra at each temperature are modeled as the sum of three Gaussian functions (Equation 6.1, Figure 6.4),

$$\mathrm{Abs}(\lambda) = \sum_{n=1}^{3} \frac{c_n a_n}{\sqrt{\pi}} \exp\left(-a_n^2\left(\lambda - \lambda_{max,n}\right)\right) \qquad (6.1)$$

where the parameter c_n is the area of each peak, a_n is related to the width (FWHM) of the peak, and $\lambda_{max,n}$ is the wavelength of maximum absorption for each peak. The areas of these Gaussian peaks (parameter c_n) are then correlated with the concentration of the low-spin species. These can be fit to a Boltzmann equilibrium expression for the spin crossover to extract thermodynamic parameters,

$$x_{ls}(\mathrm{T}) = \frac{1}{1+\exp\left(-\frac{\Delta \mathrm{H}}{\mathrm{R}}\left(\frac{1}{\mathrm{T}}-\frac{1}{\mathrm{T}_c}\right)\right)} \quad (6.2)$$

$$x_{ls} = c/c_{max} \quad (6.3)$$

where $x_{ls}(\mathrm{T})$ is the low-spin mole fraction as a function of the temperature T, c is the Gaussian fit parameter as in Equation 1, c_{max} is the value of c when $x_{ls} = 1$, *i.e.* in the low-temperature limit, ΔH is the enthalpy difference between the low- and high-spin states, and T_c is the critical temperature, *i.e.* the temperature at which equal amounts of the high- and low-spin form are present. The enthalpy and entropy differences between the states, ΔH and ΔS ($\Delta S = \Delta H/T_c$), are assumed to be approximately independent of temperature over the range studied. A first-order baseline was included in the fits to roughly account for the tailing of absorption bands outside the modeled range; in most cases this correction is negligible.

The temperature dependent UV-vis spectra for complexes **6.1-6.4** are shown in Figure 6.3, and the resulting fits to the transition intensities according to Equation 6.2 for complexes **6.1-6.6** are given in Figure 6.5. The maximum and minimum intensities are allowed to refine freely and only one peak (that at ~700 nm for each species) is considered. Repeating the analysis with the other major peaks, or with the total area of all three peaks, gives similar results. Robust values for the critical temperature T_c are obtained in each case, while the exact values of ΔH and ΔS are subject to a higher degree of error and can fluctuate depending on the details of the fitting procedure. However, trends between different complexes are well-reproduced as long as the data are treated in a consistent fashion. Further discussion of the UV-vis data analysis and detailed results are provided in Appendix B.

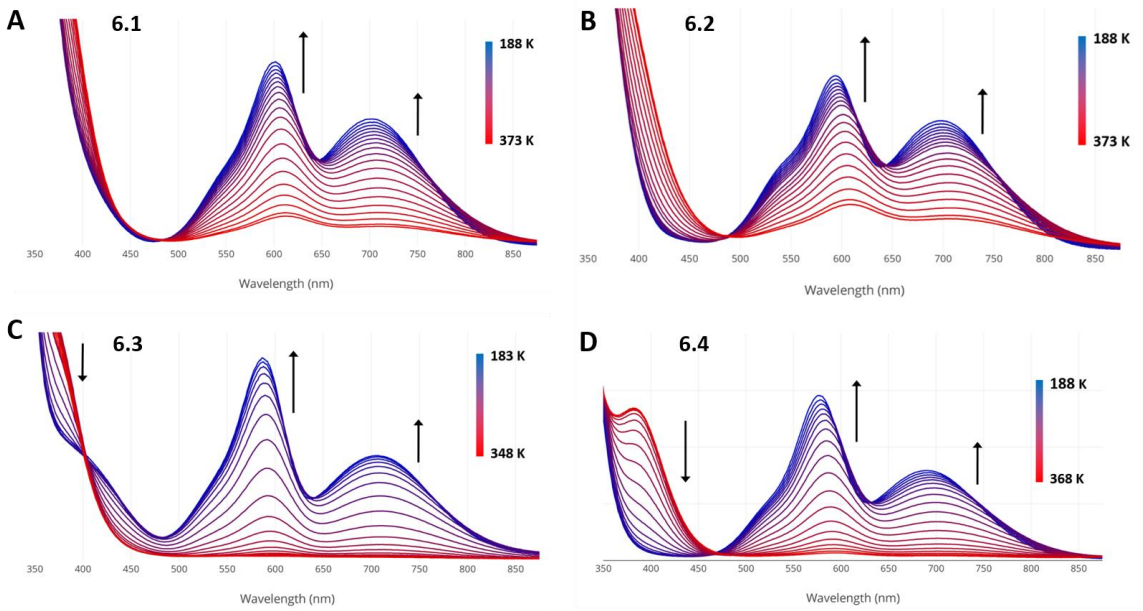

Figure 6.3. Temperature-dependent UV-vis spectra of complexes **6.1**-**6.4**. Arrows represent the direction of change when the temperature is lowered. Spectra for complexes **6.5**, **6.6**, and **6.9** can be found in Appendix B.

	6.1	***6.2***	***6.3***	***6.4***	***6.5***	***6.6***	***6.9***
R,R'	Ph,Ph	Ph,Cy	CH_2Cy, Ph	CH_2Cy, Cy	*m*-ter,Ph	*m*-ter,Cy	*i*Pr,Et
λ_{max} *(188 K, nm)*	563	549	552	534	557	547	558
-	603	596	590	579	604	598	600
-	703	698	705	690	713	707	734
ε $(M^{-1} cm^{-1})^a$	1700	1400	1100	560	2700	940	--[b]

Table 6.2. Absorption maxima for three ligand-field transitions in the low-spin forms of **6.1**-**6.6** and **6.9**. [a]Extinction coefficients are provided for the lowest energy transition (~700 nm) of each complex at the lowest temperature measured in each case. [b]ε was not calculated for **6.9** due to the highly incomplete spin crossover at accessible temperatures.

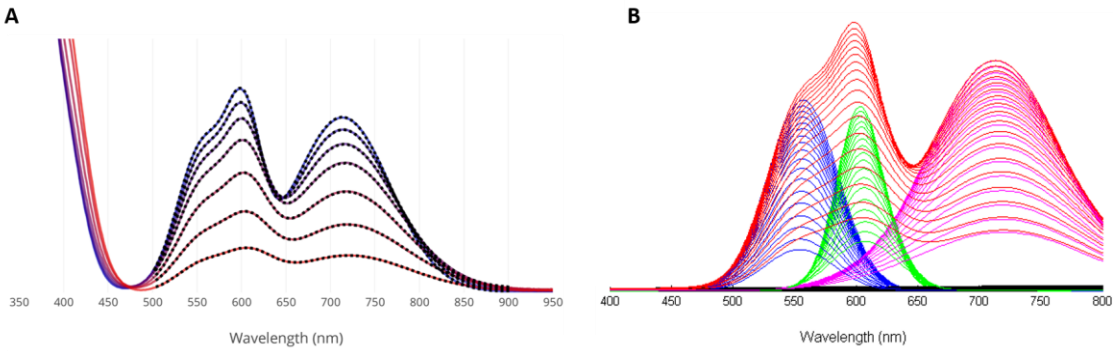

Figure 6.4. Example of the decomposition of the temperature-dependent UV-Vis spectra of **6.5** into sets of three Gaussian functions. (**A**) Fits (dotted lines) to the absorbance spectra at temperatures ranging from 188 K to 383 K. For clarity, only a subset of the full data set is shown. (**B**) Decomposition of the fitted spectra (red) into three Gaussian functions (blue, green, pink) with a minor linear baseline (black).

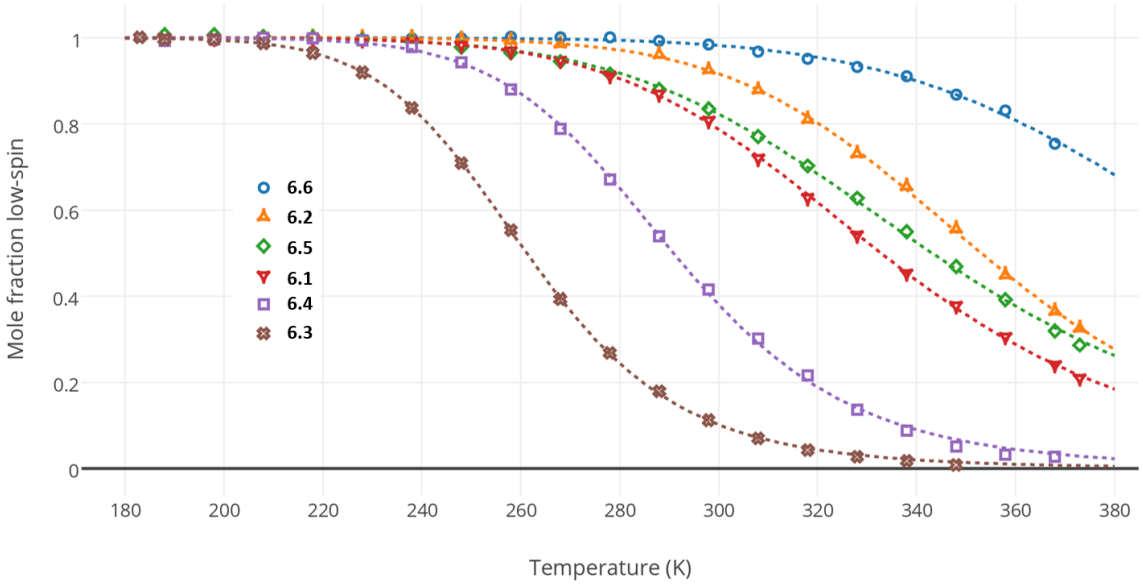

Figure 6.5. Fractional occupation of the low-spin state modeled according to a spin equilibrium showing Boltzmann behavior, based on UV-vis intensity data for the compounds **6.1**-**6.6**. Dotted lines are fits to Equation 6.3.

	6.1	***6.2***	***6.3***	***6.4***	***6.5***	***6.6***
R,R'	Ph,Ph	Ph,Cy	CH_2Cy,Ph	CH_2Cy,Cy	*m*-ter,Ph	*m*-ter,Cy
ΔH (cm^{-1})	2751	3302	3032	3213	2532	3198
ΔS (cm^{-1}/K)	8.3	9.4	11.6	11.0	7.4	7.9
T_c *(K)*	333	353	261	291	343	405

Table 6.3. Thermodynamic parameters for the spin equilibria in compounds **6.1**-**6.6** derived from variable temperature UV-vis measurements.

While compounds **6.7** and **6.8** ([PhBP$^{i\text{Pr}}_3$]Fe(NPPh$_3$) and [PhBP$^{i\text{Pr}}_3$]Fe(NPCy$_3$), respectively) do not undergo observable spin crossover in the temperature range studied, the less sterically hindered triethyl phosphiniminato complex **6.9** begins to populate a low-spin state at very low temperatures; such solutions concomitantly acquire a greenish tinge when cooled below about -50 ^{o}C. Low temperature UV-vis data confirms that a species with spectral parameters similar to the other low spin complexes grows in at very low temperature in toluene solution.[23] T_c for this complex is well below that observed for complexes **6.1**-**6.6**.

6.2.4 NMR Characterization and Solution Magnetic Susceptibility Measurements

All of the complexes studied display paramagnetically shifted and broadened NMR spectra at room temperature, consistent with at least partial occupation of a paramagnetic state. As the temperature is lowered, for complexes **6.1**-**6.6** and **6.9**, the ^{1}H NMR chemical shifts approach the expected region for diamagnetic complexes (~0-9 ppm), and, in most cases, broad ^{31}P NMR peaks become discernible. This behavior is consistent with spin-crossover to a diamagnetic state at low temperature. For a paramagnetic complex showing Curie behavior, the chemical shift range is expected to expand as the temperature is lowered due to the inverse relationship between temperature and magnetization. Deviations from the expected Curie behavior for the chemical shifts can

be quantitatively accounted for by the spin equilibrium and modeled to extract the thermodynamic parameters of the Boltzmann equilibrium, as given in Equation 6.4,[24]

$$\delta = \delta_{ls} + \frac{C}{T(1+\exp(-\frac{\Delta H}{R}(\frac{1}{T}-\frac{1}{T_c}))} \quad (6.4)$$

where δ is the measured chemical shift, δ_{ls} is the corresponding shift in the diamagnetic state, and *C* is the appropriate Curie's law constant. This method has been used to model the solution-state spin-crossover properties of other spin-crossover complexes in previous work.[16,25]

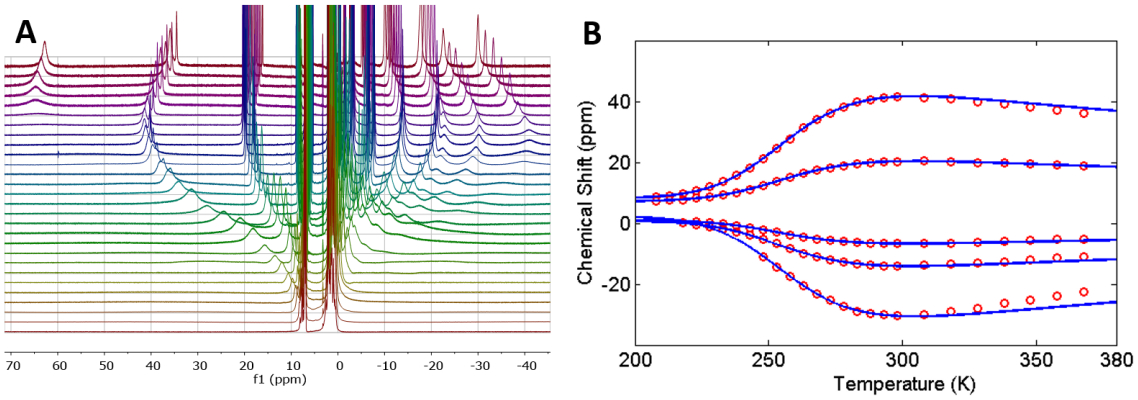

Figure 6.6. (A) Variable-temperature ^{1}H NMR spectra of **6.3** in d_8-toluene from 188 K (bottom) to 368 K (top), in 5 K increments from 188-298 K and 10 K increments above 298 K. **(B)** Change in the NMR chemical shift for several resonances from the ^{1}H NMR of **6.3** with temperature from 188 K to 368 K (red circles). Low-temperature data is omitted when the peak becomes too broad to be discerned clearly. Data was fit to a Curie Law/Boltzmann equilibrium expression (Eqn. 6.4) to model spin crossover (blue lines). Data above 300 K was omitted from the fits.

The values extracted from these fits are given in Table 6.4. A representative example of the temperature-dependent chemical shifts of **6.3** and the resulting fits to Equation 4

are shown in Figure 6.6; corresponding data for complexes **6.1**, **6.2**, and **6.4**-**6.5** can be found in Appendix B. For complexes **6.6** and **6.9**, although variable temperature NMR did show evidence of spin-crossover through changes in the chemical shifts and the variation in the solution magnetic moment (see below, Figure 6.7), the temperature range accessible was inadequate to allow for reliable fitting and extraction of thermodynamic parameters.

	6.1	***6.2***	***6.3***	***6.4***	***6.5***
R, R'	Ph, Ph	Ph, Cy	CH_2Cy, Ph	CH_2Cy, Cy	*m*-ter, Ph
ΔH (cm^{-1})	2659	2979	3194	3326	2291
ΔS (cm^{-1}/K)	8.0	8.3	12.3	11.6	6.6
T_c (K)	331	361	259	286	349

Table 6.4. Thermodynamic parameters for the spin equilibria in compounds **6.1**-**6.5** derived from variable temperature NMR chemical shift measurements. Thermodynamic parameters are derived from the average of the fitted parameters from at least two different resonances in the NMR spectra (see text and Appendix B for additional details).

The thermodynamic parameters derived from the fits to the chemical shifts according to Equation 2 qualitatively reproduce the trends in Δ*H* and Δ*S* extracted from the UV-vis data. Quantitatively, the parameters are also in good agreement; the Δ*H* values derived from the two methods agree within 10% in all cases and within 5% in most cases; the Δ*S* values agree within 12% in all cases and within 6% in most. The largest deviation is observed for complexes **6.2** and **6.5**. These complexes also exhibit the highest T_c of the compounds shown in Table 6.4 and thus undergo the most incomplete conversion to the high-spin form under the conditions studied.

The solution paramagnetism of these complexes was further examined by variable-temperature Evans method measurements which more directly probed the change in the

paramagnetic susceptibility and effective magnetic moment with temperature.[26] The variable-temperature Evans method results qualitatively confirm the change in spin state and the corresponding change in susceptibility of complexes **6.1**-**6.6** and **6.9** with temperature; representative data is shown in Figure 6.7. While the data could be fit to a Boltzmann-equilibrium expression, the fit parameters suffered from large uncertainties due to the relatively small range of temperatures for which χT could be reliably measured by this method.

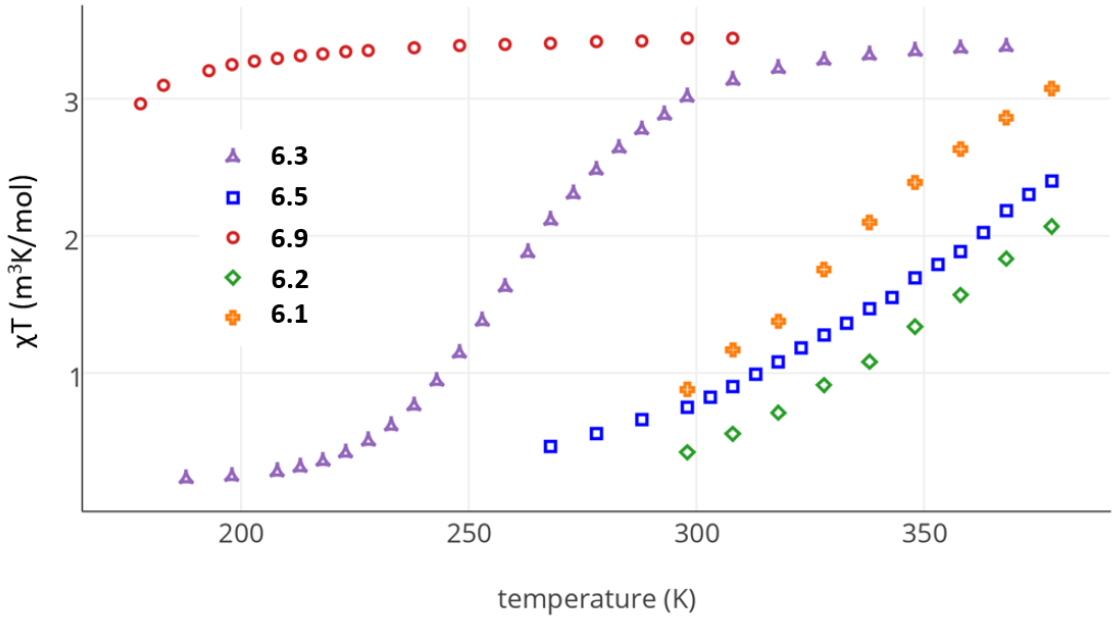

Figure 6.7. Variable-temperature magnetic susceptibility data, measured using the Evans method in d_8-toluene, for compounds **6.1**, **6.2**, **6.3**, **6.5**, and **6.9**. Susceptibility values have been corrected for diamagnetic contributions using Pascal's constants.

6.2.5 Solid-state (SQUID) magnetometry

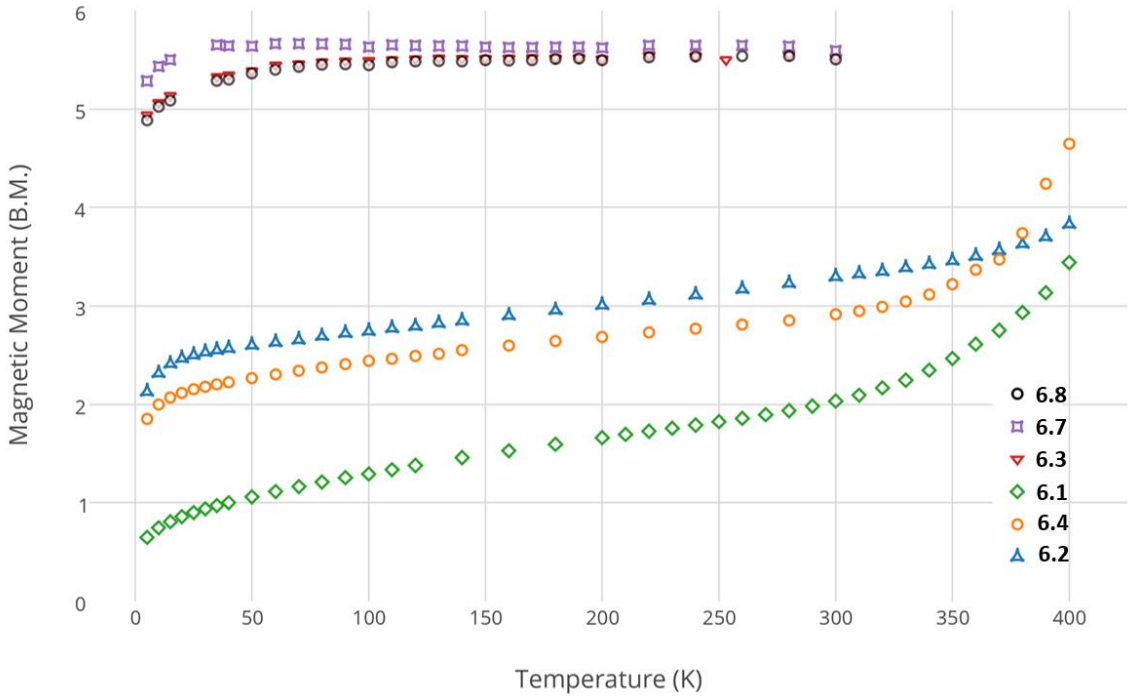

Figure 6.8. Solid-state magnetic moments of compounds **6.1**-**6.4**, **6.7**, and **6.8** measured by SQUID magnetometry. All samples were neat microcrystalline solids or powders, and the magnetic susceptibility was corrected for the approximate diamagnetic contribution derived from Pascal's constants. Measurements were carried out from low temperature to high temperature following initial cooling in zero field.

Spin-crossover molecules frequently show different behavior in the solid state than in solution. Often, the spin-state change in the solid state is no longer well described as a simple thermodynamic equilibrium and instead becomes dependent on crystallographic cooperativity, domain formation and interactions, and other solid-state effects which can cause either very abrupt or very gradual and incomplete spin-crossover.[27] These factors sometimes lead to hysteresis of T_c depending on the direction of temperature change.

Although neither hysteresis nor a very abrupt spin-crossover were observed for any of the complexes studied herein, they did show more complex behavior in the solid state than in solution.

The magnetic moments of solid samples of **6.1**-**6.4**, **6.7**, and **6.8** were measured using SQUID magnetometry in the temperature range from 4 K to 400 K (Figure 6.8). Compounds **6.7** and **6.8** do not appear to undergo a spin transition at any temperature recorded. For compounds **6.1**-**6.4** spin crossover is gradual and incomplete; both the degree and rate of crossover proved to be extremely dependent on sample preparation and particularly on the degree of crystallinity, a phenomenon which is frequently observed in the solid-state magnetic behavior of mononuclear spin-crossover complexes and often rationalized on the basis of domain formation and grain size effects.[27,28] For instance, grinding a microcrystalline sample with a mortar and pestle typically resulted in a more incomplete spin crossover (Figure 6.9). In the most striking example of these effects, a yellow, crystalline sample of **6.3** exhibited no spin-crossover, maintaining a magnetic moment near 5.4μ_B at least down to 20 K, despite the fact that in solution this species has a T_c of 255 K. However, if the sample is lyophilized from benzene instead of crystallized, it takes on a greenish-blue color, and a gradual and incomplete spin crossover is observed instead (Figure 6.9). Many of the complexes display irreversible changes in their magnetic behavior after heating above 300 K, a phenomenon which is attributed to loss of co-crystallized solvent upon heating under vacuum in the magnetometer (see Appendix B for illustrative data). However, the change in the behavior of **6.3** upon lyophilization is not due to solvent loss, as neither crystalline nor lyophilized **6.3** includes co-crystallized solvent molecules (as determined by NMR).

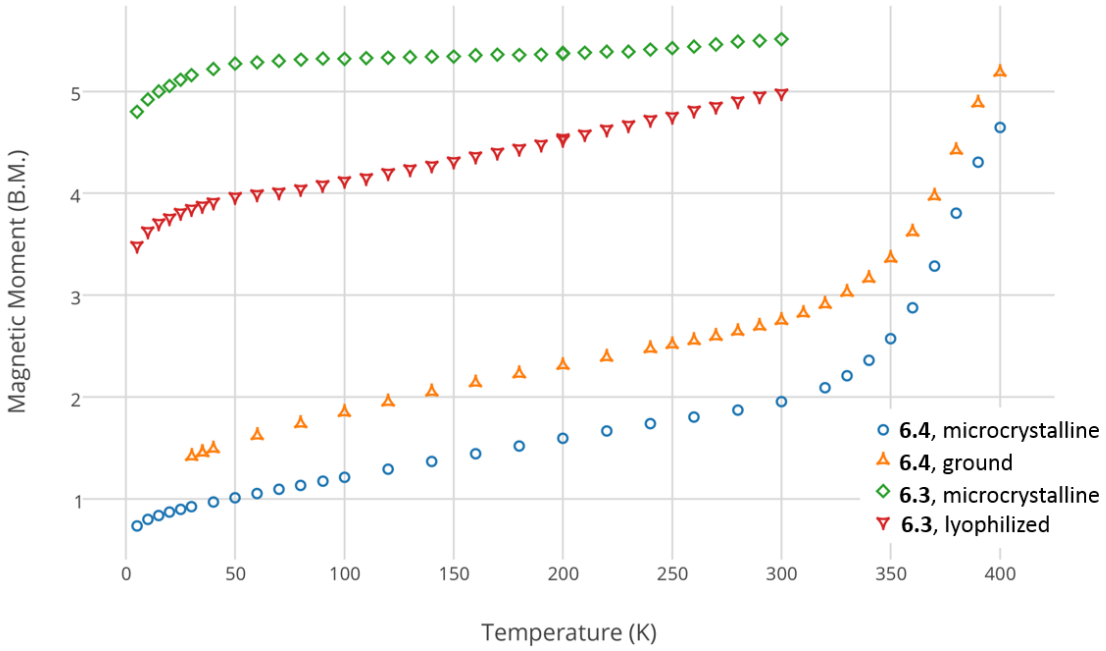

Figure 6.9. Variable-temperature solid-state SQUID magnetometry showing the effect of sample preparation on the measured properties of **6.3** and **6.4**. Measurements were carried out from low temperature to high temperature following initial cooling in zero field.

6.2.6 Solid-State Infrared Spectroscopy

Phosphiniminato ligands typically show a strong ν(N=P) vibration in their infrared spectra near 1200 cm^{-1}; this is observed for complexes **6.3**, **6.7**, **6.8**, and **6.9**. However, no strong vibration in this region is present in the low-spin states of the respective $[PhBP^{R}_{3}]Fe(NPR'_{3})$ complexes, as evident in the room temperature solid-state IR spectra of complexes **6.1**, **6.2**, and **6.4-6.6** (Figure 6.10)**.** This is consistent with weakening of the N=P bond due to increased π-bonding between N and Fe in the low-spin state (*vide infra*). This data corroborates the important role of the electronic flexibility of the

phosphiniminato ligand in facilitating access to both low- and high-spin states across this series of pseudotetrahedral iron(II) complexes.

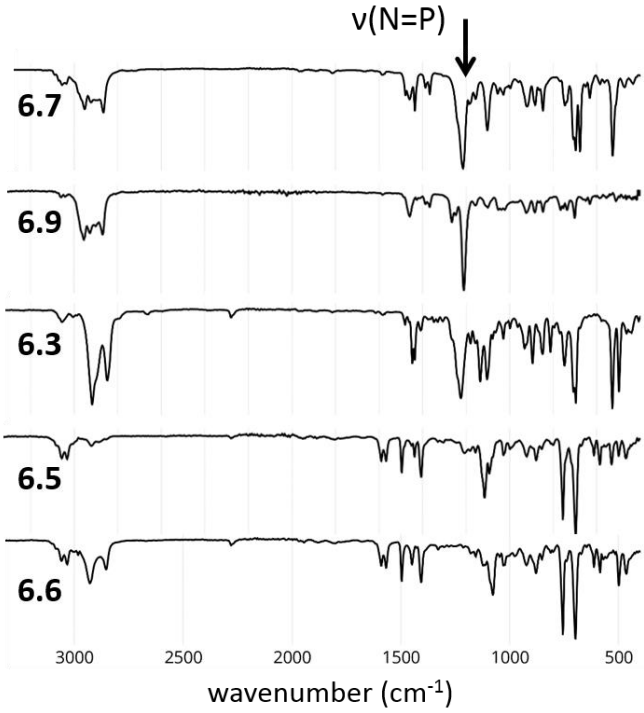

Figure 6.10. Representative solid-state infrared transmission spectra of complex **6.7**, **6.9**, **6.3**, **6.5**, and **6.6**, illustrating the presence of an ν(N=P) vibrational band at about 1207 cm^{-1} in the high spin complexes (**6.7**, **6.9**, **6.3**) that is absent in low-spin complexes **6.5** and **6.6**.

6.2.7 Mössbauer Spectroscopy

High- and low-spin states of an iron complex typically show distinctly different Mössbauer parameters (isomer shift and quadrupole splitting),[29] providing another convenient method of characterization of the iron compounds presented in this study. Mössbauer spectra were hence collected for examples of both predominantly low-spin (**6.1** as a microcrystalline solid and **6.4** as a glassed solution in 2-MeTHF) and high-spin

(microcrystalline **6.7** and **6.3**) complexes at 80 K, as well as for one example (lyophilized **6.3**) for which both spin forms can be distinguished across a series of temperatures (Figure 6.11; additional variable-temperature data is found in Appendix B). The relevant parameters are provided in Table 6.5. The high-spin species show a higher isomer shift and a larger quadrupole splitting relative to the low-spin species.

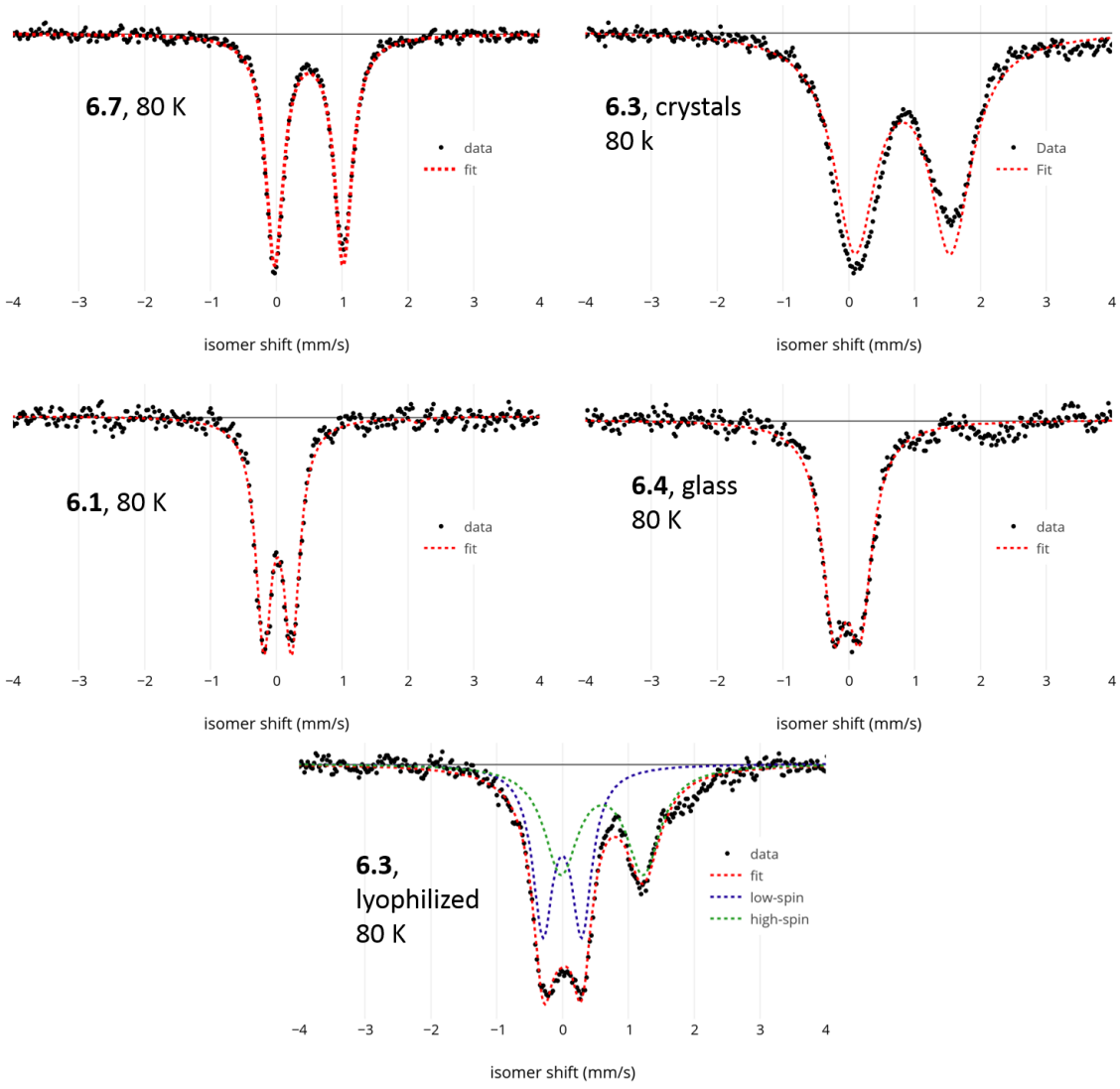

Figure 6.11. Representative 80 K Mössbauer spectra and parameters for low-spin **6.1** (crystalline) and **6.4** (Me-THF glass); high-spin **6.7** (crystalline) and **6.3** (crystalline); and lyophilized **6.3**, exhibiting a mixture of high- and low-spin populations.[30]

	isomer shift (δ, mm/s)	*quadrupole splitting (ΔE_Q, mm/s)*	*% composition*
***6.1** (crystalline)*	0.008	0.559	--
***6.4** (2-MeTHF glass)*	0.025	0.392	--
***6.7** (crystalline)*	0.617	1.373	--
***6.3** (crystalline)*	0.820	1.449	--
***6.3** (lyophilized)*	0.000	0.603	51
--	0.607	1.252	49

Table 6.5. Mössbauer parameters for complexes **6.1**, **6.3**, **6.4**, and **6.7**.

6.3 Discussion

A qualitative sketch of the d-orbital manifold (Figure 6.12) for Fe(II) in [PhBP$^R_3$]Fe(NPR'$_3$) in the high-spin and low-spin states provides some context for interpreting the spin-crossover behavior and trends delineated in the Results section. The ligand field splitting in these complexes is qualitatively similar to that of an octahedral complex[13] with three low-lying, primarily nonbonding orbitals and an antibonding, doubly degenerate orbital set at higher energy. This analogy is noteworthy given that the overwhelming majority of spin crossover compounds are octahedral. This orbital scheme—an approximate 2-over-3 splitting with a low-lying d_{z2} orbital—is well established both theoretically and experimentally for pseudotetrahedral Fe and Co complexes with [PhBP$^R_3$]$^-$ ligands. It can be attributed in part to mixing of d_{z2} with the metal-based $4p_z$ and 4s orbitals and also to the 90° P-Fe-P bond angles favored by the ligand chelate; these angles lower the relative energy of the a_1 orbital of primarily d_{z2} parentage.[11,31,32]

For the Fe(II) complexes of present interest the LUMO in the low-spin state is an approximately degenerate set of orbitals with d_{xz}/d_{yz} character and π^* symmetry with respect to the apical ligand. Spin-crossover to the $S = 2$ state involves population of this

level with two electrons. The thermodynamic parameters (ΔH) of the spin equilibrium are therefore expected to depend strongly on the energy of this level.

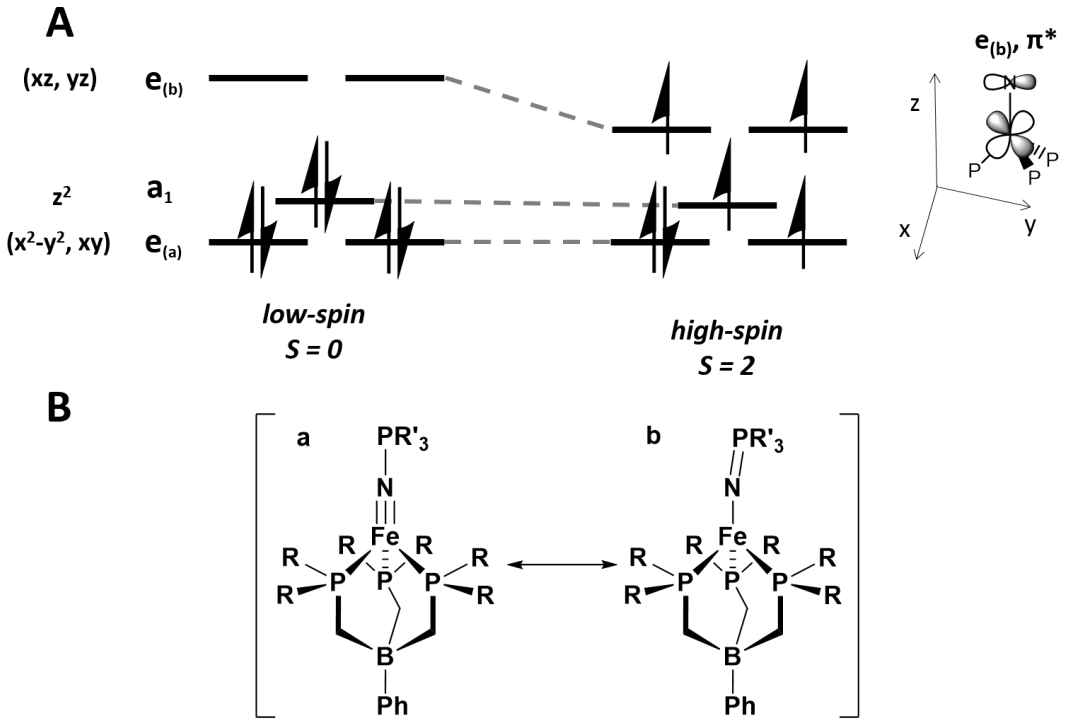

Figure 6.12. (**A**) Schematic of the d-orbital manifold for the low- and high-spin states of pseudotetrahedral [$PhBP^{R}_{3}$]Fe(NPR'$_3$) complexes. (**B**) Limiting Lewis-structure depictions of the electronic structure in the low-spin (**a**) and high-spin (**b**) states.

The qualitative orbital picture (Figure 6.12) is supported by DFT calculations carried out using the crystallographically determined structures of complexes **6.4** and **6.8** in their low- and high-spin forms, respectively (Figure 6.13). In **6.4** the high-lying π-symmetry d-orbitals are mixed with P-N π-bonding orbitals and are unoccupied. In **6.8**, the related orbitals in the α manifold are occupied, consistent with the observed shorter P-N bond due to a higher P-N bond order. The HOMO of low-spin **6.4** is an a_1 orbital of d_{z2}

parentage that lies slightly higher in energy than the near-degenerate non-bonding orbitals of d_{xy}/d_{x2-y2} parentage (HOMO-1 and HOMO-2).

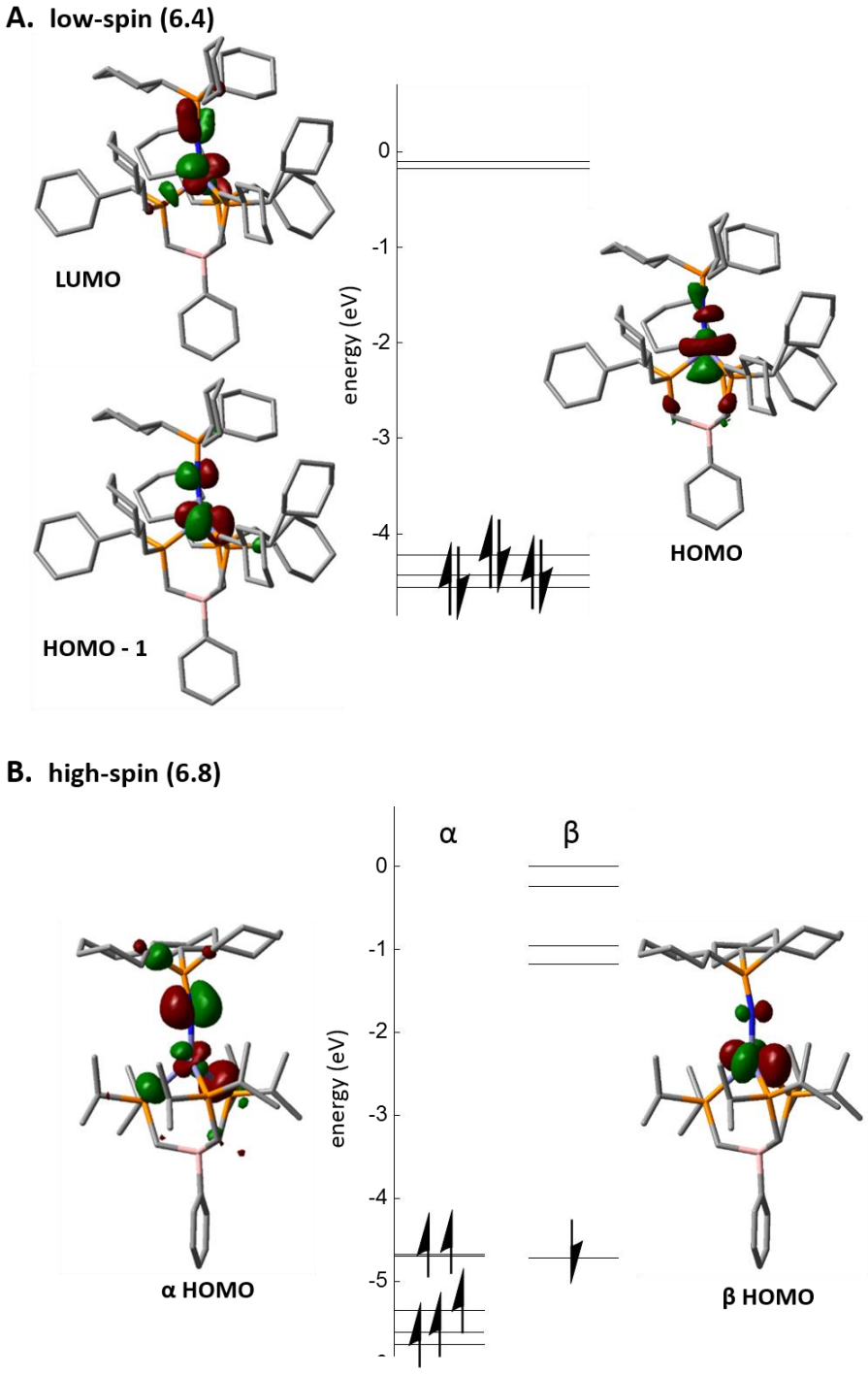

Figure 6.13. Valence molecular orbitals calculated for (**A**) low-spin [PhBP$^{CH2Cy}{}_3$]Fe(NPCy$_3$) (**6.4**) and (**B**) high-spin [PhBP$^{iPr}{}_3$]Fe(NPCy$_3$) (**6.8**).

Based on the variation of the spin crossover equilibrium parameters among **6.1**-**6.9**, some trends can be gleaned (Figure 6.14). There is a strong correlation between the magnitude of ΔH and the identity of the phosphiniminato substituent R' (Ph or Cy); among the $[PhBP^{R}_{3}]Fe(NPR'_{3})$ complexes that undergo spin crossover, for a given R ($-CH_2Cy$, Ph, or *m*-terphenyl), the complex where R' is the more electron-donating Cy has a larger ΔH and undergoes spin crossover at a higher temperature than the complex with R' = Ph. This observation can be rationalized; the more electron-donating phosphine (R = CH_2Cy) engenders better π-donation from N to Fe, raising the energy of the π* orbitals to favor the low-spin state. Consistent with this idea, the metrical parameters (e.g., N-Fe and N-P bond lengths; Table 6.1) suggest a stronger bond between Fe and N in the low-spin state, and a compensatory weakening of the multiple bonding between N and P. This can be represented as a more important contribution from an electronic structure picture involving Fe-N multiple bonding in the low-spin state (Figure 6.12B, structure **a**). This electronic structure is reminiscent of the previously characterized anionic Fe(II) imido complex, $\{[PhBP^{Ph}_{3}]Fe(NR)\}^{-}$.[32]

The influence of the $[PhBP^{R}_{3}]^{-}$ substituent R on the spin equilibrium parameters is less straightforward to interpret. It seems evident by comparison of **6.3** and **6.4** (R = CH_2Cy) versus the electronically similar **6.7** and **6.8** (R = *i*Pr), that steric factors play a large role. It is difficult to rationalize the difference between these pairs of complexes purely on the basis of electronic considerations; **6.3** and **6.4** have T_c values of 266 and 290 K while **6.7** and **6.8** are high spin at all temperatures. As observed in these complexes, increased steric crowding is expected to favor the high-spin state due to the much longer Fe-P bond lengths, resulting in a less strained environment around the metal center. The fact that **6.9**

([PhBP$^{iPr}_3$]Fe(NPEt$_3$)) undergoes spin-crossover, albeit at a relatively low temperature, further corroborates the role of steric crowding. Steric effects were also previously hypothesized to play a role in the greater propensity of [PhBP$^{iPr}_3$]CoX complexes to occupy high-spin states (versus the corresponding [PhBP$^{Ph}_3$]CoX complexes); the data presented here bolsters this hypothesis.[13]

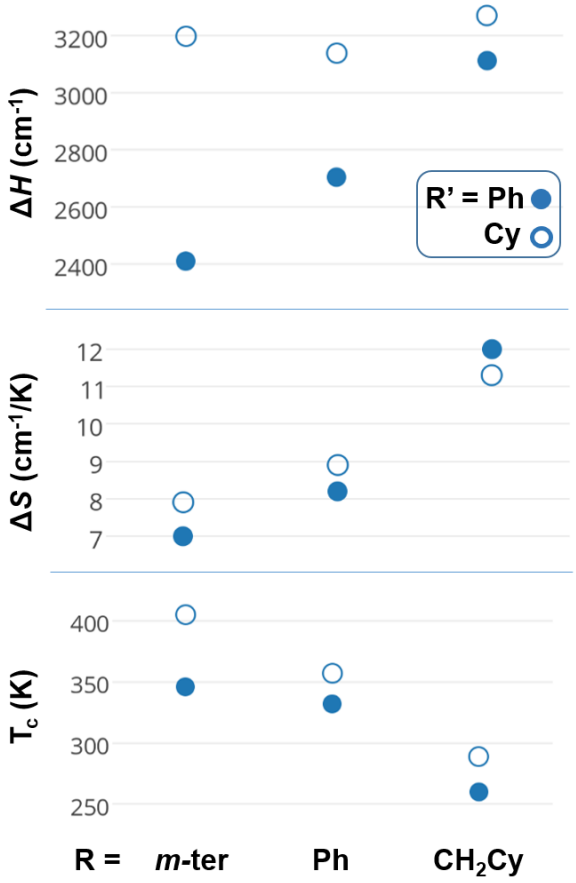

Figure 6.14. Comparison of Δ*H*, Δ*S*, and T_c for [PhBP$^R_3$]Fe(NPR'$_3$) complexes **6.1-6.6**. Average values from Tables 6.3 and 6.4 are plotted.

There is a strong trend in the Δ*S* values for the different [PhBP$^R_3$]$^-$ ligands. For a given R, the pairs of complexes with R' = Ph or Cy have similar Δ*S* values, and amongst the

three ligands (R = *m*-terphenyl, Ph, or -CH_2Cy), Δ*S* is smallest for the more rigid R = *m*-terphenyl (~7.5 cm^{-1}/K) and largest for the less rigid R = -CH_2Cy (~12 cm^{-1}/K). This trend can be qualitatively rationalized; the less sterically crowded environment of the high-spin state allows the more "floppy" substituents (-CH_2Cy) to move more freely, thus contributing substantially more to the vibrational entropy of the molecule. In contrast, the entropic contributions of the *m*-terphenyl-substituted ligand do not change as much due to the inherent rigidity of the aryl groups and the steric demands of the bulky terphenyls, which likely constrain the molecular geometry even in the high-spin state.

Electronic considerations with respect to R likely also contribute to Δ*H*, but the trend is less clear. Amongst complexes **6.1**, **6.3**, and **6.5** (with R' = Ph), Δ*H* increases significantly going from R = *m*-ter < Ph < CH_2Cy. One likely rationale is that the more strong-field alkyl phosphine donors in the $[PhBP^{R}_{3}]^{-}$ ligand help raise the energy of the $e_{(b)}$ orbital set, which is σ* antibonding with respect to the phosphines. The R' = Cy complexes (**6.2**, **6.4**, and **6.6**) do not follow quite the same trend, but the absolute differences between the Δ*H* values for this series are smaller and may be within the error of our measurements.

One aspect of our analysis that should be underscored is that it is only upon distilling the equilibrium parameters into Δ*S* and Δ*H* that the trends imparted by the ligand substituents become clear (Figure 6.14). Studies of spin equilibria often attempt to extract trends by considering only T_c, a parameter which convolutes both entropic and enthalpic contributions. Such an analysis could in some cases lead to misinterpretations or make it difficult to identify robust trends concerning the effect of the primary coordination environment on the spin equilibria. While it is sometimes more challenging to determine

reliable values for ΔS and ΔH, the present results emphasize that it is worthwhile to do so when possible.

Further analysis of the UV-vis spectra of the low-spin forms of complexes **6.1**-**6.6** and **6.9** could potentially provide additional insight into the ligand field landscape of these molecules. In all cases, the spectra display three bands of appreciable intensity in the visible range: a peak at around 600 nm with a high-energy shoulder at around 550 nm, and a second peak at around 700 nm. The exact positions of these peaks, as derived from spectral decomposition, were tabulated above in Table 6.1. The energies and intensities of these bands, as well as the fact that they are present in all complexes at similar energies regardless of the identities of R and R', corroborates their assignment as primarily ligand field d-d transitions (which are Laporte-allowed in C_{3v} symmetry, with strengthened intensity by d-p mixing induced by strong covalency) rather than charge transfer transitions to the ligand backbone. Significant mixing, especially with the P-N π-orbitals, contributes as well. TD-DFT calculations on complex **6.4** support this assignment (see Appendix B for details). The lack of similar bands in the high-spin forms of the complexes likely results from the fact that the d-d transitions in the high-spin molecules are shifted farther into the near-infrared due to the smaller ligand field splitting.

Qualitative crystal field considerations in idealized C_{3v} symmetry—which approximates well the local geometry around the iron centers in the low-spin complexes—allow a tentative assignment of these three optical bands (Figure 6.15). Considering only spin-allowed transitions to singlet excited states, the $^1A_1$ low-spin ground state $(e_{(a)})^4(a_1)^2(e_{(b)})^0$ can undergo one-electron excitations to either a

$(e_{(a)})^4(a_1)^1(e_{(b)})^1$ or a $(e_{(a)})^3(a_1)^2(e_{(b)})^1$ configuration. The former is a ^1E state while the latter has ^1E, $^1A_1$ and $^1A_2$ components. In C_{3v} symmetry, $^1A_1 \rightarrow {}^1E$ and $^1A_1 \rightarrow {}^1A_1$ optical transitions are orbital-symmetry allowed, while the $^1A_1 \rightarrow {}^1A_2$ transition is forbidden. Therefore, three ligand-field transitions are expected for this state, consistent with the observed spectra. Assigning these reliably is nontrivial; we tentatively assign the lower-energy, well-separated band at ~700 nm to the $(e_{(a)})^4(a_1)^2(e_{(b)})^0 \rightarrow (e_{(a)})^4(a_1)^1(e_{(b)})^1$ transition ($^1A_1 \rightarrow {}^1E$), and the two higher-energy, closely-spaced bands to the allowed $(e_{(a)})^4(a_1)^2(e_{(b)})^0 \rightarrow (e_{(a)})^3(a_1)^2(e_{(b)})^1$ transitions ($^1A_1 \rightarrow {}^1E$ and $^1A_1 \rightarrow {}^1A_1$).

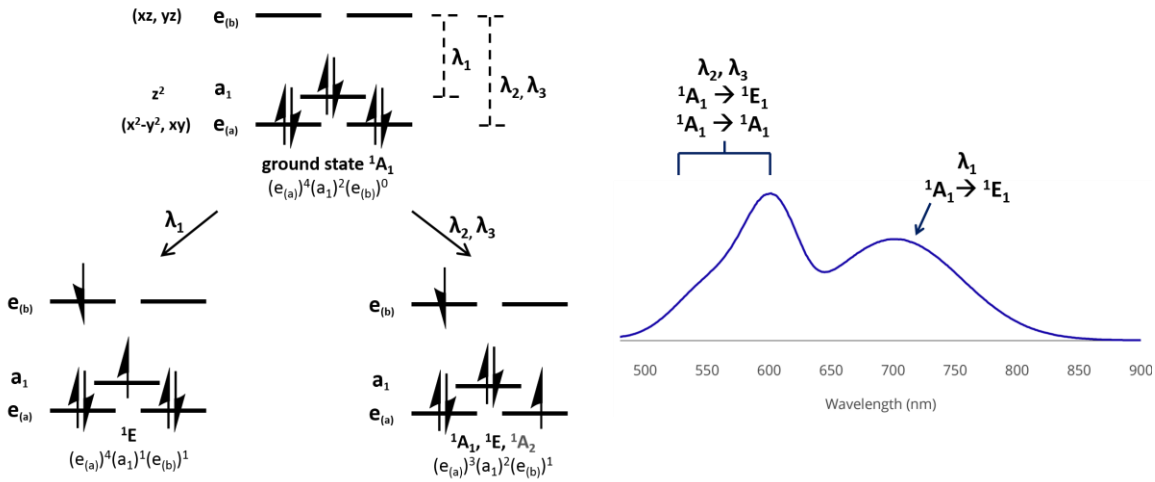

Figure 6.15. Proposed assignments of UV-vis transitions in low-spin phosphiniminato complexes. (Left) Qualitative orbital diagrams and electron configurations of ground state and singlet one-electron excited states. (Right) Absorption spectra of **6.1** at 188 K with proposed assignments labeled.

In the lowered symmetry (C_1) that more rigorously describes the solid-state structure of these complexes, a qualitatively similar assignment can be proposed; the 700 nm band likely arises from transitions between the valence orbital of d_{z2} parentage to the

unoccupied, d_{xz}/d_{yz}-derived π-symmetry orbitals, while the higher-energy bands derive from transitions from the near-degenerate d_{xy} and d_{x2-y2} nonbonding orbitals. Notably, d^6 metallocenes such as ferrocene, which have qualitatively similar valence d-orbital electronic structures, likewise show three symmetry-allowed optical d-d transitions, although the precise assignment of these differs due to the different point-group symmetry.[33]

The energies of the visible transitions can therefore provide some information about the ligand field splitting of the d-orbitals in the low-spin complexes. Again, the clearest trend is in the dependence of the transition energies on the identity of the phosphiniminato substituent. In all cases for a given R all three absorptions are lower in energy for R' = Ph than R' = Cy, consistent with the conclusions discussed above; the $e_{(b)}$ π* orbital is raised higher in energy in the case of the more strongly electron-donating and π-bonding alkyl phosphiniminato. Interestingly, for complex **6.9** the transition energies are substantially lower than for the other alkyl phosphiniminato complexes; this may suggest that although this complex is able to populate a low-spin state, steric strain still enforces longer bond lengths and therefore a weaker ligand field than in **6.2**, **6.4**, and **6.6**.

The correlations and trends discussed above suggest that in these spin-crossover iron(II) complexes, both the specific properties of the [$PhBP^R_3$] ligands, enforcing a pseudo-tetrahedral geometry and a corresponding "pseudo-octahedral" orbital arrangement, and the ability of the phosphiniminato ligand to modulate its π-donation between two possible limiting electronic structures, are important to the spin-equilibrium behavior observed. Tuning the electron-donating ability of the phosphiniminato

phosphine is a straightforward way to strongly alter the T_c and thermodynamic properties of the complexes, which can be further fine-tuned by modifying the steric and electronic properties of the trisphosphine borate ligand. Further modification of such complexes along these two independent axes could give rise to molecules with more desirable properties for magnetic memory applications, such as strongly cooperative or hysteretic spin-crossover, or light-induced spin state trapping (LIESST).

6.4 Experimental Details

6.4.1 General considerations.

All syntheses and measurements, unless otherwise stated, were carried out under an inert atmosphere (N_2) in a glovebox or using standard Schlenk techniques, and solvents were dried and degassed by thoroughly sparging with N_2 and then passed through an activated alumina column in a solvent purification system supplied by SG Water, LLC. Non-halogenated solvents were tested with a standard purple solution of sodium benzophenone ketyl in tetrahydrofuran in order to confirm effective moisture removal. $[PhBP^{Ph}_3]FeCl$,[21a] $[PhBP^{mter}_3]FeCl$,[21d] $[PhBP^{iPr}_3]FeCl$,[21b] $[PhBP^{CH2Cy}_3]FeCl$,[21c] and $[Ph_3PNH_2]Cl$[22] were prepared according to literature procedures. All other reagents were purchased from commercial vendors and used without further purification unless otherwise stated.

6.4.2 Physical methods.

Elemental analyses were performed by Midwest Microlab (Indianapolis, IN). Deuterated solvents were purchased from Cambridge Isotope Laboratories, Inc., degassed, and dried over active 3-Å molecular sieves prior to use. ^1H and ^{13}C chemical shifts are reported in ppm relative to tetramethylsilane, using residual proton and ^{13}C

resonances from solvent as internal standards. ^{31}P chemical shifts are reported in ppm relative to 85% aqueous H_3PO_4. Solution phase magnetic measurements were performed by the method of Evans.[26] The NMR spectrometer temperature was calibrated using 100% methanol (25 ^{o}C to -85 ^{o}C) or 100% ethylene glycol (25 ^{o}C to 105 ^{o}C). Optical spectroscopy measurements were taken on a Cary 50 UV-vis spectrophotometer using a 1-cm two-window quartz cell, with a Unisoku CoolSpek cryostat for temperature control. Thin-film infrared (IR) spectra were obtained on a Bruker Alpha spectrometer equipped with a diamond ATR probe. Solid-state magnetic data was obtained using a Quantum Designs SQUID magnetometer running MPMSR2 software (Magnetic Property Measurement System Revision 2) at a field strength of 5000 G. Samples were inserted into the magnetometer in plastic straws sealed under nitrogen with polycarbonate capsules. Loaded samples were centered within the magnetometer using the DC centering scan at 35 K and 500 gauss. The magnetic susceptibility was adjusted for diamagnetic contributions using the constitutive corrections of Pascal's constants as well as a diamagnetic correction due to the holder diamagnetism. Mössbauer spectra were recorded on a spectrometer from SEE Co (Edina, MN) operating in the constant acceleration mode in a transmission-geometry. Spectra were recorded with the temperature of the sample maintained at 80 K except as otherwise noted. The sample was kept in an SVT-400 dewar from Janis (Wilmington, MA), at zero field. The quoted isomer shifts are relative to the centroid of the spectrum of a metallic foil of α-Fe at room temperature. Solid samples were prepared by mounting in a cup fitted with a screw-cap as a boron nitride pellet. Data analysis was performed using the program WMOSS (www.wmoss.org) and quadrupole doublets were fit to Lorentzian lineshapes.

6.4.3 Computations.

Single-point DFT energy calculations on **6.4** (S = 0) and **6.8** (S = 2) were calculated using the Gaussian 09 software package[34] and the hybrid B3LYP functional. The 6-311G(df) basis set was used for the iron and phosphorus atoms and 6-31G(d) was used on the remaining atoms.

6.4.4 X-ray Crystallography.

XRD studies were carried out at the Beckman Institute Crystallography Facility on a Bruker Kappa Apex II diffractometer (Mo Kα radiation). Structures were solved using SHELXS and refined against F^2 on all data by full-matrix least squares with SHELXL.[35] The crystals were mounted on a wire loop. All crystals were measured at a temperature of 100 K. Methyl group hydrogen atoms not involved in disorder were placed at calculated positions starting from the point of maximum electron density. All other hydrogen atoms were placed at geometrically calculated positions and refined using a riding model. The isotropic displacement parameters of the hydrogen atoms were fixed at 1.2 (1.5 for methyl groups) times the U_{eq} of the atoms to which they are bonded. 1,2- and 1,3-rigid bond restraints were applied to all non-hydrogen atoms.

6.4.5 Synthesis and characterization data

Tricyclohexylphosphiniminium chloride. Tricyclohexylphosphine (1.00 g, 3.57 mmol) and hexachloroethane (844 mg, 3.57 mmol) were combined in 80 mL of THF and stirred for two hours at room temperature, during which time a white precipitate develops. The suspension was then cooled to -20 ^{o}C and anhydrous gaseous ammonia was bubbled through the solution. The reaction mixture was allowed to warm to room temperature overnight under NH_3 and then concentrated to dryness. The white residue

was taken up in 500 mL of dry dichloromethane, filtered through Celite, and concentrated to dryness. The residue was redissolved in minimal MeOH, then 200 mL of Et_2O were added and the mixture stored in the freezer (-40 ^oC) for 2 hours. The resulting white crystalline solids were collected on a sintered glass frit and washed with Et_2O, giving 977 mg of the desired product as a white solid (83%). $^{31}P\{^1H\}$ NMR ($CDCl_3$, 162 MHz, 25 ^oC): δ 53.4 (s) ppm. ^1H NMR ($CDCl_3$, 400 MHz, 25 ^oC): δ 5.70 (br s, 2H, N*H*$_2$), 2.33 (q, *J* = 12 Hz, 3H), 2.01 (d, *J* = 12 Hz, 6H), 1.86 (d, *J* = 12 Hz, 6H), 1.72 (d, *J* = 12 Hz, 3H), 1.56 (q, *J* = 12 Hz, 6H), 1.37-1.22 (m, 9H) ppm. ^{13}C NMR ($CDCl_3$, 101 MHz, 25 ^oC) δ 32.2 (d, *J*(P) = 54 Hz), 26.4 (d, *J*(P) = 13 Hz), 26.0 (d, *J*(P) = 3 Hz), 25.6 (s) ppm. Anal. Calcd. for $C_{18}H_{35}NPCl$: C, 65.14; H, 10.63; N, 4.22. Found: C, 65.38; H, 11.05; N, 4.14.

Triethylphosphiniminium chloride. Triethylphosphine (0.500 g, 4.23 mmol) was dissolved in THF and hexachloroethane (1.00 g, 4.22 mmol) was added dropwise as a solution in THF. White precipitate formed immediately, and the reaction was stirred for two hours at room temperature and then cooled to -20 ^oC. Anhydrous gaseous ammonia was bubbled through the solution, and the reaction mixture was allowed to warm to room temperature and stir overnight under NH_3. The mixture was then concentrated to dryness and the white residue was extracted with dichloromethane, filtered through Celite, and concentrated to a volume of 3 mL. This concentrated solution was layered with 10 mL of Et_2O and stored at -40 ^oC for two hours. The resulting white crystals were isolated atop a sintered glass frit and washed with Et_2O. The desired product was obtained as 683 mg of a white solid (95%). $^{31}P\{^1H\}$ NMR ($CDCl_3$, 162 MHz, 25 ^oC): δ 59.8 (s) ppm. ^1H NMR ($CDCl_3$, 400 MHz, 25 ^oC): δ 5.65 (br s, 2H, N*H*$_2$), 2.18 (dq, *J* = 8, 15 Hz, 6H), 1.22 (dt, 8, 18 Hz, 9H) ppm. ^{13}C NMR ($CDCl_3$, 101 MHz, 25 ^oC) δ 15.9 (d, *J*(P) = 61 Hz), 5.4 (d,

J(P) = 5 Hz) ppm. Anal. Calcd. for $C_6H_{17}ClNP$: C, 42.48; H, 10.10; N, 8.26. Found: C, 42.41; H, 9.94; N, 8.08.

[PhBP$^{Ph}_3$]Fe(NPPh$_3$) (6.1). [H_2NPPh_3][Cl] (88.9 mg, 0.283 mmol) was suspended in THF (5 mL) and cooled to -78 ^oC with stirring. *n*-Butyllithium (354 μL, 1.6 M in hexane, 0.566 mmol) was added to the solution, which was stirred at low temperature for 30 minutes, then allowed to warm to room temperature for 30 minutes, then cooled back to -78 ^oC. This solution was added dropwise to a separately cooled solution of **[**PhBP$^{Ph}_3$]FeCl (200 mg, 0.257 mmol) in THF (5 mL), and the reaction mixture was stirred at low temperature for 30 minutes before being allowed to warm to room temperature and stirred overnight. The resulting blue solution was concentrated to dryness, extracted with benzene, and filtered through Celite. The filtrate was concentrated to give a blue residue that was recrystallized by taking up in THF (5 mL), layered with pentane (15 mL), and allowing to stand at room temperature overnight. The resulting blue crystals were thoroughly washed with pentane and 1:1 THF/pentane, giving 251 mg of the desired product (95%). Crystals suitable for X-ray diffraction were grown by vapor diffusion of pentane into a concentrated THF solution at room temperature. ^1H NMR (C_6D_6, 300 MHz, 25 ^oC): δ 42.076 (br), 15.390, 10.449, 10.075, 9.909, 7.292, 5.999, 2.743, 2.529 ppm. Anal. Calcd. for $C_{67}H_{63}BFeNP_4O$ (**1**·THF): C, 73.91; H, 5.83; N, 1.29. Found: C, 73.01; H, 5.96; N, 1.06.

[PhBP$^{Ph}_3$]Fe(NPCy$_3$) (6.2). [H_2NPCy_3][Cl] (88.3 mg, 0.266 mmol) was suspended in THF (5 mL) and cooled to -78 ^oC with stirring. *n*-Butyllithium (333 μL, 1.6 M in hexane, 0.533 mmol) was added to the solution, which was stirred at low temperature for 30 minutes, then allowed to warm to room temperature for 30 minutes, then cooled back to -

78 °C. This solution was added dropwise to a separately cooled solution of **[**PhBP$^{Ph}_3$]FeCl (196.8 mg, 0.253 mmol) in THF (2 mL), and the reaction mixture was stirred at low temperature for 10 minutes before being allowed to warm to room temperature for 15 minutes and then concentrated. The resulting blue solution was concentrated to dryness, extracted with benzene, and filtered through Celite. The filtrate was concentrated to give a blue residue which was recrystallized by taking up in minimal THF, layering with pentane (15 mL), and allowing to stand at -40 °C overnight. The resulting blue crystals were thoroughly washed with pentane, giving 213 mg of the desired product (81%). Crystals suitable for X-ray diffraction were grown by layering pentane over a concentrated THF solution at -40 °C. ^{1}H NMR (C_6D_6, 300 MHz, 25 °C): δ 14.107 (br), 10.454, 8.564, 8.218, 6.653, 5.552, 4.400, 4.162, 3.646, 2.758, 1.886 ppm. Anal. Calcd. for $C_{63}H_{79}BFeNP_4$: C, 73.05; H, 7.20; N, 1.35. Found: C, 72.85; H, 7.17; N, 1.24.

[PhBP$^{CH2Cy}_3$]Fe(NPPh$_3$) (6.3). [H_2NPPh$_3$][Cl] (81 mg, 0.258 mmol) was suspended in THF (5 mL) and cooled to -78 °C with stirring. *n*-Butyllithium (321 μL, 1.6 M in hexane, 0.616 mmol) was added to the solution, which was stirred at low temperature for 30 minutes, then allowed to warm to room temperature for 30 minutes, then cooled back to -78 °C. This solution was added dropwise to a separately cooled solution of PhBP$^{CH2Cy}_3$FeCl (199.1 mg, 0.245 mmol) in THF (2 mL), and the reaction mixture was stirred at low temperature for 10 minutes, resulting in a dark blue solution, before being allowed to warm to room temperature. The solution, which is dark green at room temperature, was stirred for one hour and then concentrated to dryness, extracted with benzene, and filtered through Celite. The filtrate was concentrated to dryness, taken up

in minimal THF, layered with pentane, and allowed to stand overnight at room temperature. The resulting yellow crystals were thoroughly washed with pentane, giving 172 mg of the desired product (62%). ^{1}H NMR (C_6D_6, 300 MHz, 25 ^{o}C): δ 163.157 (br), 40.619, 39.980, 20.025, 18.122, 8.935, -0.485, -1.423, -3.109, -6.549, -7.765, -13.726, -20.784, -21.843, -29.899, -40.637 ppm. ^{31}P{^{1}H} NMR (C_6D_6, 202 MHz, -75 ^{o}C): δ 77.324 (br s, 3P), 41.747 (br s, 1P) ppm. Anal. Calcd. for $C_{69}H_{104}BFeNP_4$: C, 72.82; H, 9.21; N, 1.23. Found: C, 72.62; H, 9.27; N, 1.22.

[PhBP$^{CH2Cy}{}_3$]Fe(NPCy$_3$) (6.4). [H_2NPCy$_3$][Cl] (86 mg, 0.259 mmol) was suspended in THF (5 mL) and cooled to -78 ^{o}C with stirring. *n*-Butyllithium (323 μL, 1.6 M in hexane, 0.518 mmol) was added to the solution, which was stirred at low temperature for 30 minutes, then allowed to warm to room temperature for 30 minutes, then cooled back to -78 ^{o}C. This solution was added dropwise to a separately cooled solution of **[**PhBP$^{CH2Cy}{}_3$]FeCl (200 mg, 0.246 mmol) in THF (2 mL), and the reaction mixture was stirred at low temperature for 10 minutes, resulting in a dark blue solution, before being allowed to warm to room temperature. The solution was stirred for an additional 15 minutes and then concentrated to dryness, extracted with pentane, and filtered through Celite, and concentrated to dryness. The blue residue was taken up in pentane and recrystallized by slow evaporation of the pentane solution. The resulting blue crystals were washed with cold pentane and dried, giving 179 mg of the desired product (63%). Crystals suitable for X-ray diffraction were grown by slow evaporation of a concentrated pentane solution into HMDSO. ^{1}H NMR (C_6D_6, 300 MHz, 25 ^{o}C): δ 44.099, 29.181, 22.770, 21.259, 15.750, 14.508, 11.485, 7.489, 5.072, 3.227, -0.712, -1.171, -2.220, -3.020, -4.262, -5.169, 7.568, -8.376, -14.255, -15.775, -18.992, -24.007 ppm. ^{31}P{^{1}H}

NMR (C_6D_6, 202 MHz, -75 °C): δ 82.2 (br s, 3P), 62.2 (br s, 1P) ppm. Anal. Calcd. for $C_{69}H_{122}BFeNP_4$: C, 71.67; H, 10.64; N, 1.21. Found: C, 71.30; H, 10.25; N, 0.91.

[PhBP$^{m\text{ter}}_3$]Fe(NPPh$_3$) (6.5). [H_2NPPh_3][Cl] (40.2 mg, 0.128 mmol) was suspended in THF (5 mL) and cooled to -78 °C with stirring. *n*-Butyllithium (160 μL, 1.6 M in hexane, 0.256 mmol) was added to the solution, which was stirred at low temperature for 30 minutes, then allowed to warm to room temperature for 30 minutes, then cooled back to -78 °C. This solution was added dropwise to a separately cooled solution of PhBP$^{m\text{ter}}_3$FeCl (206.1 mg, 0.122 mmol) in THF (2 mL), and the reaction mixture was stirred at low temperature for 10 minutes before being allowed to warm to room temperature for two hours and then concentrated. The resulting blue solution was concentrated to dryness, extracted with benzene, and filtered through Celite. The filtrate was concentrated to 2 mL, layered with 15 mL of pentane and allowed to stand at room temperature overnight. The resulting blue crystals were thoroughly washed with pentane, giving 132 mg of the desired product (56%). Crystals suitable for X-ray diffraction were grown by vapor diffusion of pentane into a concentrated benzene solution. ^{1}H NMR (C_6D_6, 300 MHz, 25 °C): δ 39.417 (br), 14.705, 14.598, 9.977, 9.943, 9.154, 6.975, 6.858, 6.669, 5.896, 3.258, -1.336 ppm. ^{31}P{^{1}H} NMR (C_6D_6, 152 MHz, -75 °C): δ 100.2 (br s, 3P), 50.0 (br s, 1P) ppm. Anal. Calcd. for $C_{135}H_{104}BFeNP_4$: C, 83.98; H, 5.43; N, 0.73. Found: C, 83.33; H, 5.57; N, 0.54.

[PhBP$^{m\text{ter}}_3$]Fe(NPCy$_3$) (6.6). [H_2NPPh_3][Cl] (41.2 mg, 0.124 mmol) was suspended in THF (5 mL) and cooled to -78 °C with stirring. *n*-Butyllithium (155 μL, 1.6 M in hexane, 0.248 mmol) was added to the solution, which was stirred at low temperature for 30 minutes, then allowed to warm to room temperature for 30 minutes, then cooled back

to -78 °C. This solution was added dropwise to a separately cooled solution of PhBP$^{m\text{ter}}_3$FeCl (200 mg, 0.118 mmol) in THF (2 mL), and the reaction mixture was stirred at low temperature for 10 minutes before being allowed to warm to room temperature for two hours and then concentrated. The resulting blue solution was concentrated to dryness, extracted with benzene, and filtered through Celite. The filtrate was concentrated to 2 mL, layered with 15 mL of pentane and allowed to stand at room temperature overnight. The resulting blue crystals were thoroughly washed with pentane, giving 170 mg of the desired product (87%). ^{1}H NMR (C_6D_6, 300 MHz, 25 °C): δ 8.972, 7.749, 7.483, 7.077, 7.047, 6.992, 3.206, 2.378, 1.716, 1.314, 0.705, 0.538 ppm. ^{31}P{^{1}H} NMR (C_6D_6, 202 MHz, -75 °C): δ 100.5 (br s, 3P), 66.7 (br s, 1P) ppm.

[PhBP$^{i\text{Pr}}_3$]Fe(NPPh$_3$) (6.7). [H_2NPPh$_3$][Cl] (56.4 mg, 0.180 mmol) was suspended in THF (5 mL) and cooled to -78 °C with stirring. *n*-Butyllithium (224 μL, 1.6 M in hexane, 0.360 mmol) was added to the solution, which was stirred at low temperature for 30 minutes, then allowed to warm to room temperature for 30 minutes, then cooled back to -78 °C. This solution was added dropwise to a separately cooled solution of **[**PhBP$^{i\text{Pr}}_3$ FeCl (99.0 mg, 0.173 mmol) in THF (2 mL), and the reaction mixture was stirred at low temperature for 10 minutes before being allowed to warm to room temperature for two hours and then concentrated. The resulting yellow solution was concentrated to dryness, extracted with benzene, filtered through Celite, and concentrated to dryness again. The yellow-orange residue was taken up in minimal ether, layered with pentane, and stored at -40 °C overnight, resulting in the formation of yellow crystals. The isolated material displayed the same spectroscopic characteristics as previously reported for this compound.[18] Crystals suitable for X-ray diffraction were grown by layering pentane

over a concentrated ether solution at -40 °C. ^{1}H NMR (C_6D_6, 300 MHz, 25 °C): δ 198.178, 52.974, 49.325, 23.593, 21.154, 8.264, 1.979, 1.769, -5.752, -27.166, -48.558 ppm.

[PhBP$^{iPr}_3$]Fe(NPCy$_3$) (6.8). [H_2NPCy$_3$][Cl] (62.9 mg, 0.190 mmol) was suspended in THF (5 mL) and cooled to -78 °C with stirring. *n*-Butyllithium (237 μL, 1.6 M in hexane, 0.380 mmol) was added to the solution, which was stirred at low temperature for 30 minutes, then allowed to warm to room temperature for 30 minutes, then cooled back to -78 °C. This solution was added dropwise to a separately cooled solution of [PhBP$^{iPr}_3$]FeCl (104.5 mg, 0.181 mmol) in THF (2 mL), and the reaction mixture was stirred at low temperature for 10 minutes before being allowed to warm to room temperature for two hours and then concentrated. The resulting yellow solution was concentrated to dryness, extracted with benzene, filtered through Celite, and concentrated to dryness again. The yellow-orange residue was taken up in minimal ether, layered with pentane, and stored at -40 °C overnight, resulting in the formation of yellow crystals which were collected, washed with cold pentane, and dried to give 69 mg of the desired compound (46%). Crystals suitable for X-ray diffraction were grown by slow evaporation of a pentane solution. ^{1}H NMR (C_6D_6, 300 MHz, 25 °C): δ 194.199, 84.699, 50.311, 42.546, 23.669, 21.365, 20.109, 13.877, 7.743, 6.035, -7.682, -26.198, -49.308 ppm. Anal. Calcd. for $C_{45}H_{86}BFeNP_4$: C, 64.98; H, 10.42; N, 1.68. Found: C, 64.79; H, 10.42; N, 1.61.

[PhBP$^{iPr}_3$]Fe(NPEt$_3$) (6.9). [H_2NPEt$_3$][Cl] (63.9 mg, 0.377 mmol) was suspended in THF (5 mL) and cooled to -78 °C with stirring. *n*-Butyllithium (468 μL, 1.6 M in hexane, 0.754 mmol) was added to the solution, which was stirred at low temperature for 30

minutes, then allowed to warm to room temperature for 30 minutes, then cooled back to -78 °C. This solution was added dropwise to a separately cooled solution of **[**PhBP$^{iPr}_3$]FeCl (200 mg, 0.346 mmol) in THF (2 mL), and the reaction mixture was stirred at low temperature for 10 minutes before being allowed to warm to room temperature for two hours and then concentrated. The resulting yellow solution was concentrated to dryness, extracted with benzene, filtered through Celite, and concentrated to dryness again. The yellow-orange residue was taken up in minimal ether, layered with pentane, and stored at -40 °C overnight, resulting in the formation of yellow crystals. The isolated material displayed the same spectroscopic characteristics as previously reported for this compound.[18] Crystals suitable for X-ray diffraction were grown by slow evaporation of a pentane solution. ^{1}H NMR (C_6D_6, 300 MHz, 25 °C): δ 197.031, 84.790, 48.691, 47.709, 23.016, 20.954, -6.623, -23.806, -48.717 ppm.

6.5 References

1. *Spin Crossover in Transition Metal Compounds* I-III; Gutlich, P., Goodwin, H. A., Eds.; Topics in Current Chemistry, Vols 233-235; Springer: Berlin, Heidelberg, Germany, 2004.

2. Gutlich, P. *Eur. J. Inorg. Chem.* **2013**, *5-6*, 581.

3. Kahn, O.; Martinez, C. J. *Science*, **1998**, *279*, 44.

4. Decurtins, S.; Gutlich, P.; Hasselbach, K.M.; Hauser, A.; Spiering, H. *Inorg. Chem.* **1985**, *24*, 2174.

5. Bousseksou, A.; Molnar, G.; Matouzenko, G. *Eur. J. Inorg. Chem.* **2004**, 4353.

6. Jeon, I.-R.; Park, J. G.; Haney, C. R.; Harris, T. D. *Chem. Sci.* **2014**, *5*, 2461.

7. (a) Manner, V. W.; Lindsay, A. D.; Mader, E. A.; Harvey, J. N.; Mayer, J. M. *Chem. Sci.* **2012**, *3*, 230. (b) Landis, C. R.; Morales, C. M.; Stahl, S. S. *J. Am. Chem. Soc.* **2004**, *126*, 16302. (c) Lord, R. L.; Schultz, F. A.; Baik, M.-H. *J. Am. Chem. Soc.* **2008**, *47*, 4413. (d) Veige, A. S.; Slaughter, L. M.; Lobkovsky, E. B.; Wolczanski, P. T.; Matsunaga, N.; Decker, S. A.; Cundari, T. R. *Inorg. Chem.* **2003**, *42*, 6204. (e) Saouma, C. T.; Mayer, J. M. *Chem. Sci.* **2014**, *5*, 21. (f) Detrich, J. L.; Reinaud, O. M.; Rheingold, A. L.; Theopold, K. H. *J. Am. Chem. Soc.* **1995**, *117*, 11745.

8. Halcrow, M. *Chem. Soc. Rev.* **2011**, *40*, 4119.

9. Gutlich, P.; Garcia, Y.; Goodwin, H. A. *Chem. Soc. Rev.* **2000**, *29*, 419.

10. Harcrow, M. A. *Polyhedron* **2007**, *26*, 3523.

11. Jenkins, D. M.; Di Bilio, A. J.; Allen, M. J.; Betley, T. A.; Peters, J. C. *J. Am. Chem. Soc.* **2002**, *124*, 15336.

12. Jenkins, D. M.; Peters, J. C. *J. Am. Chem. Soc.* **2003**, *125*, 11162.

13. Jenkins, D.M.; Peters, J. C. *J. Am. Chem. Soc.* **2005**, *127*, 7148.

14. Bacci, M.; Midollini, S.; Stoppioni, P.; Sacconi, L. *Inorg. Chem.* **1973**, *12*, 1801.

15. Scepaniak, J. J.; Harris, T. D.; Vogel, C.; Sutter, J.; Meyer, K.; Smith, J. M. *J. Am. Chem. Soc.* **2011**, *133*, 3824.

16. Lin, H.-J.; Siretanu, D.; Dickie, D.A.; Subedi, D.; Scepaniak, J.J.; Mitcov, D.; Clerac, R.; Smith, J. M. *J. Am. Chem. Soc.* **2014**, *136*, 13326.

17. Bowman, A. C; Milsmann, C.; Bill, E.; Turner, Z. R.; Lobkovsky, E.; DeBeer, S.; Wieghardt, K.; Chirik, P.J. *J. Am. Chem. Soc.* **2011**, *133*, 17353.

18. Betley, T. A.; Peters, J. C. *J. Am. Chem. Soc.* **2004**, *126*, 6252.

19. (a) Ghesner, I.; Fenwick, A.; Stephan, D. W. *Organometallics*, **2006**, *25*, 4985. (b) Grob, T.; Seybert, G.; Massa, W.; Weller, F.; Palaniswami, R.; Greiner, A.; Dehnicke, K. *Angew. Chem. Int. Ed.* **2000**, *39*, 4373 (c) Graham, T. W.; Kickham, J.; Courtenay, S.; Wei, P.; Stephan, D. W. *Organometallics*, **2004**, *23*, 3309. (d) Guerin, F.; Stewart, J. C.; Beddie, C.; Stephan, D. W. *Organometallics*, **2000**, *19*, 2994. (e) Hollink, E.; Stewart, J. C.; Wei, P.; Stephan, D. W. *Dalton Trans.* **2003**, 3968. (f) Courtenary, S.; Stephan, D. W. *Organometallics*, **2001**, *20*, 1442.

20. (a) Bennett, B. K.; Saganic, E.; Lovell, S.; Kaminsky, W.; Samuel, A.; Mayer, J. M. *Inorg. Chem.* **2003**, *42*, 4127. (b) Chen, G.; Man W.-L.; Yiu, S.-M.; Wong, T.-W.; Szeto, L.; Wong, W.-T.; Lau, T.-C. *Dalton Trans.* **2011**, *40*, 1938. (c) Phillips, F. L.; Skapski, A. C. *J. Chem. Soc., Dalton Trans.* **1976**, 1448. (d) Hang, M.; Huynh, V.; White, P. S.; Meyer, T. J. *Inorg. Chem.* **2000**, *39*, 2825. (e) Fang G.-S.; Huang, J.-S.; Zhu, N.; Che, C.-M. *Eur. J. Inorg. Chem.* **2004,** 1341. (f) Bakir, M.; White, P. S.; Dovletoglou, A.; Meyer, T. J. *Inorg. Chem.* **1991**, *30*, 2835. (g) Demadis, K. D.; Bakir, M.; Klesczewski, B. G.; Williams, D. S.; White, P. S.; Meyer, T. J. *Inorg. Chim. Acta* **1998**, *270*, 511. (h) Scepaniak, J. J.; Fulton, M. D.; Bontchev, R. P.; Duesler, E. N.; Kirk, M. L.; Smith, J. M. *J. Am. Chem. Soc.* **2008**, *130*, 10515. (i) Leung, C.-F.; Yiu, D. T. Y.; Wong, W.-T.; Peng, S.-M.; Lau, T.-C. *Inorg. Chim. Acta.* **2009**, *362*, 3576. (j) Yi, X.-Y.; Lam T. C. H.; Sau, Y.-K.; Zhang, Q.-F.; Williams, I. D.; Leung, W.-H. *Inorg. Chem.* **2007**, *46*, 7193. (k) Ho, C.-M.; Leung, H.-C.; Wu, S.; Low, K.-H.; Lin, Z.; Che, C.-M. *Eur. J. Inorg. Chem.* **2012**, 151. (l) Wong, T.-W.; Lau, T.-C.; Wong, W.-T. *Inorg. Chem.* **1999**, *38*, 6181. (m) Demadis, K. D.; Bakir, M.; Klesczewski, B. G.; Williams, D. S.; White, P. S.; Meyer, T. J. *Inorg. Chim. Acta* **1998**, *270*, 511. (n)

Leung, W.-H.; Chan, E. Y. Y.; Lai, T. C. Y.; Wong, W.-T. *J. Chem. Soc., Dalton Trans.* **2000**, 51.

21. (a) Brown, S. D.; Betley, T. A.; Peters, J. C. *J. Am. Chem. Soc.* **2003**, *125*, 322. (b) Betley, T. A.; Peters, J. C. *Inorg. Chem.* **2003**, *42*, 5074. (c) Lu, C. C.; Saouma, C. T.; Day, M. W.; Peters, J. C. *J. Am. Chem. Soc.* **2007,** *129*, 4. (d) Saouma, C. T.; Lu, C. C.; Peters, J. C. *Inorg. Chem.* **2012**, *51*, 10043.

22. Taillefer, M.; Rahier, N.; Hameau, A.; Volle, J.-N. *Chem. Commun.* **2006,** 3238.

23. The small extent of crossover at the temperatures accessible in solution precluded reliably fitting this data to a Boltzmann equilibrium expression.

24. Klaui, W.; Eberspch, W.; Gutlich, P. *Inorg. Chem.* **1987**, *26*, 3977.

25. (a) Brunker, T. J.; Green, J. C.; O'Hare, D. *Inorg. Chem.* **2003**, *42*, 4366. (b) Smith, M. E.; Andersen, R. A. *J. Am. Chem. Soc.* **1996**, *118*, 11119. (c) Gutlich, P.; McGarvey, B. R.; Klaui, W. *Inorg. Chem.* **1980**, *19*, 3704.

26. Evans, D. F. *J. Chem. Soc.* **1959**, 2003.

27. Sorai, M.; Seki, S. *J. Phys. Chem. Solids* **1974**, *35*, 555.

28. Haddad, M. S.; Federer, W. D.; Lynch, M. W.; Hendrickson, D. N. *J. Am. Chem. Soc.* **1980**, *102*, 1468.

29. Gütlich, P.; Goodwin, H. A.. *Top. Curr. Chem.* **2004**, *233*, 1.

30. The asymmetry of the quadrupole doublet for crystalline **3** is likely due to the presence of a small amount of the low-spin form of the complex. The broad peak discernible around 2 mm/s in the spectrum of lyophilized **3** is presumed to be due to modest decomposition during sample handling.

31. Rhode, J.-U.; Betley, T. A.; Jackson, T. A.; Saouma, C. T.; Peters, J. C.; Que, L., Jr. *Inorg. Chem.* **2007**, *46*, 5720.

32. Brown, S. D.; Peters, J. C. *J. Am. Chem. Soc.* **2005**, *127*, 1913.

33. Sohn, Y. S.; Hendrickson, D. N.; Gray, H. B. *J. Am. Chem. Soc.* **1971**, *93*, 3603.

34. Gaussian 09, Revision A.1, Frisch, M. J.; Trucks, G. W.; Schlegel, H. B.; Scuseria, G. E.; Robb, M. A.; Cheeseman, J. R.; Scalmani, G.; Barone, V.; Mennucci, B.; Petersson, G. A.; Nakatsuji, H.; Caricato, M.; Li, X.; Hratchian, H. P.; Izmaylov, A. F.; Bloino, J.; Zheng, G.; Sonnenberg, J. L.; Hada, M.; Ehara, M.; Toyota, K.; Fukuda, R.; Hasegawa, J.; Ishida, M.; Nakajima, T.; Honda, Y.; Kitao, O.; Nakai, H.; Vreven, T.; Montgomery, Jr., J. A.; Peralta, J. E.; Ogliaro, F.; Bearpark, M.; Heyd, J. J.; Brothers, E.; Kudin, K. N.; Staroverov, V. N.; Kobayashi, R.; Normand, J.; Raghavachari, K.; Rendell, A.; Burant, J. C.; Iyengar, S. S.; Tomasi, J.; Cossi, M.; Rega, N.; Millam, N. J.; Klene, M.; Knox, J. E.; Cross, J. B.; Bakken, V.; Adamo, C.; Jaramillo, J.; Gomperts, R.; Stratmann, R. E.; Yazyev, O.; Austin, A. J.; Cammi, R.; Pomelli, C.; Ochterski, J. W.; Martin, R. L.; Morokuma, K.; Zakrzewski, V. G.; Voth, G. A.; Salvador, P.; Dannenberg, J. J.; Dapprich, S.; Daniels, A. D.; Farkas, Ö.; Foresman, J. B.; Ortiz, J. V.; Cioslowski, J.; Fox, D. J. Gaussian, Inc., Wallingford CT, 2009.

35. Sheldrick, G.M. *Acta Cryst. A.* **2008**, *82*, 169.

Appendix A. Supplementary data for Chapter 4

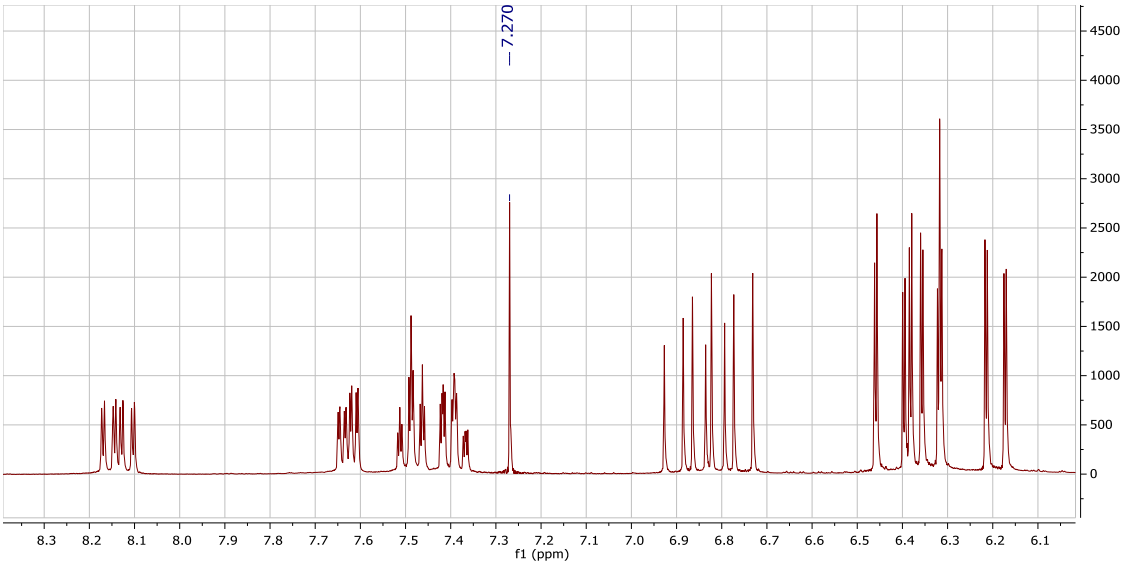

Figure A1. ^{1}H NMR of (2-bromophenyl)divinylphosphine oxide ($CDCl_3$, 300 MHz, 298 K). For clarity, only the downfield region is shown; no resonances appear outside of the region depicted.

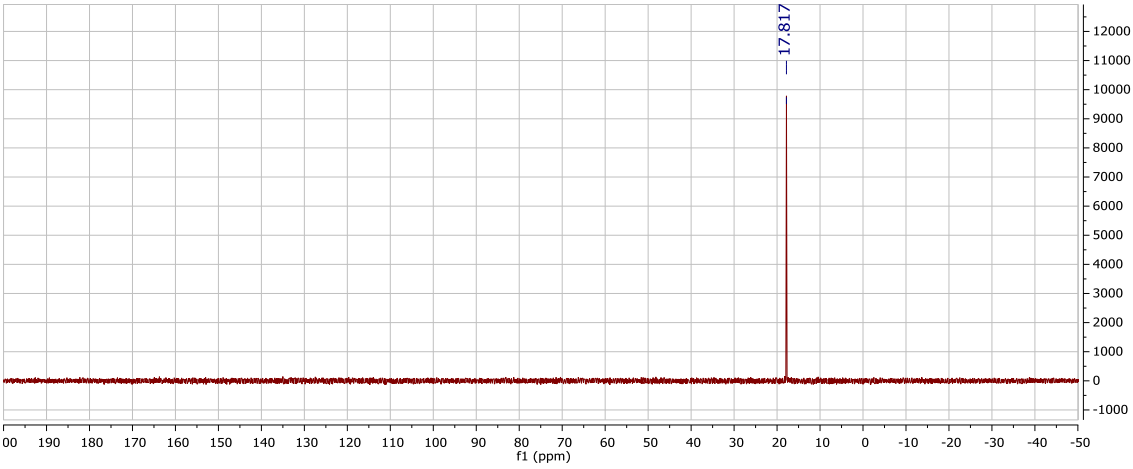

Figure A2. ^{31}P NMR of (2-bromophenyl)-divinylphosphine oxide ($CDCl_3$, 121 MHz, 298 K).

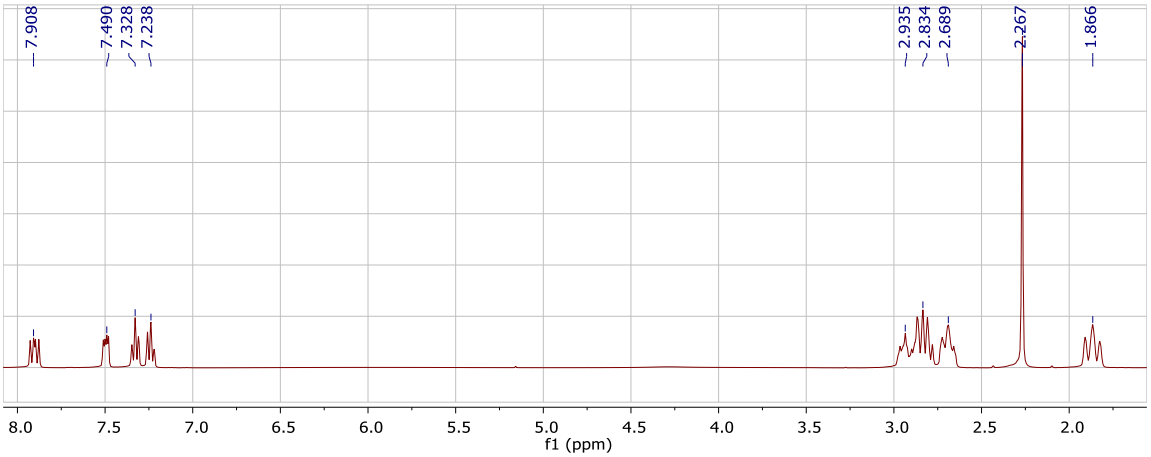

Figure A3. ^{1}H NMR of 4-(2-bromophenyl)-1-methyl-1,4-azaphosphinane-4-oxide ($CDCl_3$, 400 MHz, 298 K).

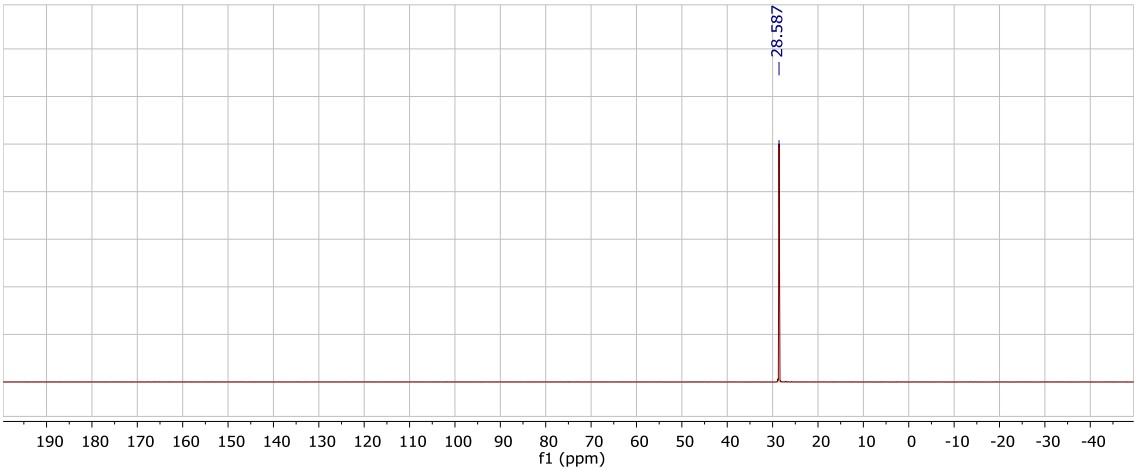

Figure A4. ^{31}P NMR of 4-(2-bromophenyl)-1-methyl-1,4-azaphosphinane-4-oxide ($CDCl_3$, 162 MHz, 298 K).

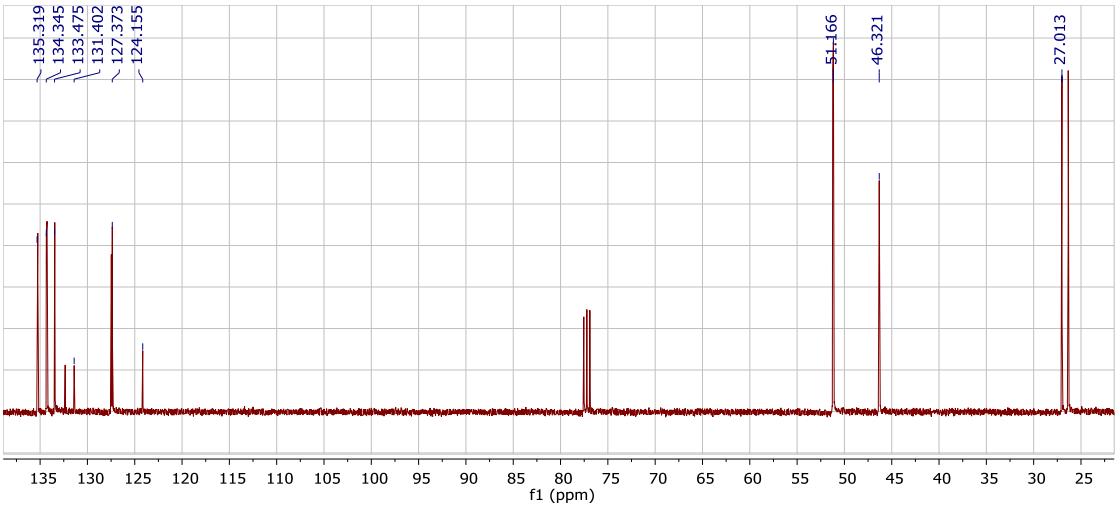

Figure A5. ^{13}C NMR of 4-(2-bromophenyl)-1-methyl-1,4-azaphosphinane-4-oxide ($CDCl_3$, 101 MHz, 298 K).

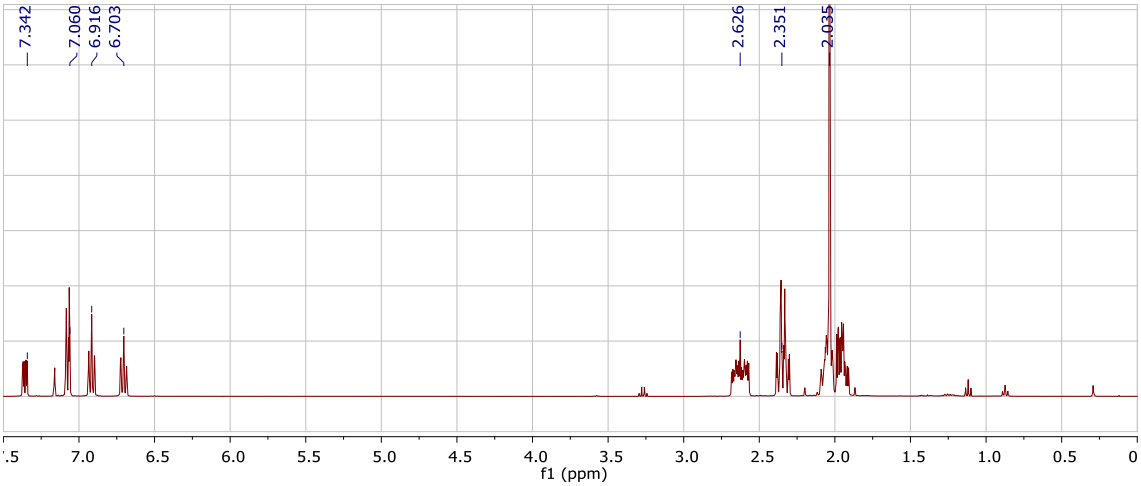

Figure A6. ^{1}H NMR of **L_0** (C_6D_6, 400 MHz, 298 K).

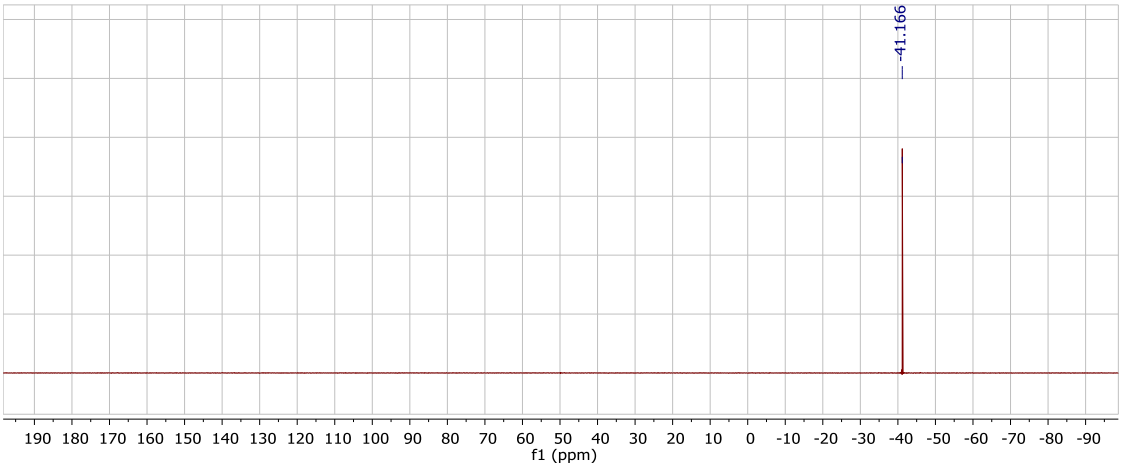

Figure A7. ^{31}P NMR of **L₀** (C_6D_6, 162 MHz, 298 K).

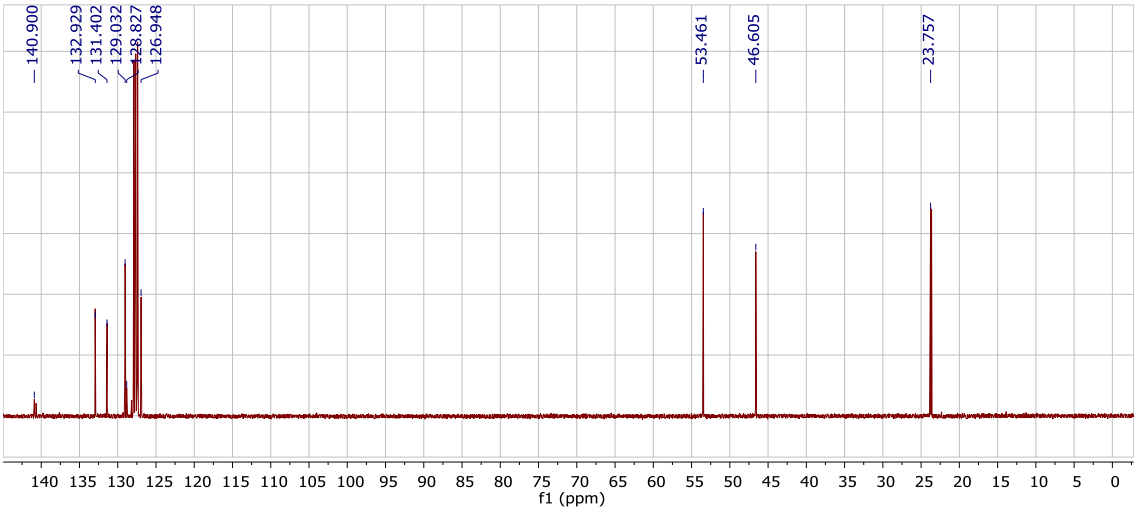

Figure A8. ^{13}C NMR of **L**$_0$ (C_6D_6, 101 MHz, 298 K).

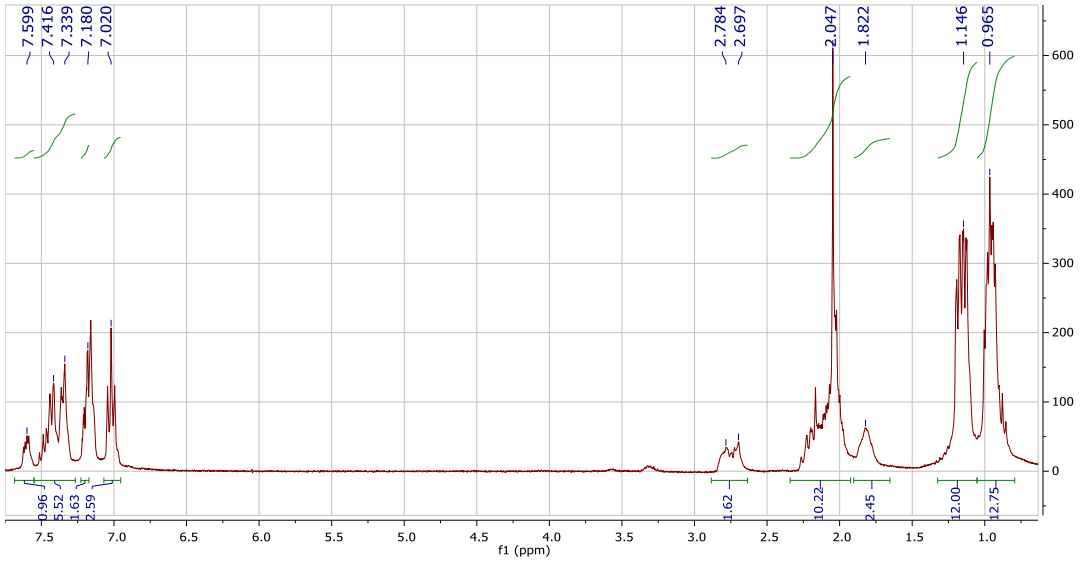

Figure A9. ^{1}H NMR of **L₁** (C_6D_6, 300 MHz, 298 K).

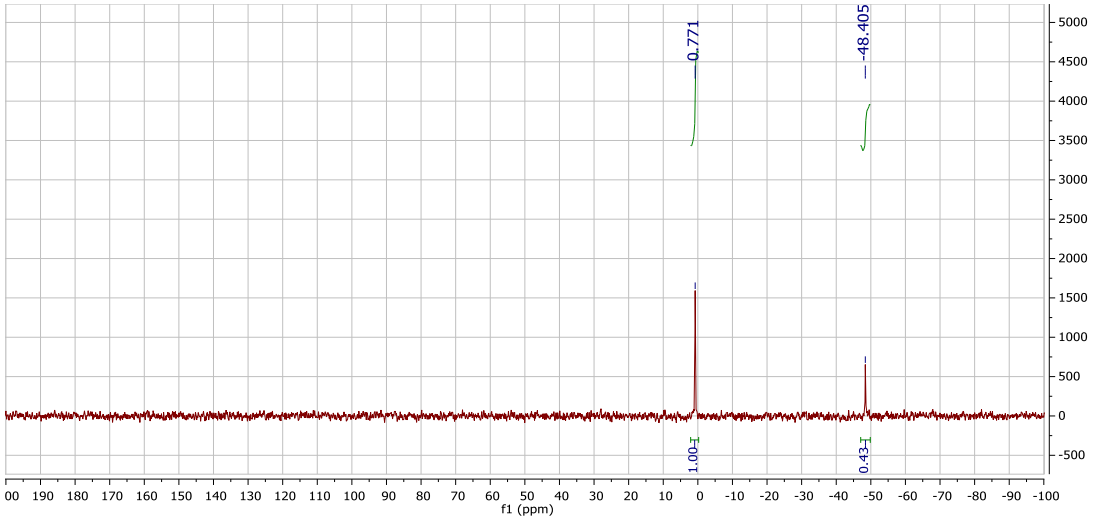

Figure A10. ^{31}P NMR of **L₁** (C_6D_6, 121 MHz, 298 K).

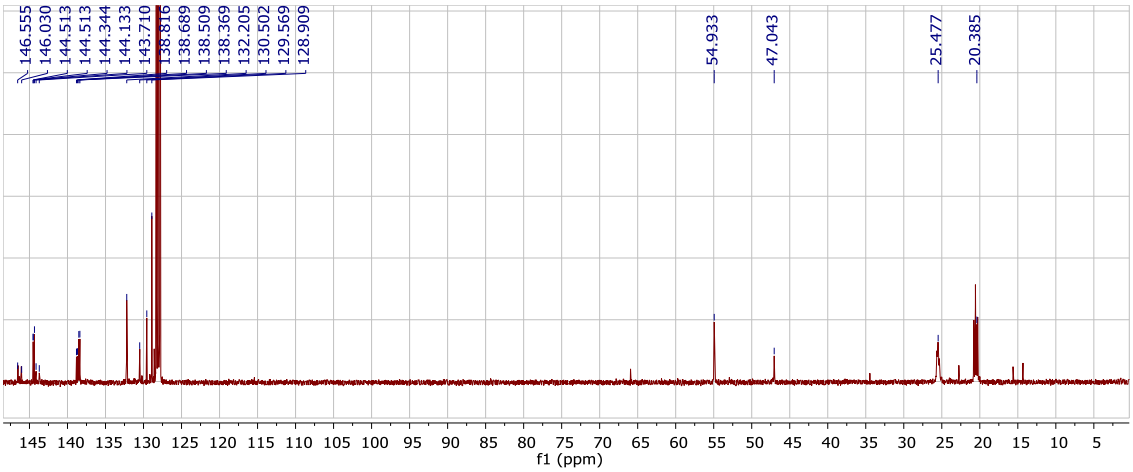

Figure A11. ^{13}C NMR of **L₁** (C_6D_6, 75 MHz, 298 K).

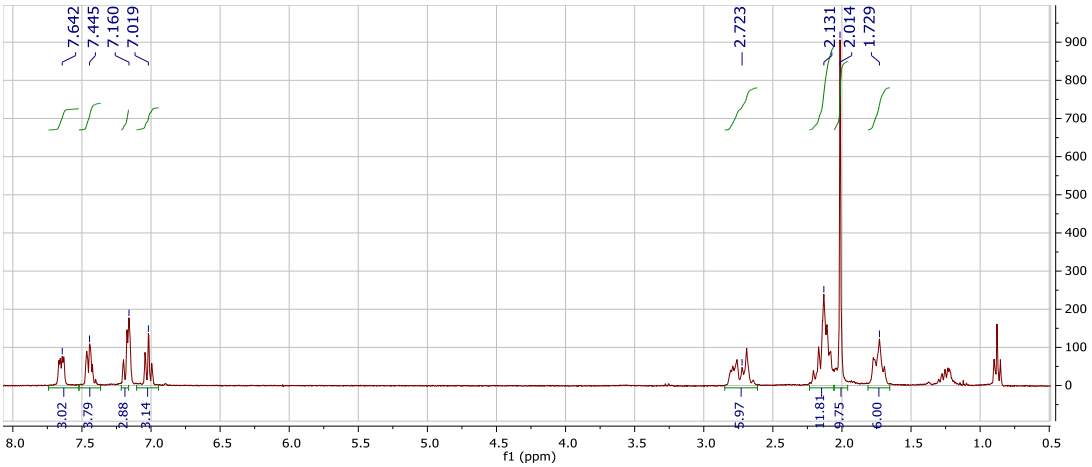

Figure A12. ^{1}H NMR of **L₂** (C_6D_6, 300 MHz, 298 K).

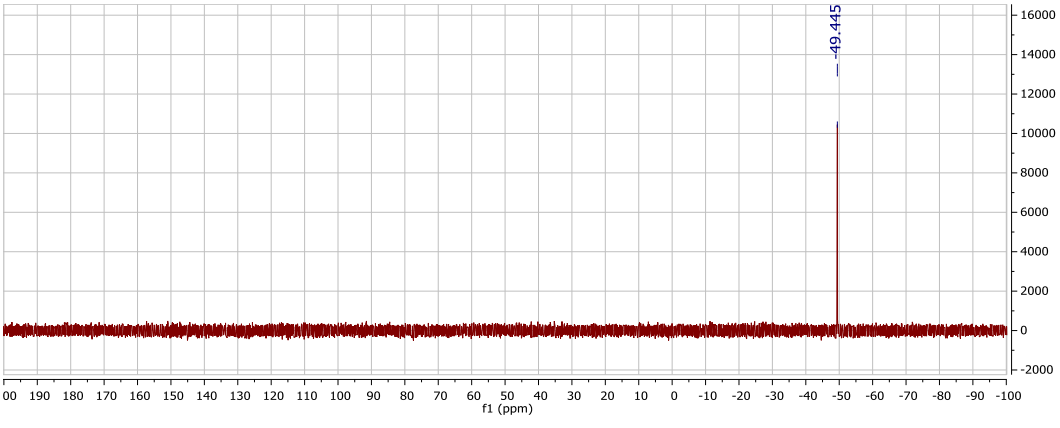

Figure A13. ^{31}P NMR of **L₂** (C_6D_6, 121 MHz, 298 K).

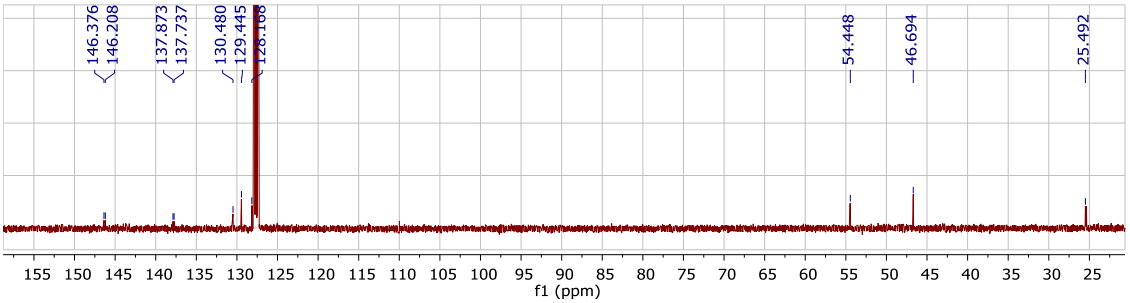

Figure A14. ^{13}C NMR of **L₂** (C_6D_6, 75 MHz, 298 K).

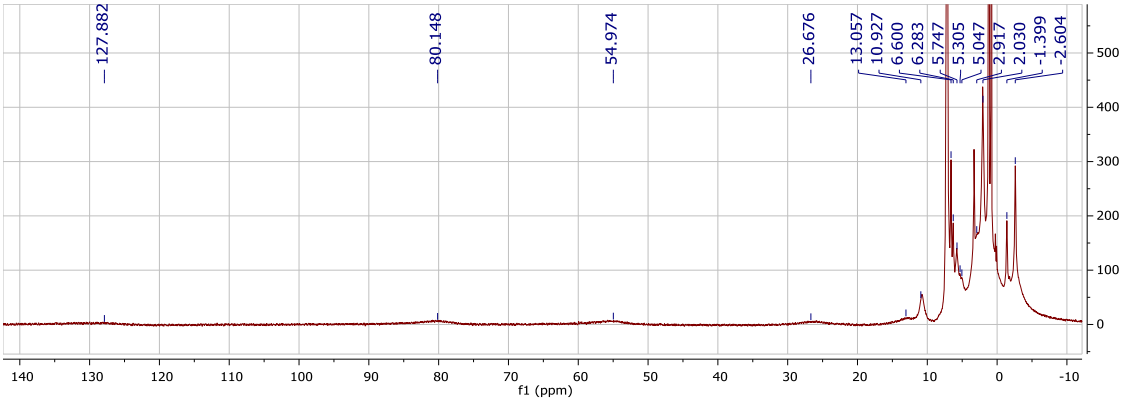

Figure A15. ^{1}H NMR of **4.1** (C_6D_6, 300 MHz, 298 K).

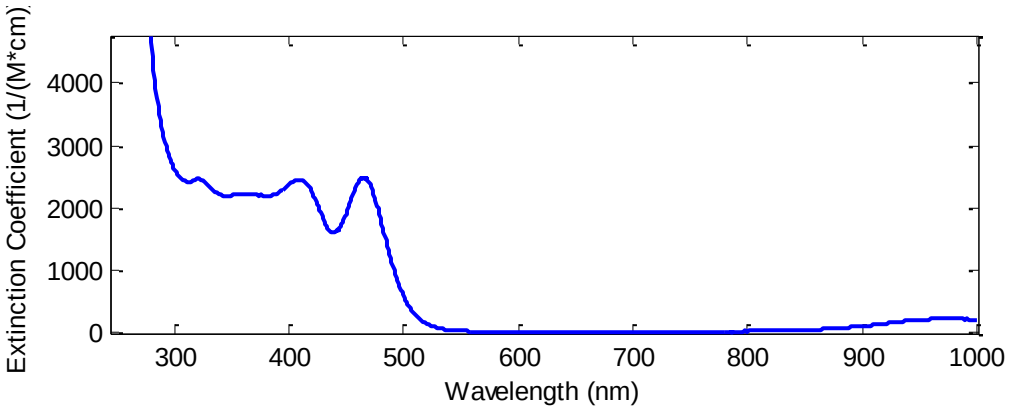

Figure A16. UV-vis spectrum of **4.1** in THF.

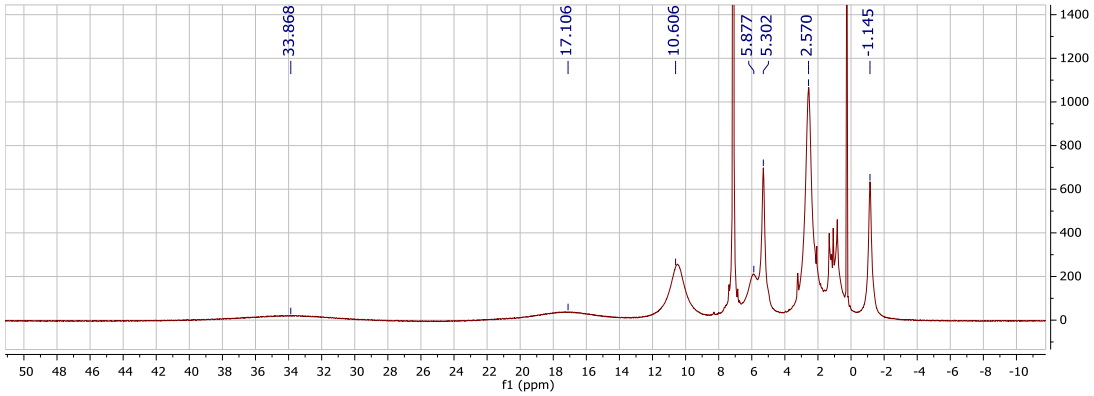

Figure A17. ^{1}H NMR of **4.1'** (C_6D_6, 300 MHz, 298 K).

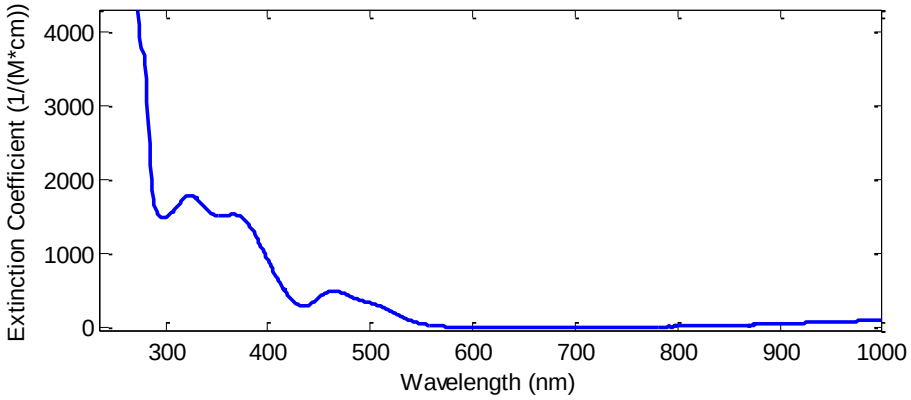

Figure A18. UV-vis spectrum of **4.1'** in THF.

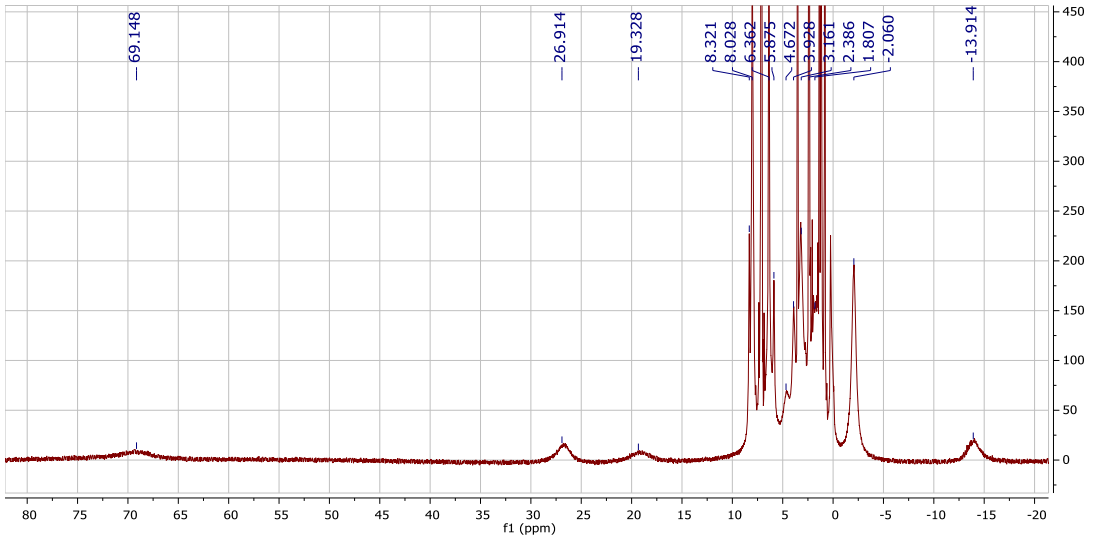

Figure A19. ^{1}H NMR of **4.2** (C_6D_6, 300 MHz, 298 K).

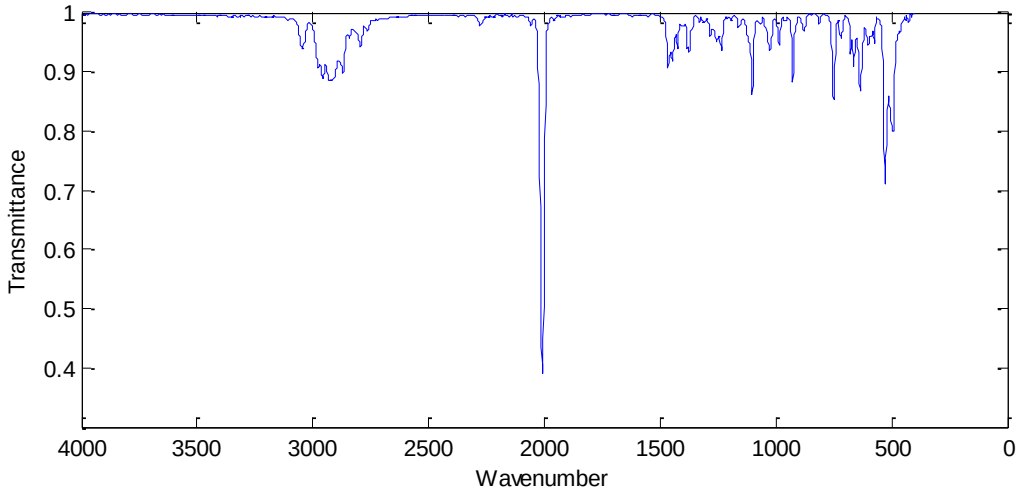

Figure A20. IR spectrum of **4.2** (thin film deposited from benzene).

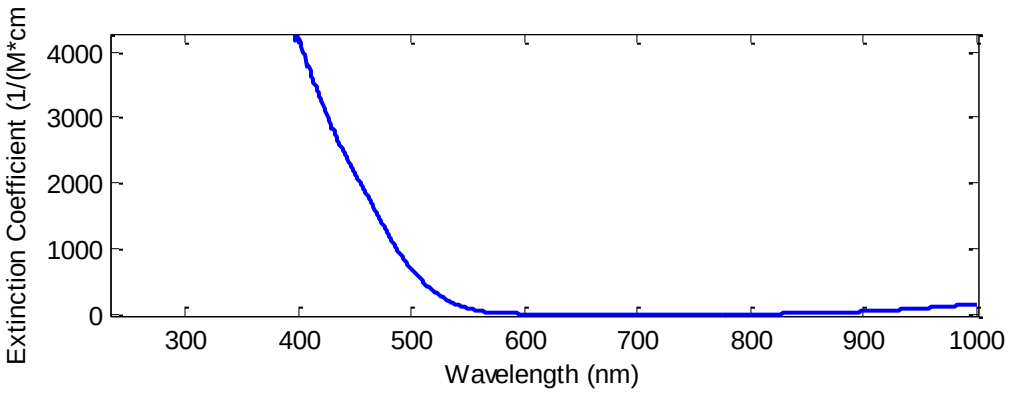

Figure A21. UV-vis spectrum of **4.2** in THF.

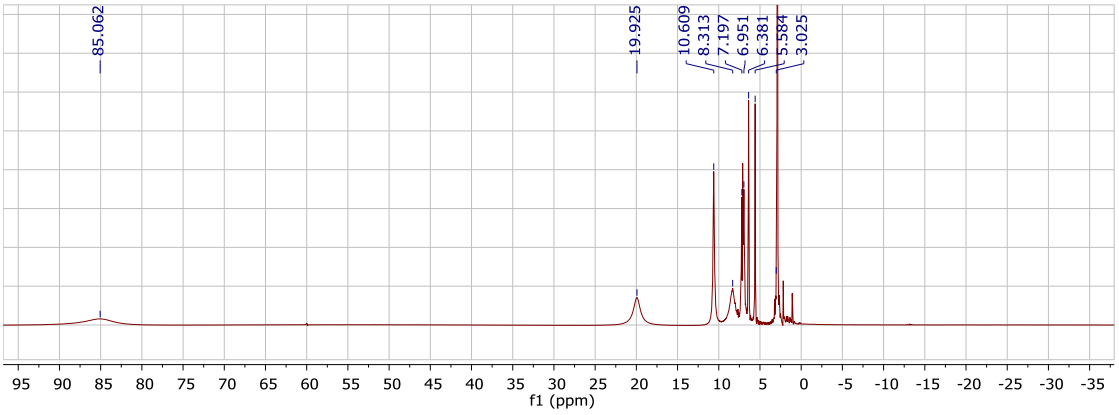

Figure A22. ^{1}H NMR of **4.2'** (C_6D_6, 300 MHz, 298 K).

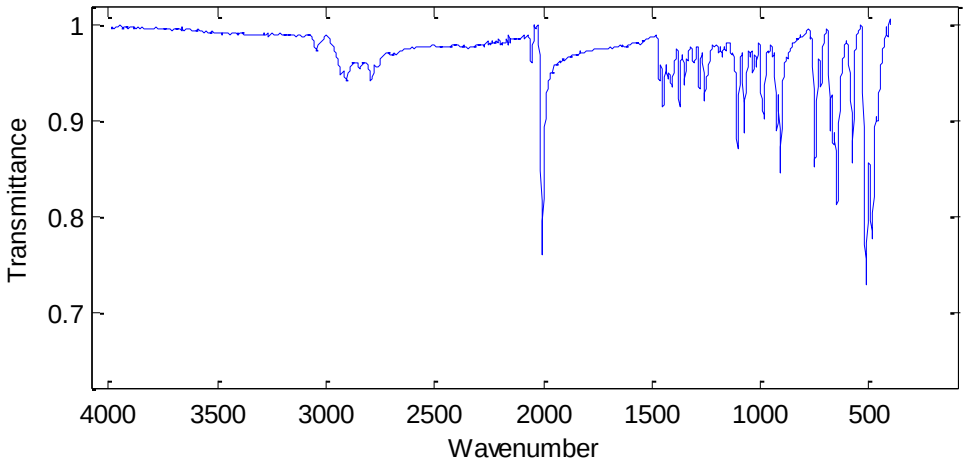

Figure A23. IR spectrum of **4.2'**(thin film deposited from benzene).

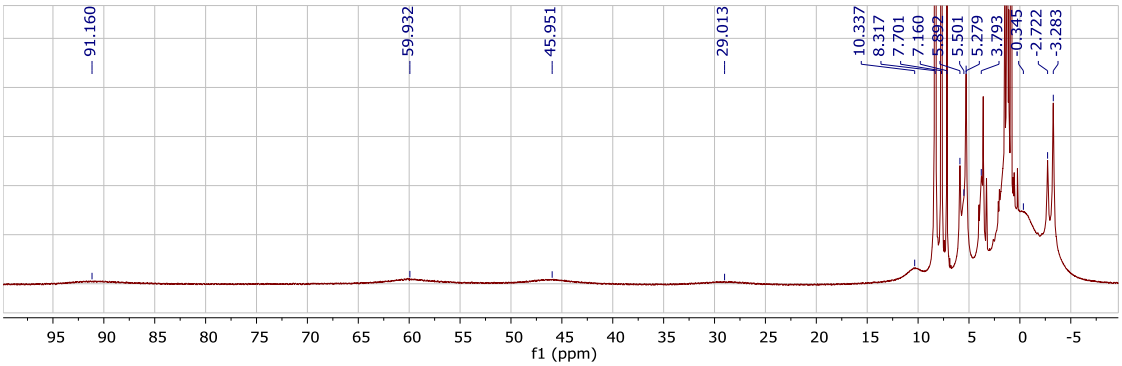

Figure A24. ^{1}H NMR of **4.3** (5:1 C_6D_6:d_8-THF, 300 MHz, 298 K).

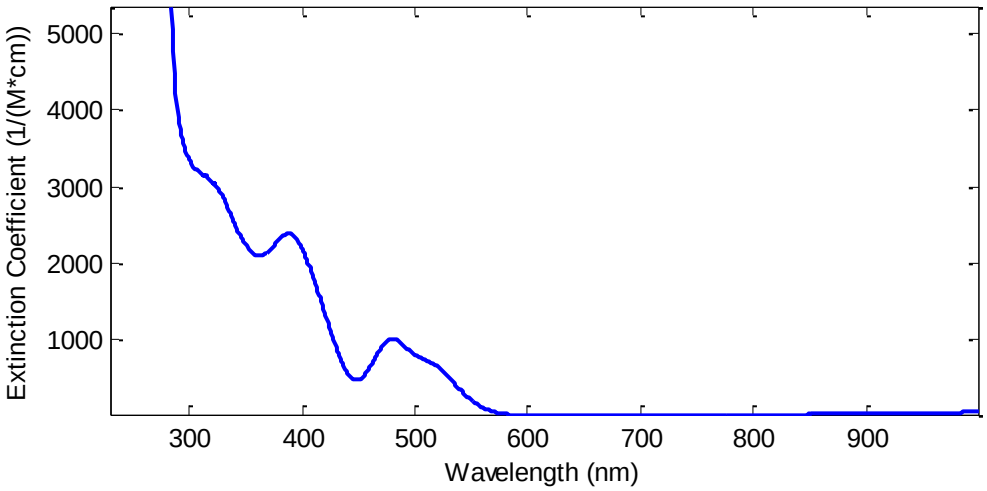

Figure A25. UV-vis spectrum of **4.3** in THF.

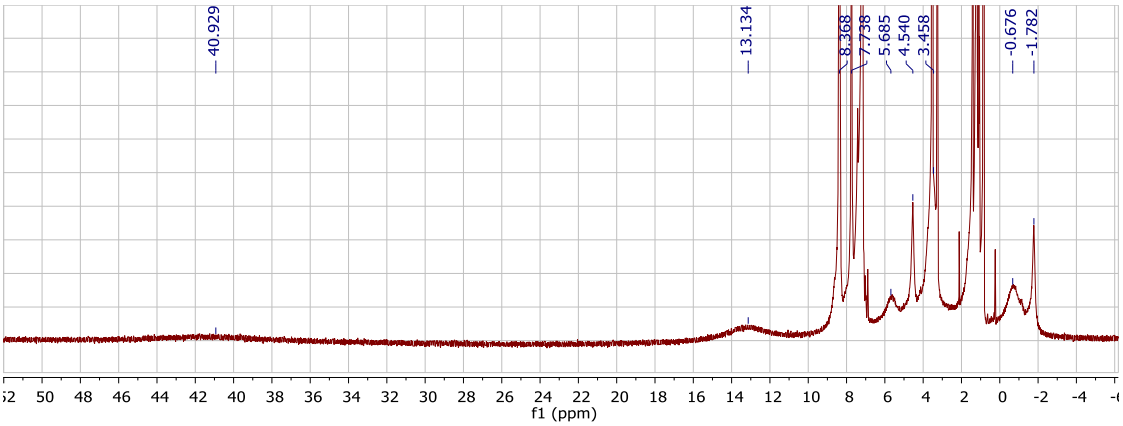

Figure A26. ^{1}H NMR of **4.3'** (5:1 C_6D_6:d_8-THF, 300 MHz, 298 K).

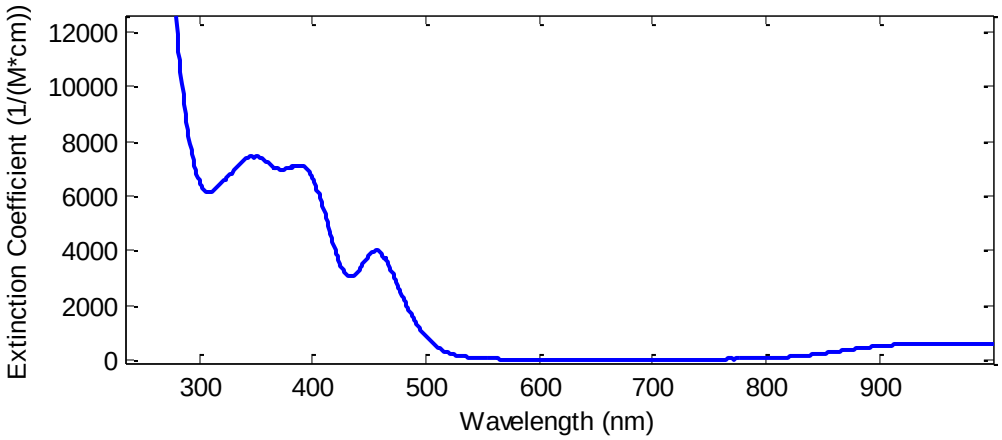

Figure A27. UV-vis spectrum of **4.3'** in THF.

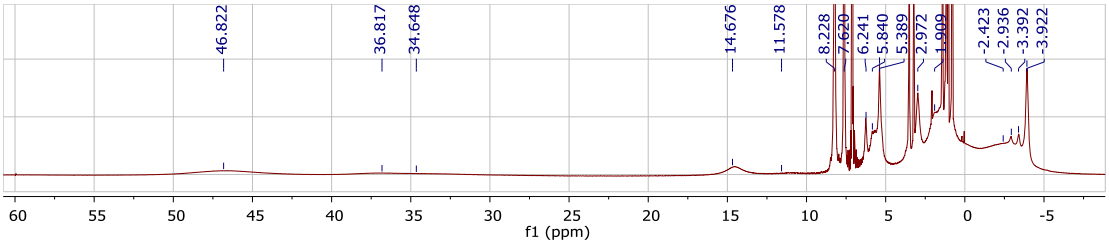

Figure A28. ^{1}H NMR of **4.4** (4:1 C_6D_6:d_8-THF, 300 MHz, 298 K).

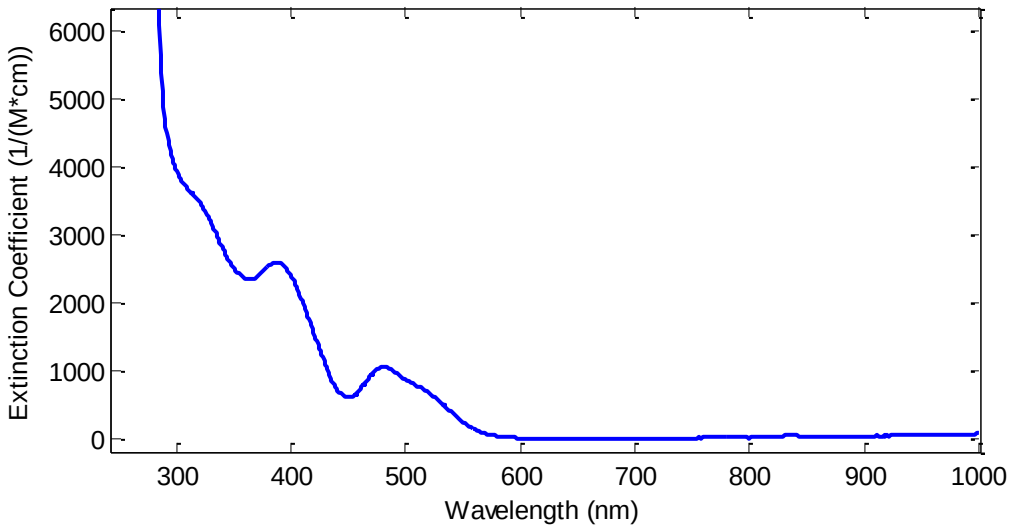

Figure A29. UV-vis spectrum of **4.4** in THF.

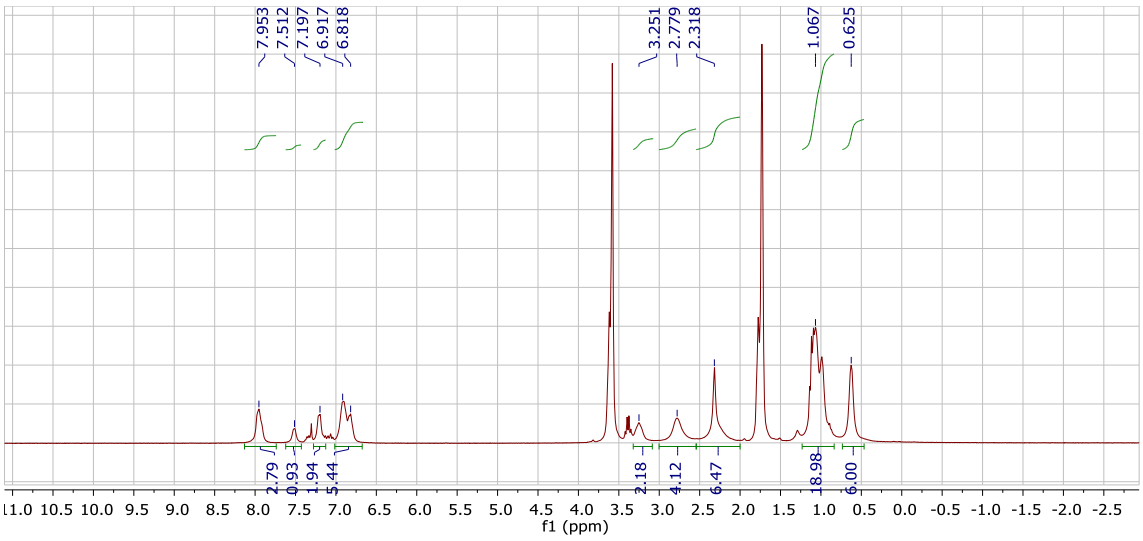

Figure A30. ^{1}H NMR of **4.6** in d_8-THF (300 MHz, 298 K).

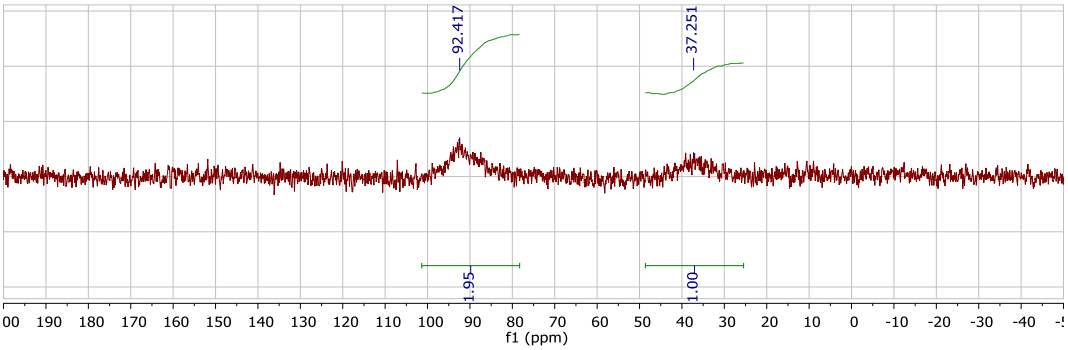

Figure A31. ^{31}P NMR of **4.6** in d_8-THF (121 MHz, 298 K).

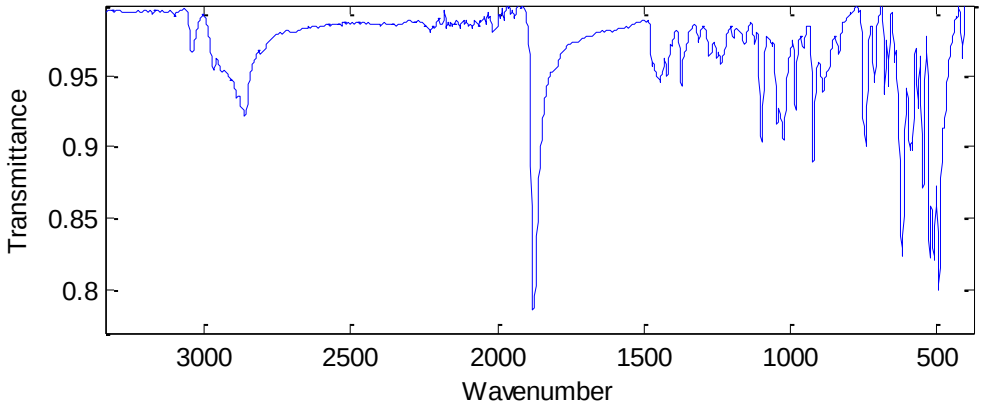

Figure A32. IR spectrum of **4.6** as a thin film deposited from THF.

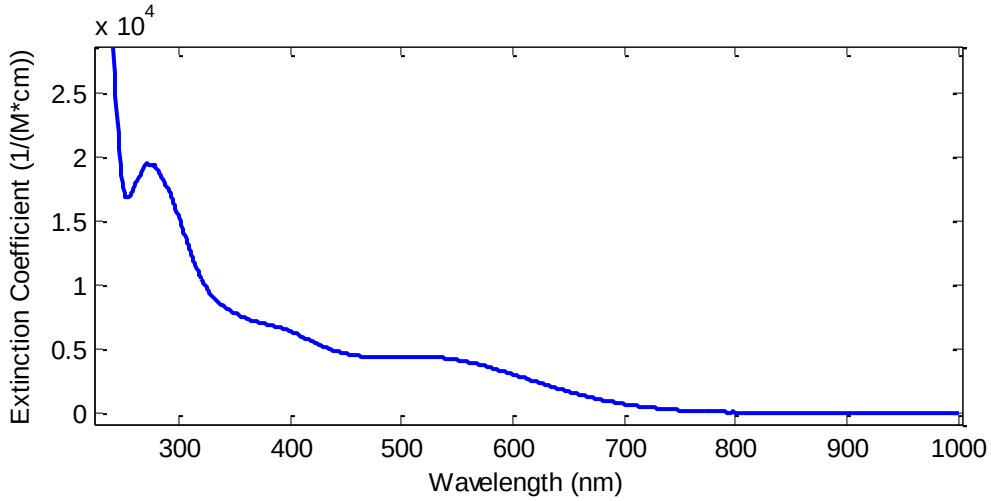

Figure A33. UV-vis spectrum of **4.6** in THF.

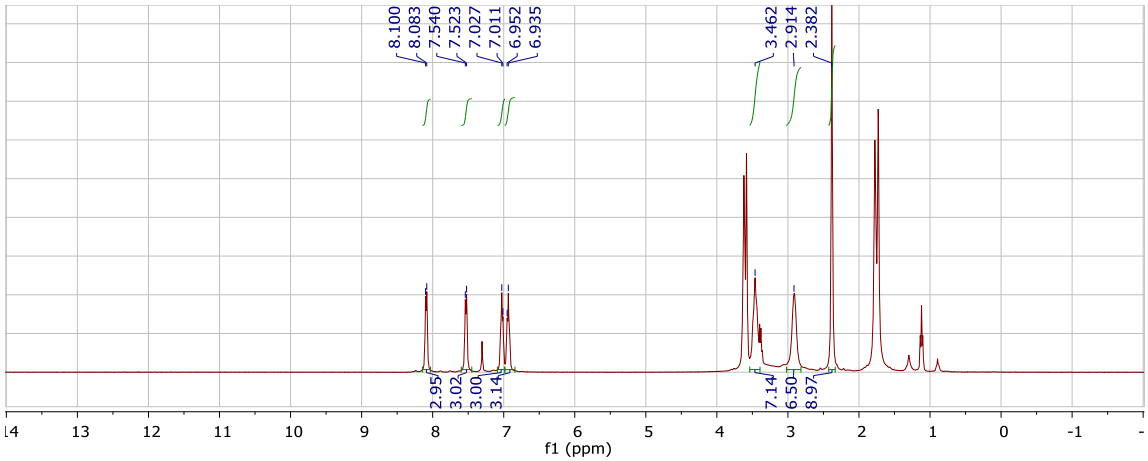

Figure A34. ^{1}H NMR spectrum of **4.6'** in d_8-THF (300 MHz, 298 K).

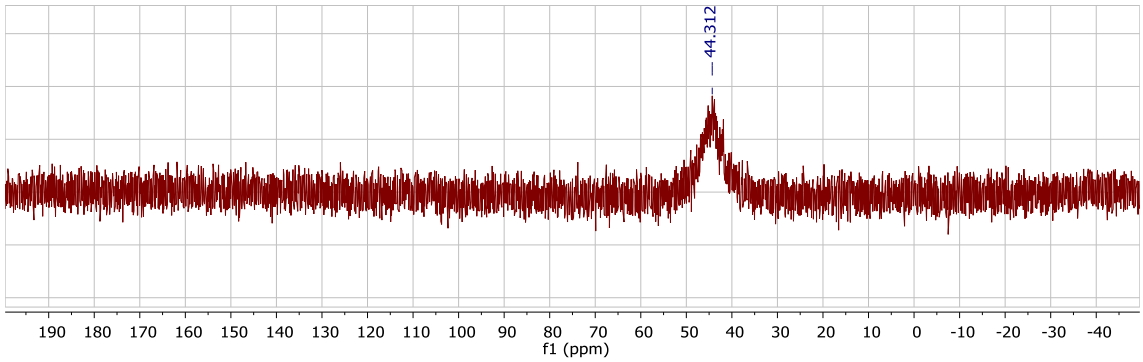

Figure A35. ^{31}P NMR spectrum of **4.6'** in d_8-THF (300 MHz, 298 K).

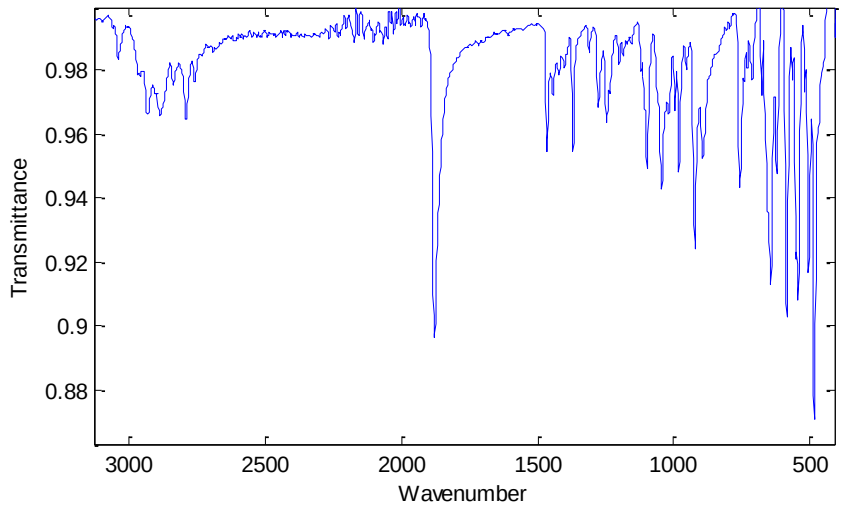

Figure A36. IR spectrum of **4.6'** as a thin film deposited from THF.

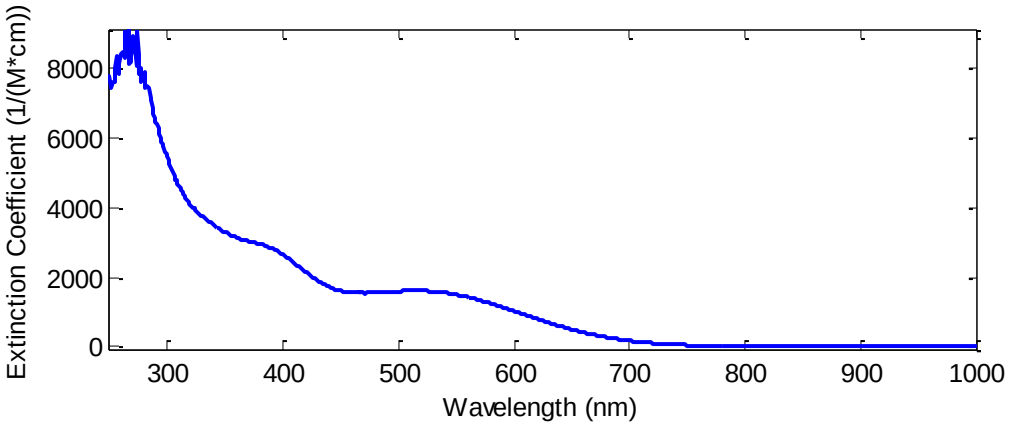

Figure A37. UV-vis spectrum of **4.6'** in THF.

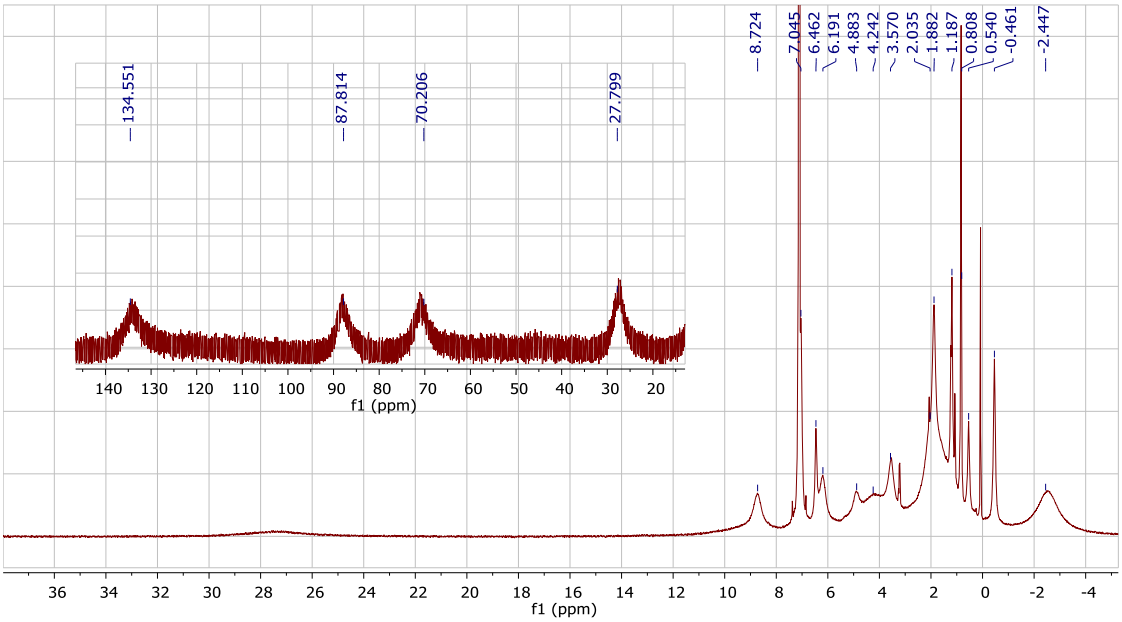

Figure A38. ^{1}H NMR of **4.5** in C_6D_6 (300 MHz, 298 K) with inset showing broad upfield resonances.

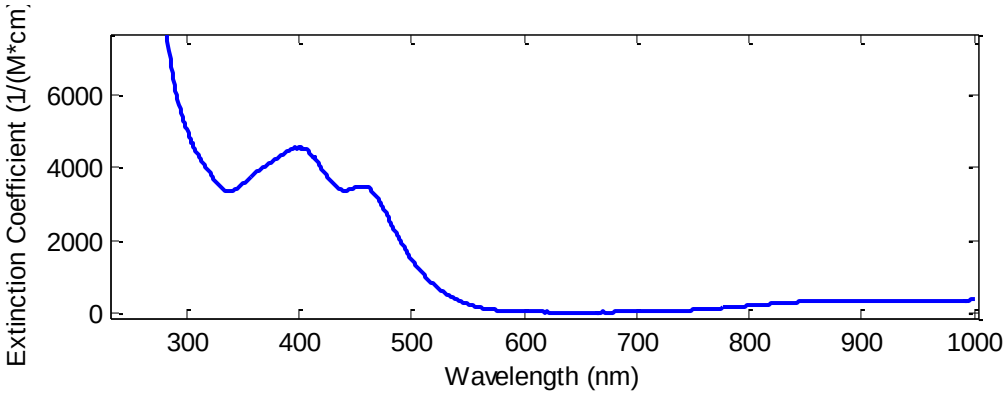

Figure A39. UV-vis spectrum of **4.5** in THF.

Oxidation of $SiP^{iPr}_2P^{NMe}FeNH_2$. **A.** $SiP^{iPr}_2P^{NMe}FeNH_2$ (25 mg, 0.037 mmol) was dissolved in Et_2O (3 mL) and cooled to -78 °C. A similarly cooled solution of $FcBAr^F_4$ (36.8 mg, 0.035 mmol) in Et_2O (3 mL) was added dropwise over two minutes. The orange solution turned a deeper red-orange color. The reaction mixture was allowed to warm to room temperature, concentrated to a volume of 1 mL, layered with pentane, and allowed to stand overnight. NMR analysis of the resulting orange crystalline precipitate confirmed the formation of $[SiP^{iPr}_2P^{NMe}FeNH_3][BAr^F_4]$. **B.** (For EPR analysis) $SiP^{iPr}_2P^{NMe}FeNH_2$ (5.8 mg, 0.009 mmol) was dissolved in 2-MeTHF (0.5 mL) and frozen. A thawing solution of $FcBAr^F_4$ (8.1 mg, 0.008 mmol) in 2-MeTHF (0.5 mL) was added and the solution was allowed to thaw briefly, mixed, and transferred to a pre-cooled EPR tube. The reaction mixture was analyzed by EPR spectroscopy.

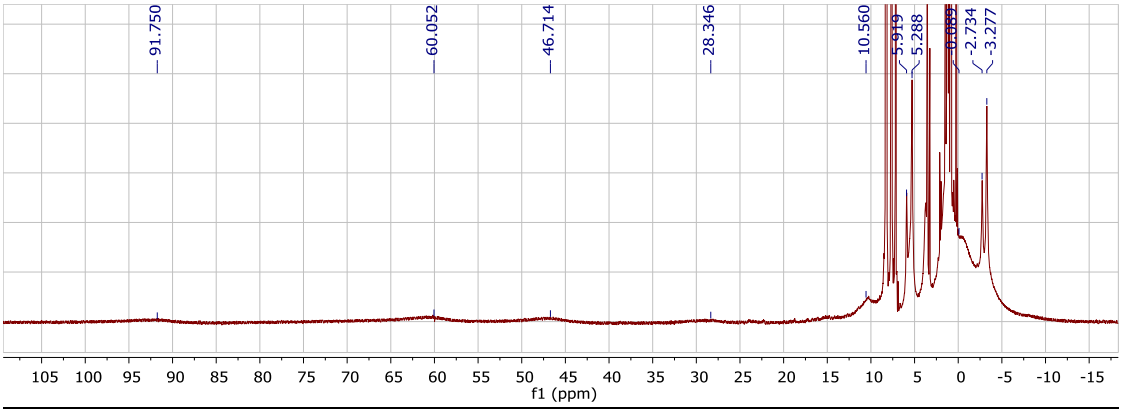

Figure A40. ^{1}H NMR (4:1 C_6D_6:d_8-THF, 300 MHz, 298 K) of terminal oxidation product of **4.5**.

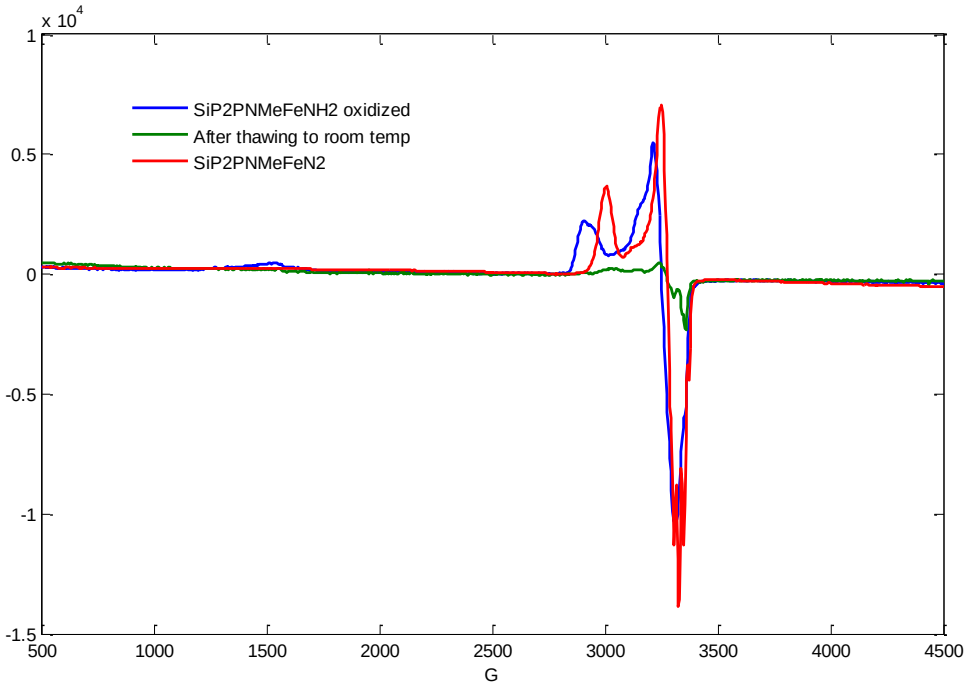

Figure A41. EPR spectrum of oxidation of **4.5** in thawing 2-MeTHF (blue), and after warming to room temperature (green). The EPR spectrum of **4.2** is also shown (red).

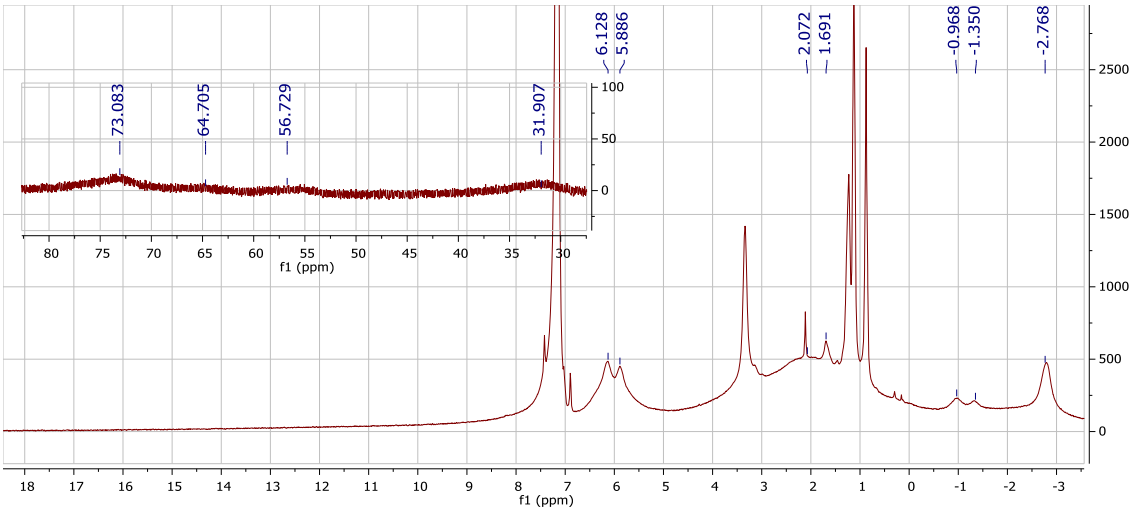

Figure A42. ^{1}H NMR spectrum of unpurified [SiP$^{iPr}_{2}$P^{NMe2}FeCl]OTf (C_6D_6, 300 MHz, 298 K).

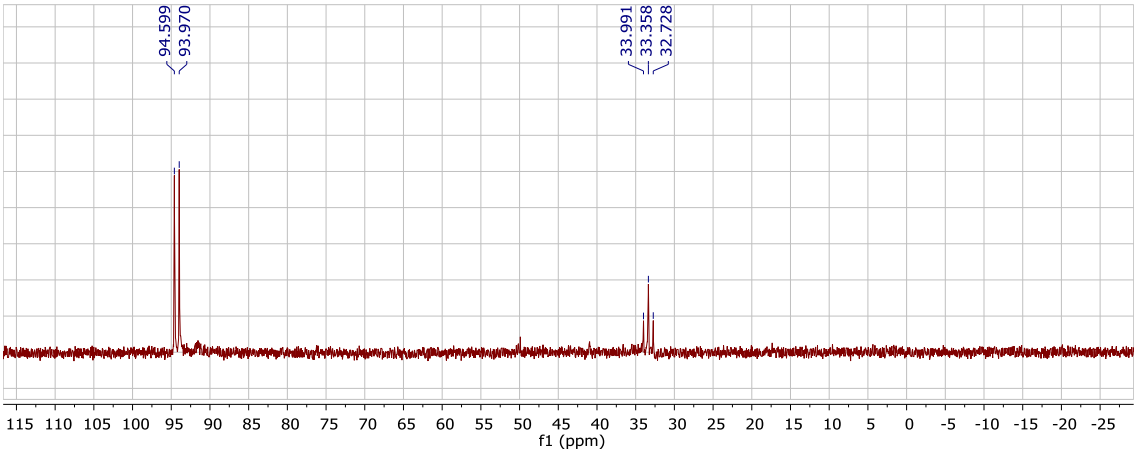

Figure A43. ^{31}P NMR of **4.7** (C_6D_6, 121 MHz, 298 K).

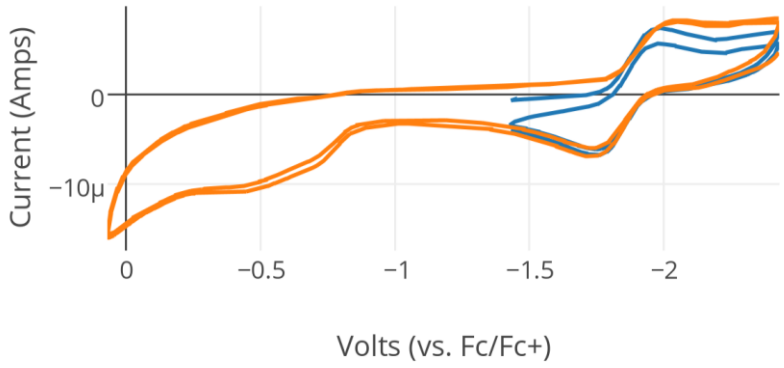

Figure A44. Cyclic voltammogram of $SiP^{iPr}{}_2P^{NMe2}FeN_2$ (**4.7**) (0.2 mM in 0.2 M [TBA][PF_6]). Scans performed at a scan rate of 0.1 V/s.

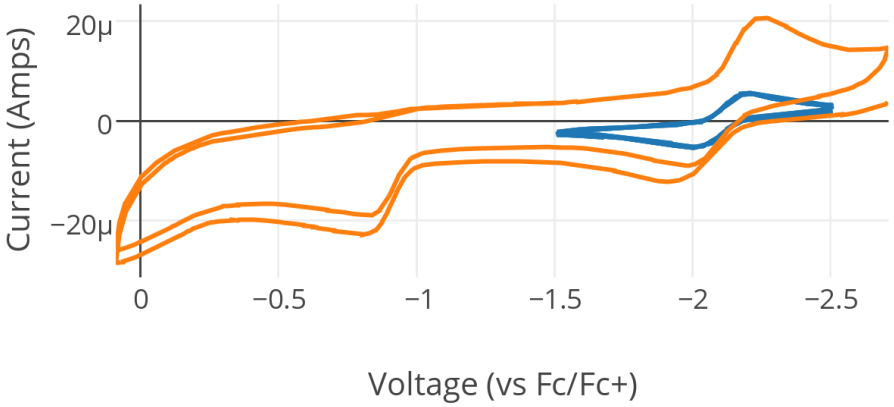

Figure A45. Cyclic voltammogram of $[SiP^{iPr}{}_2P^{NMe}FeN_2][Na(THF)_2]$ (**4.6**) (0.2 mM in 0.2 M [TBA][PF_6]). Scans performed at a scan rate of 0.1 V/s (blue) or 0.5 V/s (orange).

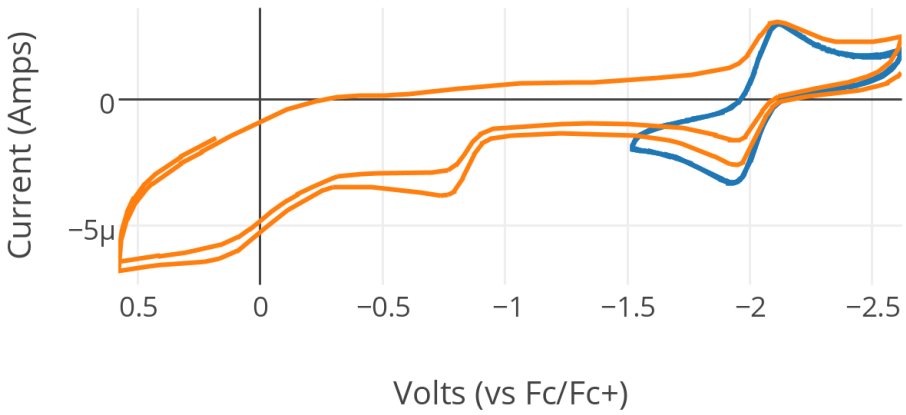

Figure A46. Cyclic voltammogram of $[SiP_3^{NMe}FeN_2][Na(THF)_3]$ (**4.6'**) (0.2 mM in 0.2 M [TBA][PF_6]). Scans performed at a scan rate of 0.1 V/s.

Attempted NH_3 production from $[SiP_3^{NMe}FeN_2][Na(THF)_3]$ (4.6'). $[SiP_3^{NMe}FeN_2][Na(THF)_3]$ (3.2 mg, 0.0035 mmol) was dissolved in Et_2O (1 mL) and cooled to -78 ºC. Similarly cooled solutions of KC_8 (40 mg, 80 eq, in 1 mL Et_2O) and $HBAr_4^F.2Et_2O$ (111 mg, 31 eq, in 1 mL Et_2O) were added rapidly and sequentially. The resulting reaction mixture was allowed to stir at low temperature for 2 hours before being allowed to warm to room temperature for one hour. The reaction mixture was then analyzed for ammonia production; no detectable ammonia was present.

NH_3 production from $SiP^{iPr}P^{NMe2}FeN_2$(4.7). $SiP^{iPr}P^{NMe2}FeN_2$ (2.0 mg, 0.0028 mmol) was suspended in Et_2O (1 mL) and cooled to -78 ºC. Similarly cooled solutions of KC_8 (19 mg, 50 eq, in 1 mL Et_2O) and $HBAr_4^F.2Et_2O$ (135 mg, 48 eq, in 1 mL Et_2O) were added rapidly and sequentially. The resulting reaction mixture was allowed to stir at low temperature for 2 hours before being allowed to warm to room temperature for one hour.

The reaction mixture was then analyzed for ammonia production. 0.53 equivalents of ammonia were detected.

Stoichiometric protonation of [$SiP_3^{NMe}FeN_2$][$Na(THF)_3$] (4.6'). [$SiP_3^{NMe}FeN_2$][$Na(THF)_3$] (5 mg, 0.0054 mmol) was dissolved in THF (1 mL) and cooled to -78 ºC. A similarly cooled solution of $HBAr_4^F.2Et_2O$ (6.5 mg, 1.2 equiv.) in Et_2O (1 mL) was added in one portion and the reaction mixture, which immediately turned yellow, was stirred at low temperature for one hour before being allowed to warm to room temperature. The yellow residue was then analyzed by NMR, which showed that the primary product is an iron hyride, $SiP_3^{NMe}Fe(N_2)(H)$. No oxidation product, $SiP_3^{NMe}FeN_2$, could be detected.

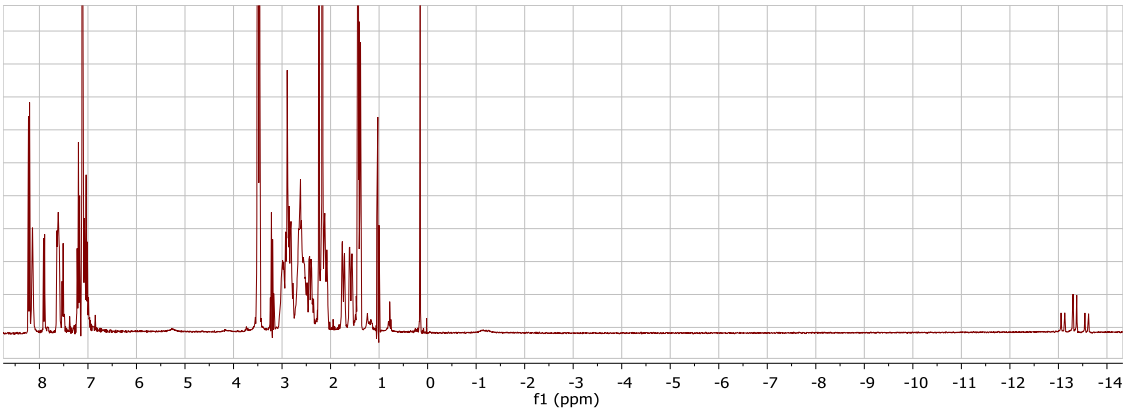

Figure A47. ^1H NMR (C_6D_6, 300 MHz, 298 K) of the protonation reaction of **4.6'** with one equivalent of $HBAr^F_4{\cdot}2Et_2O$.

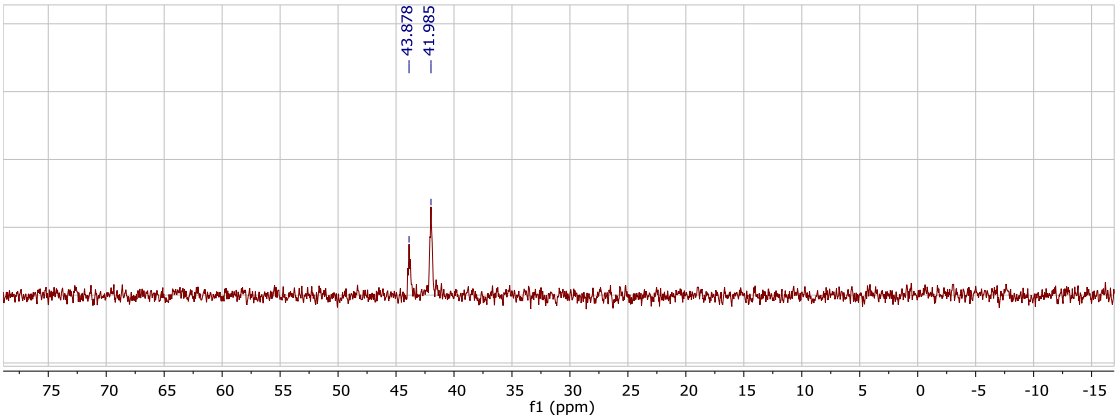

Figure A48. ^{31}P NMR (C_6D_6, 121 MHz, 298 K) of the protonation reaction of **4.6'** with one equivalent of $HBAr^F_4 \cdot 2Et_2O$.

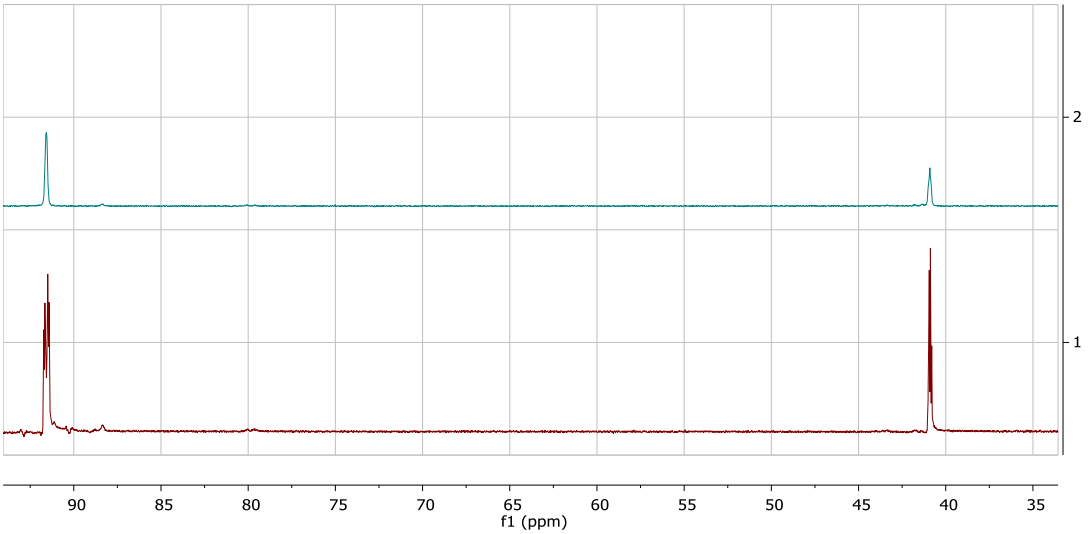

Figure A49. $^{31}P\{1H\}$ (top) and ^{31}P NMR spectra of the reaction mixture from protonation of **4.6** with one equivalent of $HBAr^F_4 \cdot 2Et_2O$ (C_6D_6, 298 K, 121 MHz).

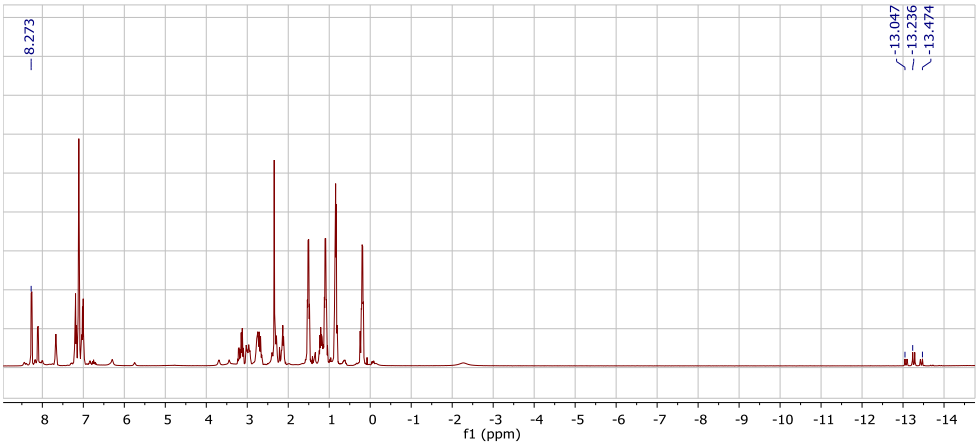

Figure A50. ^{1}H NMR spectrum of the reaction mixture from protonation of **4.6** with one equivalent of $HBAr^{F}_{4}\cdot 2Et_2O$ (C_6D_6, 298 K, 300 MHz).

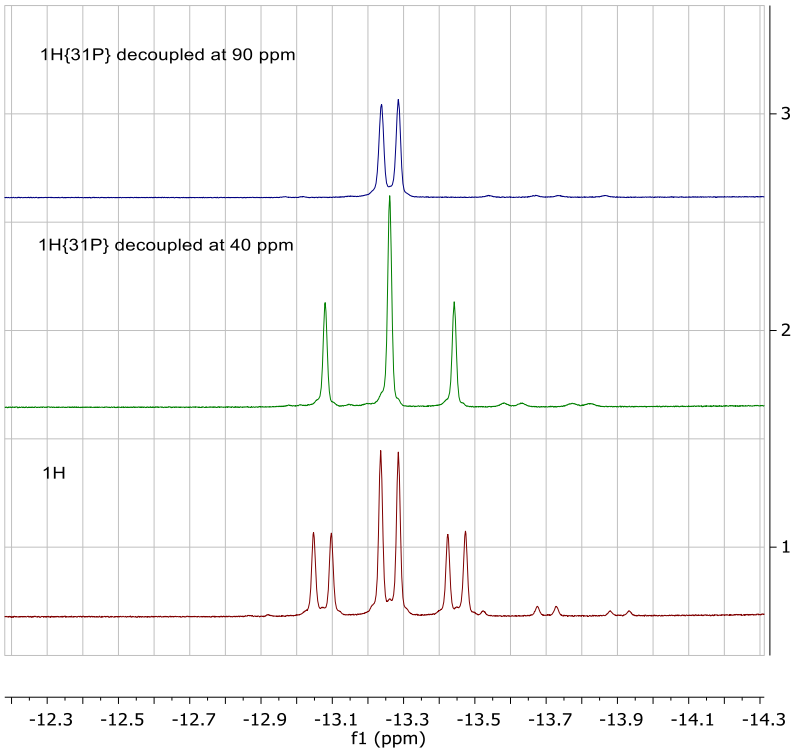

Figure A51. Close up on the Fe-H peak in the ^{1}H NMR spectrum, showing non-decoupled and ^{31}P-decoupled (decoupler set at 90 ppm and 40 ppm) spectra from protonation of **4.6** with one equivalent of $HBAr^{F}_{4}\cdot 2Et_2O$ (C_6D_6, 298 K, 300 MHz).

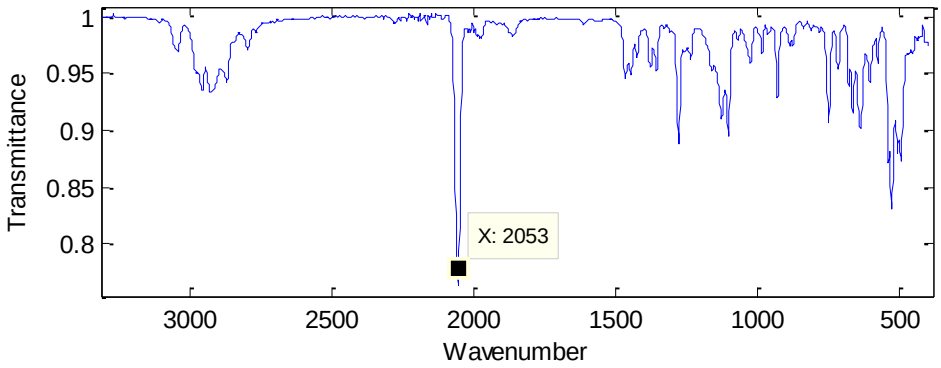

Figure A52. IR spectrum of the reaction mixture from protonation of **4.6** with one equivalent of $HBAr^{F}_{4}\cdot 2Et_2O$ (thin film deposited from benzene).

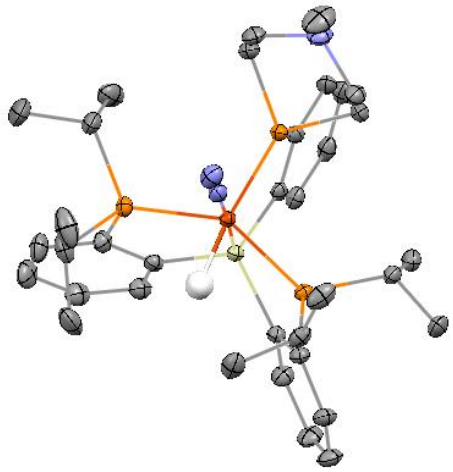

Figure A53. Structure of the $SiP^{iPr}_{2}P^{NMe}Fe(N_2)(H)$ product of the above reaction. Thermal ellipsoids are shown at 50% probability and hydrogen atoms are omitted for clarity. The metal-bound hydrogen atom was located crystallographically and the wide P-Fe-P angle *trans* to the unique ligand arm confirms its placement.

Stoichiometric protonation of $SiP^{iPr}P^{NMe2}FeN_2$ (4.7). $SiP^{iPr}P^{NMe2}FeN_2$ (10 mg, 0.014 mmol) was dissolved in 2:1 Et_2O/THF and cooled to -78 °C. A similarly cooled solution

of $HBAr_4^F.2Et_2O$ (14 mg, 0.014 mmol) was added in in one portion, resulting in an immediate color change to yellow-orange. This was allowed to stir at low temperature for 3 hours before being warmed to room temperature for 30 minutes and concentrated to dryness. The orange residue was analyzed by NMR and IR, which was consistent with oxidation to an Fe(I) complex, $[SiP^{ipr}P^{NMe2}FeN_2]^+$, as the primary product.

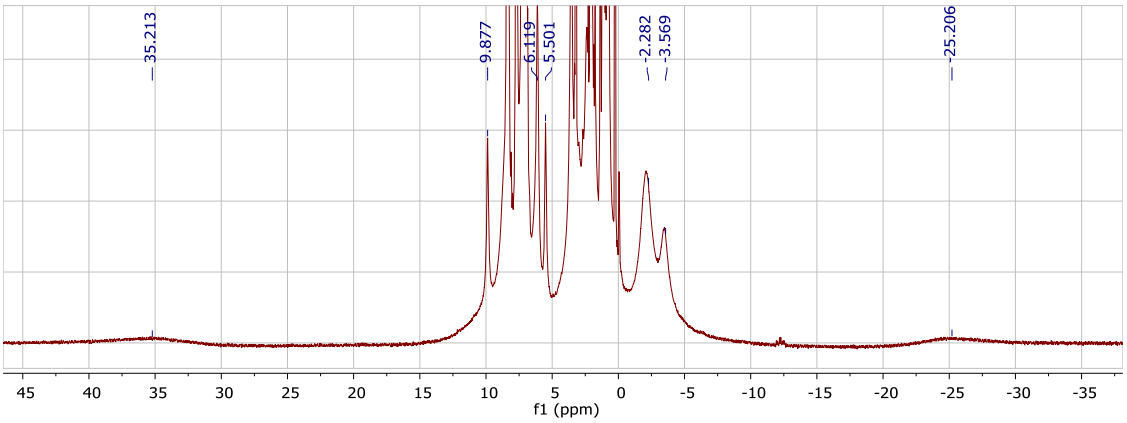

Figure A54. ^1H NMR spectrum of the reaction mixture from protonation of **4.7** with one equivalent of $HBAr^F_4{\cdot}2Et_2O$ (C_6D_6, 298 K, 300 MHz).

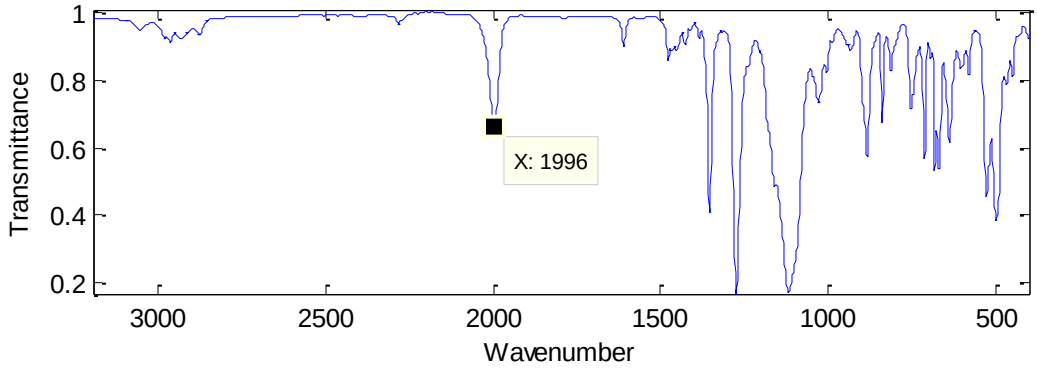

Figure A55. IR spectrum of the reaction mixture from protonation of **4.7** with one equivalent of $HBAr^F_4{\cdot}2Et_2O$ (thin film deposited from benzene).

Protonation of [SiP$^{iPr}_3$FeN$_2$][Na(THF)$_3$]. (a) [SiP$^{iPr}_3$FeN$_2$][Na(THF)$_3$] (20 mg, 0.022 mmol) was dissolved in Et$_2$O (2 mL) and cooled to -78 ºC. A similarly cooled solution of [HNEt^{i}Pr$_2$][BAr$_4^F$] (21.4 mg, 0.022 mmol) in Et$_2$O (2 mL) was added in one portion, and the reaction mixture was stirred at low temperature for 2 hours, resulting in a color change to yellow-orange. It was then warmed to room temperature for 1 hour before concentrating to dryness and analyzing the product by NMR and IR, which showed that it was solely the previously reported oxidation product, SiP$_3^{iPr}$FeN$_2$.[5] (b) [SiP$^{iPr}_3$FeN$_2$][Na(THF)$_3$] (10 mg, 0.011 mmol) was dissolved in Et$_2$O (2 mL) and cooled to -78 ºC. A similarly cooled solution of HBAr$^F_4$·2Et$_2$O (12 mg, 0.011 mmol) in Et$_2$O (2 mL) was added in one portion, and the reaction mixture was stirred at low temperature for 2 hours, resulting in a color change to yellow-orange. It was then warmed to room temperature for 1 hour before being concentrated to dryness and analyzed by NMR and IR, which showed that the product was solely the oxidation product, SiP$_3^{iPr}$FeN$_2$.

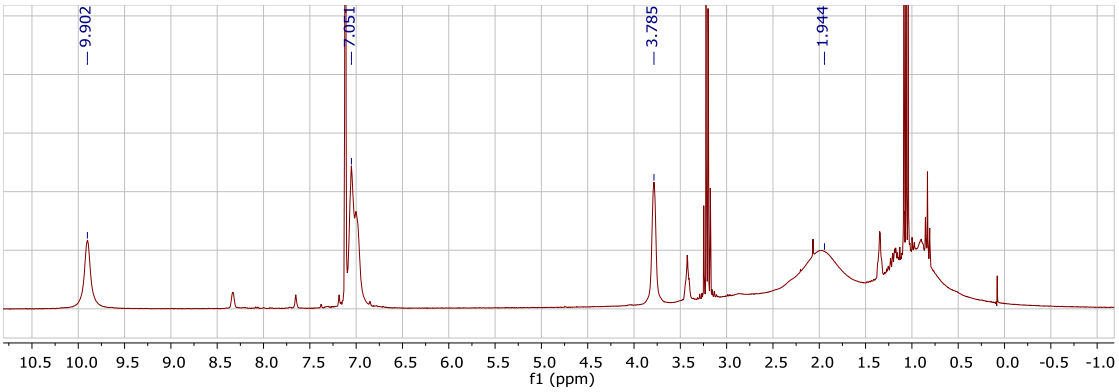

Figure A56. ^{1}H NMR (C$_6$D$_6$, 300 MHz, 298 K) from protonation of [SiP$^{iPr}_3$FeN$_2$][Na(THF)$_3$] with one equivalent of HBAr$^F_4$·2Et$_2$O (thin film deposited from benzene).

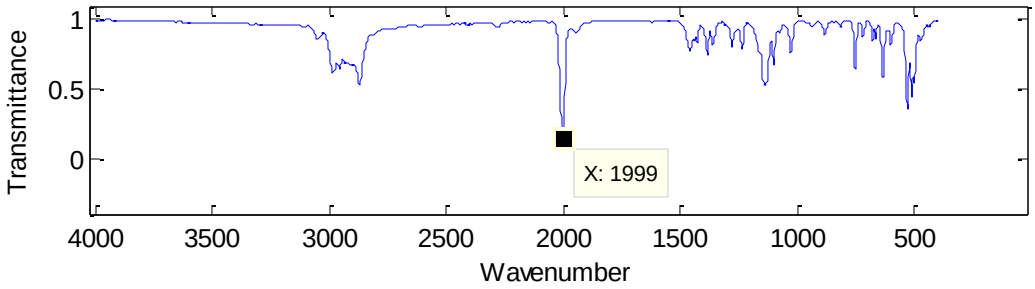

Figure A57. IR spectrum from protonation of $[SiP^{iPr}_3FeN_2][Na(THF)_3]$ with one equivalent of $HBAr^F_4{\cdot}2Et_2O$ (thin film deposited from benzene).

Decomposition of $[SiP^{iPr}_2P^{NMe}FeN_2H_4][BAr^F_4]$ (4.4). The decomposition of a 0.02 M solution of **4.4** in 5:1 C_6D_6:d_8-THF at 60 °C. The decomposition was complete within four hours.

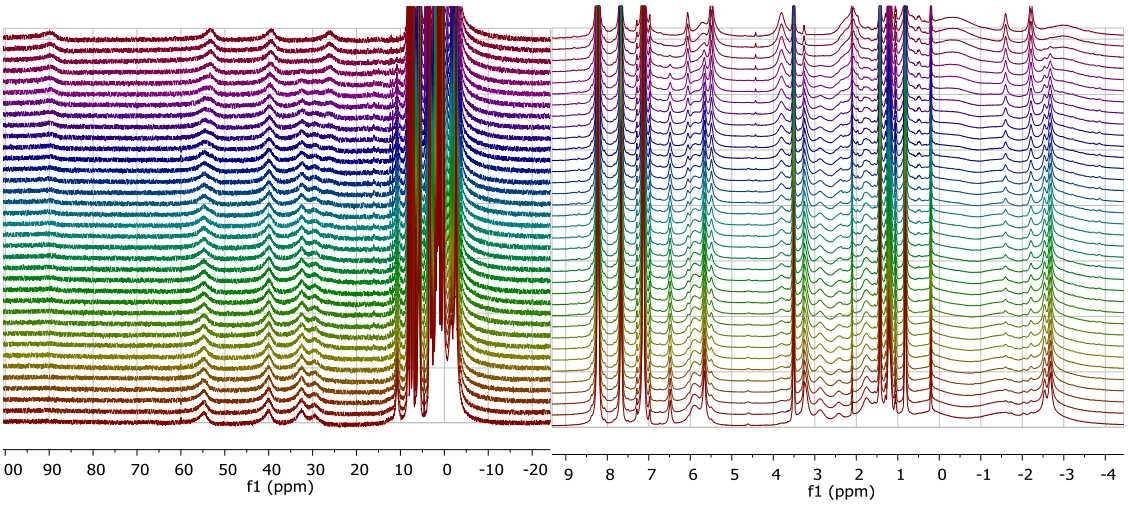

Figure A58. Arrayed ^{1}H NMR spectra (500 MHz, 333 K, 5:1 C_6D_6:d_8-THF) following decomposition of **4.4** (bottom) to **4.3** (top) over the course of four hours, showing full (left) and close-up (right) spectra.

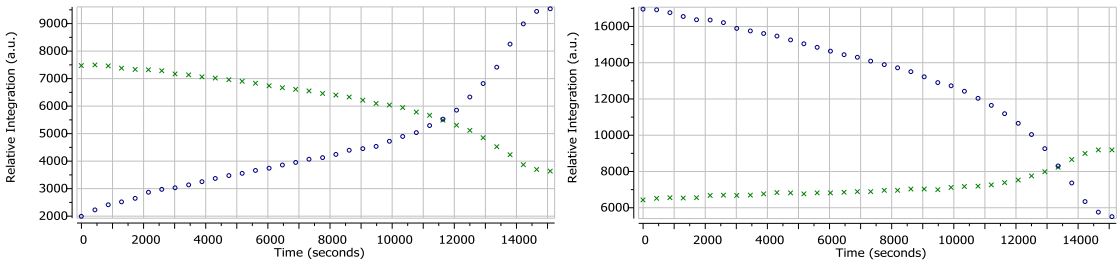

Figure A59. Relative integration of arbitrary peaks corresponding to **4.4** and **4.3** from the arrayed spectra shown in Fig. S57. Left graph shows the relative integration of the peak at 5.66 ppm corresponding to **4.4** (green) and the peak at 5.49 ppm corresponding to **4.3** (blue). Right graph shows the relative integration of the two peaks centered at -2.6 ppm corresponding to **4.4** (blue) and the peak at -2.25 ppm corresponding to **4.3** (green).

Computational analysis of conformer energies. In order to roughly approximate the difference in energy between ligand conformational isomers bearing the six-membered azaphosphine ring in a "chair-like" versus a "boat-like" conformation, DFT geometry optimizations and energy calculations were carried out on the uncoordinated ligand $HSiP^{Me}{}_2P^{NMe}$ (**L1'**), identical to **L1** except that the isopropyl groups have been truncated to methyls. The starting geometries for **L1'-chair** and **L1'-boat** were obtained from the crystal structures of $SiP^{iPr}{}_2P^{NMe}FeNH_2$ and $[SiP^{iPr}{}_2P^{NMe}FeNH_3][BAr^F{}_4]$, respectively, following removal of the $[FeNH_2]$ and $[FeNH_3]$ fragments, removal of the counterion, and addition of a proton bonded to silicon. Geometry optimizations followed by frequency calculations were carried out at the BP86/6-31g(d) level of theory.

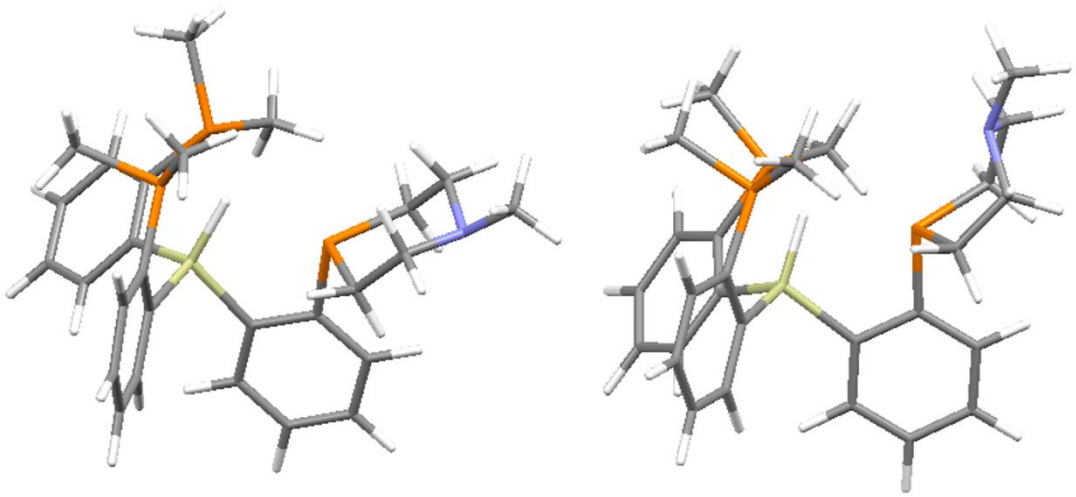

Figure A60. Optimized structures of **L1** in the chair (left) and boat (right) conformations.

The calculated ΔG(298K) between the two isomers is 4.1 kcal/mol, with the boat conformer lying higher in energy as expected.

Charge distribution in Fe(0)N_2 complexes. In order to examine the influence of charged moieties in the secondary coordination sphere on the electronic properties of the metal and bound N_2 ligand, electrostatic potential maps and atomic charges were calculated by DFT and compared for the $SiP^{iPr}_3FeN_2^-$ anion and the $SiP^{iPr}_2P^{NMe2}FeN_2$ zwitterion. Single-point energy calculations were carried out at the B3LYP/6-31g(d) level of theory using the crystallographically determined coordinates for both species (using the crystal structure of $[SiP^{iPr}_3FeN_2][Na(12\text{-crown-}4)_2]$ with the cation omitted for the anion structure). Electrostatic potential maps are generated on the electron density = 0.15 isosurface.

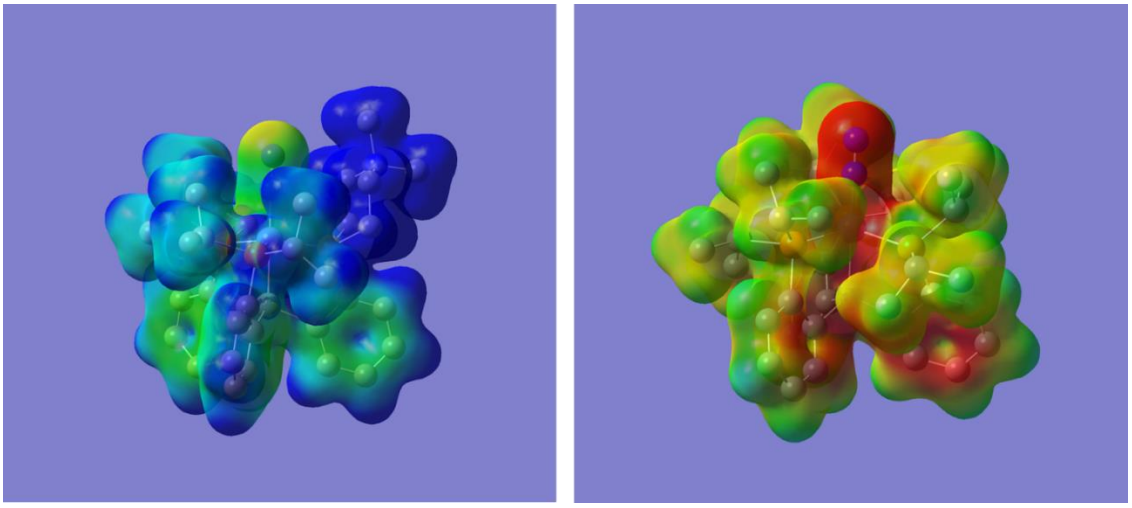

Figure A61. Electrostatic potential maps for **4.7** (left) and **4.6** (right).

Proton affinity calculations. Proton affinities (-ΔH(298K)) were calculated for the protonation of the $SiP^{iPr}{}_2P^{NMe}FeN_2^-$ truncated model anion at three different locations—at the terminal nitrogen of the N_2 ligand, at the tertiary amine, and at the metal to give an iron hydride. Geometry optimizations and energy calculations were carried out for the starting material and products based on the crystallographically determined coordinates of $[SiP^{iPr}{}_2P^{NMe}FeN_2][Na(THF)_2]$ following removal of the cation and solvent and addition of a proton were applicable, or starting from the crystallographically determined coordinates of $SiP^{iPr}{}_2P^{NMe}Fe(N_2)(H)$, at the BP86/6-31g(d) level of theory. All species were calculated as singlets. The calculations suggest that, consistent with the experimental results, protonation at the metal to give a hydride is the thermodynamically preferred product by a substantial margin, while, thermodynamically, protonation at the N_2 ligand is slightly favored over protonation of the tertiary amine.

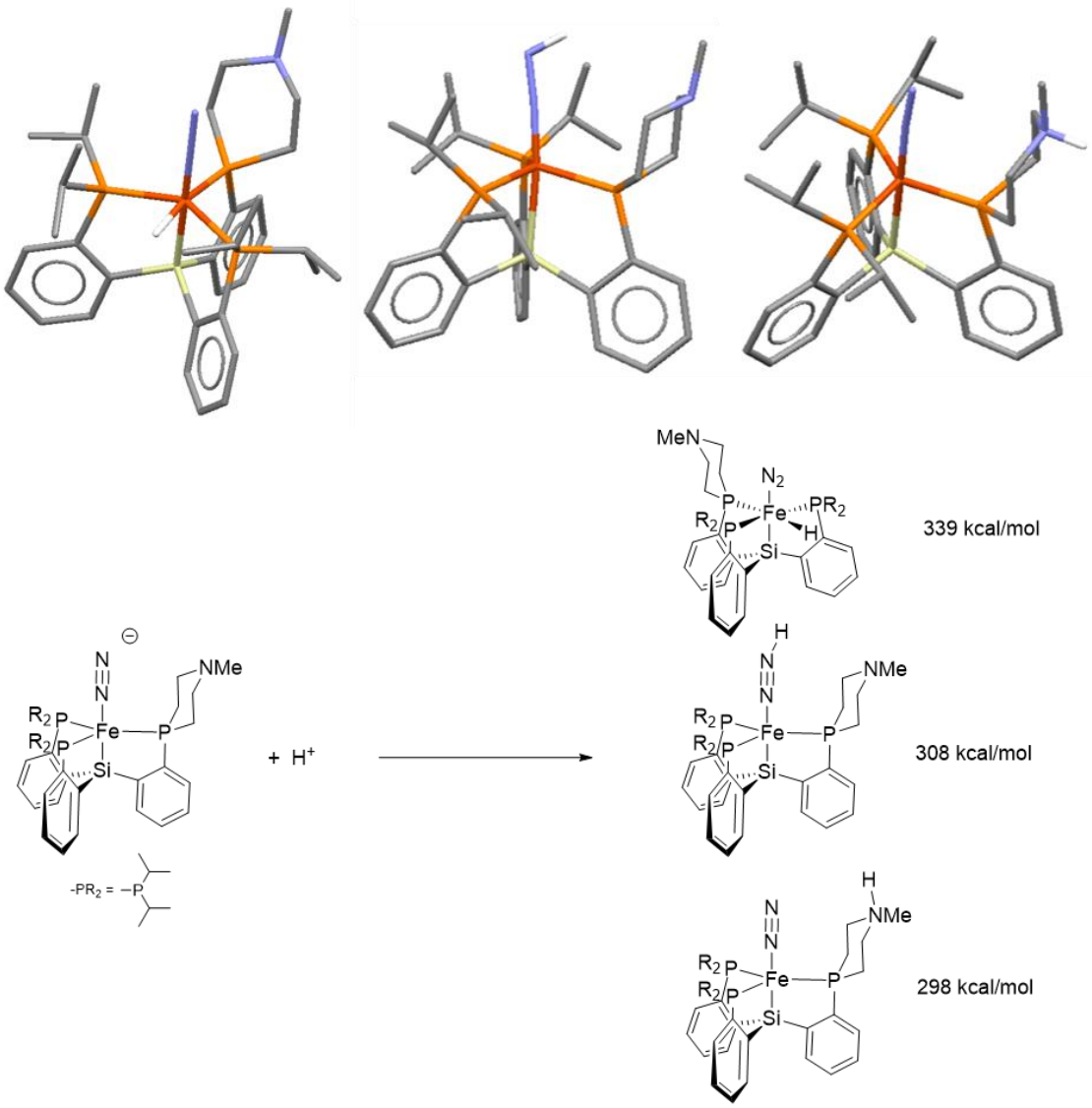

Figure A62. Calculated structures of different possible protonation products of **4.6**, and calculated proton affinities for each isomer.

Crystallographic details. XRD studies were carried out at the Beckman Institute Crystallography Facility on either a Bruker Kappa Apex II diffractometer or a Bruker D8 Venture Kappa Duo Photon 100 CMOS instrument (Mo Kα or Cu Kα radiation). Structures were solved using SHELXS and refined against F2 on all data by full-matrix least-squares

with SHELXL. The crystals were mounted on a wire loop or glass fiber under paratone oil. Methyl group hydrogen atoms not involved in disorder were placed at calculated positions starting from the point of maximum electron density. All other hydrogen atoms, except where otherwise noted, were placed at geometrically calculated positions and refined using a riding model. The isotropic displacement parameters of the hydrogen atoms were fixed at 1.2 (1.5 for methyl groups) times the U_{eq} of the atoms to which they are bonded. 1,2- and 1,3- rigid bond restraints were applied to all non-hydrogen atoms.

Compound	**4.1'**	**4.2'**	**4.4**
Identification code	a14104_final	a14107_final	a14133_final
Empirical formula	$C_{78}H_{94}Cl_2Fe_2N_6P_6Si_2$	$C_{33}H_{45}ClFeN_5P_3Si$	$C_{73}H_{82}BF_{24}FeN_3O_{1.5}P_3Si$
Formula weight	1540.23	688.59	1669.07
Temperature/K	100(2)	100(2)	100(2)
Crystal system	orthorhombic	monoclinic	triclinic
Space group	$Pna2_1$	$P2_1$	P-1
a/Å	38.962(2)	10.6457(5)	12.6269(13)
b/Å	11.0406(6)	19.2443(9)	16.1557(17)
c/Å	18.1487(9)	16.2208(8)	20.397(2)
α/°	90	90	86.951(5)
β/°	90	91.270(3)	77.672(5)
γ/°	90	90	72.605(5)
Volume/Å^3	7807.0(7)	3322.3(3)	3878.7(7)
Z	4	4	2
ρ_{calc}g/cm^3	1.348	1.377	1.429
μ/mm^{-1}	0.640	0.666	0.375
F(000)	3224.0	1452.0	1718.0
Radiation	MoKα (λ = 0.71073)	MoKα (λ = 0.71073)	MoKα (λ = 0.71073)
2Θ range for data collection/°	3.066 to 62.012	2.512 to 56.686	2.642 to 66.56
Index ranges	$-56 \le h \le 41$, $-15 \le k \le 15$, $-26 \le l \le 26$	$-14 \le h \le 14$, $-25 \le k \le 25$, $-21 \le l \le 21$	$-19 \le h \le 19$, $-24 \le k \le 24$, $-31 \le l \le 31$
Reflections collected	150704	126704	247472
Independent reflections	24608 [R_{int} = 0.0476, R_{sigma} = 0.0370]	16433 [R_{int} = 0.0531, R_{sigma} = 0.0342]	29765 [R_{int} = 0.0480, R_{sigma} = 0.0287]
Data/restraints/parameters	24608/1/866	16433/1/776	29765/1087/1041
Goodness-of-fit on F^2	1.158	1.100	1.021
Final R indexes [I>=2σ (I)]	R_1 = 0.0481, wR_2 = 0.1089	R_1 = 0.0461, wR_2 = 0.1121	R_1 = 0.0552, wR_2 = 0.1576
Final R indexes [all data]	R_1 = 0.0532, wR_2 = 0.1108	R_1 = 0.0501, wR_2 = 0.1145	R_1 = 0.0743, wR_2 = 0.1750
Largest diff. peak/hole / e Å^{-3}	0.74/-0.54	1.66/-0.71	1.98/-1.33
Flack parameter	0.147(14)	0.027(16)	--

Table A1. Crystallographic data for the structures of **4.1', 4.2',** and **4.4.**

Compound	**4.3'**	**4.7**	**4.6**
Identification code	a14143	a14145_final	a14450_final
Empirical formula	$C_{69}H_{70}BF_{24}FeN_4OP_3Si$	$C_{40}H_{64}FeN_3OP_3Si$	$C_{43}H_{65}FeN_3NaO_2P_3Si$
Formula weight	1614.95	779.79	855.82
Temperature/K	100(2)	100(2)	100(2)
Crystal system	triclinic	monoclinic	monoclinic
Space group	P-1	$P2_1/n$	$P2_1/c$
a/Å	17.5105(12)	13.5340(10)	13.454(5)
b/Å	20.6792(14)	19.6635(13)	10.208(4)
c/Å	22.9097(16)	15.3570(11)	32.264(14)
α/°	102.798(3)	90	90
β/°	94.824(3)	92.185(2)	90.860(8)
γ/°	111.770(3)	90	90
Volume/Å^3	7385.0(9)	4083.9(5)	4431(3)
Z	4	4	4
ρ_{calc}g/cm^3	1.453	1.268	1.283
μ/mm^{-1}	0.391	0.551	0.524
F(000)	3304.0	1672.0	1824.0
Radiation	MoKα (λ = 0.71073)	MoKα (λ = 0.71073)	MoKα (λ = 0.71073)
2Θ range for data collection/°	3.128 to 56.86	3.366 to 61.212	3.262 to 75.85
Index ranges	$-23 \le h \le 23$, $-27 \le k \le 27$, $-30 \le l \le 30$	$-16 \le h \le 19$, $-28 \le k \le 28$, $-21 \le l \le 21$	$-23 \le h \le 22$, $-17 \le k \le 17$, $-54 \le l \le 55$
Reflections collected	227665	129542	108180
Independent reflections	37050 [R_{int} = 0.0751, R_{sigma} = 0.0544]	12532 [R_{int} = 0.0617, R_{sigma} = 0.0359]	23557 [R_{int} = 0.0795, R_{sigma} = 0.0880]
Data/restraints/parameters	37050/2604/2118	12532/887/576	23557/0/496
Goodness-of-fit on F^2	1.014	1.233	1.055
Final R indexes [I>=2σ (I)]	R_1 = 0.0549, wR_2 = 0.1287	R_1 = 0.0833, wR_2 = 0.1748	R_1 = 0.0860, wR_2 = 0.1956
Final R indexes [all data]	R_1 = 0.0929, wR_2 = 0.1496	R_1 = 0.1021, wR_2 = 0.1821	R_1 = 0.1237, wR_2 = 0.2116
Largest diff. peak/hole / e Å^{-3}	1.50/-1.13	1.02/-0.97	1.42/-1.49
Flack parameter	--	--	--

Table A2. Crystallographic data for the structures of **4.3', 4.7,** and **4.6.**

Compound	**4.6'**	**4.5**	**4.3**
Identification code	a15176_200_a	p14062_final	p14067_final
Empirical formula	$C_{45}H_{69}FeN_5NaO_3P_3Si$	$C_{35}H_{53}FeN_2P_3Si$	$C_{69}H_{71}BF_{24}FeN_2O_{0.5}P_3Si$
Formula weight	927.89	678.64	1579.93
Temperature/K	200(2)	100(2)	100(2)
Crystal system	orthorhombic	orthorhombic	triclinic
Space group	Pnma	$Pca2_1$	P-1
a/Å	24.918(6)	17.8087(5)	13.2134(6)
b/Å	16.256(4)	11.3207(3)	16.5453(8)
c/Å	12.349(3)	17.3127(5)	19.1158(9)
α/°	90	90	107.944(3)
β/°	90	90	103.367(3)
γ/°	90	90	104.913(3)
Volume/$Å^3$	5002(2)	3490.36(17)	3616.2(3)
Z	4	4	2
$\rho_{calc}g/cm^3$	1.232	1.291	1.451
μ/mm^{-1}	0.472	0.631	3.393
F(000)	1976.0	1448.0	1618.0
Radiation	MoKα (λ = 0.71073)	MoKα (λ = 0.71073)	CuKα (λ = 1.54178)
2Θ range for data collection/°	3.268 to 62.642	5.82 to 72.676	5.162 to 150.52
Index ranges	$-34 \leq h \leq 36$, $-23 \leq k \leq 23$, $-17 \leq l \leq 16$	$-29 \leq h \leq 29$, $-18 \leq k \leq 18$, $-28 \leq l \leq 28$	$-16 \leq h \leq 16$, $-20 \leq k \leq 20$, $-23 \leq l \leq 23$
Reflections collected	92587	101085	134383
Independent reflections	8081 [R_{int} = 0.0837, R_{sigma} = 0.0509]	16906 [R_{int} = 0.0536, R_{sigma} = 0.0453]	14802 [R_{int} = 0.1344, R_{sigma} = 0.0621]
Data/restraints/parameters	8081/521/356	16906/3/425	14802/2398/1078
Goodness-of-fit on F^2	1.063	1.034	1.014
Final R indexes [I>=2σ (I)]	R_1 = 0.0639, wR_2 = 0.1529	R_1 = 0.0393, wR_2 = 0.0784	R_1 = 0.0690, wR_2 = 0.1612
Final R indexes [all data]	R_1 = 0.1081, wR_2 = 0.1717	R_1 = 0.0571, wR_2 = 0.0845	R_1 = 0.1025, wR_2 = 0.1811
Largest diff. peak/hole / e $Å^{-3}$	0.66/-0.29	0.79/-0.54	0.70/-0.61
	--	0.020(11)	

Table A3. Crystallographic data for the structure of **4.6', 4.5,** and **4.3.**

Compound	**$SiP^{iPr}_2P^{NMe}Fe(N_2)(H)$**
Identification code	p15558_2
Empirical formula	$C_{70}H_{106}Fe_2N_6P_6Si_2$
Formula weight	1385.30
Temperature/K	100(2)
Crystal system	triclinic
Space group	P-1
a/Å	10.4778(10)
b/Å	17.2329(17)
c/Å	20.001(2)
α/°	92.885(4)
β/°	96.497(3)
γ/°	98.431(3)
Volume/$Å^3$	3541.2(6)
Z	2
$\rho_{calc}g/cm^3$	1.299
μ/mm^{-1}	0.624
F(000)	1476.0
Radiation	MoKα (λ = 0.71073)
2Θ range for data collection/°	4.896 to 61.17
Index ranges	$-14 \leq h \leq 14$, $-24 \leq k \leq 24$, $-28 \leq l \leq 28$
Reflections collected	301134
Independent reflections	21650 [R_{int} = 0.0487, R_{sigma} = 0.0222]
Data/restraints/parameters	21650/831/809
Goodness-of-fit on F^2	1.021
Final R indexes [I>=2σ (I)]	R_1 = 0.0358, wR_2 = 0.0832
Final R indexes [all data]	R_1 = 0.0458, wR_2 = 0.0883
Largest diff. peak/hole / e $Å^{-3}$	1.79/-0.98

Table A4. Crystallographic data for the structure of $SiP^{iPr}_2P^{NMe}Fe(N_2)(H)$.

Appendix B. Supplementary data for Chapter 6

B.1 Spectroscopic characterization of complexes 6.1-6.9

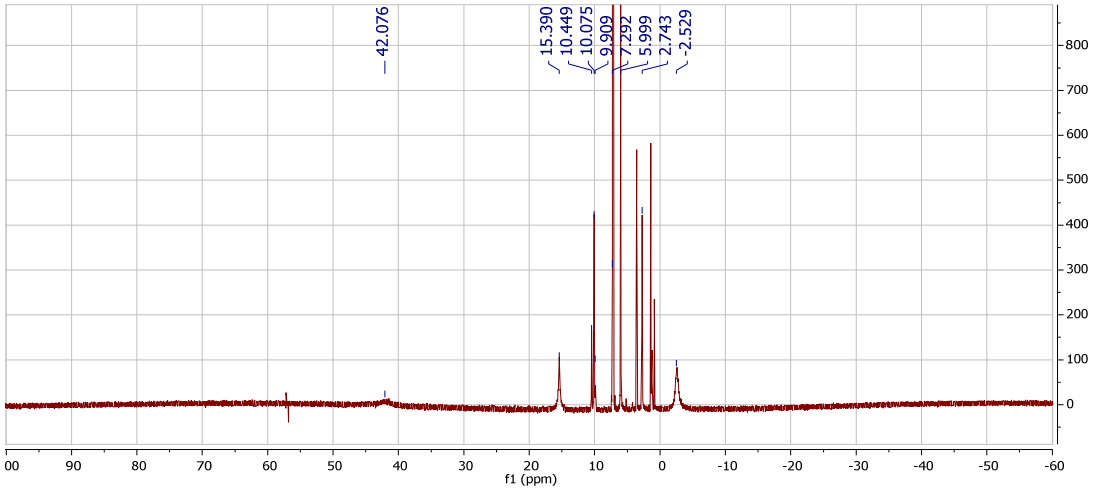

Figure B1. ^{1}H NMR spectrum of **6.1** in C_6D_6 (300 MHz, 298 K)

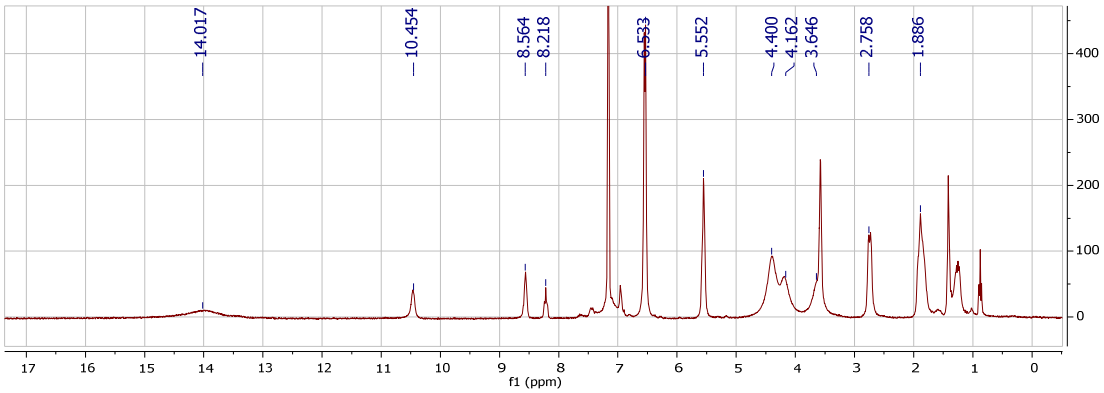

Figure B2. ^{1}H NMR spectrum of **6.2** in C_6D_6 (300 MHz, 298 K)

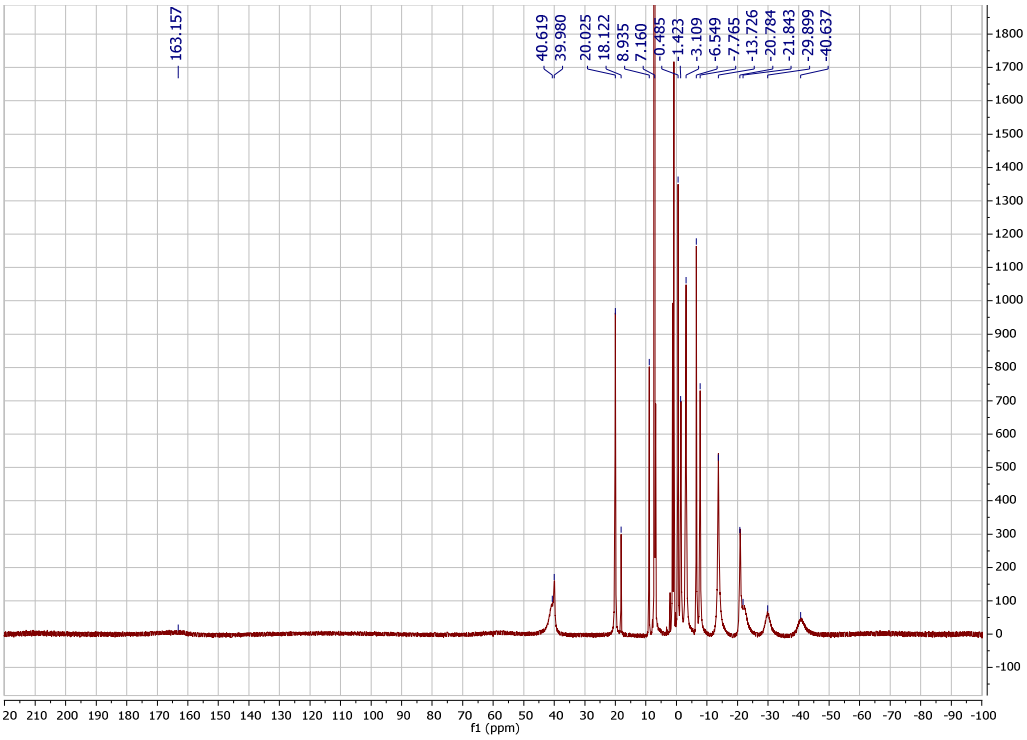

Figure B.3. ^{1}H NMR of **6.3** in C_6D_6 (300 MHz, 298 K)

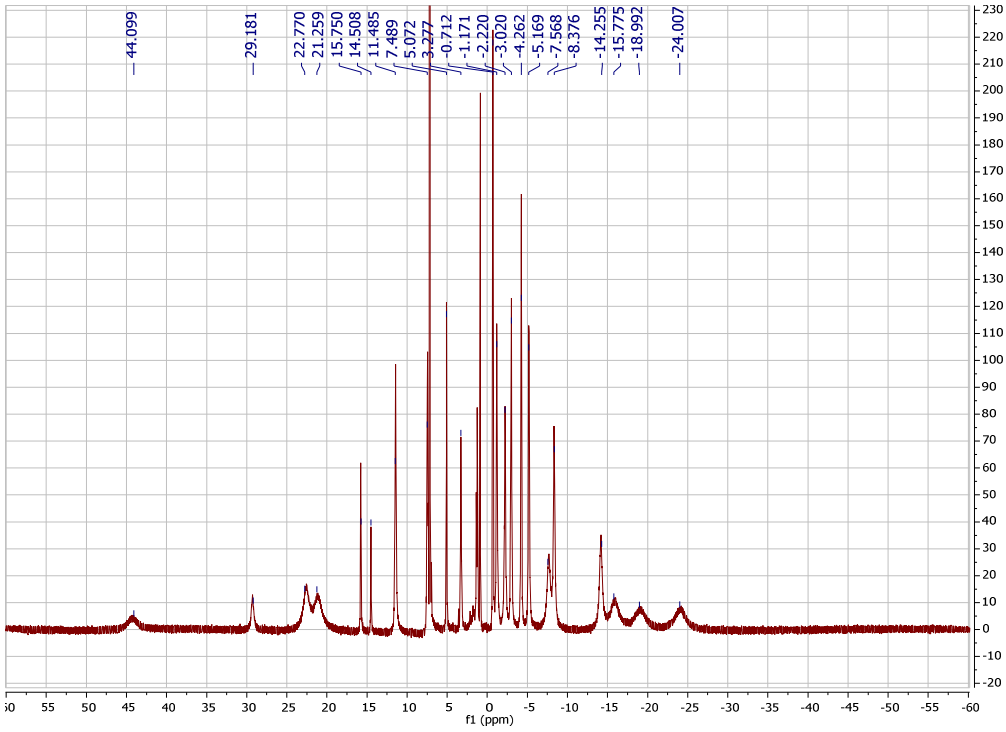

Figure B4. ^{1}H NMR spectrum of **6.4** in C_6D_6 (300 MHz, 298 K)

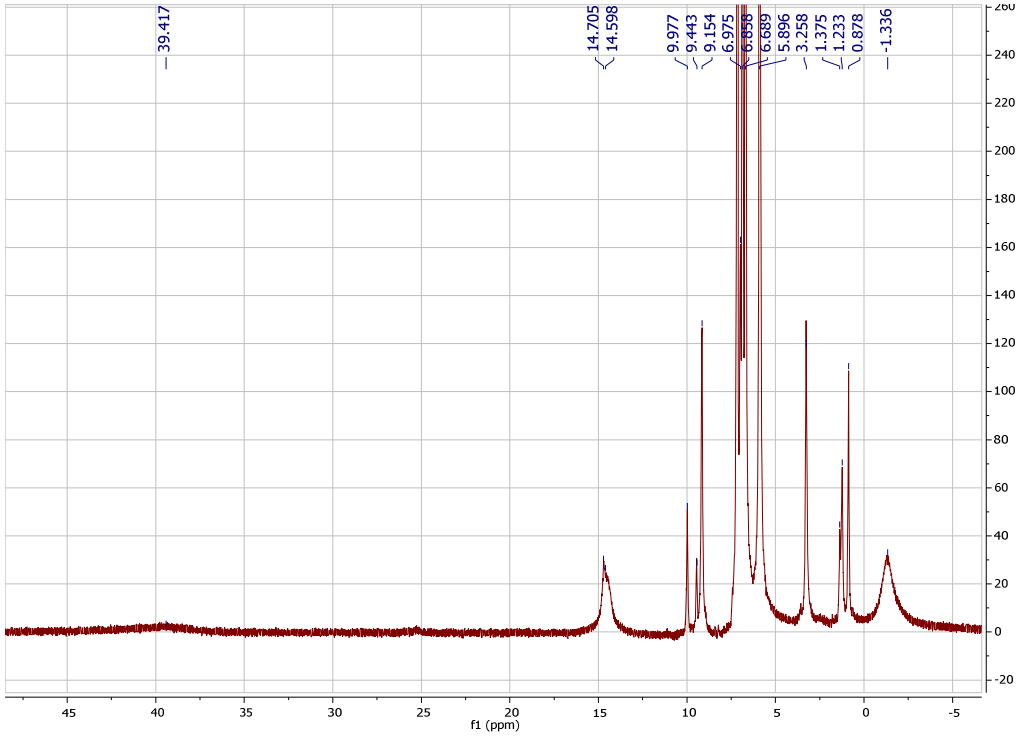

Figure B5. ^{1}H NMR of **6.5** in C_6D_6 (300 MHz, 298 K)

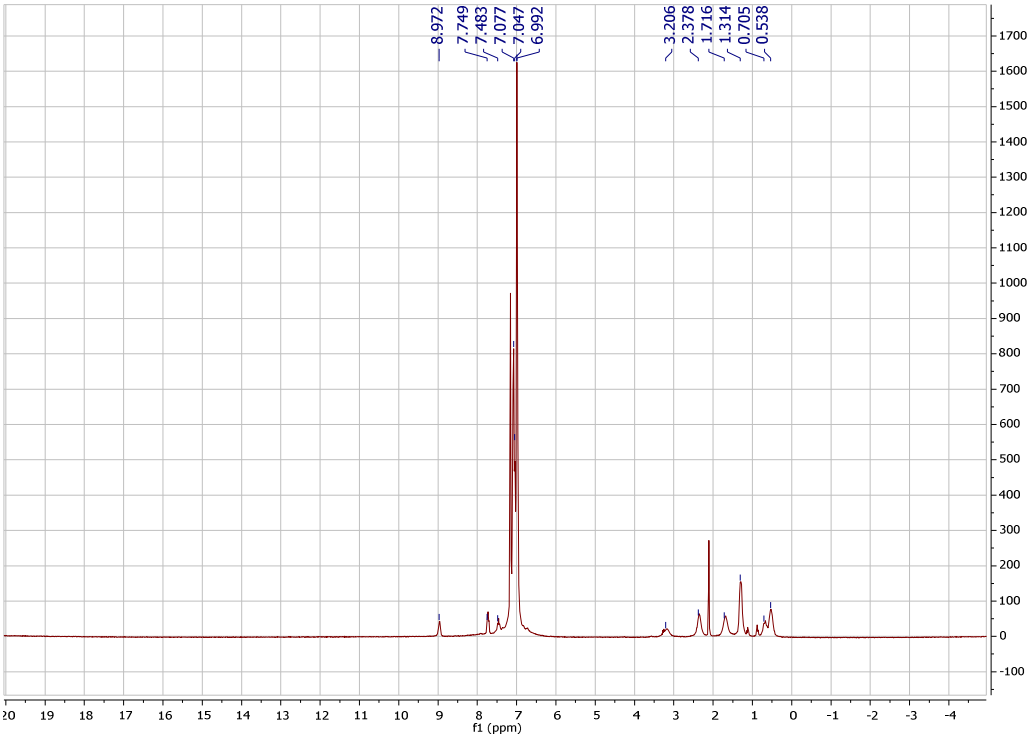

Figure B6. ^{1}H NMR of **6.6** in C_6D_6 (300 MHz, 298 K)

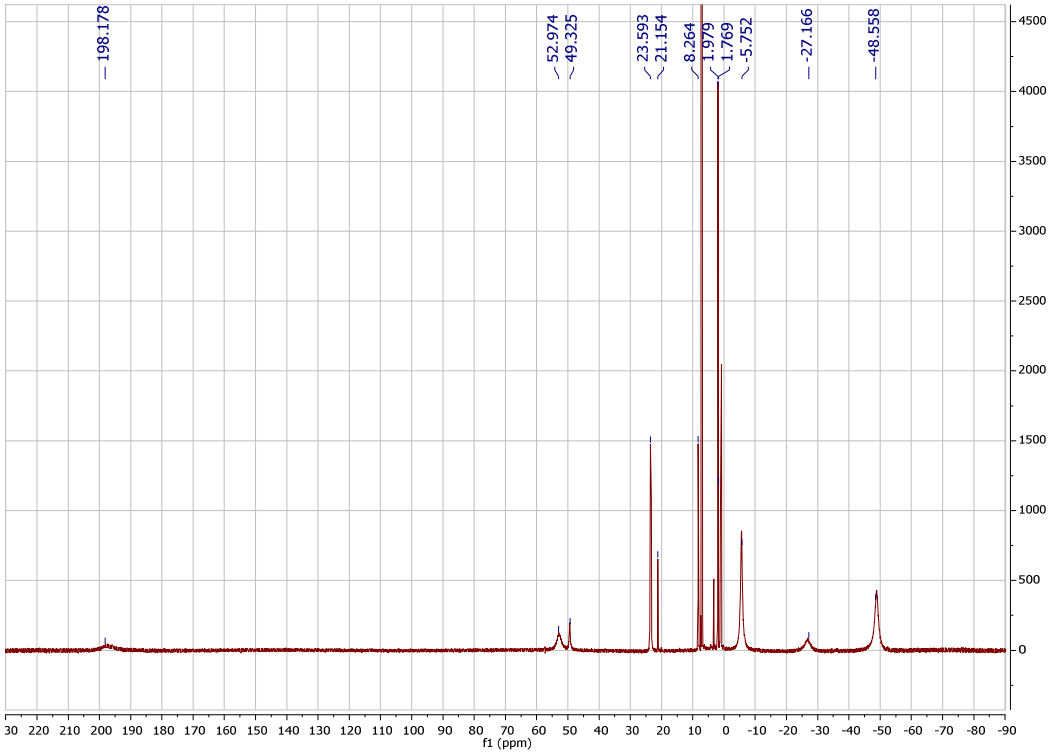

Figure B7. ^{1}H NMR of **6.7** in C_6D_6 (300 MHz, 298 K)

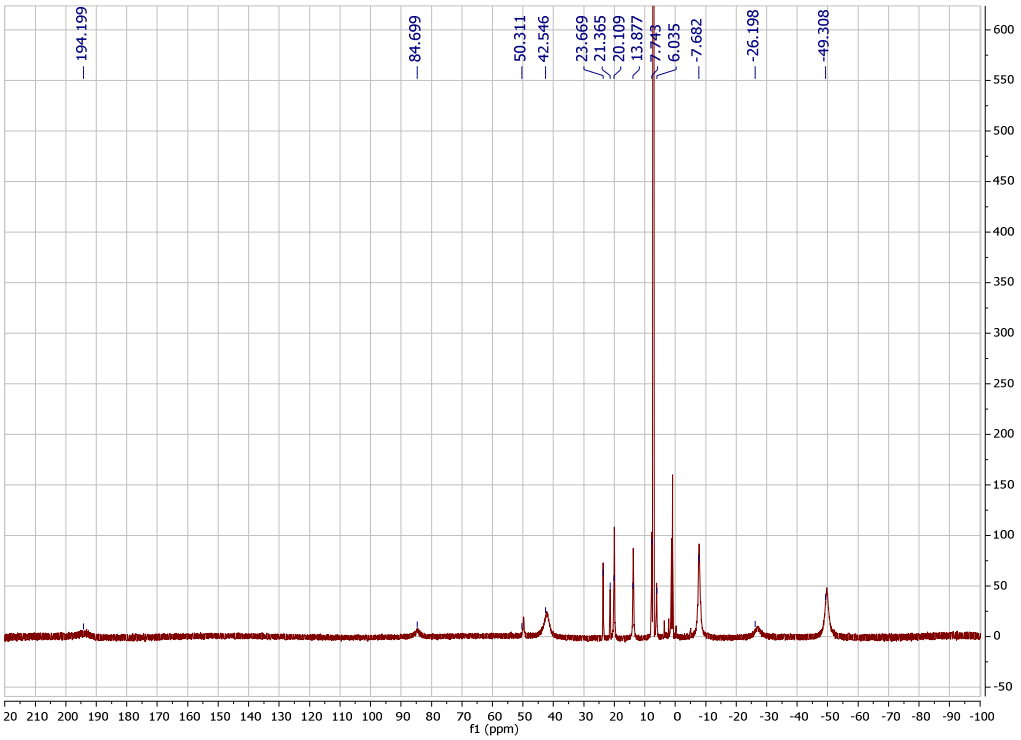

Figure B8. ^{1}H NMR of **6.8** in C_6D_6 (300 MHz, 298 K)

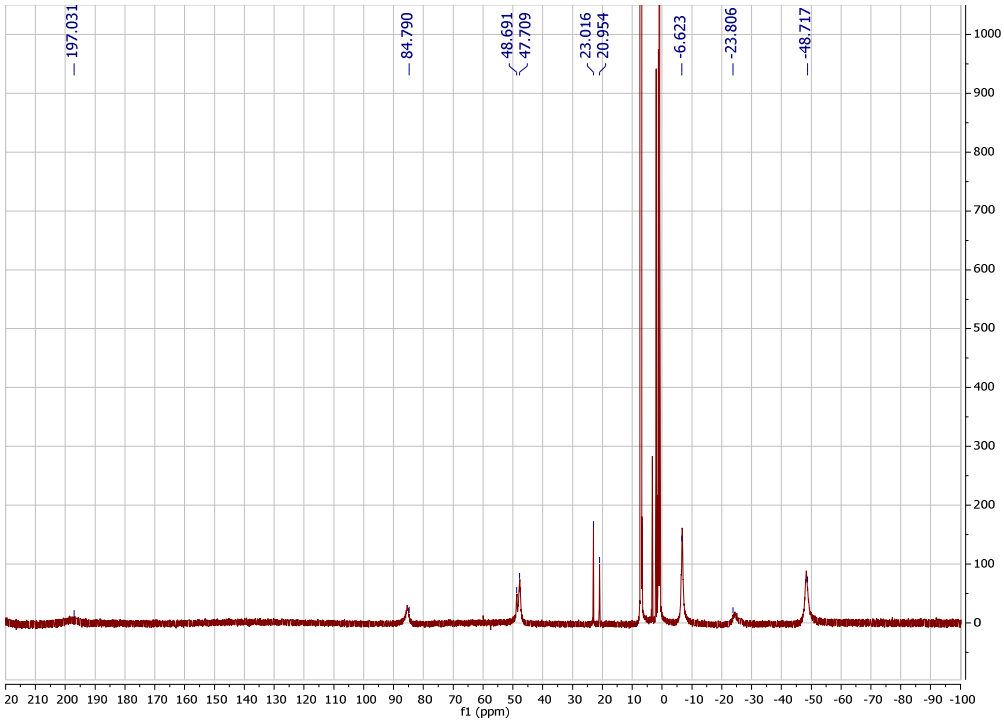

Figure B9. ^{1}H NMR of **6.9** in C_6D_6 (300 MHz, 298 K)

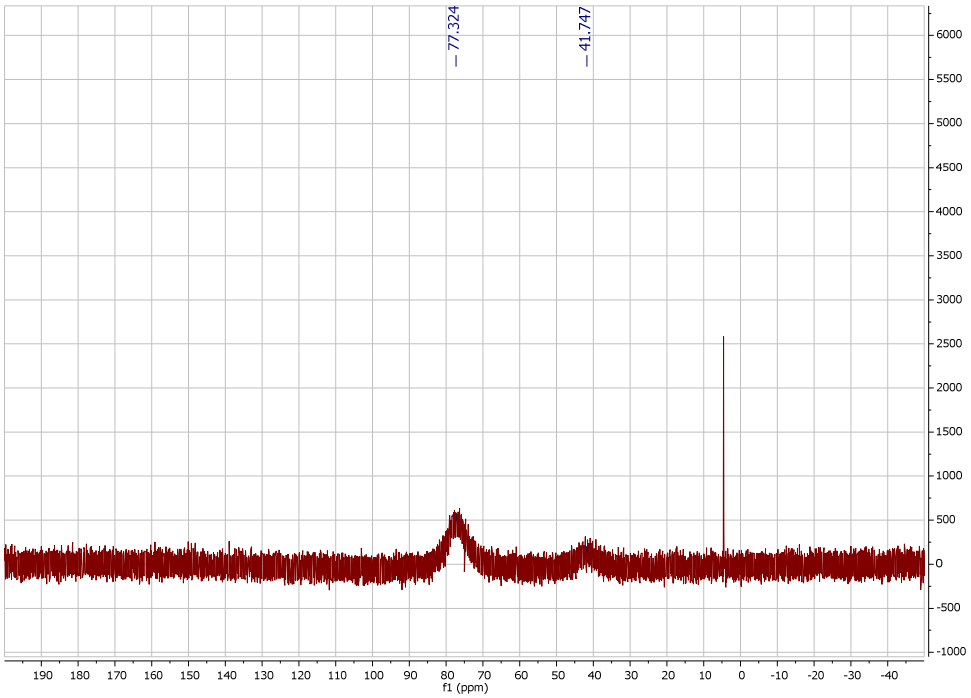

Figure B10. ^{31}P NMR of **6.3** in d_8-toluene (202 MHz, 198 K). The impurity is PPh_3, present in very small amounts.

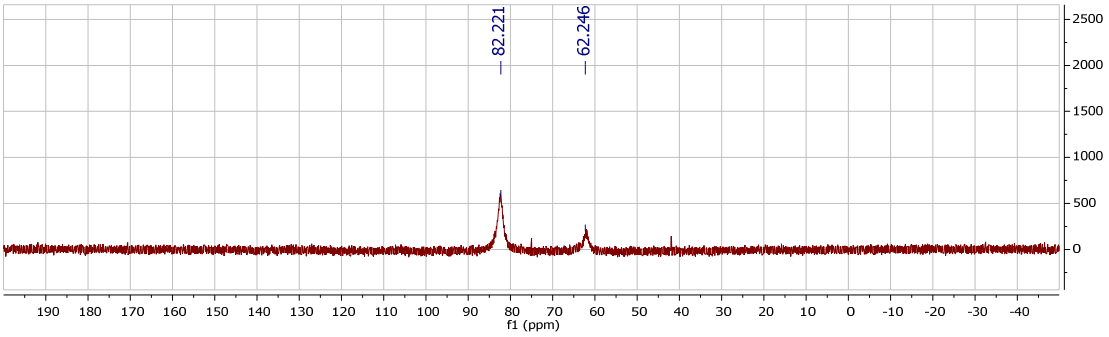

Figure B11. ^{31}P NMR of **6.4** in d_8-toluene (202 MHz, 198 K)

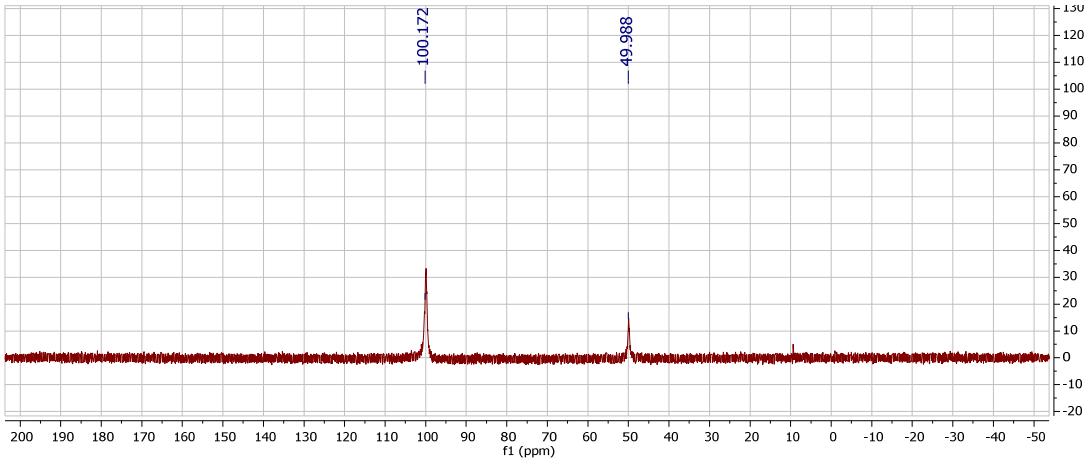

Figure B12. ^{31}P NMR of **6.5** in d_8-toluene (152 MHz, 198 K)

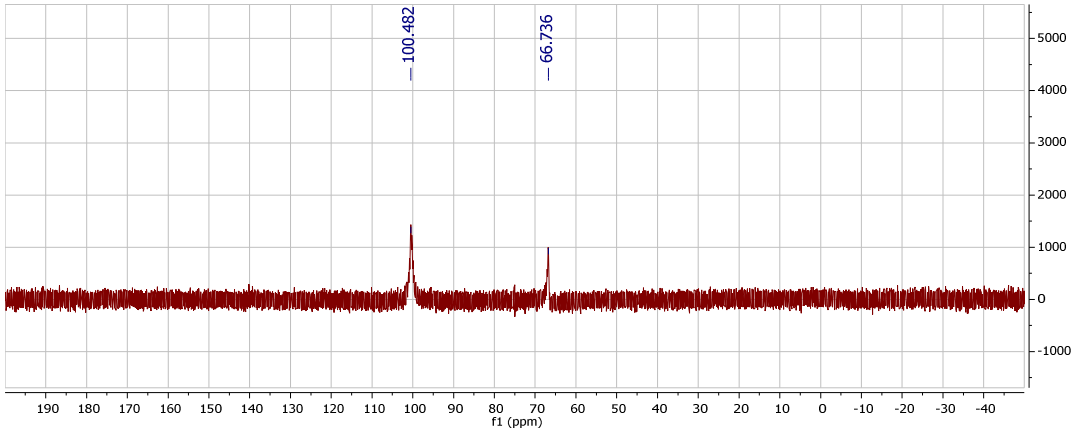

Figure B13. ^{31}P NMR of **6.6** in d_8-toluene (202 MHz, 188 K)

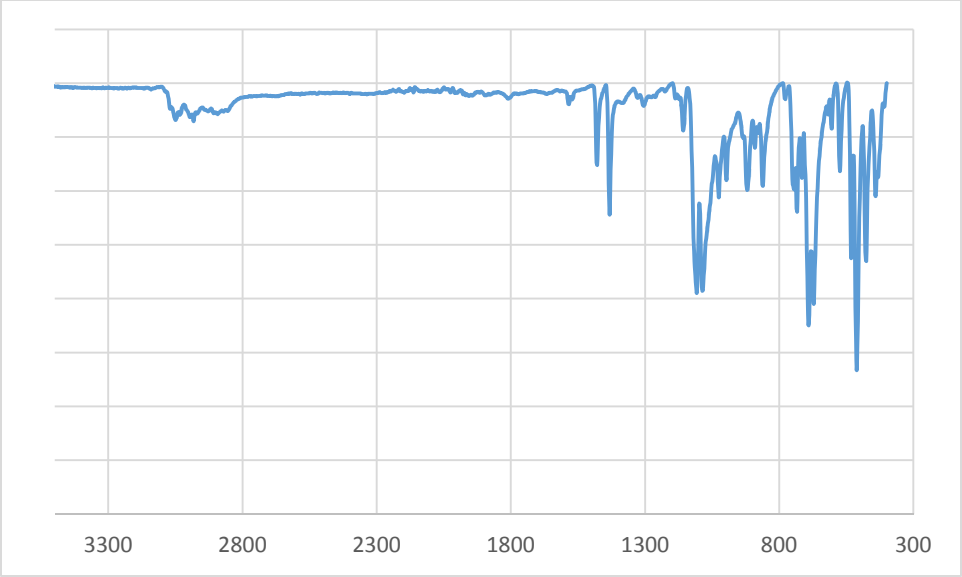

Figure B14. Infrared spectrum of **6.1** as a powdered solid.

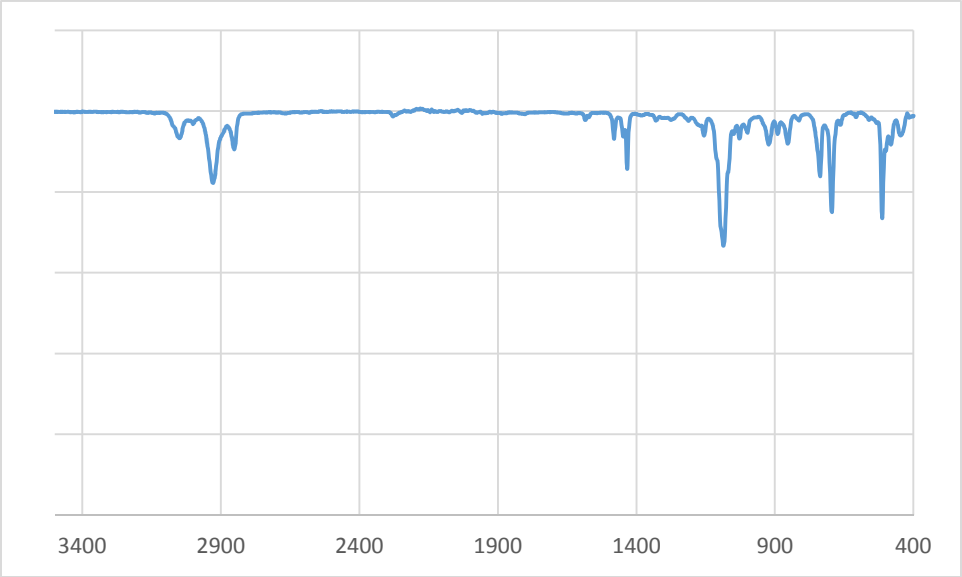

Figure B15. Infrared spectrum of **6.2**, deposited as a thin film from benzene solution.

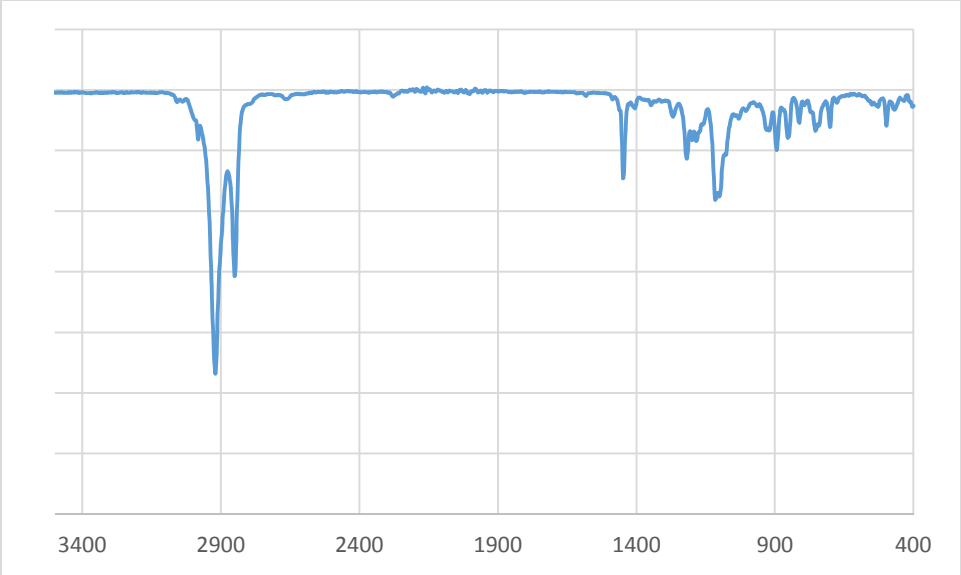

Figure B16. Infrared spectrum of **6.4**, deposited as a thin film from benzene.

B.2 Variable-temperature NMR spectroscopy

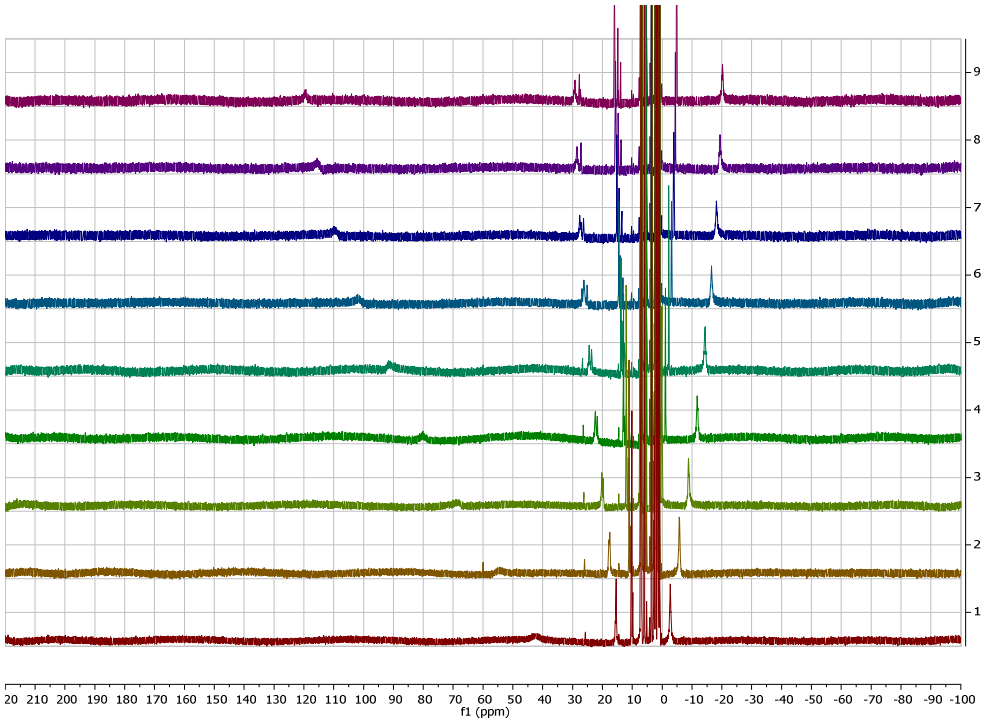

Figure B17. Variable-temperature ^{1}H NMR of **6.1** from 298 K (bottom) to 388 K (top) in d_8-toluene (500 MHz).

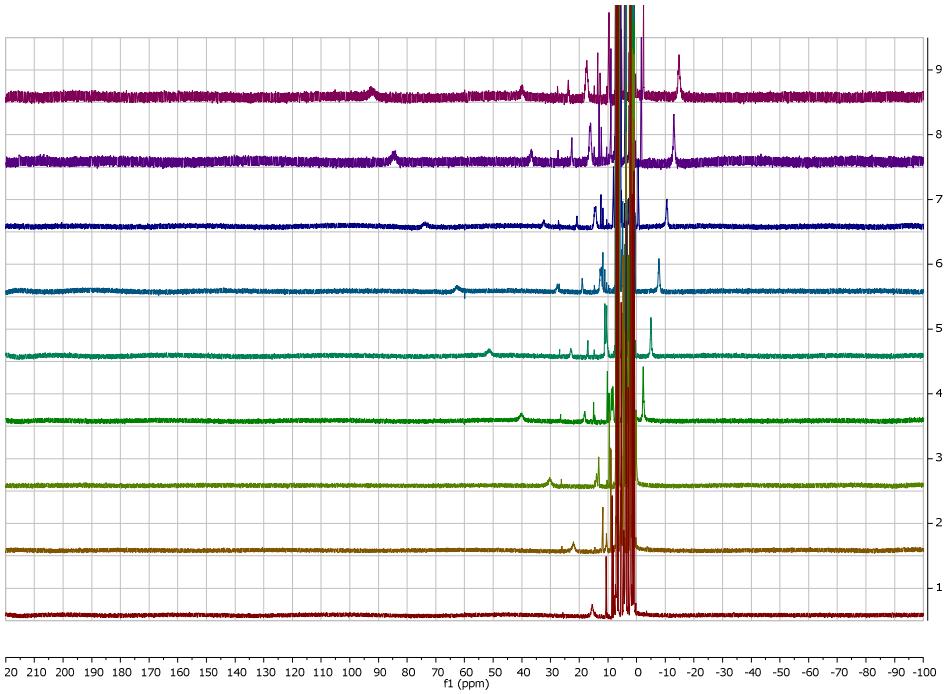

Figure B18. Variable temperature ^{1}H NMR spectra of **6.2** from 298 K (bottom) to 378 K (top) in d_8-toluene (500 MHz).

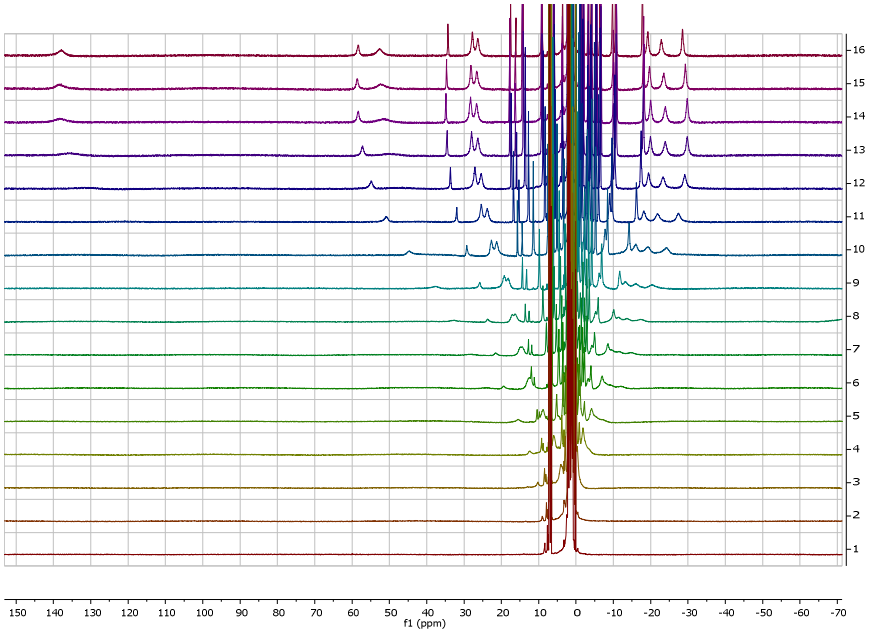

Figure B19. Variable-temperature ^{1}H NMR spectra of **6.4** from 223 K (bottom) to 358 K (top) in d_8-toluene (500 MHz).

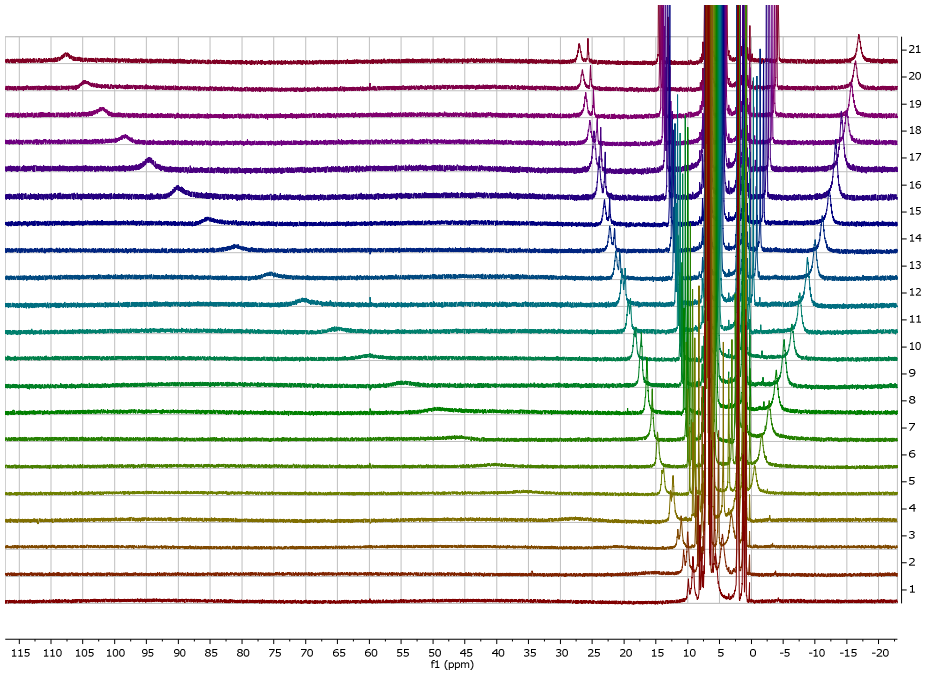

Figure B20. Variable-temperature ^{1}H NMR spectra of **6.5** from 258 K (bottom) to 378 K (top) in d_8-toluene (500 MHz).

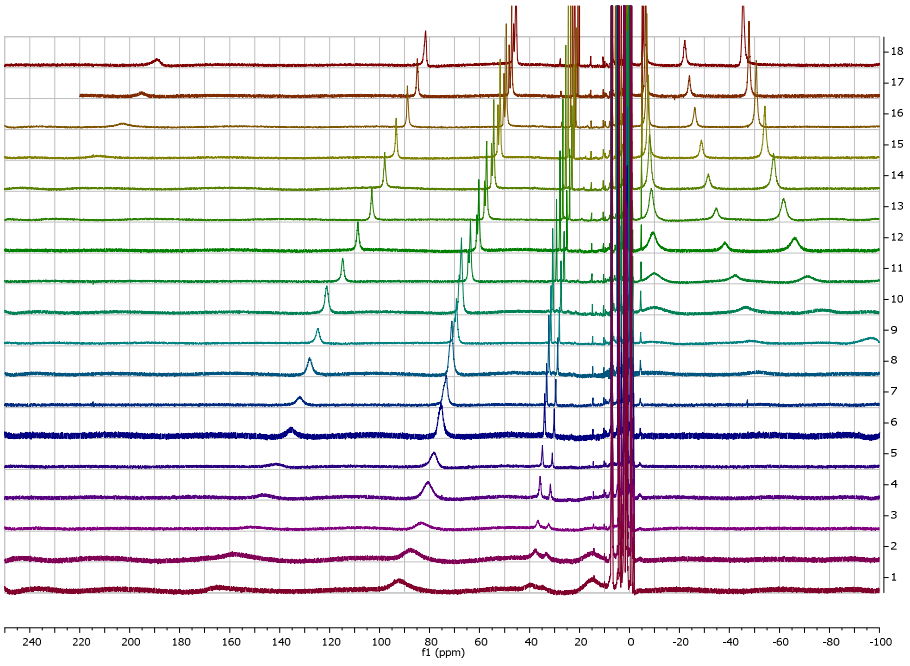

Figure B21. Variable-temperature ^{1}H NMR spectra of **6.9** from 283 K (bottom) to 408 K (top) in d_8-toluene (500 MHz).

Fits to the variable-temperature NMR chemical shifts were carried out using the following model:

$$\delta = \delta_{ls} + C/(T*(1+\exp(\Delta H/0.69*(1/T-1/T_c)))) \quad \text{Equation B1}$$

where the parameters are as defined in the main text (Equation 6.4). Fit parameters, confidence bounds, and goodness-of-fit parameters are given below for each species.

The fits to the modified Curie law expression are generally good over the temperature regime where the chemical shifts are either monotonically increasing or decreasing, however the fit tends to become poor in the high-temperature regime where the high-spin state is close to fully occupied and the chemical shifts tend back towards δ_{ls}, in complexes where this regime is accessible. This may suggest that the chemical shifts of the high-spin state do not display simple Curie behavior, or that some other assumption of the model is inadequate, illustrating a possible weakness of this model. For the purposes of this study these points were excluded from the fit in order to maintain consistency between different complexes; attempting to include them (when applicable) typically results in a higher apparent value for ΔH as well as a significantly poorer overall fit.

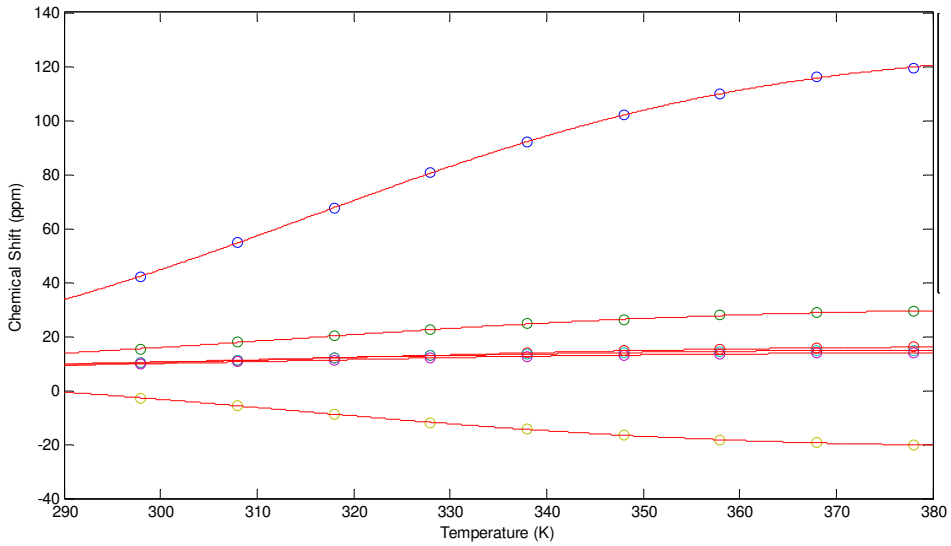

Figure B22. Variation of the chemical shifts in the ^{1}H NMR of **6.1** with temperature, and fits to Equation B1.

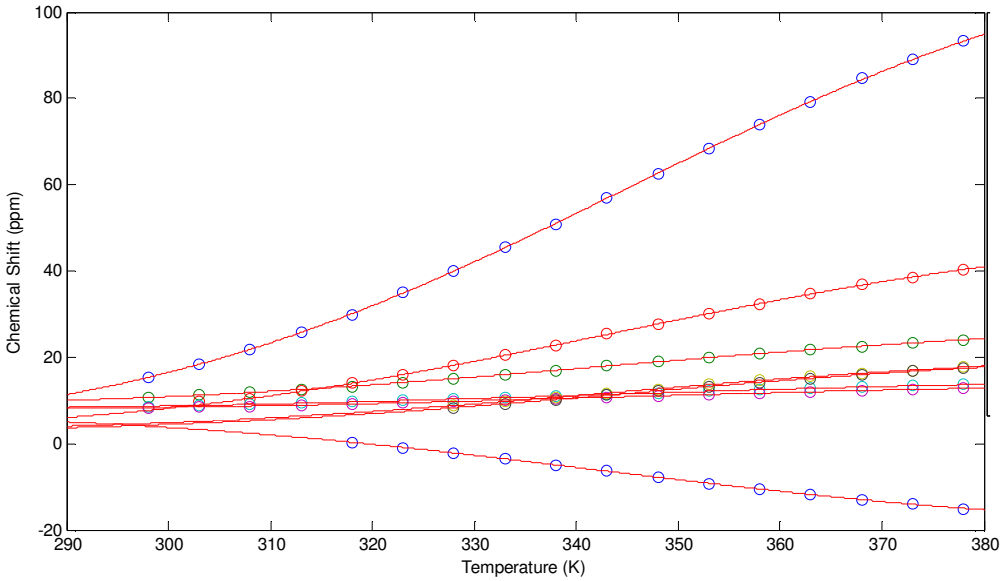

Figure B23. Variation of the chemical shifts in the ^{1}H NMR of **6.2** with temperature, and fits to Equation B1.

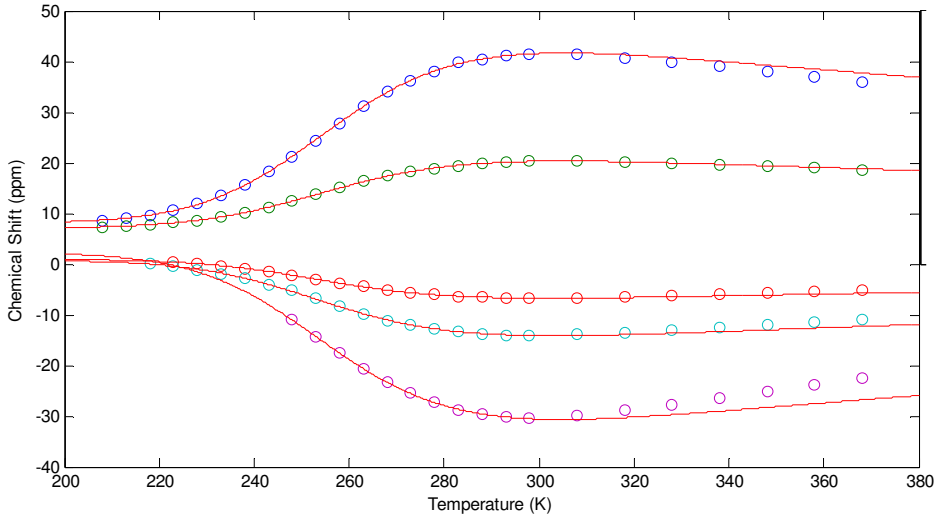

Figure B24. Variation of the chemical shifts in the ^{1}H NMR of **6.3** with temperature, and fits to Equation B1 with points above 300 K omitted from the fits.

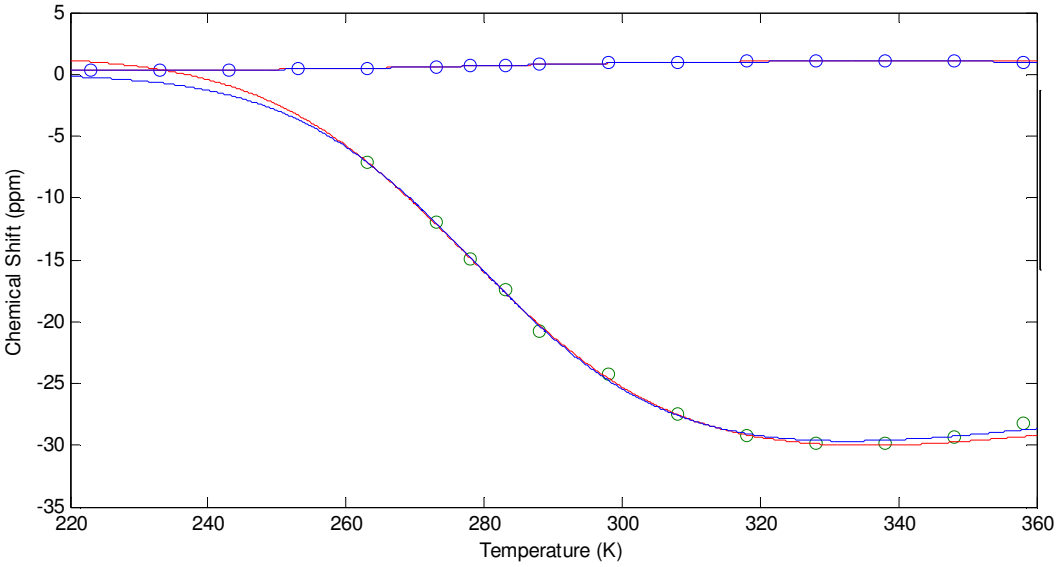

Figure B25. Variation of the chemical shifts in the ^{1}H NMR of **6.4** with temperature, and fits to Equation B1 with points above 300 K omitted (red lines) or included (blue lines).

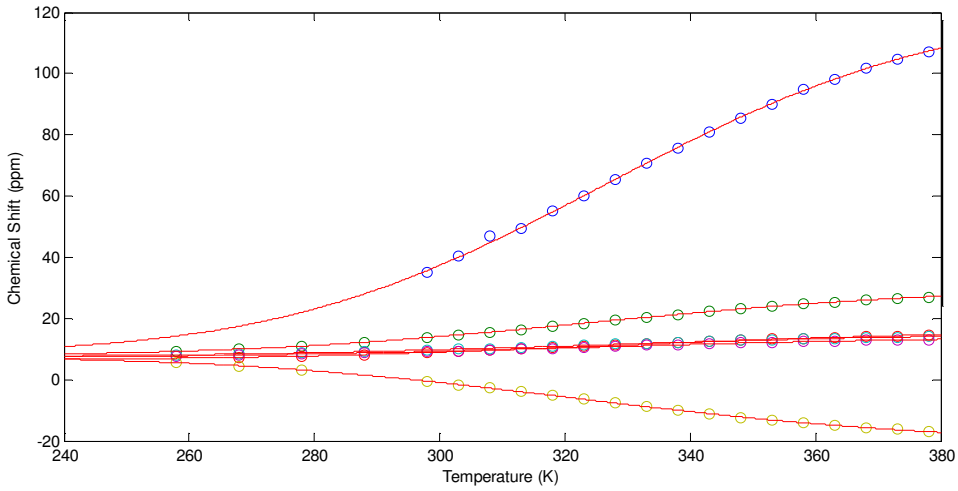

Figure B26. Variation of the chemical shifts in the ^{1}H NMR of **6.5** with temperature, and fits to Equation B1.

Variable temperature Evans method data (corrected for density changes) was fit to the following equation:

$$\chi T = (\chi T)_{HS}/(1+\exp(\Delta H/0.69*(1/T-1/T_c)))+ (\chi T)_{LS} \qquad \text{Equation B2}$$

Although the resulting fits are not unreasonable, except for complex **6.3** (for which the largest range of the transition was probed) the uncertainties (as represented by the 95% confidence bounds) in the fit parameters are very large. The temperature over which χT could be measured is limited for most complexes both by the boiling/freezing points of the solvents as well as the fact that at temperatures well below T_c the very small magnetic moment is difficult to determine accurately from the Evans method shift.

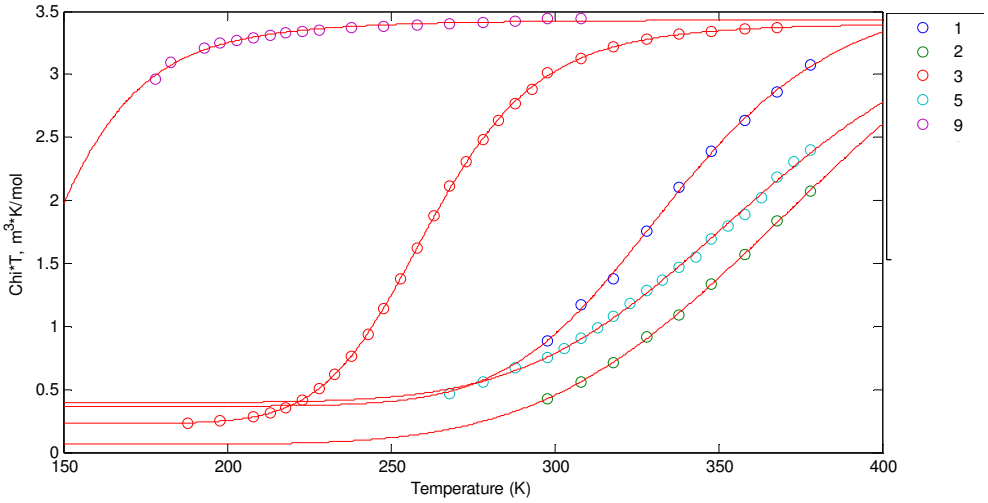

Figure B27. Variable temperature Evans method data, with fits to Equation B2.

	6.1	**6.2**	**6.3**	**6.5**	**6.9**
$(\chi T)_{HS}$ (m^3K/mol)	3.365 [2.267, 4.464]	4.777 [1.223, 8.331]	3.181 [3.164, 3.197]	3.5 [2.522, 4.478]	3.379 [-16.28, 23.03]
ΔH (cm^{-1})	2990 [1746, 4234]	2109 [1189, 3029]	2836 [2800, 2872]	2349 [1877, 2822]	1064 [418.8, 1709]
T_c (K)	337.2 [331.1, 343.3]	393.4 [332.7, 454]	262.1 [261.8, 262.3]	367.4 [348.5, 386.3]	146.3 [39.15, 253.4]
$(\chi T)_{LS}$ (m^3K/mol)	0.3665 [-0.1379, 0.8709]	0.06145 [-0.2008, 0.3237]	0.2266 [0.2168, 0.2363]	0.3954 [0.3053, 0.4856]	0.05959 [-19.57, 19.69]
Adj. R^2	0.9983	0.9994	0.9999	0.9981	0.9880
RMSE	0.320	0.0136	0.0093	0.0256	0.0137

Table B1. Fit parameters to Equation S2 for variable-temperature Evans method data for compounds **6.1-6.3**, **6.5**, and **6.9.** 95% confidence bounds for each fit parameter are provided in brackets following the fitted value. Nonzero values for $(\chi T)_{LS}$ may reflect either paramagnetic impurities or uncertainties in the fit.

B.3 Variable-temperature UV-Vis spectroscopy

Note: in all spectral decomposition figures shown below, the red trace represents the overall (fit) spectrum, and the blue, green, and purple traces represent the individual Gaussian functions.

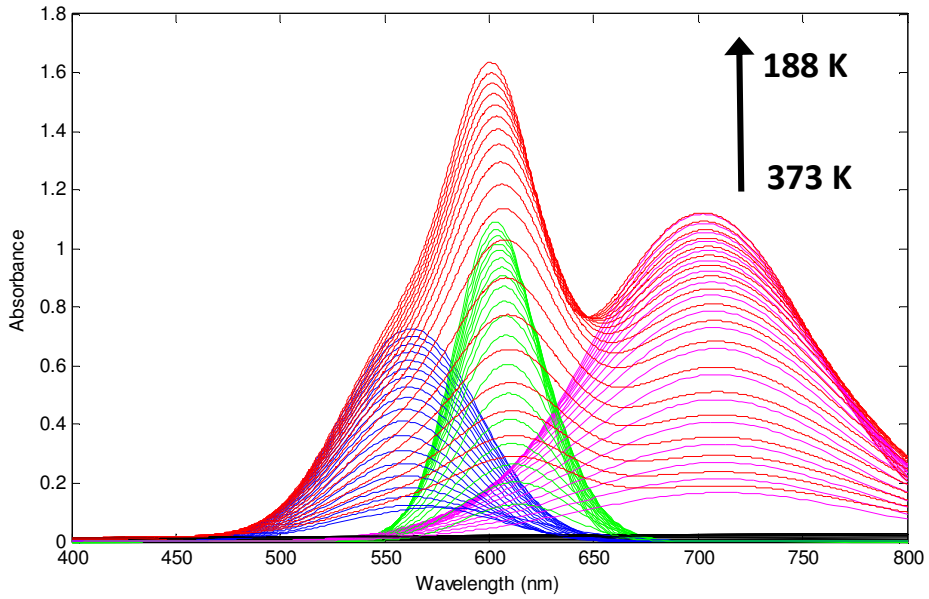

Figure B28. Spectral decomposition of the variable temperature UV-Vis spectra of **6.1**.

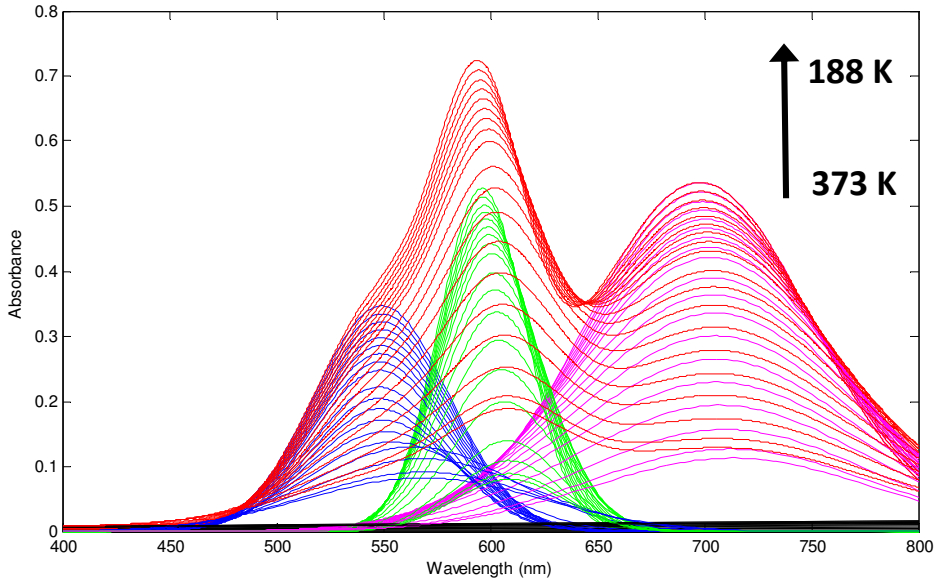

Figure B29. Spectral decomposition of the variable temperature UV-Vis spectra of **6.2**.

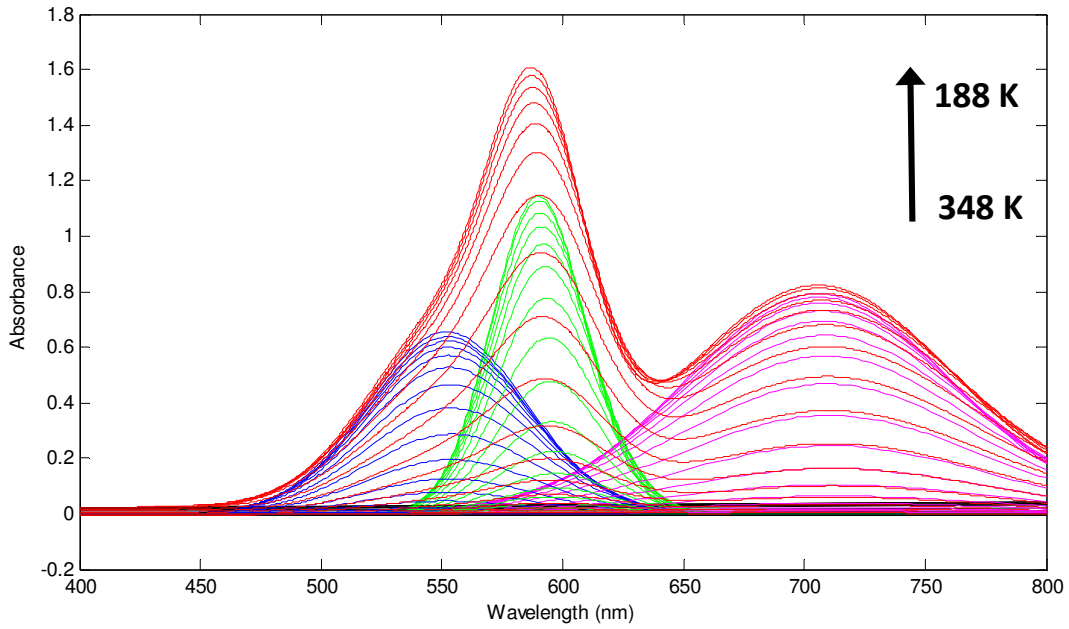

Figure B30. Spectral decomposition of the variable temperature UV-Vis spectra of **6.3**.

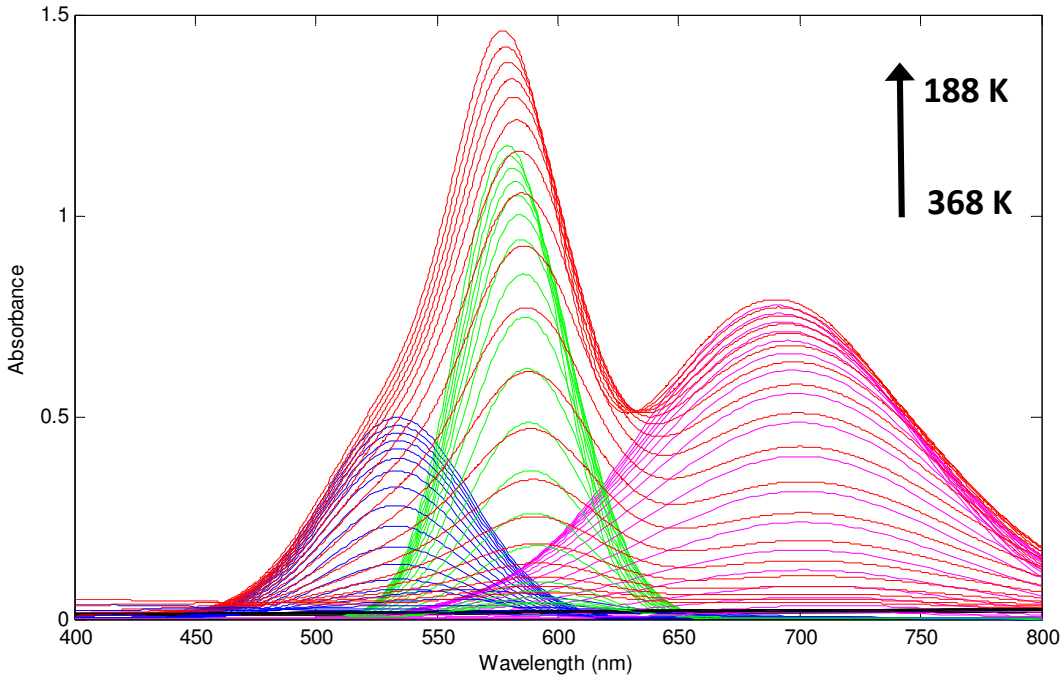

Figure B31. Spectral decomposition of the variable temperature UV-Vis spectra of **6.4**.

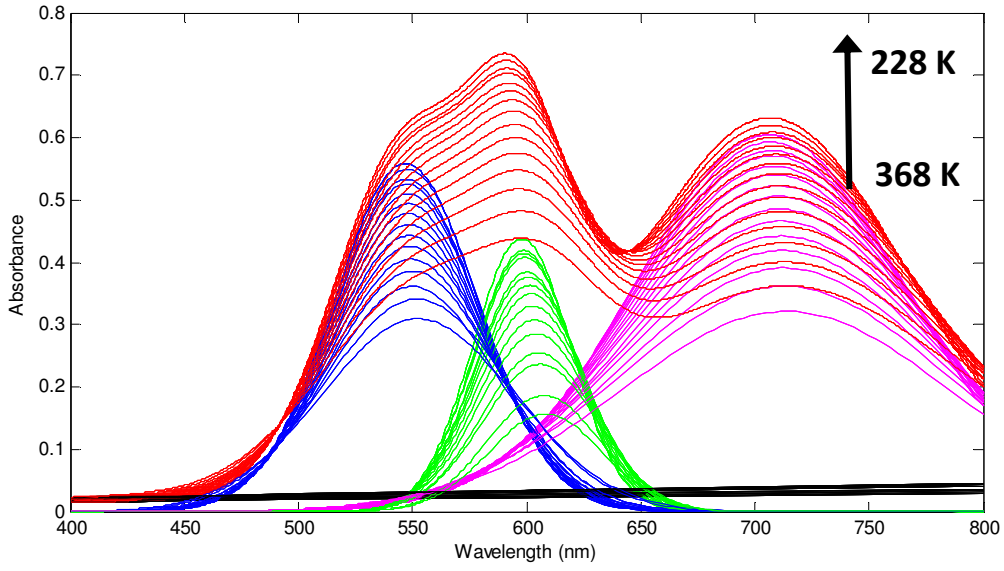

Figure B32. Spectral decomposition of the variable temperature UV-Vis spectra of **6.6.**

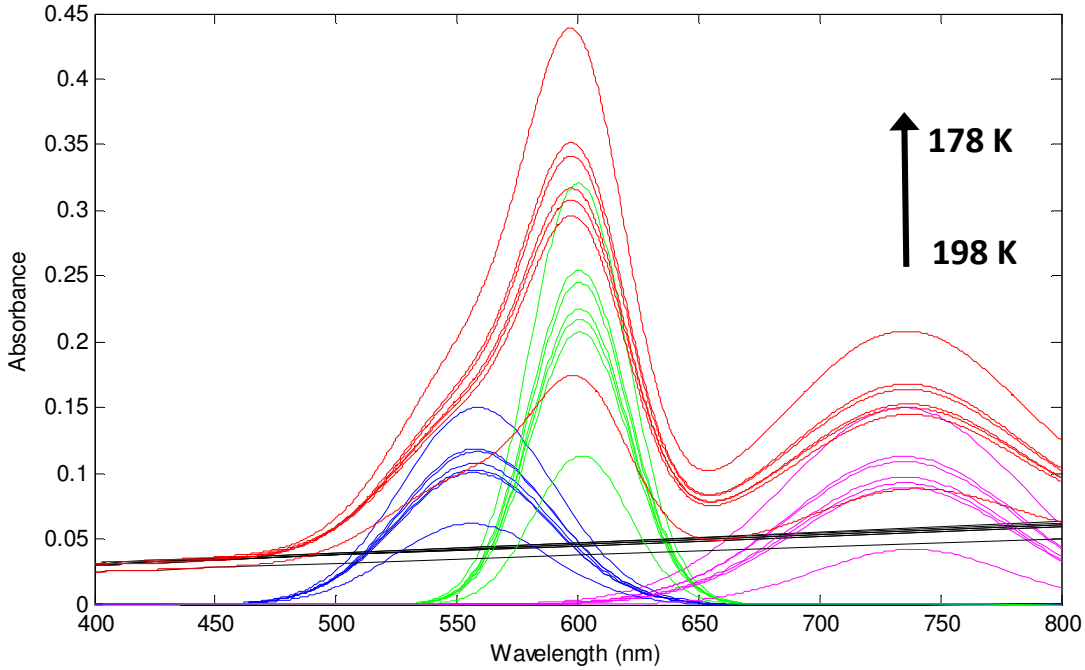

Figure B33. Spectral decomposition of the variable temperature UV-Vis spectra of **6.9**.

Each set of variable temperature UV-Vis spectra was fit to the sum of three Gaussian functions plus a first-order baseline (Equation B3) in the relevant spectral region. Complex **6.1** is discussed below in detail as an example (Figure B29). Data was fit from 501 nm to 851 nm to the following equation using a least-squares fitting procedure in Matlab:

$$Abs = a * l/\sqrt{\pi} * e^{(-a^2*(x-b)^2)} + c * m/\sqrt{\pi} * e^{(-c^2*(x-d)^2)} + f * n/\sqrt{\pi} * e^{(-f^2*(x-g)^2)} + (q * x)$$

Equation B3

Parameters a, c, and f relate to the FWHM of each Gaussian function, l, m, and n are the area under the peak, and b, d, and g correspond to the wavelength of the peak maximum. The q parameter corresponds to the linear baseline term. Figures B34-B37 show the resulting fit parameters for complex **6.1**.

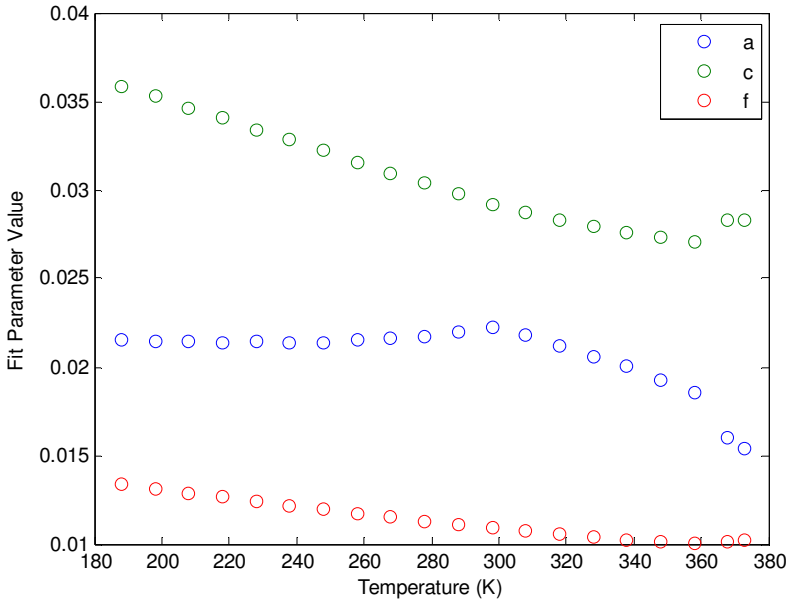

Figure B34. Fit values of the parameters a, c, and f (Equation B3) for compound **6.1**.

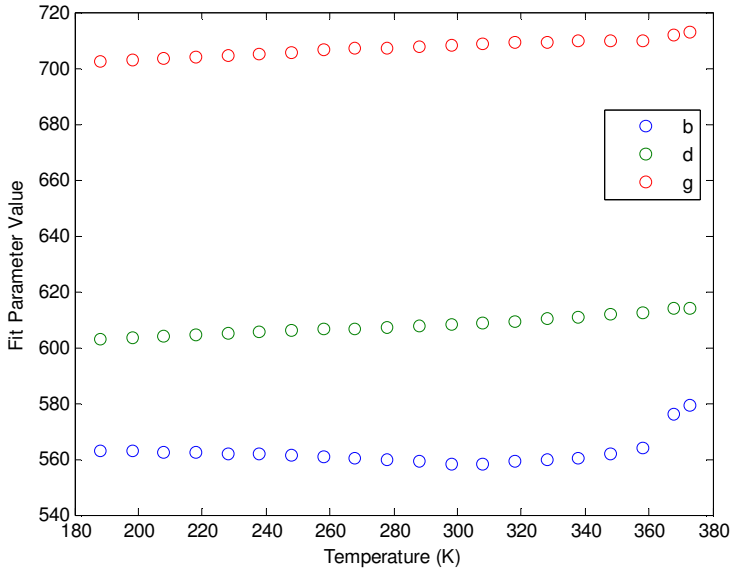

Figure B35. Fit values of the parameters b, d, and g (Equation B3) for compound **6.1**.

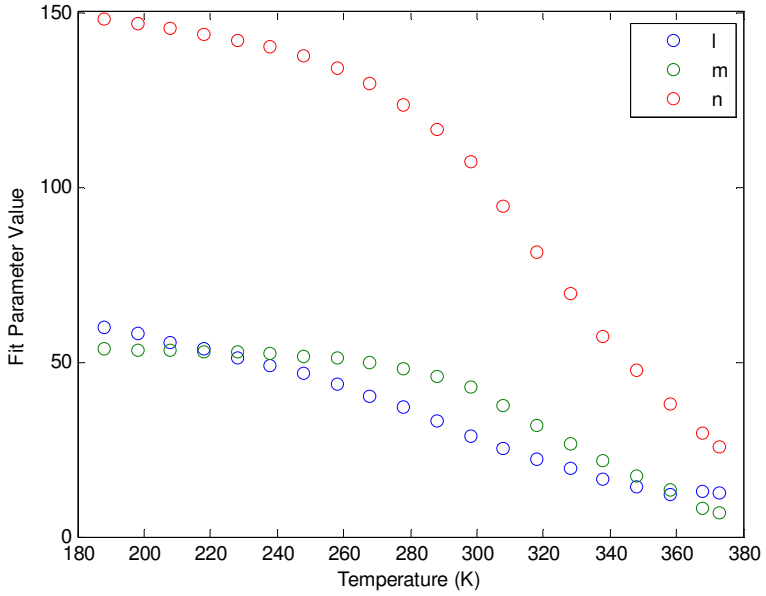

Figure B36. Fit values for the parameters l, m, and n (Equation B3) for compound **6.1**.

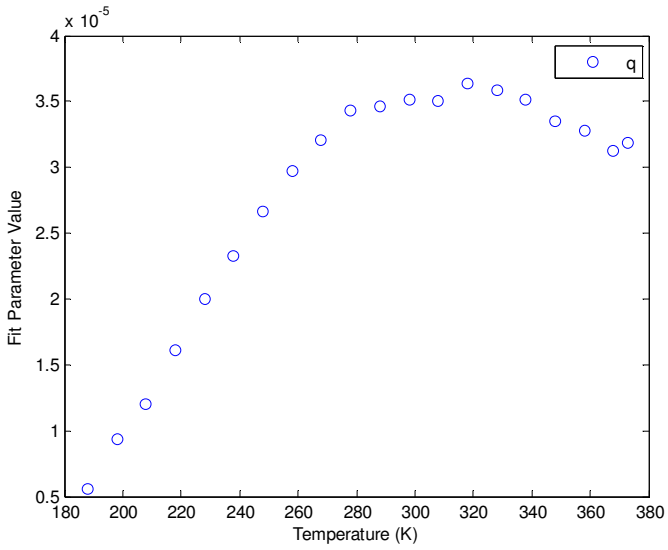

Figure B37. Fit values for the parameter q (Equation B3) for compound **6.1**.

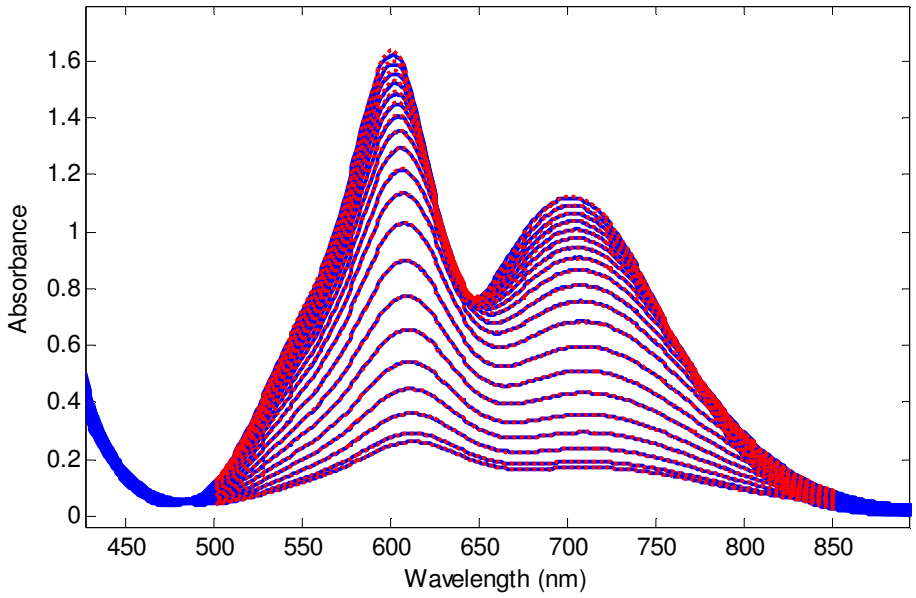

Figure B38. Fits (dotted red lines) according to Equation B3 for the variable-temperature UV-Vis spectra (solid blue lines) of complex **6.1**.

Parameters l, m, and n, which should be proportional to the concentration of the low-spin form of **6.1**, were adjusted to account for the change in total concentration of **6.1** with temperature due to the change in density of toluene.

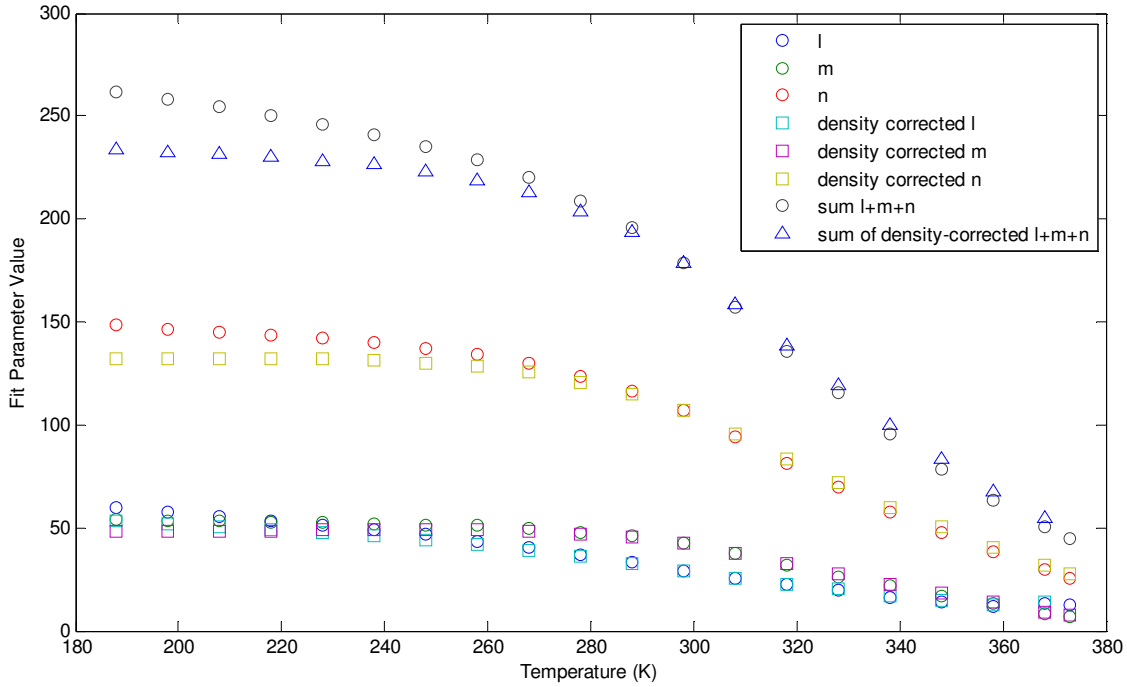

Figure B39. Density correction on fit parameters l, m, and n.

Note that simply plotting the maximum absorbance for a given absorption feature as a function of temperature gives unsatisfactory results (Figure B40) and cannot be well fit to Equation 6.2 (Figure B41), as compared to the results given in Figure 6.5.

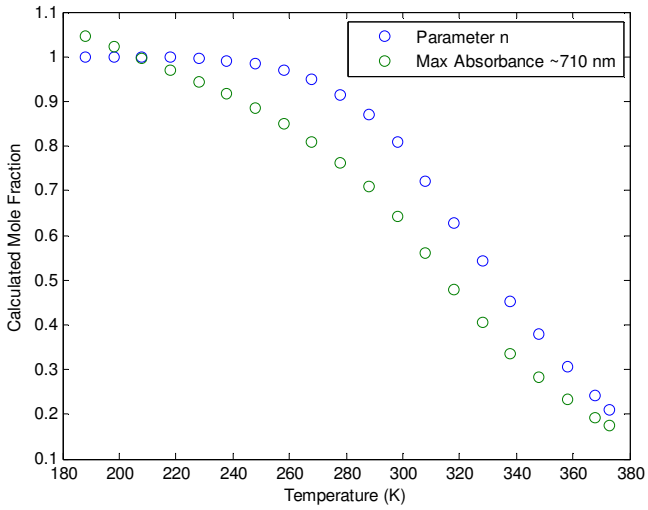

Figure B40. Calculated mole fraction of low-spin form of compound **6.1** as a function of temperature, calculated (Eqn. 6.2 and 6.3, normalized in accordance with the fit to the Boltzmann Equilibrium) based on either parameter n (area of the 710 nm peak) or the maximum absorbance of the 710 nm peak (after correction for density variations).

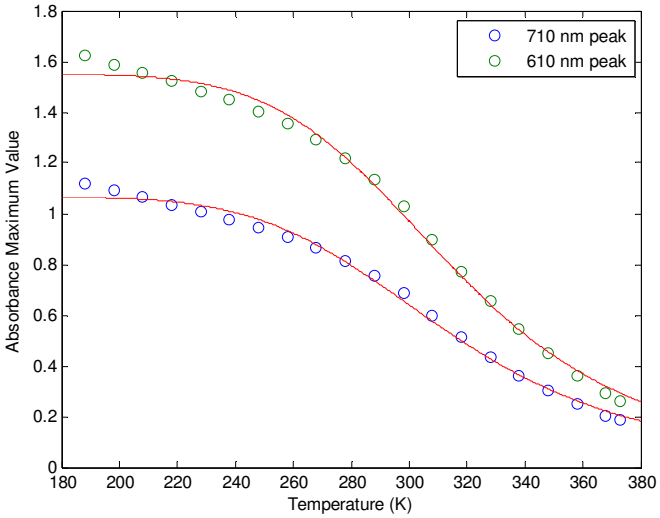

Figure B41. Best fits according to a Boltzmann equilibrium expression (Eqn. 6.2) for the maximum absorbances of the UV-Vis bands at 710 nm and 610 nm as a function of temperature for compound **6.1**.

B.4 Variable-temperature Mossbauer spectroscopy

A sample of lyophilized **6.3** was measured across a series of temperatures, and fits to the data were used to probe the Mossbauer parameters and mole fractions of the high- and low-spin states. The lack of measurable change in the low-spin mole fraction between 80 K and 150 K is reflective of the gradual and incomplete solid-state spin-crossover as observed by SQUID magnetometry.

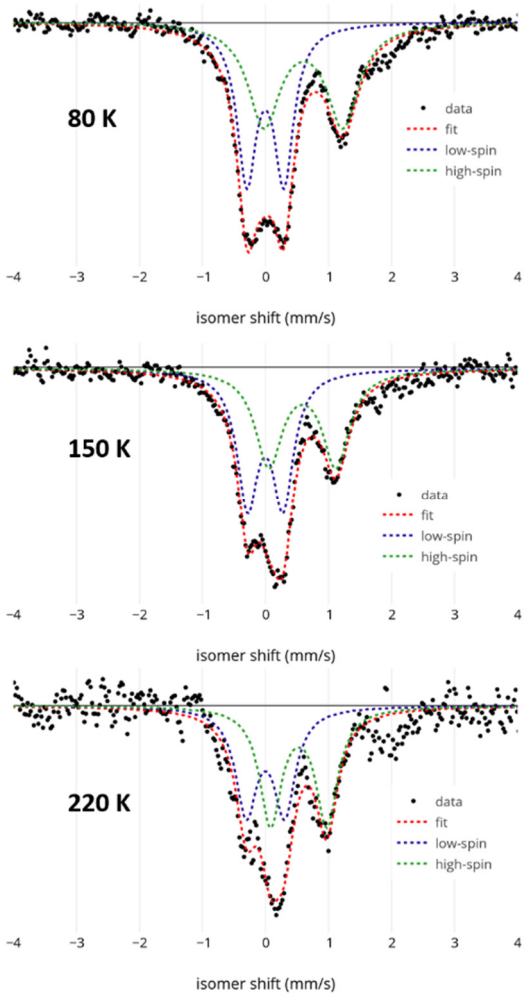

Figure B42. Variable-temperature Mossbauer of lyophilized **6.3**. A peak discernible around 2 mm/s is likely due to some decomposition of this highly air/water-sensitive sample during handling and measurement.

	isomer shift (δ, mm/s)	quadrupole splitting (ΔE_Q, mm/s)	% composition
6.3 (lyophilized, 80 K)	0.000	0.603	51
--	0.607	1.252	49
6.3 (lyophilized, 150 K)	0.000	0.568	51
--	0.584	1.052	49
6.3 (lyophilized, 220 K)	-0.054	0.612	41
--	0.511	0.919	59

Table B2. Fits to variable-temperature Mossbauer spectra shown in Fig. B42.

B.5 Additional SQUID magnetometry data

A complicating effect in the solid-state magnetometry is that the samples appear to undergo an irreversible change in the spin-transition properties upon heating to 400 K. This is apparent in Figure B43 which shows the magnetic moment curves upon heating the sample from 4 K to 400 K and then back. After the first heating cycle no further change is seen regardless of how many times the sample is heated back to 400 K. This does not appear to be due to sample decomposition; NMR analysis of a sample after measurement shows minimal change, and independent experiments confirm that the complexes are thermally stable towards heating to 400 K for several hours in the solid state. Instead, it is likely due to loss of co-crystallized solvent during heating under vacuum, and/or to some other irreversible change in the crystal lattice. This would likely result in decreased crystallinity or more defect-ridden crystals with a higher concentration of grain boundaries, which would be expected to lead to a more gradual and incomplete spin transition, as is observed. If the sample is heated to 400 K under vacuum for several hours *prior* to measurement in the SQUID magnetometer, this change is no longer observed and the initial heating and cooling curves are identical (Figure B44).

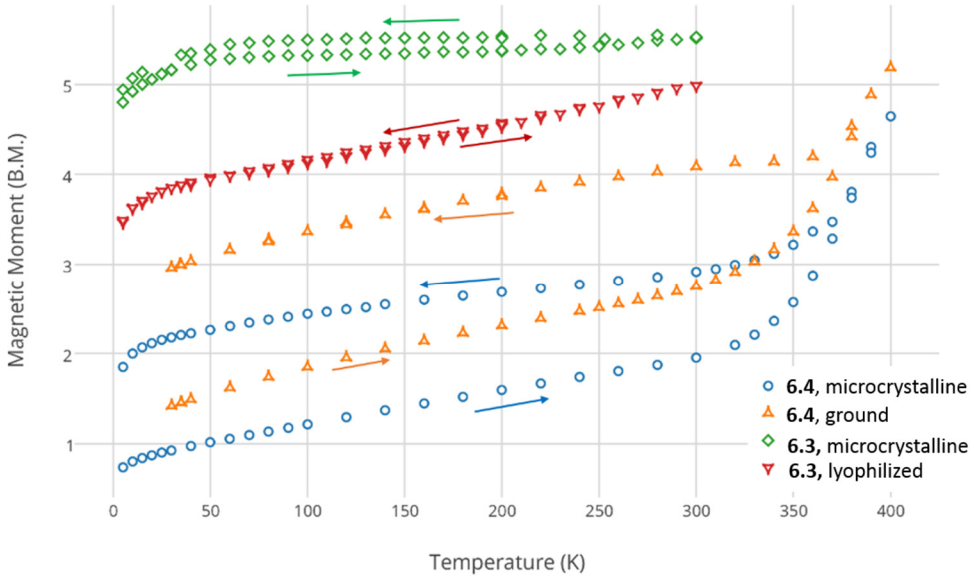

Figure B43. Solid-state magnetometry showing the effect of sample preparation and heating on the measured properties. Arrows show the direction of temperature change for the accompanying trace.

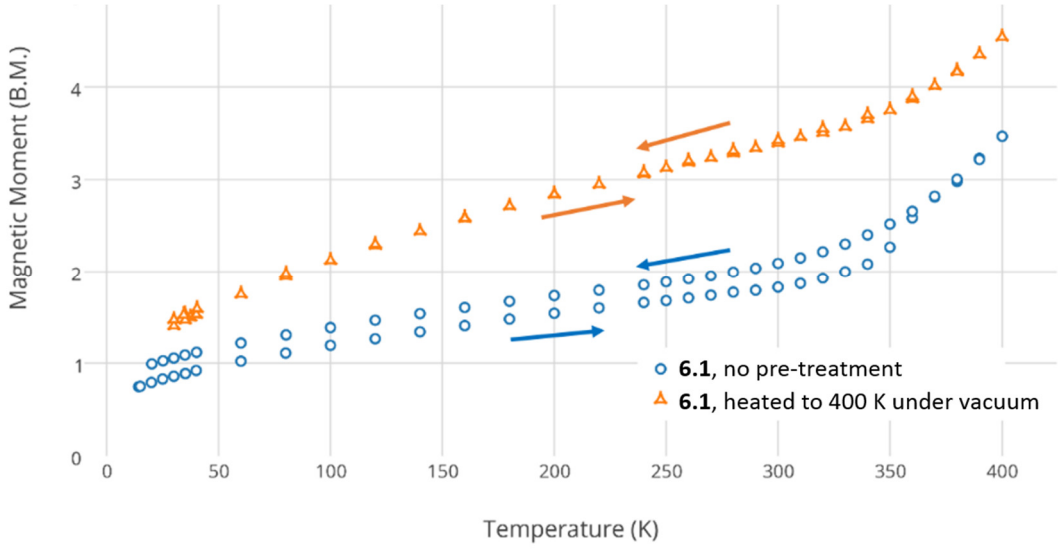

Figure B44. Effect of high-temperature annealing on the observed solid-state magnetic moment of compound **6.1**. Arrows show the direction of temperature change for the accompanying trace.

B.6 Crystallographic Details

	6.1	**6.2**	**6.4**	**6.5**
Crystal system	Triclinic	Triclinic	Monoclinic	Monoclinic
Space group	P-1	P-1	P21/c	P21/n
a (Å)	14.1262(16)	13.4315(6)	26.3693(16)	19.044(4)
b (Å)	14.4698(16)	13.7422(6)	21.5683(16)	26.976(5)
c (Å)	29.339(3)	19.4813(9)	27.7869(19)	21.047(4)
α (deg)	93.996(2)	102.539(2)	90	90
β (deg)	97.983(2)	90.247(2)	92.170(2)	91.667(5)
γ (deg)	105.183(2)	116.120(1)	90	90
Z	2	2	2	4
V (Å^3)	5613.8(11)	3131.1(2)	15792.2(19)	10808(4)
Indep. Reflections	26580	19113	71324	35272
R(int)	0.054	0.043	0.112	0.096
R1	0.0588	0.0517	0.0582	0.0745
wR2	0.1703	0.1545	0.1654	0.1873
GOF	1.04	1.05	0.92	1.20

Table B3. Crystallographic details for compounds **6.1**, **6.2**, **6.4**, and **6.5**.

	6.7	**6.8**	**6.9**
Crystal system	Orthorhombic	Cubic	Triclinic
Space group	P212121	P213	P-1
a (Å)	10.339(4)	16.8490(5)	10.5753(3)
b (Å)	14.733(5)	16.8490(5)	12.4643(3)
c (Å)	29.561(13)	16.8490(5)	14.9052(4)
α (deg)	90	90	88.155(1)
β (deg)	90	90	79.993(1)
γ (deg)	90	90	89.882(1)
Z	4	4	2
V (Å^3)	4503(3)	4783.2(4)	1933.80(9)
Indep. Reflections	21240	8421	12083
R(int)	0.097	0.054	0.032
R1	0.0682	0.0529	0.0427
wR2	0.1607	0.1351	0.1243
GOF	1.06	0.94	1.12

Table B4. Crystallographic details for compounds **6.7**-**6.9**.

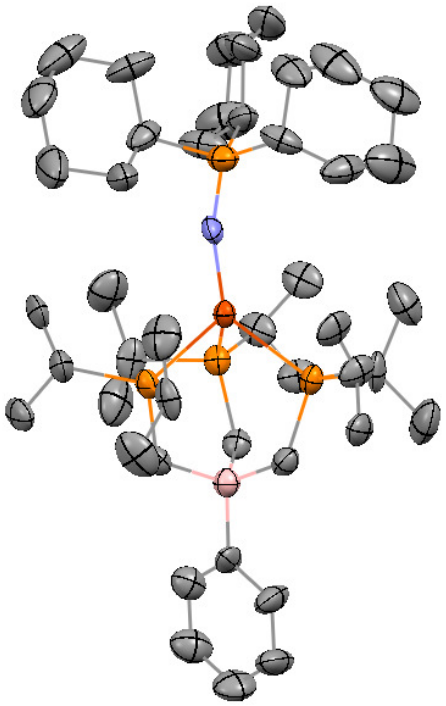

Figure B45. Crystal structure of complex **6.8**. For clarity, hydrogen atoms are omitted and only one component of disordered groups is shown. The molecule lies on a three-fold axis of symmetry with only one third of the molecule present in the asymmetric unit and the rest generated by symmetry. Thermal ellipsoids are shown at 50%.

B.7 Computational Results

A time-dependent DFT calculations was carried out with Gaussian 09 on complex **6.4** (S = 0) using the crystallographically determined atomic coordinates, and the hybrid B3LYP functional. The 6-311G(df) basis set was used for the iron and phosphorus atoms and 6-31G(d) was used on the remaining atoms. Only the first three singlet excited states were calculated. Although the results are not quantitatively consistent with the measured spectra (this would likely require the use of more sophisticated functional and basis set), they do suggest that the absorbance features absorbed in the visible region do correspond primarily to d-d transitions. The orbitals involved are depicted pictorially in Figure 6.13.

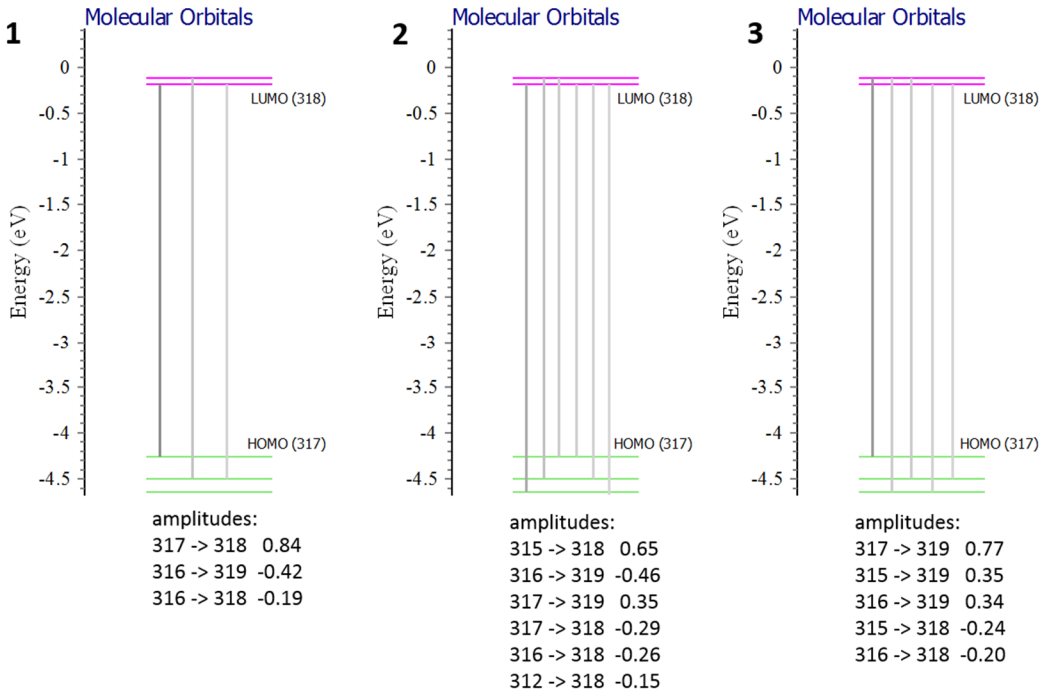

Figure B46. TDDFT results: orbital compositions of the first three calculated singlet excitations.

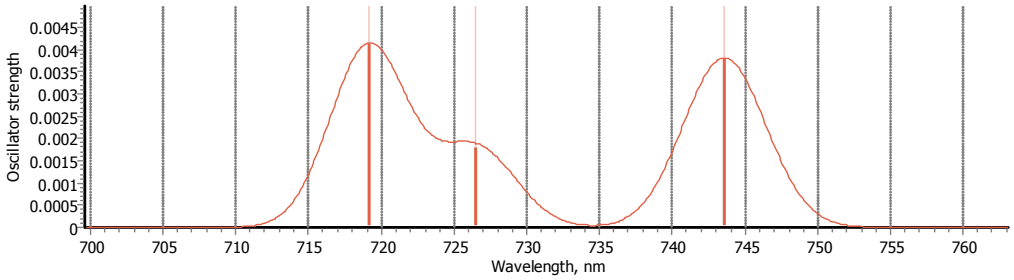

Figure B47. Calculated spectrum (first three singlet excitations).